

ABSTRACT

ROBERTS, JAMES GARLAND. Advancing Microelectrode Technology for Neuroscience Applications. (Under the direction of Dr. Leslie A. Sombers).

Understanding of the central nervous system has advanced tremendously by the ability to link chemical fluctuations with behavioral, cognitive, and emotional states of animals. Electrochemical techniques are well-suited for these measurements, especially when utilizing background-subtracted fast-scan cyclic voltammetry (FSCV) coupled with carbon-fiber microelectrodes. This union combines the high spatial resolution of the microelectrode with the selectivity and the temporal resolution of fast-scan voltammetry, and has led to exciting progress in many fields of neuroscience. However, there are also many possible avenues to improve FSCV. Electrodes can be engineered to produce more sensitive and selective sensors, data analysis can be improved to extract more information from *in vivo* data, and applied waveforms can be altered to elicit more sensitivity and chemical selectivity.

This research aims to advance FSCV to applications monitoring non-electroactive molecules, as well as those that are traditionally difficult to detect. Hydrogen peroxide (H_2O_2) is an endogenously produced reactive oxygen species that has recently gained appeal as a neuromodulator and is widely used as a reporter molecule in the biosensing community. The first voltammetric measurement of H_2O_2 on carbon electrodes in living tissue is described, and the chemical mechanisms underlying this detection are investigated. Electron paramagnetic spectroscopy identified that hydroxyl radicals were electrochemically generated at the electrode surface and anodic current was dependent on the presence of this radical. Carbon and platinum electrode substrates were investigated to determine the most

appropriate sensor for monitoring H_2O_2 in biological samples. Carbon electrodes coated with Nafion, a cation-exchange polymer, showed enhanced sensitivity to H_2O_2 detection.

Additional research sought to advance electrode sensitivity, by evaluating electrode substrates, electrode coatings, and surface chemistry. Utilizing Raman Spectroscopy, it was found that higher anodic wavelimits increased the population of oxygen-containing functional groups, resulting in enhanced sensitivity to dopamine detection. Furthermore, FSCV was adapted to monitor methionine-enkephaline (mENK), a naturally-occurring opioid peptide and neuromodulatory that is present in very low concentrations in vivo. Additionally, peptides are inherently difficult to monitor electrochemically because of electrode fouling. An optimized waveform was developed to enable the detection of tyrosine-containing peptides, such as mENK, in brain tissue.

In all electrochemical experiments, current must be converted to analyte concentration by way of a calibration that usually takes place at the end of the experiment. However, studies in neuroscience also require verification of electrode placement in brain tissue. This is accomplished at the end of the experiment by passing a large current through the electrode to lesion the area, destroying the electrode. Advanced statistical methods were successfully developed to meet a critical need to eliminate traditional calibration methods. This calibration method will allow researchers to use non-faradaic background currents, collected during the experiment, to accurately predict calibration factors without removing the electrode from the brain, and will thus enable the electrode to be sacrificed for tissue lesion.

Finally, this dissertation describes the application of FSCV to the characterization of a bacterially-produced metal chelator, protochelin, which is associated with the sequestration

and mobility of iron. This voltammetric approach provides a comprehensive functional analysis relating the redox chemistry of the chelator to structural changes in real-time. It was found that the ligand was easier to oxidize than the bound metal, suggesting an alternative metal release mechanism.

Overall, the fundamental experiments and advances described herein can be exploited to enable lower limits of detection, target new molecules, obtain higher spatial resolution, and simultaneously measure multiple analytes in a single location. These results will enable FSCV to fill critical needs across scientific disciplines ranging from neuroscience to environmental monitoring.

© Copyright 2013 by James Garland Roberts

All Rights Reserved

Advancing Microelectrode Technology for Neuroscience Applications

by
James Garland Roberts

A dissertation submitted to the Graduate Faculty of
North Carolina State University
in partial fulfillment of the
requirements for the degree of
Doctor of Philosophy

Chemistry

Raleigh, North Carolina

2013

APPROVED BY:

Leslie A. Sombers
Committee Chair

Kenneth W. Hanck
Professor Emeritus

Edmond F. Bowden
Professor

Gregory S. McCarty
Assistant Professor, Biomedical
Engineering

DEDICATION

To my family and friends, past and present, thank you all for the love and support to finish this chapter of my life. To Crystal for understanding my path and being by my side the whole way through. I especially want to dedicate this dissertation to my late grandparents, Helen and James Tillman, who always wanted to see me get an education, but they never thought I would take it this far.

Speak softly and carry a big stick, you will go far

- Theodore Roosevelt, 1900

BIOGRAPHY

On October 5th 1979, James Garland Roberts was born in Hickory, NC to Jerry and Rosemary Roberts. He spent his adolescent years in Conover, NC, and attended as much public school as was required. His interest in science began at an early stage, when no one could answer his questions and found out that science could.

As a truck driver, welder, and machinist, his father taught him the true meaning of hard work and resourcefulness. His mother, a homemaker, taught him how to love and the fine art of independent living. Joshua, his older brother, educated him on everything else about life, good and bad.

Through high school, James was employed by several fast-food chains and retail stores, where he found the true meaning of minimum wage. His love for the car and automobile racing led him to a career as an automotive mechanic, after high school. He soon realized that he could build, repair, or race anything he desired. After a several years of hard, but rewarding work, he found a better opportunity to adapt his knowledge and talents. He joined a local company that designed, built, and sold computer controlled 3-axis cutting machines. Several years were spent manufacturing, designing, programming, and improving these unique machines. He rapidly progressed through the company by completing machine sales and performing off-site training of the equipment and software. Eventually he made Vice President of the company. He soon left the company after realizing there was no room for advancement and sought the better life and new challenges that a formal education could bring.

In the summer of 2004, he enrolled in the chemistry program at Catawba County Community College. His choice of chemistry was solely based on the principle that it sounded difficult and seemed to be the most applicable science for a different career in industry. This was his first step towards a college degree and soon realized the goal was attainable. He won many awards in mathematics and chemistry, and even helped the college win a national mathematics competition. In 2006, Lenoir-Rhyne College (now University) accepted him into the chemistry program, where he continued to excel. He earned more awards and graduated with honors in 2008. As no one in his immediate family has a college degree, he felt that he would be a better role model for the younger family members if he attained his doctorate. Following this decision, he enrolled in the Ph.D. chemistry program at North Carolina State University to pursue research related to novel neuroscience applications under the direction of Leslie Sombers.

ACKNOWLEDGMENTS

To all who have generously gave their time and energy during my completion of this dissertation.

First, I would especially like to thank Dr. Leslie Sombers for her continual support and leadership throughout my graduate career. Thanks to all the members of the Sombers lab, past and present, for helpful discussions on research related topics and any help along the way. I would also like to thank Andreas “Andy” Schmidt for getting me out of the lab and onto the soccer field, Leyda Lugo-Morales for always being kind and willing to study, and Dr. Thomas Chen for answering research related questions and the entertaining socioeconomical discussions. Furthermore, I want to thank my collaborators from other research groups at NCSU that I have worked with over the years (Dr. Tatyana Smirnova, Dr. Owen Duckworth, and Dr. Gregory McCarty). Additionally, I would like to acknowledge Dr. Tommy Guillot for teaching me how to perform rat brain-slice experiments.

Finally, none of this research would have been possible without the funding from the National Science Foundation, BASF, and the North Carolina State University Chemistry Department.

TABLE OF CONTENTS

LIST OF TABLES	xvii
LIST OF FIGURES	xviii
CHAPTER 1: Introduction to Monitoring Neurotransmission with Voltammetric Methods and Approaches for Technique Optimization.....	1
1.1 Neurons, Neurotransmission, and Neuronal Degradation	1
1.2 Methods for Studying Neurotransmission	4
1.2.1 Electrophysiology	5
1.2.2 Microdialysis	6
1.2.3 Electrochemical	7
1.2.4 Amperometry	8
1.2.5 Differential Pulse Voltammetry	9
1.2.6 Fast-Scan Cyclic Voltammetry (FSCV)	9
1.3 Carbon-Fiber Microelectrodes	13
1.4 Advancing Electrode Substrate, Coating, and Geometry	15
1.5 Altering the Applied Waveform	17
1.6 Advanced Data Analysis	18
1.7 Dissertation Overview	19
1.8 References	21
CHAPTER 2: Real-Time Chemical Measurements of Dopamine Release in the Brain	27

2.1	Introduction	27
2.1.1	Use of FSCV in Dopamine Detection	28
2.2	Materials	30
2.2.1	Electrode Fabrication	29
2.2.2	Surgery	31
2.2.3	Electrochemistry	32
2.2.4	Stimulation	33
2.2.5	Electrode Postcalibration	34
2.3	Methods	34
2.3.1	Electrochemistry, Instrumentation, and Software	34
2.3.2	Bipolar Electrical Stimulation	36
2.3.3	Electrode Fabrication	37
2.3.3.1	Carbon-Fiber Microelectrode	37
2.3.3.2	Ag/AgCl Reference Electrode	39
2.3.4	Surgery	40
2.3.4.1	Anesthetized Preparation	40
2.3.4.2	Freely-Moving Preparation	41
2.3.5	Freely-Moving Rat Experiment	44
2.3.5.1	Making the Connection	44
2.3.5.2	Lowering the Carbon-Fiber Microelectrode	45
2.3.6	Anesthetized Rat Experiment	46
2.3.7	After the Experiment	47

2.3.7.1	Verification of Electrode Placement	47
2.3.7.2	Electrode Postcalibration	48
2.3.8	Data Analysis	49
2.3.9	FSCV Combined with Electrophysiology	50
2.3.10	FSCV Combined with Intracranial Self-Stimulation	50
2.3.11	FSCV and Methods of Localized Pharmacological Manipulation	51
2.3.12	Recent Advances	52
2.4	Notes	54
2.5	References	55
 CHAPTER 3: Specific Oxygen-Containing Functional Groups on the Carbon		
	Surface Underlie an Enhanced Sensitivity to Dopamine at	
	Electrochemically Pretreated Carbon Fiber Microelectrodes	59
3.1	Introduction	59
3.2	Experimental Section	61
3.2.1	Chemicals	61
3.2.2	Electrode Fabrication	61
3.2.3	Flow Injection	62
3.2.4	Electrochemical Data Acquisition	62
3.2.5	Surface Analysis	63
3.2.6	Chemical Derivatization	63
3.2.7	Statistics	64
3.3	Results and Discussion	64

3.3.1	Electrochemical Pretreatment Enhances Electrode Sensitivity	64
3.3.2	Atomic Force Microscopy	67
3.3.3	Adsorption Isotherm	68
3.3.4	Raman Spectroscopy of Carbon-Fiber Microelectrode Surface	71
3.3.5	Electrochemical Characterization of Chemically Modified Electrodes	76
3.4	Conclusions	78
3.5	References	79
CHAPTER 4: Voltammetric Detection of Hydrogen Peroxide at		
	Carbon-Fiber Microelectrodes	84
4.1	Introduction	84
4.2	Experimental Section	86
4.2.1	Chemicals	86
4.2.2	Electrode Fabrication	87
4.2.3	Data Acquisition	87
4.2.4	Flow Injection	88
4.2.5	Enzyme Coating of Microelectrodes	88
4.2.6	Brain Slice Experiment	89
4.2.7	Statistics	89
4.3	Results and Discussion	90
4.3.1	H ₂ O ₂ Cyclic Voltammetry	90
4.3.2	Signal Validation	93
4.3.3	Characterization of H ₂ O ₂ Electrochemistry	94

4.3.4	Voltammetric Detection of H ₂ O ₂ in a Brain Slice	98
4.3.5	Enzymatic Production of H ₂ O ₂	99
4.4	Conclusions	100
4.5	References	101
CHAPTER 5: Comparison of Electrode Materials for the Detection of Rapid		
Hydrogen Peroxide Fluctuations Using Background-Subtracted		
Fast Scan Cyclic Voltammetry		
		104
5.1	Introduction	104
5.2	Experimental	106
5.2.1	Chemicals	106
5.2.2	Electrode Fabrication	107
5.2.3	Data Acquisition	107
5.2.4	Flow Injection System	108
5.2.5	Statistics	108
5.3	Results and Discussion	109
5.3.1	Waveform Optimization	109
5.3.2	FSCV of H ₂ O ₂ on Carbon and Platinum Electrodes	111
5.3.3	Enzymatic Verification	115
5.3.4	Mechanistic Insights	116
5.3.5	Interfering Species	118
5.4	Conclusions	122
5.5	References	123

CHAPTER 6: The Role of Hydroxyl Radical Generation in the Voltammetric	
Detection of Hydrogen Peroxide	128
6.1 Introduction	128
6.2 Materials and Methods	130
6.2.1 Chemicals	130
6.2.2 Electrode Fabrication	130
6.2.3 Data Acquisition	131
6.2.4 Flow Injection System	131
6.2.5 Spin-Trapping Experiments	132
6.2.6 EPR Measurements	132
6.2.7 Digital Simulations	133
6.2.8 Digital Simulation Parameters	133
6.2.9 Statistics	133
6.3 Results and Discussion	134
6.4 Conclusions	144
6.5 References	145
CHAPTER 7: Analyte Specific Waveform for the Voltammetric Detection	
and Characterization of Met-Enkephalin in Brain Tissue	147
7.1 Introduction	147
7.2 Methods	150
7.2.1 Chemicals	150
7.2.2 Electrode Fabrication	150

7.2.3	Flow Injection	151
7.2.4	Electrochemical Waveform and Data Acquisition	151
7.2.5	Brain Slice Experiments	152
7.2.6	Statistics	153
7.3	Results	153
7.3.1	Met-Enkephalin Cyclic Voltammetry	153
7.3.2	Electrochemical Moiety	156
7.3.3	Reproducibility of Met-Enkephalin Electrochemistry	157
7.3.4	Selectivity Compared to Common Interferents	159
7.3.5	Comparing Other Tyrosine-Containing Peptides to mENK	161
7.3.6	Detection Met-Enkephalin in Living Brain Tissue	163
7.4	Conclusions	164
7.5	References	165
CHAPTER 8: Eliminating Standard Electrode Calibration with a Novel		
	Approach to Accurately Quantify <i>in vivo</i> Voltammetric Data	168
8.1	Introduction	168
8.2	Materials and Methods	170
8.2.1	Chemicals	170
8.2.2	Electrode Fabrication	170
8.2.3	Flow-Injection System	171
8.2.4	Data Acquisition	171
8.2.5	Traditional Electrode Calibration	172

8.2.6	Anesthetized Animal Experiments	173
8.2.7	Statistics	173
8.3	Results and Discussion	174
8.3.1	Electrochemical Properties and Sensitivity	174
8.3.2	Calibration Model	180
8.3.3	Testing the Model	182
8.4	Conclusions	185
8.5	References	186
 CHAPTER 9: Trace Metal Complexation by the Triscatecholate Siderophore		
	Protochelin: Structure and Stability	188
9.1	Introduction	188
9.2	Material and Methods	191
9.2.1	Materials	191
9.2.2	Ligand Characteristics	192
9.2.3	Fe(III)-Protochelin Spectrophotometric Titration	193
9.2.4	Mass Spectrometry Analysis of the Degradation Products of Protochelin and the Metal-Protochelin Complexes	193
9.2.5	Computations of Metal-Protochelin Complexes	194
9.2.6	X-ray Spectroscopy of Metal-Protochelin Complexes	194
9.2.7	Competition of Fe(III) and Mn(III) for Protochelin and Desferrioxamine B	196
9.2.8	Background-Subtracted Fast-Scan Cyclic Voltammetry (FSCV)	197

9.3 Results and Discussion	199
9.3.1 Solubility of Protochelin	199
9.3.2 Degradation of Protochelin and Metal-Protochelin Complexes	200
9.3.3 Formation of Metal-Protochelin Complexes	203
9.3.4 Determination of Mn(III)Proto ³⁻ Stability Constant	204
9.3.5 Fe(III)-Protochelin Complex Coordination Modes	207
9.3.6 Redox Chemistry of Protochelin and Metal Protochelin Complexes	210
9.3.7 Metal Protochelin Complex Computational Simulations	213
9.3.8 X-ray Spectroscopy of Metal-Protochelin Complexes	217
9.3.9 Relating Complex Structure to Stability	224
9.3.10 Implication for Metal Transport and Uptake	224
9.4 References	228
APPENDICES	236
APPENDIX A: Supplemental Information to Chapter 1	237
A.1 Material and Methods	237
A.1.1 Chemicals	237
A.1.2 Electrode Fabrication	237
A.1.3 Flow Injection	238
A.1.4 Electrochemical Data Acquisition	239
A.1.5 Statistics	239
A.2 Comparing Electrode Substrates for H ₂ O ₂ Oxidation	239
A.3 Development of a Two-Channel, Carbon-Fiber, Microdisc-Electrode Array	241

A.4 pH Dependence of Charging Current and the Oxidation of H ₂ O ₂ and Dopamine	244
A.5 References	249
APPENDIX B: WolfChrome: a Chromatography Program	251
B.1 Description	251
B.2 Hardware and Software Requirements	251
B.2.1 National Instruments and MATLAB	251
B.2.2 HPLC System	252
B.3 Overview of LabView	252
B.4 Background Information on HPLC and UV-VIS Absorbance Detection	253
B.5 Hardware Construction and Software Setup of WolfChrome	256
B.6 Data-Collection Software	259
B.7 Data-Analysis Software	262
B.8 Block Diagram of WolfChrome	267
B.9 Block Diagram of WolfChrome Analysis	271
B.10References	280
APPENDIX C: WolfAmp: an Amperometry Program	281
C.1 Description	281
C.2 Hardware and Software Requirements	281
C.2.1 National Instruments and MATLAB	281
C.2.2 Amperometric System	282
C.2.3 Flow Injection System	283

C.3 Overview of LabView	283
C.4 Amperometry Overview	284
C.5 Hardware Construction and Software Setup of WolfAmp	285
C.6 Data-Collection Software	288
C.7 Data-Analysis Software	293
C.8 Block Diagram of WolfAmp	299
C.9 Block Diagram of WolfAmp Analysis	303
C.10References	310
APPENDIX D: Supplemental Information to Chapter 9	311
D.1 Preparation of Protochelin Complexes	311
D.2 Formulation of Structural Models Used to Fit EXAFS Spectra	313
D.3 Background-Subtracted Fast-Scan Cyclic Voltammetry (FSCV) and Ligand Adsorption	315
D.4 References	321

LIST OF TABLES

Table 5.1	Sensitivities and limits of detection for various electrode substrates for H ₂ O ₂ detection	115
Table 6.1	Predicted concentrations of H ₂ O ₂ within a solution containing only H ₂ O ₂ , and within a solution containing H ₂ O ₂ plus a trapping agent ...	142
Table 6.2	Predicted concentration of histamine within a solution containing only histamine, and within a solution containing histamine plus DMPO ...	143
Table 8.1	Coefficients determined by multiple linear regression on Equation 1 for the training set	181
Table 9.1	Log of the stability constant of the metal complexes of a number of siderophores (T = 25 °C)	206
Table 9.2	Amplitude reduction factors, coordination numbers, interatomic distances, and Debye-Waller factors for M-siderophore complexes investigated in this study	220
Table D.1	Calculated theoretical bond length of the Fe and Mn complexes of protochelin	320
Table D.2	Calculated strain energies for Mn-protochelin complexes bound in the catecholate [M(III)Proto ³⁻] and salicylate [M(III)H ₃ Proto] forms	320

LIST OF FIGURES

Figure 1.1	Diagram of synaptic transmission	3
Figure 1.2	Background-Subtracted fast-scan cyclic voltammetry scheme	11
Figure 1.3	Flow chart illustrating the color plot	12
Figure 1.4	Representative images of different carbon-fiber microelectrode geometries	14
Figure 2.1	Principles of background-subtracted FSCV	29
Figure 2.2	Headstage (UNC-CH Electronics Design Facility)	33
Figure 2.3	Electrical stimulation	37
Figure 2.4	Micromanipulator (UNC-CH Machine Shop)	39
Figure 2.5	A top view illustration of a rat skull	41
Figure 2.6	Stimulation electrode	44
Figure 2.7	Oscilloscope output	46
Figure 2.8	Flow injection analysis system	48
Figure 2.9	Iontophoresis probe	52
Figure 2.10	Microelectrode array	53
Figure 3.1	Electrochemical pretreatment enhances electrode sensitivity	65
Figure 3.2	Electrochemical conditioning does not alter surface roughness	68
Figure 3.3	Electrochemical pretreatment increases adsorption of dopamine to the carbon microelectrode surface	70
Figure 3.4	Electrochemical conditioning increases surface carbonyl	

	and hydroxyl groups	72
Figure 3.5	Chemical derivatization of oxidized, edge-plane graphitic carbon at a microelectrode surface	75
Figure 3.6	Hydroxyl groups on the carbon fiber surface gained by electrochemical pretreatment with extended wavelimits underlie signal enhancement in the detection of DA	77
Figure 4.1	Fast-scan cyclic voltammetry of H ₂ O ₂	91
Figure 4.2	An oxidized electrode surface is required to accommodate the irreversible oxidation of H ₂ O ₂	92
Figure 4.3	Effect of various scan rates (V·s ⁻¹) on H ₂ O ₂ cyclic voltammetry	93
Figure 4.4	Enzymatic degradation of H ₂ O ₂	94
Figure 4.5	Characterization of H ₂ O ₂ electrochemistry	96
Figure 4.6	Selectivity and sensitivity in the presence of multiple interferents	97
Figure 4.7	H ₂ O ₂ detection in a brain slice contacting the striatum	99
Figure 4.8	Enzymatic production H ₂ O ₂ of at a glucose-oxidase modified carbon-fiber electrode	100
Figure 5.1	Background Current	110
Figure 5.2	Electrochemical response to H ₂ O ₂	113
Figure 5.3	Enzymatic verification of H ₂ O ₂ oxidation	116
Figure 5.4	Comparison of background-subtracted cyclic voltammograms collected on carbon and platinum	118
Figure 5.5	Background-subtracted cyclic voltammograms for interfering species	120

Figure 5.6	Selectivity of electrode substrates	121
Figure 6.1	Representative voltammograms	135
Figure 6.2	Representative voltammograms for H ₂ O ₂ on both carbon and platinum electrodes	136
Figure 6.3	Suspected radicals generated from the electrochemical oxidation of H ₂ O ₂	137
Figure 6.4	Representative EPR spectra of solutions containing DMPO and H ₂ O ₂ or DMPO alone	138
Figure 6.5	Representative voltammograms for individual analytes and a mixture of trapping agent and H ₂ O ₂	141
Figure 6.6	Representative voltammograms for histamine and adenosine collected on cylindrical carbon-fibers microelectrodes	144
Figure 7.1	Representative voltammetric data of 2 μM mENK on 100 μm cylindrical carbon-fiber microelectrodes, collected <i>in vitro</i>	154
Figure 7.2	Met-enkephalin is a five amino-acid peptide with terminating tyrosine and methionine groups	157
Figure 7.3	Effects of tyrosine fouling of the electrode surface	158
Figure 7.4	Calibration of mENK showing linear relationship between peak current and concentration	159
Figure 7.5	Selectivity and sensitivity in the presence of multiple interferents	160
Figure 7.6	Colorplots of 1 μM mENK	162
Figure 7.7	mENK detection in rat brain slices containing the striatum	164

Figure 8.1	Background-subtracted fast-scan cyclic voltammetry	174
Figure 8.2	Total background current plotted against the switching potential of the applied waveform	176
Figure 8.3	Traditional method of determining electrode sensitivity	178
Figure 8.4	Electrode sensitivity plotted against the switching potential of the applied waveform	179
Figure 8.5	Electrode sensitivity plotted against the total background current for each waveform	180
Figure 8.6	Predicted electrode sensitivity plotted against electrode sensitivity	182
Figure 8.7	Comparison of electrode calibration methods	184
Figure 9.1	Structures of the catecholate siderophore enterobactin, petrobactin, azotochelin, aminochelin, and protochelin	189
Figure 9.2	Plot of the change in absorbance spectrum of a solution of protochelin over time as ligand degradation occurs	201
Figure 9.3	UV-visible spectra obtained from the competition experiment between the Fe(III)Proto ³⁻ complex and the Mn(III)HDFOB ⁺ complex	205
Figure 9.4	Spectrophotometric titration of the Fe(III)Proto ³⁻ system as a function of pH from pH 9.1 to 4.4	208
Figure 9.5	Representative background-subtracted cyclic voltammograms measured for 20 μ M protochelin and 1 mM dopamine using a waveform ranging from -0.4 to +1.3 V at 400 V·s ⁻¹	211
Figure 9.6	Representative background-subtracted cyclic voltammograms	

	measured for protochelin and metal-protochelin complexes of manganese(III), iron(III), and cobalt(III)	212
Figure 9.7	Theoretical structure of the Mn(III)Proto ³⁻ complex in aqueous solution calculated by density functional theory	214
Figure 9.8	K-edge EXASF spectra of the Mn(III)Proto ³⁻ complex, the Fe(III)Proto ³⁻ complex bound through the catecholate binding mode, and the Fe(III)H ₃ Proto complex bound through salicylate binding mode	221
Figure A.1	Comparison of electrode substrate sensitivity to hydrogen peroxide Oxidation	240
Figure A.2	Representative scanning-electron micrograph of a dual-channel electrode	243
Figure A.3	Analysis of multichannel electrodes for discrete information	244
Figure A.4	Effects of pH on charging current	246
Figure A.5	Effects of pH on dopamine and H ₂ O ₂ detection	247
Figure A.6	pH dependant oxidative peak shifting for dopamine	248
Figure B.1	Diagram of a typical HPLC system	254
Figure B.2	Chromatogram collected with WolfChrome	255
Figure B.3	Diagram of electrical connections for data recording	258
Figure B.4	Schematic representation of data flow in WolfChrome	260
Figure B.5	Screenshot of WolfChrome	261
Figure B.6	Screenshot of WolfChrome Analysis front panel.....	263
Figure B.7	Screenshot of tabulated peak analyzer section	266

Figure B.8	Screenshot of WolfChrome block diagram	268
Figure B.9	WolfChrome block diagram, Part 1 of 2	269
Figure B.10	WolfChrome block diagram, Part 2 of 2	270
Figure B.11	Screenshot of WolfChrome Analysis block diagram	273
Figure B.12	WolfChrome Analysis block diagram, Part 1 of 6	274
Figure B.13	WolfChrome Analysis block diagram, Part 2 of 6	275
Figure B.14	WolfChrome Analysis block diagram, Part 3 of 6	276
Figure B.15	WolfChrome Analysis block diagram, Part 4 of 6	277
Figure B.16	WolfChrome Analysis block diagram, Part 5 of 6	278
Figure B.17	WolfChrome Analysis block diagram, Part 6 of 6	279
Figure C.1	Schematic of flow injection system	285
Figure C.2	Diagram of electrical connection for data recording	287
Figure C.3	Schematic representation of data flow in WolfAmp	289
Figure C.4	Screenshot of WolfAmp front panel	290
Figure C.5	Screenshots of the tabulated file-collection settings	292
Figure C.6	Screenshot of WolfAmp Analysis front panel	294
Figure C.7	Screenshot of the tabulated peak analyzer section	296
Figure C.8	Screenshot of the tabulated concentration analyzer section	298
Figure C.9	Screenshot of WolfAmp block diagram	300
Figure C.10	WolfAmp block diagram, Part 1 of 2	301
Figure C.11	WolfAmp block diagram, Part 2 of 2	302
Figure C.12	Screenshot of WolfAmp Analysis block diagram	305

Figure C.13	WolfAmp Analysis block diagram, Part 1 of 4	306
Figure C.14	WolfAmp Analysis block diagram, Part 2 of 4	307
Figure C.15	WolfAmp Analysis block diagram, Part 3 of 4	308
Figure C.16	WolfAmp Analysis block diagram, Part 4 of 4	309
Figure D.1	Plot showing the change in the Mn-protocochelin EXAFS spectrum with time	316
Figure D.2	ESI mass spectrum measured for protocochelin	316
Figure D.3	ESI mass spectrum measured for protocochelin after degradation at high solution pH	317
Figure D.4	ESI mass spectrum measured for Mn-protocochelin complex allowed to air oxidize for 2 hours	317
Figure D.5	ESI mass spectrum measured for protocochelin after degradation for 4 hours	318
Figure D.6	ESI mass spectrum measured for Co-protocochelin complex allowed to air oxidize for 30 minutes	318
Figure D.7	ESI mass spectrum measured for Co-protocochelin complex allowed to air oxidize for 3 hours	319
Figure D.8	Plot of reductive peak current collected at -0.2 V as a function of scan rate for the redox reaction of protocochelin in aqueous solution	319

CHAPTER 1

Introduction to Monitoring Neurotransmission with Voltammetric Methods and Approaches for Technique Optimization

1.1 Neurons, Neurotransmission, and Neuronal Function

The nervous system is a complex structure of interconnecting cells, neurons, which have the ability to rapidly communicate over long distances. It can be divided into the central (brain and spinal cord) and peripheral nervous system (all remaining neurons projecting from the spinal cord). Neurons are specialized cells that transmit information by electrical and chemical means (*I*). The branch-like structures of the neuron are responsible for receiving input from surrounding neurons and converting these inputs into electrical signals called action potentials. These action potentials are generated by ions moving across the cell membrane, depolarizing the neuron (*I*). Once the action potential is generated, it travels to the terminal region of the neuron. This terminal acts as the primary output of the neuron and propagates the signal to the connected neuron. An electrical connection of two neurons occurs across gap junctions where ions and small molecules are transmitted directly through an interconnecting channel (Figure 1.1). This exchange of ions alters the charge of the cell relative to its surroundings and this action potential is further propagated to other neurons. Between electrical and chemical signaling, the electrical form of neuronal signaling is more rapid and regionally specific. Chemical communication happens via synaptic transmission as molecules are released from the presynaptic neuron's terminal into the synaptic cleft, where these small molecules are either bound to specific receptors on the

postsynaptic terminal, reuptaken into the presynaptic terminals, enzymatically degraded, or diffuse into the surrounding extracellular space (1). These molecules are called neurotransmitters and neuromodulators, where their size varies from small-molecules to peptides, with various charge states, and they are primarily synthesized within the cell body of the neuron. Neurotransmitters are either packaged into vesicles for future release, freely diffuse through the cells membrane, or shuttled across the membrane by surface bound transporter proteins.

For the scope of this work, there exists far too many neurotransmitters and their metabolites to discuss in entirety (2), however from an electroanalytical perspective all can be divided into either electrochemically or nonelectrochemically active. Of the electrochemically detectable molecules, the focus will be directed onto dopamine, hydrogen peroxide (H_2O_2), and methionine-enkephalin (mENK). Dopamine is part of the catecholamine class of neurotransmitters and a tyrosine derivative, synthesized and packaged within dopaminergic cell bodies. After synaptic release it can be enzymatically degraded via monoamine oxidase and catechol-*o*-methyltransferase, to 3,4-dihydroxyphenylacetic acid and 3-methoxytyramine, respectively. H_2O_2 is generally considered a product of oxidative metabolism, where its concentration is tightly regulated within the cellular environment by peroxidases, but recently has been implicated in the modulation of neurochemical messaging (3). Naturally occurring opioid peptides, such as methionine-enkephalin, bind to opioid receptors on neurons, effectively altering neurotransmission (4, 5). It is suggested that methionine-enkephalin (Tyr-Gly-Gly-Phe-Met) specifically binds to μ -opioid receptors on γ -aminobutyric acid (GABA) neurons, effectively increasing dopamine release events (6, 7).

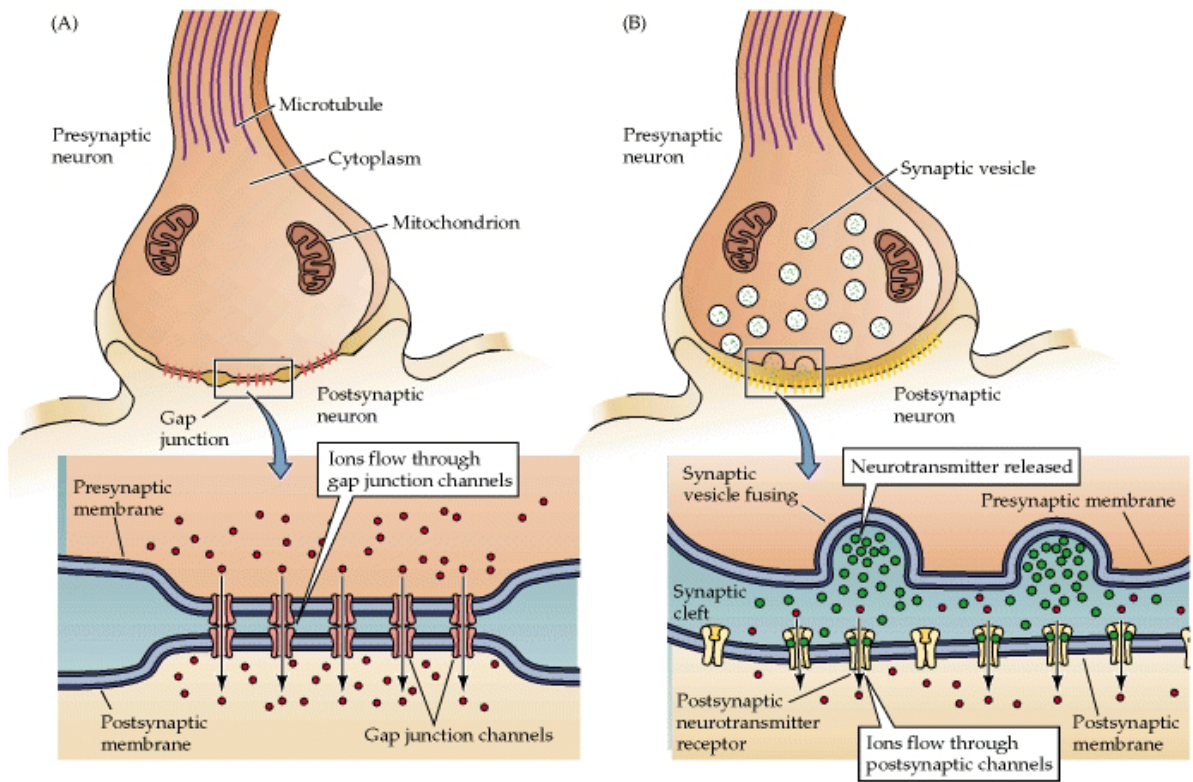


Figure 1.1 - Diagram of synaptic transmission. Synaptic transmission from the presynaptic to the postsynaptic terminal either occurs (A) electrically through a gap junction or (B) chemically across a synapse. (<http://kin450-neurophysiology.wikispaces.com/Synaptic+Transmission>)

The brain's complex system of cells and signaling molecules is the result of billions of years of evolution and appears to orchestrate the entire body's function in perfect harmony; however this system is susceptible to malfunction resulting in neurological disease states stemming from both genetic and environmental influences. Among these illnesses, several are associated with the neurotransmitters studied in this work. Dopaminergic dysfunction has been implicated with disorders such as schizophrenia (8), Parkinson's

disease (9), and substance abuse (10). H_2O_2 is a reactive-oxygen species and its dysregulation has been claimed to signal apoptosis and is implicated in the progression of Parkinson's disease (11, 12). Methionine-enkephalin has been shown to regulate a number of biological functions that include feeding, analgesia, and sedation (13, 14). Additionally, opiates (semi-synthetic opioids or opium poppy extracts) like hydrocodone or heroin are commonly associated with substance abuse because they activate the mesolimbic dopamine system, a region of the brain associated with reward-based learning. Research directed toward understanding the role of these select neuromodulators has a broad impact across many scientific disciplines and society as a whole.

1.2 Methods for Studying Neurotransmission

Many techniques have been employed to monitor neuronal signaling in the central nervous system and these can be classified into methods that either monitors neuronal activity or neurotransmitter concentration. Neural activity is a measure of the electrical signaling commonly studied by electrophysiology is a common method to study the activity of neurons (15). With this approach, electrodes measure the action potentials that results in synaptic release. The energy source for this activity is in the form of glucose and oxygen, and is supplied to the brain by a network of blood vessels and capillaries. Typical methods for monitoring localized changes in blood flow, glucose, metabolites or specific markers are functional magnetic resonance imaging (fMRI) and positron emission tomography (PET) (16, 17). These whole-brain spectroscopic methods are noninvasive and are routinely used in human experiments with adequate spatial and temporal resolution, but these techniques lack

the ability to accurately determine concentrations. Other methods for quantitation of neurotransmitter fluctuations require a bit more invasion, where probes must be implanted or tissue samples collected. Two of the most popular methods developed to efficiently quantitate neurotransmission are adaptations of microdialysis and voltammetry. These methods vary on many fronts, but the most principle difference is that microdialysis is a sampling method requiring fluid to be extracted from the brain and voltammetry monitors the fluid around an implanted electrode, without extraction. Additionally, the frequency of data collection varies between detection methods. This results in different interpretation of the information, as neurotransmission is monitored at different time scales. Both of these methods have distinct advantages.

1.2.1 Electrophysiology

Electrophysiology is one of the oldest and simplest methods to monitor neuronal activity (18). This technique measures changes in the electric field across the cell membrane, arising from the propagation of action potentials. Electroencephalography (EEG) is an adaptation of electrophysiology, where it measures brain activity across the scalp from a large number of electrodes. When electrophysiology is coupled with implanted microelectrodes, it can accurately and rapidly measure the firing rate and extent of membrane depolarization of an individual cell.

Analysis of the frequency and shape of these events is used to interpret various properties of the neuron. Like electrochemical techniques, electrophysiology benefits from excellent spatial and temporal resolution and its simplicity allows compatibility with many

behavioral paradigms. However, this method offers no chemical information about the local environment.

1.2.2 Microdialysis

In the field of neuroscience, microdialysis is the primary sampling method for monitoring neurochemical fluctuations over multiple minutes (19). Microdialysis relies on the perfusion of fluid through an implanted dialysis probe, where a semi-permeable membrane allows molecules in the brain to diffuse down a concentration gradient into the perfusion fluid. The eluting dialysate is collected at regular time intervals for future quantitative analysis. The cylindrically shaped membrane typically has a diameter of 0.5 mm and a length of 2.0 mm. The strength of the technique results from the inherent selectivity of the subsequent chromatographic techniques and the quantitation power of the selected detector. These detectors are typically spectroscopic or electrochemical and chromatography is classically high-performance liquid chromatography (HPLC) or capillary electrophoresis (20). Appendix B covers the development of a custom LabView-based chromatography program for HPLC with ultraviolet-visible spectroscopy, with an additional program written for analysis of chromatograms. The retention times and signal intensities are compared with standards to determine actual extracellular concentrations and analyte identity.

One disadvantage to dialysis is the poor temporal resolution, as the artificial cerebral spinal fluid must be slowly perfuse to allow analyte equilibration, and aliquots of sufficient volume must be collected for analysis. Also, this method of sampling induces significant tissue damage (21, 22) and lacks the spatial resolution to determine specific regional

differences, because the probe is larger than many brain nuclei in rodents (23). Traditionally, the technique operates with minute resolution, but more elaborate methodology has decreased this time to 5 sec (24). However collection and neurotransmitter release are not on the same time scale, resulting in information loss.

1.2.3 Electrochemical

Although electrochemical sensors cannot match the selectivity and sensitivity of microdialysis, the data collection frequency far exceeds any other methods for chemical measurements. There are multiple electrochemical techniques that are commonly employed to make rapid measurements of neurotransmission; these methods include: amperometry, differential pulse voltammetry (DPV), and fast scan cyclic voltammetry (FSCV) (25). Electrochemistry involves measuring the transfer of charged particles between two phases (26). For these methods, the charged particles are electrons and the two phases are the working electrode and the extracellular space.

The weakness of electrochemical methods is simply that the molecule must be electroactive, so many desirable analytes are not directly detectable. This obstacle can be overcome with the use of biosensors, which allows detection of nonelectroactive molecules through some interaction with a biological component and the sensor. This fundamental weakness is not entirely inconvenient, as some chemical selectivity is imparted by excluding nonelectroactive molecules from the electrochemical response. Additionally, voltammetric methods offer more chemical selectivity than amperometric, because the differing redox

properties of molecules result in chemical fingerprints that can be used to identify analytes in complex mixtures (27).

1.2.4 Amperometry

In constant-potential amperometry, the electrode is continually held at a potential so that any redox-active molecule at the electrode surface will either be oxidized or reduced and produce faradaic currents (26). These currents are recorded and plotted versus acquisition time. From these plots, the integral of the current (Q , Coulombs of charge) with respect to time is proportional to the number of molecules (N) electrolyzed at the electrode surface and follows Faraday's Law:

$$Q = nNF \quad (1)$$

where n is the number of electrons transferred and F is defined as Faraday's constant (96,485 C·mol⁻¹). A custom LabView-based amperometry program with integrated tools for data analysis was developed for routine lab use (Appendix C). When rapid data sampling rates are utilized, amperometry has excellent temporal resolution, due to the fact that electroactive molecules are consumed upon contact with the electrode surface. These properties make amperometry a useful technique to measure vesicular release from single cells, and have the ability to detect 1 – 10 attomoles of catecholamines released from single cells (28, 29). Despite these advantages, amperometry is inherently nonselective, as all electroactive molecules that can be electrolyzed at the holding potential will produce faradaic current. Therefore, it is not ideally suited for making measurements in the complex mixture of the brain.

1.2.5 Differential Pulse Voltammetry

Differential pulse voltammetry can be thought of as the result of combining both square wave and linear sweep voltammetry, where a small square wave (~ 25 mV) is superimposed at a constant frequency and duration on a linear potential ramp (26, 30). Typically, the duration of the pulsed square wave is on the order of 50 ms and the period is about 200 msec. Current is measured before and after the application of each square wave and the differential between data points is plotted versus the applied potential of the linear ramp. For reversible redox reactions, the differential current results in a symmetric peak where the pinnacle is proportional to concentration and equal to the half wave potential. In contrast to amperometry, DPV can selectively measure multiple analytes that have formal reduction potentials that differ by more than 100 mV (31). DPV has been used to monitor neurotransmitter fluctuations (32), but more selective and faster approaches are available.

1.2.6 Fast-Scan Cyclic Voltammetry (FSCV)

Cyclic voltammetry is a controlled potential technique that thermodynamically controls the ratio of the redox species at the working electrode (26). The Nernst equation:

$$E_{applied} = E^o + \frac{RT}{nF} \log \frac{[Oxidized]_{x=0}}{[Reduced]_{x=0}} \quad (1)$$

describes this ratio of species at the electrode surface when the electrochemistry is reversible. Faradaic currents arise from the reduction and oxidation of the species that diffuses or adsorbs to the electrode surface. Non-faradaic currents are generated by changes in double-layer capacitance or charging current at the electrode solution interface. These currents are

recorded versus the applied potential to build a cyclic voltammogram. This data provides a wealth of information that can be used for analyte identification and quantification. The position of the peaks in a voltammogram provides information on the redox potential, reversibility, and electron transfer kinetics (26). The shape of the peaks can be used to assess the contribution of mass transfer to the chemical process at the electrode surface, and the amplitude of the peaks can be correlated to the concentration of the detected analyte (26). These specific redox characteristics of distinct electroactive molecules allow for the discrimination and quantification of multiple species in solution.

Background-subtracted fast-scan cyclic voltammetry (FSCV) is a differential technique that is suited for monitoring real-time changes in redox species. As the scan rates are typically around $400 \text{ V}\cdot\text{s}^{-1}$, the majority of the current is a result of double-layer capacitance at the electrode surface, and given the moniker “charging current”. Appendix A.4 shows the pH dependence of this charging current. The use of background subtraction allows the removal of these stable charging currents from the cyclic voltammogram, to reveal the more interesting faradaic response from an analyte.

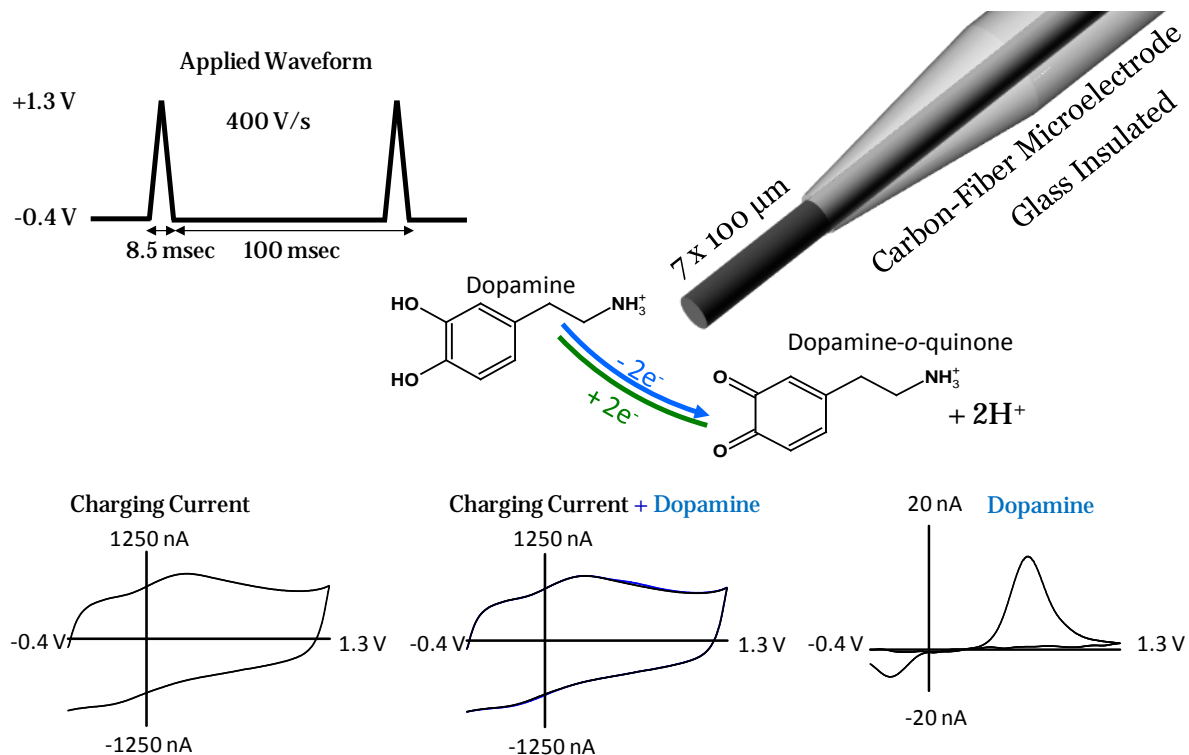


Figure 1.2 - Background-subtracted fast-scan cyclic voltammetry scheme. The applied potential controls the oxidation and reduction of a molecule (i.e. dopamine) at the electrode surface. Charging currents are generated by waveform application. The addition of dopamine creates additional current. The stable charging current can be subtracted, resulting in only faradaic current from the redox activity of the analyte.

Figure 1.2 illustrates this subtraction scheme, where a typical waveform for the electrochemical detection of dopamine at carbon-fiber microelectrodes has the working electrode held at -0.4 V vs. Ag/AgCl with periodic ramping to $+1.3\text{ V}$ at a rate of $400\text{ V}\cdot\text{s}^{-1}$ with a sampling rate of 10 Hz (27). Dopamine is a neurotransmitter commonly studied as it plays a major role in motivation, movement, and cognition (1). The time between scans when the working electrode is held at a negative potential allows positively-charged

dopamine to concentrate at the electrode surface (33). The resulting background-subtracted cyclic voltammogram can be used for analyte identification and quantification.

Figure 1.3 illustrates how this differential technique is applied to build a color plot, a three-dimensional graph of current, time, and potential. Typically a voltammogram is collected every 100 msec and a color plot consists of data collected over ~ 20 sec. This results in 200 voltammograms for each data file. To construct a color plot, cyclic voltammograms are unfolded at the switching potential and concatenated as they are collected. The current values are assigned a false color and plotted so that current, time, and potential can be viewed simultaneously. From these data, current vs. time and current vs. potential plots can be extracted.

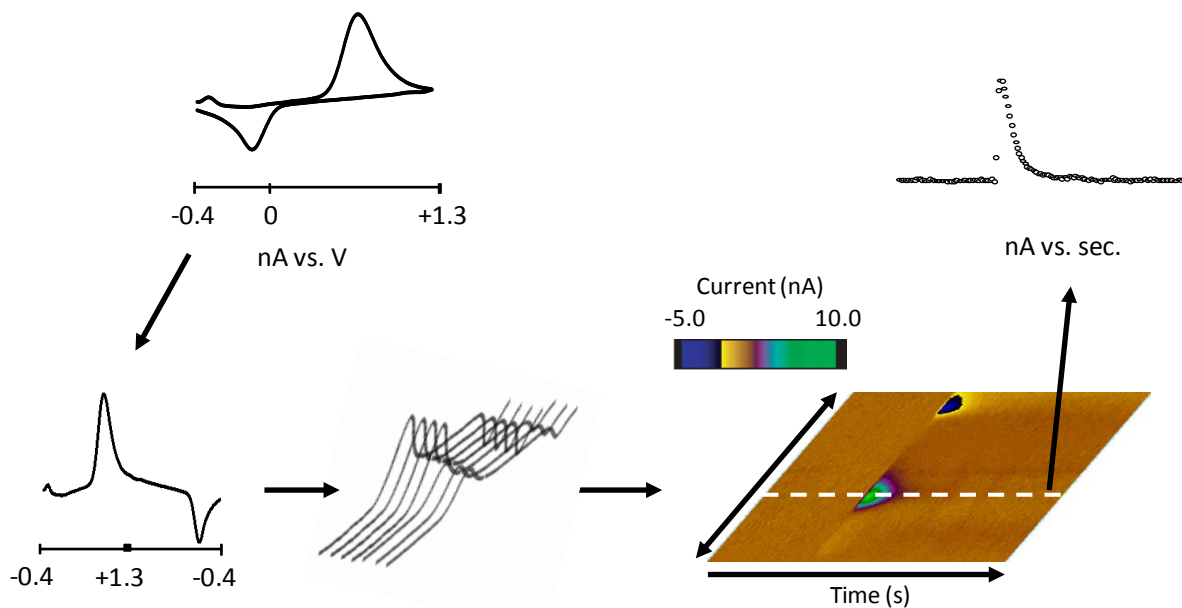


Figure 1.3 - Flow chart illustrating the color plot. Background-subtracted voltammograms are unfolded and concatenated, and then currents are assigned a false color.

FSCV with carbon-fiber microelectrodes has been used to identify and quantitate neurotransmitters both *in vivo* and *in vitro* (34). FSCV has also been shown to have ~ 400 times more sensitivity towards dopamine oxidation than amperometry (35). This enhanced sensitivity is due to the adsorption and preconcentration of dopamine at the electrode surface (33). Waveform parameters can be tailored to achieve maximum sensitivity and selectivity (36, 37). These waveforms are applied with respect to a non-polarizable reference electrode (typically Ag/AgCl). Due to the low-ohmic drop of microelectrodes, the electrochemical cell for FSCV consists of only two electrodes.

1.3 Carbon-Fiber Microelectrodes

Carbon-fiber microelectrodes are commonly employed to quantify rapid dopamine fluctuations both *in vitro* (38-40) and *in vivo* (41, 42). These electrodes have proven to be particularly useful for biological applications due to their biocompatibility, high tensile strength, low cost, wide potential window and inert nature (43-45). Although carbon materials have been extensively investigated for their distinct electronic and chemical properties, carbon fibers are significantly less characterized than macro carbon electrode materials including highly ordered pyrolytic graphite and glassy carbon electrodes (45).

The manufacturing of carbon fibers generally results in graphitic sheets that radiate out from the center of the fiber (radial type), align in concentric circles (onion type), or distribute randomly (random type) throughout the fiber (45). The basal plane forms the backbone of the graphitic lattice, and the edge plane contains a significant population of oxygen-containing functional groups (45). Importantly, the final orientation of the graphitic

structure largely determines the electrochemical performance. Since the edge plane of the graphitic sheet is more reactive than the basal plane, the desired shape of an electrode dictates the appropriate carbon fiber for a given application (radial type for cylinders and onion type for planer disc).

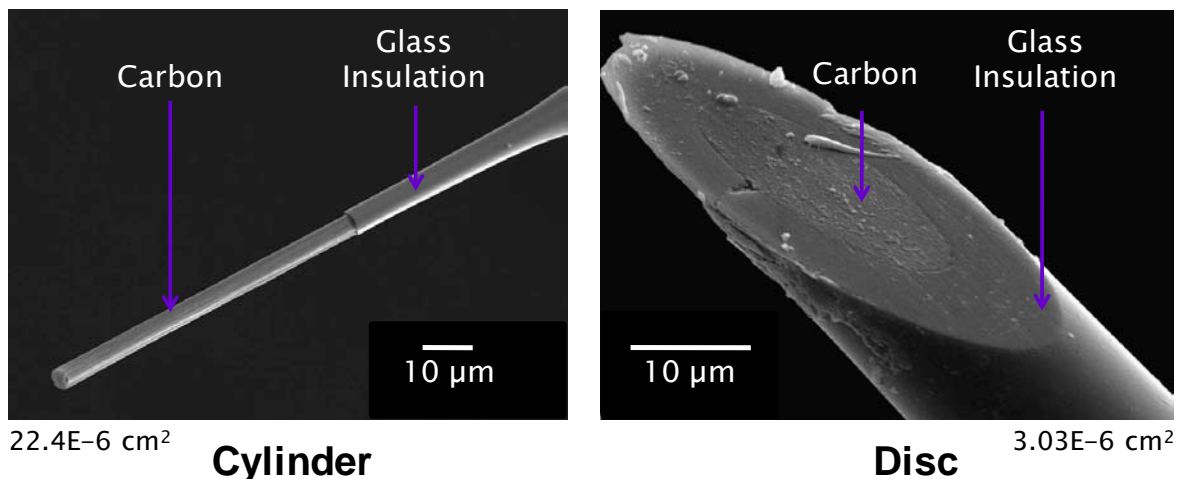


Figure 1.4 - Representative images of different carbon-fiber microelectrode geometries. Showing a ~ 7 fold difference in geometric surface area.

Carbon-fiber microelectrodes are manufactured by aspirating a single fiber into a glass capillary tube, followed by heating and pulling the tube in half with an electrode puller. This results in two glass-insulated carbon-fiber electrodes, with an exposed fiber that can be cut to the desired length for cylindrical geometries or polished for a planer disc electrode (Figure 1.4).

1.4 Advancing Electrode Substrate, Coating, and Geometry

As electrochemical methods, using transition metal electrodes, were being adapted for biological applications, it was immediately observed that there was a need for reducing electrode fouling and increasing the sensitivity of the method, because of significant nonspecific adsorption of biological molecules on the electrode. This fouling of the surface reduces electrode sensitivity, which is a major disadvantage because the concentrations of most neurotransmitters are inherently very small (nanomolar range). Gold and platinum electrodes have been used to directly detect catecholamine *in vitro* (46, 47), but due to the relatively small potential window and biofouling problems, metal electrodes are more commonly used as biosensor substrates that have multiple coatings (48).

Several strategies have been employed over the years to overcome these biological issues. Carbon-based electrodes benefit from a renewable surface (49) and operate over a wider potential window, than that of transitional metal electrodes (45). Coating the surface of the electrode with a membrane has successfully limited the issue of fouling for non-carbon electrodes (50). These coatings are generally polymers that have size and charge exclusion characteristics. Nafion, a cation exchange polymer, is commonly used as an electrode coating for catecholamine detection, as most amines are positively charged at physiological pH, 7.4 (51). Thus they readily diffuse through the membrane towards the electrode surface for detection, and Nafion excludes negatively charged analytes. Another approach uses a conductive polymer, such as overoxidized polypyrrole (52). This film also increases sensitivity to catecholamines, but because the films are noncovalently attached and have a finite thickness there is an increase in response time as the analyte has to diffuse through the

layer. Attempts have been made to account for this by using deconvolution methods (53). Carbon electrodes have also been functionalized with anionic carboxyphenyl to enhance dopamine sensitivity without compromising response time (54). Reference electrodes have also been coated. It was found that chronically implanted Ag/AgCl reference electrodes became unstable after extended tissue exposure, resulting in peak potential shifts that were prevented by Nafion coating the reference electrode (55). There have also been significant advancements in electrode substrates for H₂O₂ detection. Detection of H₂O₂ is favorable on platinum-coated carbon electrodes (56, 57), as the platinum surface is electrocatalytic. A platinized carbon-fiber microdisc electrode was constructed and tested with FSCV, which confirmed this finding (Appendix A.2). Other advanced schemes have been investigated to improve H₂O₂ sensing that include using iridium, gold, and palladium (58, 59).

The pH of the environment around the electrode also contributes to the redox activity. The electrochemical oxidation of dopamine and H₂O₂ are pH dependant. Appendix A.4 shows data demonstrating increases in anodic current for dopamine and decreases for H₂O₂ in more acidic environments. Dopamine also exhibits a pH dependant shift in its potential for oxidation, as well as unique splitting of the oxidative peak.

The geometry of a microelectrode is also an important property to consider when developing microelectrodes. The diffusion profiles and mass transport vary for the different geometries, as a disc microelectrode has more radial diffusion contributing to the mass transport to the surface than a cylindrical electrode (26). Using this information, the construction of electrode arrays with a disc geometry should exhibit higher current density than that of a cylindrical electrode. To this end, a two-channel carbon-fiber microdisc

electrode array was successfully fabricated for the detection of dopamine, with electrode spacing of $\sim 15 \mu\text{m}$ (Appendix A.3).

1.5 Altering the Applied Waveform

The parameters of the waveform can be tailored to achieve maximum sensitivity and selectivity toward a particular analyte. Often, simply increasing the scan rate of the cyclic waveform is sufficient to gain sensitivity, because the current is proportional to the scan rate for adsorbed species or to the square root of the scan rate for diffusion-controlled reactions (26). However, increasing the scan rate has some limitations. Commonly available electrochemical instrumentation is often incapable of reaching high scan rates and often lack adjustable gain to prevent amplifiers from overloading at higher currents, because of the increased non-faradaic charging current. For quasi-reversible electrochemistry, the kinetics of electron transfer also play a limiting role. As scan rate increases, the oxidation and reduction peaks shift to a more irreversible-like configuration. At extreme scan rates, these peaks can shift outside the limits of the voltammogram, thereby limiting quantification. Changing the potential limits of the cyclic waveform also affects sensitivity. It was shown that lowering the holding potential from -0.4 V to -0.6 V at a carbon-fiber electrode significantly increased dopamine sensitivity, presumably by increasing the preconcentration of positively-charged dopamine on the electrode surface (33). The same study also investigated the repetition rate of the applied waveform on electrode sensitivity and found that decreasing the time that the electrode is held at a negative potential reduced the sensitivity.

Cyclic waveforms are not limited to a basic triangular shape. An N-shaped waveform (0 V to +1.2 V to -0.6 V to 0 V at $400 \text{ V}\cdot\text{s}^{-1}$) has been found to reduce electrode fouling when monitoring the neurotransmitter 5-hydroxytryptamine (serotonin) (60, 61). This was attributed to less adsorption of serotonin to the electrode surface, because the potential was held at 0 V. This N waveform also allowed both redox peaks to be observed. A sawhorse-shaped waveform (-0.4 V to +1.3 V, held for 0.55 ms, to -0.4 V) was found to prevent signal decay when using scan rates of $2400 \text{ V}\cdot\text{s}^{-1}$ for dopamine detection (62). The carbon surface was etched during the short hold period at the anodic limit, and this was thought to improve the dopamine adsorption sites on the electrode surface.

1.6 Advanced Data Analysis

As previously described, FSCV provides qualitative information because molecules have distinct electron transfer kinetics and formal reduction potentials, giving rise to non-overlapping oxidation and reduction peaks. With a proper training set and sufficient redox peak separation, multivariate statistical analysis can be used to extract individual analyte concentration from complex mixtures. Principle component regression (PCR) has been shown to be the most effective method for deconvoluting voltammograms collected in living tissue to extract the profile of individual chemical components (27, 63, 64). This method of multivariate statistical analysis is well suited for FSCV, because each voltammogram offers 1000 data points for component identification.

One disadvantage of FSCV is that the electrode surface is in continual flux and results in background drift. This drift limits the collection time as the surface only remains

relatively stable for around 100 sec. Background subtraction over timescales exceeding this time frame limits reliable analyte quantification. One work was able to successfully eliminate background drift from the signal by including it as a principle component in the principal component regression, and thus enable continuous data collection over 60 min (65).

1.7 Dissertation Overview

This dissertation consists of eight additional chapters that will build on the topics discussed in the introduction further developing the application of FSCV at carbon-fiber electrodes to a variety of investigations. **Chapter 2** thoroughly describes the methodology of using FSCV with carbon-fiber microelectrodes to make real-time chemical measurements of dopamine release in behaving animals. **Chapter 3** describes the use of Raman Spectroscopy to identify the functional groups on the carbon-fiber surface that underlie an enhanced sensitivity to dopamine when the wavelimit is extended to +1.8 V. **Chapter 4** describes the use of FSCV to make the first real-time voltammetric measurements of H₂O₂ in living tissue. **Chapter 5** evaluates carbon-fiber and platinum microelectrodes to determine the most sensitive and selective substrate for making rapid measurements of H₂O₂. Work described in **Chapter 6** utilized electron paramagnetic spectroscopy to determine that the hydroxyl radical is a chemical intermediate in the voltammetric detection of H₂O₂. **Chapter 7** describes the development of an analyte-specific waveform that was used to make the first real-time voltammetric measurements of methionine-enkephalin in living tissue, with superior chemical selectivity. **Chapter 8** features a novel approach to eliminate standard electrode calibration procedures associated with FSCV and enable the electrode to be used to lesion the

tissue and mark the recording site. This is critical to all studies in brain tissue. Chapter 9 describes the adaptation of FSCV to a study of metal chelation by the triscatecholate, protochelin. Additionally there are appended chapters that supply supplemental information. Appendices B and C describe the development of LabView-based chromatography and amperometry programs, respectively. The fundamental findings described herein will advance the field of electrochemistry, neuroscience, and other scientific disciplines by adapting the benefits of FSCV to contribute to other sciences, monitoring additional neurochemical signaling pathways, and investigating the surface chemistry of carbon-based electrodes to develop advanced sensors.

1.8 References

1. Kandel, E. R., Schwartz, J. H., and Jessell, T. M. (2000) *Principles of neural science*, 4th ed., McGraw-Hill, Health Professions Division, New York.
2. Alexander, S. P., Mathie, A., and Peters, J. A. (2011) Guide to Receptors and Channels (GRAC), 5th edition, *Br J Pharmacol* 164 Suppl 1, S1-324.
3. Chen, B. T., Avshalumov, M. V., and Rice, M. E. (2001) H(2)O(2) is a novel, endogenous modulator of synaptic dopamine release, *J Neurophysiol* 85, 2468-2476.
4. Margolis, E. B., Hjelmstad, G. O., Bonci, A., and Fields, H. L. (2005) Both kappa and mu opioid agonists inhibit glutamatergic input to ventral tegmental area neurons, *J Neurophysiol* 93, 3086-3093.
5. Margolis, E. B., Lock, H., Chefer, V. I., Shippenberg, T. S., Hjelmstad, G. O., and Fields, H. L. (2006) Kappa opioids selectively control dopaminergic neurons projecting to the prefrontal cortex, *Proc Natl Acad Sci U S A* 103, 2938-2942.
6. Matsui, A., and Williams, J. T. (2011) Opioid-sensitive GABA inputs from rostromedial tegmental nucleus synapse onto midbrain dopamine neurons, *J Neurosci* 31, 17729-17735.
7. Mabrouk, O. S., Li, Q., Song, P., and Kennedy, R. T. (2011) Microdialysis and mass spectrometric monitoring of dopamine and enkephalins in the globus pallidus reveal reciprocal interactions that regulate movement, *J Neurochem* 118, 24-33.
8. Creese, I., Burt, D. R., and Snyder, S. H. (1976) Dopamine receptor binding predicts clinical and pharmacological potencies of antischizophrenic drugs, *Science* 192, 481-483.
9. Kish, S. J., Shannak, K., and Hornykiewicz, O. (1988) Uneven pattern of dopamine loss in the striatum of patients with idiopathic Parkinson's disease. Pathophysiologic and clinical implications, *N Engl J Med* 318, 876-880.
10. Schultz, W., Dayan, P., and Montague, P. R. (1997) A neural substrate of prediction and reward, *Science* 275, 1593-1599.
11. Halliwell, B. (2006) Oxidative stress and neurodegeneration: where are we now?, *J Neurochem* 97, 1634-1658.
12. Anantharam, V., Lehrmann, E., Kanthasamy, A., Yang, Y., Banerjee, P., Becker, K. G., Freed, W. J., and Kanthasamy, A. G. (2007) Microarray analysis of oxidative stress regulated genes in mesencephalic dopaminergic neuronal cells: relevance to oxidative damage in Parkinson's disease, *Neurochem Int* 50, 834-847.

13. Roth-Deri, I., Green-Sadan, T., and Yadid, G. (2008) beta-Endorphin and drug-induced reward and reinforcement, *Prog Neurobiol* 86, 1-21.
14. Le Merrer, J., Becker, J. A. J., Befort, K., and Kieffer, B. L. (2009) Reward Processing by the Opioid System in the Brain, *Physiol Rev* 89, 1379-1412.
15. Scanziani, M., and Hausser, M. (2009) Electrophysiology in the age of light, *Nature* 461, 930-939.
16. Ogawa, S., Lee, T. M., Kay, A. R., and Tank, D. W. (1990) Brain magnetic resonance imaging with contrast dependent on blood oxygenation, *Proc Natl Acad Sci U S A* 87, 9868-9872.
17. Videbech, P. (2000) PET measurements of brain glucose metabolism and blood flow in major depressive disorder: a critical review, *Acta Psychiatr Scand* 101, 11-20.
18. Hodgkin, A. L., and Huxley, A. F. (1939) Action potentials recorded from inside a nerve fibre, *Nature* 144, 710-711.
19. Perry, M., Li, Q., and Kennedy, R. T. (2009) Review of recent advances in analytical techniques for the determination of neurotransmitters, *Analytica Chimica Acta* 653, 1-22.
20. Schultz, K. N., and Kennedy, R. T. (2008) Time-resolved microdialysis for in vivo neurochemical measurements and other applications, *Annu Rev Anal Chem (Palo Alto Calif)* 1, 627-661.
21. Hascup, E. R., af Bjerken, S., Hascup, K. N., Pomerleau, F., Huettl, P., Stromberg, I., and Gerhardt, G. A. (2009) Histological studies of the effects of chronic implantation of ceramic-based microelectrode arrays and microdialysis probes in rat prefrontal cortex, *Brain Res* 1291, 12-20.
22. Jaquins-Gerstl, A., and Michael, A. C. (2009) Comparison of the brain penetration injury associated with microdialysis and voltammetry, *J Neurosci Methods* 183, 127-135.
23. Paxinos, G., and Watson, C. (2005) *The rat brain in stereotaxic coordinates*, 5th ed., Elsevier Academic Press, Amsterdam ; Boston.
24. Lada, M. W., and Kennedy, R. T. (1996) Quantitative in vivo monitoring of primary amines in rat caudate nucleus using microdialysis coupled by a flow-gated interface to capillary electrophoresis with laser-induced fluorescence detection, *Anal Chem* 68, 2790-2797.

25. Michael, A. C., and Borland, L. M. (2007) *Electrochemical methods for neuroscience*, CRC Press/Taylor & Francis, Boca Raton.
26. Bard, A. J., and Faulkner, L. R. (2001) *Electrochemical Methods: Fundamentals and Applications*, 2nd ed., John Wiley, New York.
27. Heien, M. L. A. V., Johnson, M. A., and Wightman, R. M. (2004) Resolving neurotransmitters detected by fast-scan cyclic voltammetry, *Analytical Chemistry* 76, 5697-5704.
28. Chen, T. K., Luo, G., and Ewing, A. G. (1994) Amperometric monitoring of stimulated catecholamine release from rat pheochromocytoma (PC12) cells at the zeptomole level, *Anal Chem* 66, 3031-3035.
29. Wightman, R. M., Jankowski, J. A., Kennedy, R. T., Kawagoe, K. T., Schroeder, T. J., Leszczyszyn, D. J., Near, J. A., Diliberto, E. J., Jr., and Viveros, O. H. (1991) Temporally resolved catecholamine spikes correspond to single vesicle release from individual chromaffin cells, *Proc Natl Acad Sci U S A* 88, 10754-10758.
30. Osteryoung, J. G., and Osteryoung, R. A. (1985) Square-Wave Voltammetry, *Analytical Chemistry* 57, A101-&.
31. Adams, R., and Marsden, C. (1982) Electrochemical Detection Methods for Monoamine Measurements in Vitro and in Vivo, In *Handbook of Psychopharmacology* (Iversen, L., Iversen, S., and Snyder, S., Eds.), pp 1-74, Springer US.
32. Gonon, F., Buda, M., Cespuglio, R., Jouvet, M., and Pujol, J. F. (1980) In vivo electrochemical detection of catechols in the neostriatum of anaesthetized rats: dopamine or DOPAC?, *Nature* 286, 902-904.
33. Bath, B. D., Michael, D. J., Trafton, B. J., Joseph, J. D., Runnels, P. L., and Wightman, R. M. (2000) Subsecond adsorption and desorption of dopamine at carbon-fiber microelectrodes, *Analytical Chemistry* 72, 5994-6002.
34. Armstrong-James, M., Millar, J., and Kruk, Z. L. (1980) Quantification of noradrenaline iontophoresis, *Nature* 288, 181-183.
35. Zachek, M. K., Takmakov, P., Moody, B., Wightman, R. M., and McCarty, G. S. (2009) Simultaneous Decoupled Detection of Dopamine and Oxygen Using Pyrolyzed Carbon Microarrays and Fast-Scan Cyclic Voltammetry, *Analytical Chemistry* 81, 6258-6265.

36. Heien, M. L. A. V., Phillips, P. E. M., Stuber, G. D., Seipel, A. T., and Wightman, R. M. (2003) Overoxidation of carbon-fiber microelectrodes enhances dopamine adsorption and increases sensitivity, *Analyst* 128, 1413-1419.
37. Gonon, F. G., Fombarlet, C. M., Buda, M. J., and Pujol, J. F. (1981) Electrochemical Treatment of Pyrolytic Carbon-Fiber Electrodes, *Analytical Chemistry* 53, 1386-1389.
38. Staal, R. G. W., Mosharov, E. V., and Sulzer, D. (2004) Dopamine neurons release transmitter via a flickering fusion pore, *Nat Neurosci* 7, 341-346.
39. Sombers, L. A., Hanchar, H. J., Colliver, T. L., Wittenberg, N., Cans, A., Arbault, S., Amatore, C., and Ewing, A. G. (2004) The effects of vesicular volume on secretion through the fusion pore in exocytotic release from PC12 cells, *J Neurosci* 24, 303-309.
40. Heien, M. L., and Ewing, A. G. (2009) Quantitative chemical analysis of single cells, *Methods Mol Biol* 544, 153-162.
41. Robinson, D. L., Hermans, A., Seipel, A. T., and Wightman, R. M. (2008) Monitoring rapid chemical communication in the brain, *Chem Rev* 108, 2554-2584.
42. Robinson, D. L., Venton, B. J., Heien, M. L., and Wightman, R. M. (2003) Detecting subsecond dopamine release with fast-scan cyclic voltammetry in vivo, *Clin Chem* 49, 1763-1773.
43. Cahill, P. S., Walker, Q. D., Finnegan, J. M., Mickelson, G. E., Travis, E. R., and Wightman, R. M. (1996) Microelectrodes for the measurement of catecholamines in biological systems, *Anal Chem* 68, 3180-3186.
44. Wightman, R. M. (2006) Detection technologies. Probing cellular chemistry in biological systems with microelectrodes, *Science* 311, 1570-1574.
45. McCreery, R. L. (2008) Advanced carbon electrode materials for molecular electrochemistry, *Chemical Reviews* 108, 2646-2687.
46. Matos, R. C., Angnes, L., Araujo, M. C., and Saldanha, T. C. (2000) Modified microelectrodes and multivariate calibration for flow injection amperometric simultaneous determination of ascorbic acid, dopamine, epinephrine and dipyrone, *Analyst* 125, 2011-2015.
47. Vandaveer, W. R., Woodward, D. J., and Fritsch, I. (2003) Redox cycling measurements of a model compound and dopamine in ultrasmall volumes with a self-contained microcavity device, *Electrochim Acta* 48, 3341-3348.

48. Burmeister, J. J., and Gerhardt, G. A. (2001) Self-referencing ceramic-based multisite microelectrodes for the detection and elimination of interferences from the measurement of L-glutamate and other analytes, *Anal Chem* 73, 1037-1042.
49. Takmakov, P., Zachek, M. K., Keithley, R. B., Walsh, P. L., Donley, C., McCarty, G. S., and Wightman, R. M. (2010) Carbon Microelectrodes with a Renewable Surface, *Analytical Chemistry* 82, 2020-2028.
50. Huffman, M. L., and Venton, B. J. (2009) Carbon-fiber microelectrodes for in vivo applications, *Analyst* 134, 18-24.
51. Baur, J. E., Kristensen, E. W., May, L. J., Wiedemann, D. J., and Wightman, R. M. (1988) Fast-scan voltammetry of biogenic amines, *Anal Chem* 60, 1268-1272.
52. Witkowski, A., and Brajter-Toth, A. (1992) Overoxidized polypyrrole films: a model for the design of permselective electrodes, *Anal Chem* 64, 635-641.
53. Kawagoe, K. T., and Wightman, R. M. (1994) Characterization of amperometry for in vivo measurement of dopamine dynamics in the rat brain, *Talanta* 41, 865-874.
54. Bath, B. D., Martin, H. B., Wightman, R. M., and Anderson, M. R. (2001) Dopamine adsorption at surface modified carbon-fiber electrodes, *Langmuir* 17, 7032-7039.
55. Hashemi, P., Walsh, P. L., Guillot, T. S., Gras-Najjar, J., Takmakov, P., Crews, F. T., and Wightman, R. M. (2011) Chronically Implanted, Nafion-Coated Ag/AgCl Reference Electrodes for Neurochemical Applications, *ACS Chem Neurosci* 2, 658-666.
56. Wang, J., Li, R. L., and Lin, M. S. (1989) Flow Cell Based on Glucose Oxidase-Modified Carbon-Fiber Ultramicroelectrode, *Electroanal* 1, 151-154.
57. Ming, L., Xi, X., and Liu, J. (2006) Electrochemically platinized carbon paste enzyme electrodes: a new design of amperometric glucose biosensors, *Biotechnol Lett* 28, 1341-1345.
58. Terashima, C., Rao, T. N., Sarada, B. V., Spataru, N., and Fujishima, A. (2003) Electrodeposition of hydrous iridium oxide on conductive diamond electrodes for catalytic sensor applications, *J Electroanal Chem* 544, 65-74.
59. Johnston, D. A., Cardosi, M. F., and Vaughan, D. H. (1995) The Electrochemistry of Hydrogen-Peroxide on Evaporated Gold/Palladium Composite Electrodes - Manufacture and Electrochemical Characterization, *Electroanal* 7, 520-526.
60. Jackson, B. P., Dietz, S. M., and Wightman, R. M. (1995) Fast-scan cyclic voltammetry of 5-hydroxytryptamine, *Anal Chem* 67, 1115-1120.

61. Hashemi, P., Dankoski, E. C., Petrovic, J., Keithley, R. B., and Wightman, R. M. (2009) Voltammetric detection of 5-hydroxytryptamine release in the rat brain, *Analytical Chemistry* 81, 9462-9471.
62. Keithley, R. B., Takmakov, P., Bucher, E. S., Belle, A. M., Owesson-White, C. A., Park, J., and Wightman, R. M. (2011) Higher sensitivity dopamine measurements with faster-scan cyclic voltammetry, *Anal Chem* 83, 3563-3571.
63. Keithley, R. B., Heien, M. L., and Wightman, R. M. (2009) Multivariate concentration determination using principal component regression with residual analysis, *Trends Analyt Chem* 28, 1127-1136.
64. Keithley, R. B., Carelli, R. M., and Wightman, R. M. (2010) Rank estimation and the multivariate analysis of in vivo fast-scan cyclic voltammetric data, *Anal Chem* 82, 5541-5551.
65. Hermans, A., Keithley, R. B., Kita, J. M., Sombers, L. A., and Wightman, R. M. (2008) Dopamine detection with fast-scan cyclic voltammetry used with analog background subtraction, *Analytical Chemistry* 80, 4040-4048.

CHAPTER 2

Real-Time Chemical Measurements of Dopamine Release in the Brain

The following work was reprinted with permission from: Roberts, J. G.; Lugo-Morales, L. Z.; Loziuk, P. L.; Sombers, L. A., Kabbani, Nadine (Ed.), *Dopamine: Methods and Protocols*, Methods in Molecular Biology, Vol. 964, Copyright 2013 Springer Science + Business Media, LLC.

2.1 Introduction

Dopamine is a neurotransmitter of particular interest due to its involvement in motivated behavior and reward-driven learning (1, 2), as well as various neurological disorders such as Parkinson's disease (3), schizophrenia (4) and drug addiction (5, 6). Extracellular dopamine concentrations in the brain vary on a subsecond timescale due to phasic firing of dopamine neurons (7). These naturally occurring dopamine transients are enhanced upon administration of drugs of abuse (8, 9), and become time-locked to cues that predict reward availability (1, 9-12). The ability to characterize and provide real-time measurements of rapidly fluctuating dopamine *in vivo* requires an analytical method with rapid temporal resolution. To date, the most widely used technique to monitor *in vivo* neurotransmitter release is microdialysis (13). This method provides excellent chemical selectivity and is well suited for measuring dopamine levels averaged over the course of minutes to hours. However, microdialysis lacks the temporal resolution to detect phasic dopamine fluctuations that occur on the subsecond to second timescale (14). In contrast, electrochemical techniques are especially useful for monitoring rapid chemical changes resulting from discrete neurochemical events due to rapid sampling rates (micro- to

millisecond time scale). Broadly speaking, the techniques that involve current flow at an electrode under potential control can be divided into two groups: voltammetric and amperometric methods (15). Of these techniques, fast-scan cyclic voltammetry (FSCV) provides the best combination of temporal resolution, sensitivity and chemical selectivity – features that are essential for the detection of rapid neurotransmitter fluctuations *in vivo* (16). Additionally, FSCV has been combined with other techniques including microinjection (7), iontophoresis (12, 17), and electrophysiology (12, 18, 19) to provide a great deal of new information regarding dopamine and its role in the brain.

2.1.1 Use of FSCV in Dopamine Detection

In FSCV, a dynamic potential is applied to a carbon fiber microelectrode (20). As the voltage is cycled through a triangular potential pattern, current is generated and recorded as a function of potential. The current generated over a single scan is plotted versus the applied potential. This resulting voltammogram is characteristic of the analyte, allowing it to be distinguished from many other electroactive species. This principle by which FSCV operates allows the identification of dopamine by the location of the potentials at which it oxidizes/reduces and the characteristic peak shape (Figure 2.1). This also allows dopamine to be distinguished from many other interferents in the brain such as ascorbic acid and changes in pH (16).

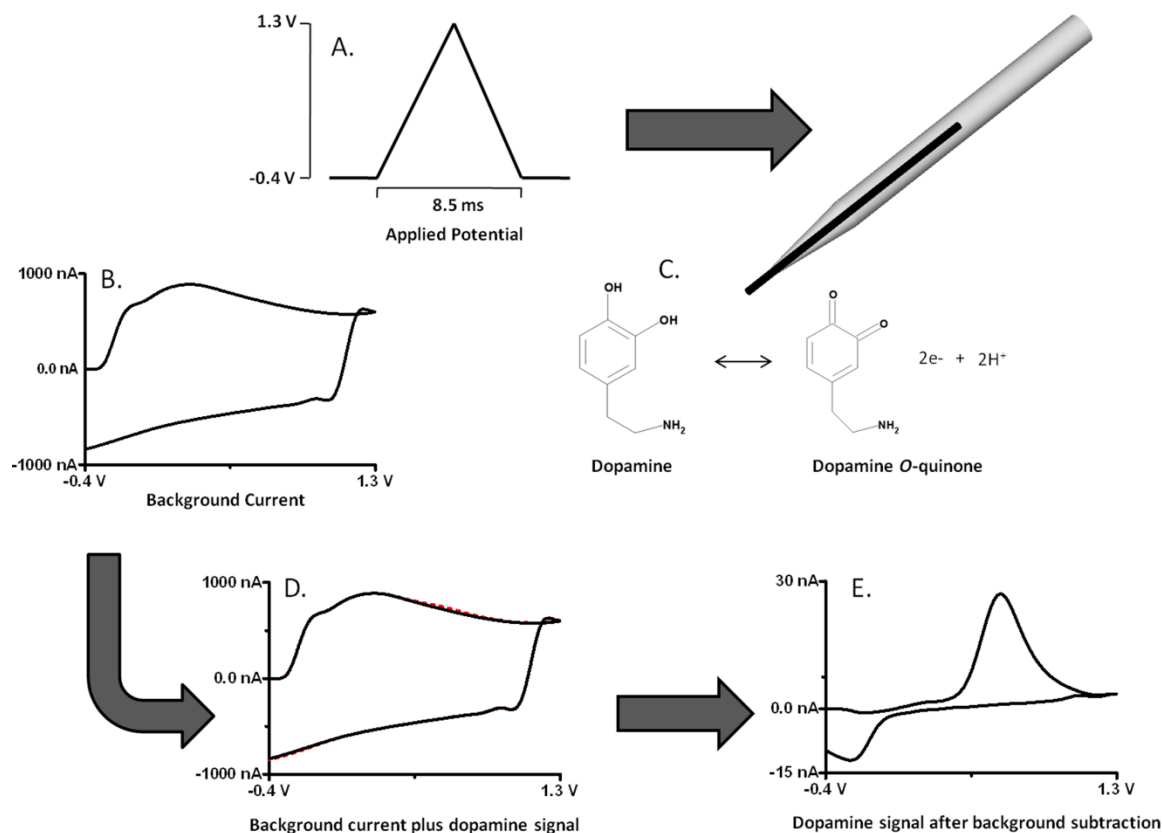


Figure 2.1 - Principles of background-subtracted FSCV. (A) First, a potential waveform is applied to a working electrode. (B) This generates a stable non-faradaic background current. (C) The redox reaction will exchange electrons at the electrode surface, generating faradaic current. (D) At low analyte concentrations, the faradaic response (dashed red line) is small compared to the background current. (E) The stable non-faradaic background current can be subtracted from the faradaic current arising from the redox reaction. The resulting cyclic voltammogram is an electrochemical fingerprint of the analyte.

Although FSCV generates characteristic voltammograms that can serve as qualitative identifiers for a molecule of interest, selectivity is always a concern. Several criteria need to be followed in order to positively confirm the identity of a voltammetric signal (21). These steps include electrochemical, anatomical, physiological, and pharmacological verification:

1. the *in vivo* signal should match the standard voltammogram collected *in vitro*
2. the signal must be collected in an anatomical region known to be analyte rich
3. stimulation of cell bodies should illicit analyte release
4. pharmacological manipulation should be used to reduce or/and increase analyte release

These steps must be taken in order to perform reliable electrochemical measurements and authenticate the identity of an analyte.

The microelectrodes typically used with FCSV are cylindrically shaped carbon fiber microelectrodes. With this approach, a 5-7 μm diameter carbon fiber electrode is sealed in a glass capillary with a portion of the fiber (75-125 μm) extending from the tip. This carbon fiber electrode is approximately 40-fold shorter and 50-fold smaller in diameter than a typical microdialysis probe, and thus it is particularly well suited to probe brain regions that have gradations in the density of neuronal terminals over these dimensions (22). This small size results in minimal tissue damage during *in vivo* experiments, allows for characterization of specific brain regions, and its cylindrical shape enables detection from all sides of the electrode by way of hemispherical diffusion to the recording surface, which enhances sensitivity.

2.2 Materials

2.2.1 Electrode Fabrication

1. Carbon fiber: T-650 (GoodFellow, Huntingdon, England).

2. Borosilicate capillary glass: 0.6 mm O.D., 0.4 mm I.D. for freely-moving experiments and 1.0 mm O.D., 0.5 mm I.D. for anesthetized experiments (A-M Systems, Sequim, WA).
3. Vertical electrode puller: PE-21 (Narishige, Tokyo, Japan).
4. Vacuum pump.
5. Optical microscope.
6. Surgical scalpel to cut the carbon fiber.
7. Micromanipulator: for freely-moving experiments (custom made, UNC-CH Chemistry, Machine Shop).
8. Silver paint: Silver Print II (GC Electronics, Rockford, IL).
9. Heat shrink tubing: EPS-200-1/8" and FP-301-3/32" (3M Electronics, Austin, TX).
10. NORIT A[®] activated carbon is used for isopropyl alcohol purification (MP Biomedicals, LLC, Solon, OH).
11. Silver wire: 0.5 mm diameter for Ag/AgCl reference electrode (Sigma-Aldrich, St. Louis, MO).
12. Gold connector: PCB socket (Newark Electronics, Chicago, IL).
13. Insulated leads: 30 gauge (Squires Electronics, Inc., Cornelius, OR).

2.2.2 Surgery

1. Anesthetic: Xylazine and ketamine for freely-moving experiments, urethane for anesthetized experiments, and 0.25% bupivacaine is used as a local anesthetic.
2. Heating pads.

3. Stereotaxic frame: Such as, Model 900 Small Animal Stereotaxic (David Kopf Instruments, Tujunga, CA).
4. Guide cannula: (Bioanalytical Systems, Inc, West Lafayette, IN).
5. Anchor screws: (Gexpro, Indianapolis, IN).
6. Cranioplastic cement: Grip Cement (Dentsply International Inc., Milford, DE).
7. Stimulating electrode: 20 mm long bipolar stainless steel (Plastics One, Roanoke, VA).

2.2.3 Electrochemistry

1. Multifunction input/output cards: PCI-6251 and PCI-6711 (16 bit, 333 kHz) (National Instruments, Austin, TX).
2. Software for data collection and analysis: TH-1 (ESA, Chelmsford, MA), or custom written in house using LabVIEW (National Instruments, Austin, TX).
3. Potentiostat. One of the following is appropriate: EI-400 biopotentiostat (Cypress Systems, Lawrence, KS), Universal Electrochemistry Instrument (UEI, UNC-Chapel Hill, Electronics Design Facility), or Universal Headstage Controller (United World Domination, Mebane, NC).
4. Headstage: miniaturized current-to-voltage converter (UNC-CH Electronics Design Facility; or United World Domination, Mebane, NC) (Figure 2.2). A larger version can be used for anesthetized experiments and postexperiment calibration.
5. Commutator: 25 channel (Crist Instruments, Hagerstown, MD).

6. Screened behavioral chamber: custom made for *in vivo* experiments (Med Associates Inc., St. Albans, VT).
7. Optional equipment: TV, DVD-R, and video character generator (for monitoring, recording, and time-stamping animal behavior).

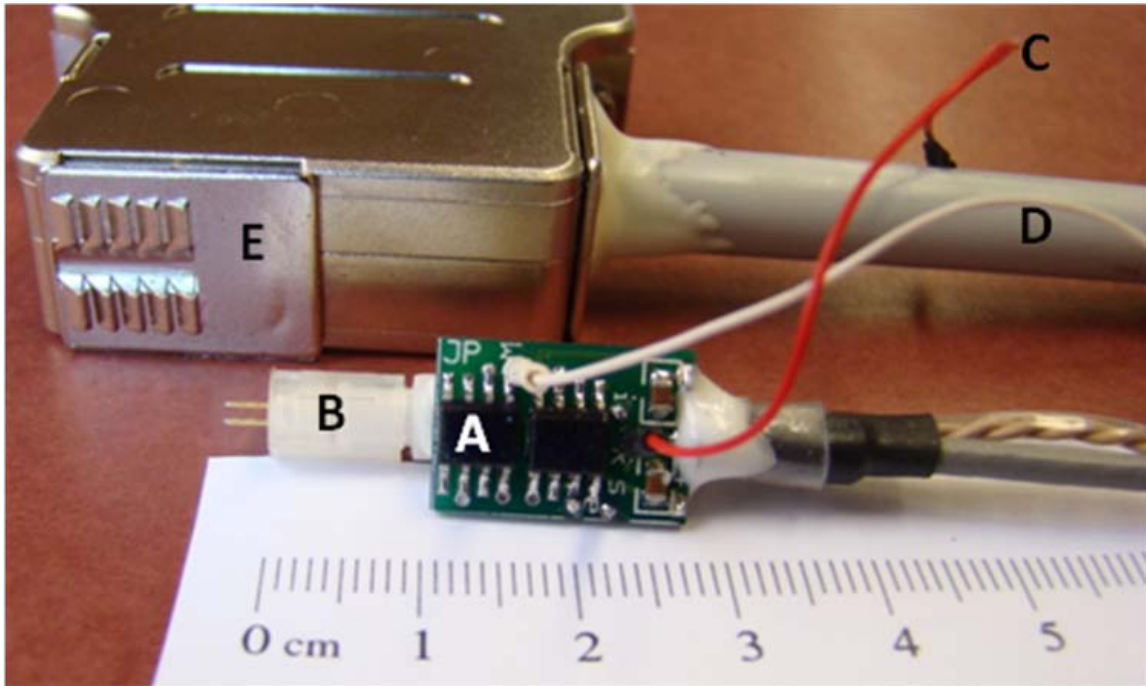


Figure 2.2 - Headstage (UNC-CH Electronics Design Facility). A miniaturized current-to-voltage convertor that consists of: (A) operational amplifier, (B) threaded connection to stimulating electrode, (C) lead for reference electrode, (D) lead for working electrode, (E) DB-25 connector.

2.2.4 Stimulation

1. Multifunction input/output card: PCI-6711 (National Instruments, Austin, TX).
2. Bi-phasic stimulus isolator: DS4 (Digitimer, Ltd, Hertfordshire, England).

2.2.5 Electrode Postcalibration

1. Dopamine HCl: 1 mM dopamine in 0.1 N HClO₄ for stock solutions, and dilutions are made in buffer (Sigma-Aldrich, St. Louis, MO).
2. Flow injection apparatus: six-port, two-position high-performance liquid chromatography (HPLC) valve, with air actuator, and digital valve interface (VICI, Houston, TX).
3. Grounded Faraday cage: custom built in house.
4. Tris buffer: 3.25 mM KCl, 1.2 mM CaCl₂, 1.2 mM MgCl₂, 2.0 mM Na₂SO₄, 1.25 mM NaH₂PO₄, 145 mM NaCl, and 15 mM Trizma[®] HCl at pH 7.4 (Sigma-Aldrich, St. Louis, MO).

2.3 Methods

2.3.1 Electrochemistry, Instrumentation, and Software

Dopamine release in brain tissue can be monitored in real-time with high spatial and temporal resolution when micron-scale electrodes and low-noise instrumentation are implemented. Dopamine is electrochemically detected at carbon-fiber microelectrodes by applying a potential sufficient to liberate two electrons from dopamine to form dopamine ortho-quinone. This provides a current that can be converted to a voltage and measured using a current transducer. Instrumentation includes the Universal Electrochemical Instrument, the Universal Headstage Controller, or a EI-400 biopotentiostat. These instruments are generally used with computer-controlled interface boards and locally written software (LabVIEW, National Instruments, Austin, TX). Software is commercially available

from ESA. The instrument provides all inputs and supplies power to the headstage, and usually consists of two main components: a low-pass filter and a headamp module. The computer-generated waveform contains digitization noise that must be smoothed by a low-pass filter before the signal reaches the working electrode. The output voltage from the current transducer is further amplified and conditioned by the headstage amplifier. The interface boards are responsible for the digital-to-analog and analog-to-digital conversions that are transmitted to and from the headstage, respectively.

The use of FSCV for the electrochemical detection of dopamine at carbon-fiber microelectrodes requires a waveform that optimizes peak currents, response time, and chemical selectivity. The most commonly used waveform holds the working electrode at -0.4 V vs. Ag/AgCl with periodic ramping to $+1.3$ V and back at a rate of 400 V \cdot s $^{-1}$ and a frequency of 10 Hz (Figure 2.1). The time between scans when the working electrode is held at a negative potential allows positively charged dopamine to preconcentrate at the electrode surface (23). Due to the fast scan rate, scanning generates a large capacitive charging current at the electrode surface (24), which is significantly larger than faradaic currents resulting from redox processes at the microelectrode surface. These background currents are stable over tens of seconds. This allows for subtraction, revealing the interesting faradaic responses. The resulting background subtracted cyclic voltammograms provide information on the analyte identity, redox potentials, reversibility, and electron transfer kinetics. The shape of the peaks allows for the discrimination of multiple species (however all catecholamines produce similar voltammograms) and can be used to assess the role of mass transfer. The amplitude of the peaks can be correlated to the concentration of the analyte at

the electrode surface. Under the conditions described, the cyclic voltammograms for dopamine should have a peak for the oxidative current at around +0.6 V.

2.3.2 Bipolar Electrical Stimulation

Electrical stimulation of dopaminergic cell bodies evokes dopamine release from the terminals in a time-locked manner, enabling the experimenter to monitor the kinetics of dopamine release and uptake with FSCV (25). The computer controlled stimulation is delivered with a biphasic stimulus isolator to the stimulating electrode. The device must be calibrated before use, to ensure proper function. The waveform applied to the stimulating electrode is a biphasic square wave that is applied with a frequency, amplitude, pulse width, and number of pulses consistent with the experimental goals. Typical stimulation parameters for dopamine neuron cell bodies are 125 biphasic pulses, 60 Hz, \pm 125-150 μ A, and 2 ms/phase. This stimulation must be applied between the ramps of the electrochemical waveform, such that the electrochemical data is not disturbed by the current stimulation (Figure 2.3).

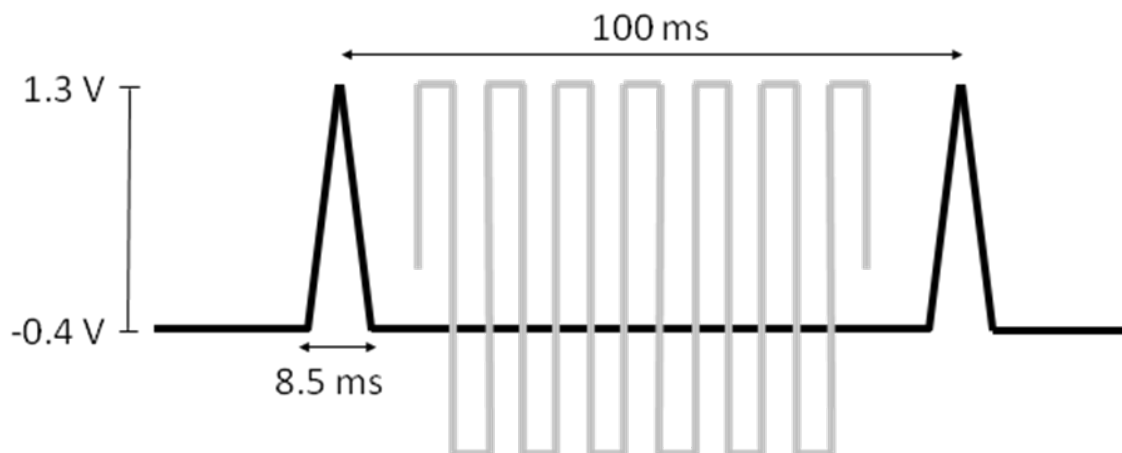


Figure 2.3 - Electrical stimulation. The bipolar electrical stimulation (grey), must not overlap with the applied electrochemical waveform (black).

2.3.3 Electrode Fabrication

2.3.3.1 Carbon-Fiber Microelectrode

1. A single carbon fiber is placed on a flat and clean surface that is well illuminated. The fiber is then aspirated into a borosilicate glass capillary, so that it extends from both ends.
2. The carbon fiber filled capillary is tapered in an electrode puller. This forms two electrodes from a single filled capillary. Each is inspected under the microscope to ensure a tight glass seal around the carbon fiber.
3. The exposed carbon fiber is then cut to length ($\sim 100 \mu\text{m}$) with a sharp scalpel under a microscope using a magnification of 10x. The electrode should also be inspected under the microscope using a higher magnification of at least 40x for visible cracks or abnormalities in the fiber or glass seal, and discarded if any are present (see Note 1).

4. In freely-moving experiments:

- a) An inspected 100 μm carbon fiber microelectrode is loaded into a custom micromanipulator and secured with heat shrink tubing (Figure 2.4).
- b) A small diameter insulated wire is painted with silver paint, and fed into the back of the capillary to make an electrical connection with the carbon fiber. A slight rotation of the wire ensures connectivity with the carbon fiber. The wire is secured to the micromanipulator with additional heat shrink tubing.
- c) All loaded manipulators are stored with the exposed carbon in purified and filtered isopropyl alcohol.

5. In anesthetized experiments:

- a) Larger diameter glass capillaries can be used.
- b) The carbon fiber microelectrode is backfilled using a saturated solution of 150 mM potassium chloride and 4 M potassium acetate. A small diameter insulated wire is fed into the back of the capillary to make electrical connection.

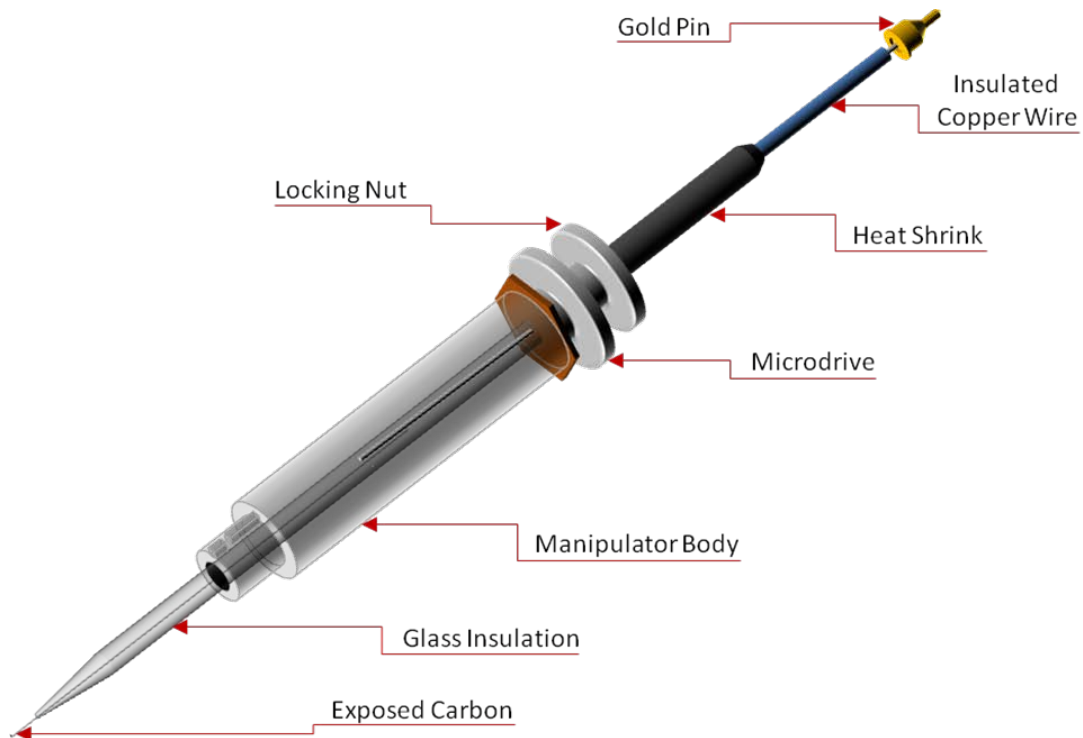


Figure 2.4 - Micromanipulator (UNC-CH Machine Shop). An illustration of a loaded micromanipulator, ready for an experiment.

2.3.3.2 Ag/AgCl Reference Electrode

1. A piece of silver wire is cut to approximately 10 mm, inserted into the socket of a gold connector, and soldered in place.
2. The solder is then covered with quick dry epoxy to avoid the contact of the soldering material with tissue.
3. On the day of surgery, the reference is chlorinated by connecting the positive terminal of a 2.5 V power supply to the gold pin on the silver wire and the negative terminal to a wire, with both leads immersed in 0.1 M hydrochloric acid. Chlorination is performed for about 1 min until the surface of the silver wire turns slightly white.

2.3.4 Surgery

2.3.4.1 Anesthetized Preparation:

1. The rat is anesthetized with urethane (3 g/kg i.p.), shaved and placed in a stereotaxic frame.
2. The scalp is locally anesthetized with a subcutaneous injection of 0.25% bupivacaine. An incision is made in the scalp, and the skin retracted to expose a 15-20 mm longitudinal and 10-15 mm lateral area of cranium.
3. Holes are drilled through the skull for stereotaxic placement of electrodes (stimulating, working, reference) (Figure 2.5). The stimulating electrode can be positioned either in regions containing dopaminergic cell bodies (substantia nigra/ventral tegmental area), or at the ascending fibers of the medial forebrain bundle. The hole for the working electrode is drilled above the target terminal region (e.g., 1.3 mm lateral and 1.3 mm rostral from bregma for the caudate-putamen and the core of the nucleus accumbens, and +1.7 mm anterior and +0.8 mm lateral for the nucleus accumbens shell). The hole for the reference electrode is drilled in the contralateral hemisphere opposite the working electrode.
4. Electrodes are lowered and secured in select areas of the brain using micromanipulators mounted on the stereotaxic frame. The reference electrode is secured with cranioplastic cement. Mild electrical stimulations are applied to evoke neurotransmitter release that is monitored at the microelectrode using FSCV. The rat is maintained on a heated pad for the duration of the experiment.

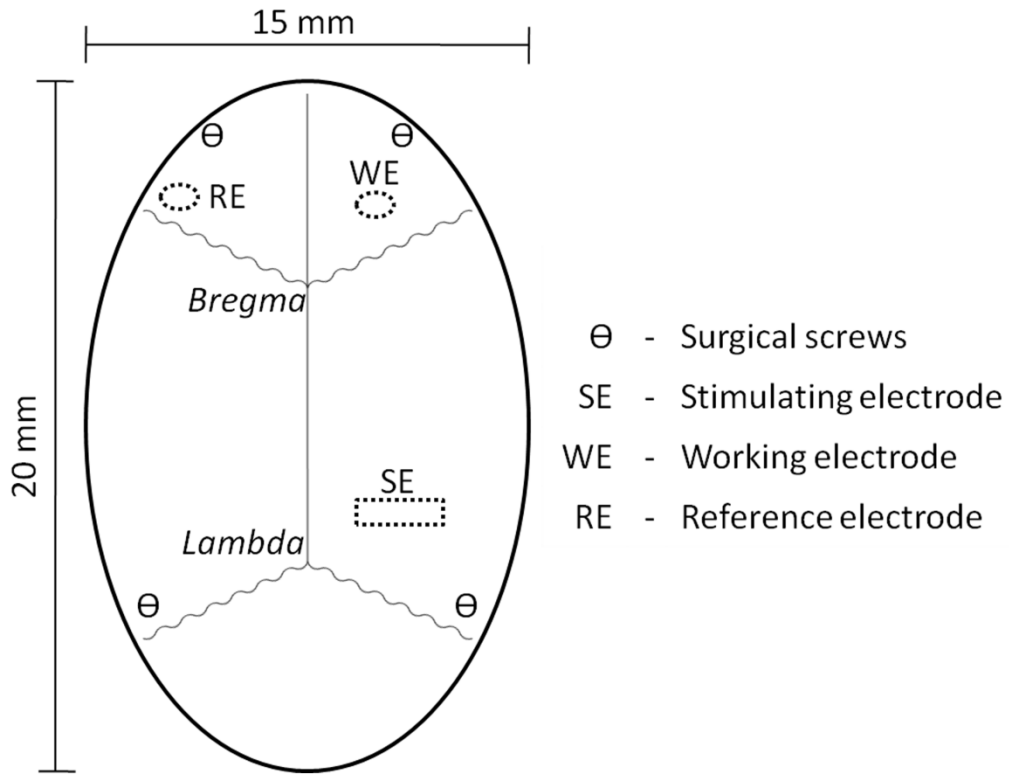


Figure 2.5 - A top view illustration of a rat skull. Highlighting the general placement of holes (dotted lines) for electrode and surgical screw placement.

2.3.4.2 Freely-Moving Preparation:

1. The rat is anesthetized with intramuscular or intraperitoneal ketamine (100 mg/kg) and intramuscular xylazine (10 mg/kg), the top of the head is shaved, and placed in a stereotaxic frame.
2. The scalp is locally anesthetized with a subcutaneous injection of 0.25% bupivacaine. An incision is made in the scalp, and the skin retracted to expose a 15-20 mm longitudinal and 10-15 mm lateral area of cranium.

3. Holes are drilled for the working electrode guide cannula, stimulating and reference electrodes (Figure 2.5). In addition, four holes are drilled at a 45° angle into which anchor screws are secured.
4. Reference electrode and guide cannula are lowered using micromanipulators mounted on the stereotaxic frame.
5. Once the components are in place, they are secured with cranioplastic cement, leaving the stimulating electrode hole exposed.
6. The stimulating electrode is modified in order to provide adequate space between the plastic hub of the stimulating electrode and the guide cannula (for the working electrode) on the animal's head cap (Figure 2.6). The stimulating electrode wires are bent at a 90° angle from the plastic hub and then bent back down at another 90° angle, to give a horizontal distance of ~5 mm between the hub and the main axis of the wires. Next, the tips are separated by 0.8-1.0 mm and carefully cut to a uniform length without disturbing the insulation. Dura mater is thoroughly cleared and the electrode is stereotaxically lowered into the tissue, oriented so that the tips of the electrode are splayed on the coronal plane. The electrode is lowered to 1 mm above the target brain region.
7. The stimulating electrode is connected to the stimulator and a mild electrical stimulation is applied through the stimulating electrode. The animal's tail should respond to this stimulation by rapidly rising and then slowly falling back to the resting position. The stimulating electrode is lowered in 0.2 mm increments until this

- response is diminished. It is then lowered further in 0.1 mm increments until this tail response is almost non-detectable.
8. Finally, cranioplastic cement is applied to the exposed cranium, carefully covering the stimulating electrode and lower half of its plastic hub.
 9. Immediately following surgery, the animal is placed on a warm heating pad until fully recovered. Once fully awake, soft food and fresh water are offered with a fruit flavored analgesic, such as acetaminophen (0.1-0.3 gm/kg) that the rat will readily lick.
 10. The animal is monitored daily and gently handled to facilitate experimental procedures. While handling, the stylet should be gently removed from the guide cannula, cleaned with an alcohol wipe, and reinserted. Experiments should be conducted within 2-5 days of surgery.

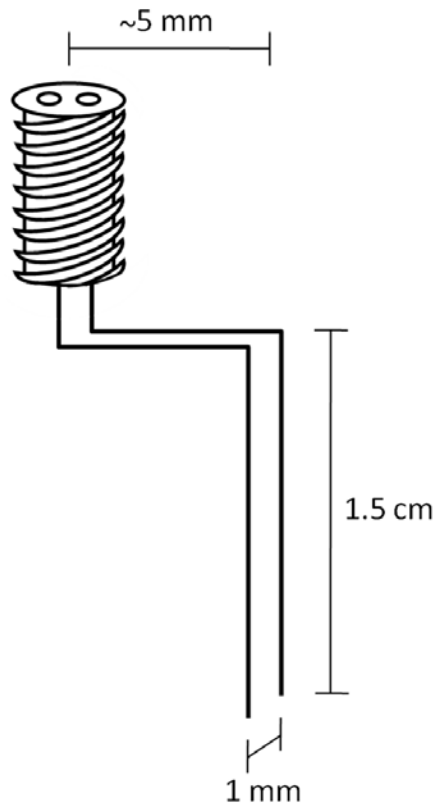


Figure 2.6 - Stimulating electrode.

2.3.5 Freely-Moving Rat Experiment

2.3.5.1 Making the Connections

Two to five days after surgery, depending on the rat's postsurgical recovery, the animal is prepared for the experiment. The animal is placed in the behavioral chamber, tethered using the stimulator cable on which the headstage is mounted (Figure 2.2), and allowed to acclimate for about 10 min. Before the loaded micromanipulator is placed into the guide cannula, the electrode is inspected once again under a microscope to double check the condition of the seal. The electrode is retracted inside the micromanipulator as the tip of

the electrode is monitored. Once the electrode tip disappears, each turn is counted until the electrode is fully retracted. This protects the electrode integrity as it is loaded into the cannula and allows the experimenter to index the tip location inside the manipulator.

All connections are cleaned, and the guide cannula stylet is removed and replaced with the micromanipulator containing the retracted microelectrode. The manipulator is locked in place and the working and reference electrodes are connected to the headstage.

2.3.5.2 Lowering the Carbon-Fiber Microelectrode

The electrode is slowly lowered into tissue as its output is monitored on an oscilloscope. To do this, the waveform is applied. As soon as the carbon fiber electrode comes in contact with tissue, the non-faradaic background current appears, and is monitored for stability as the electrode is lowered through the tissue (Figure 2.7). A break in the electrode is evident by a sudden change in the shape of the background current to a more resistive profile (approximating a triangular wave), and it should be removed and replaced with a fresh carbon fiber electrode. Once in place at the target region, the electrode is conditioned for about 20 min to stabilize the signal. Electrochemical conditioning consists of applying the triangular waveform mentioned above for at least 10 min at a frequency of 60 Hz and then changing it to 10 Hz for 10 additional minutes of potential cycling.

A mild electrical stimulation is applied to the stimulating bipolar electrode while the current output is monitored at the carbon fiber microelectrode. If a dopamine signal is not obtained, the working electrode is lowered in small increments and stimulation repeated until

electrically evoked dopamine release is observed. The electrode is then secured in position by a locking device on the micromanipulator and the experiment is initiated (see Note 2).

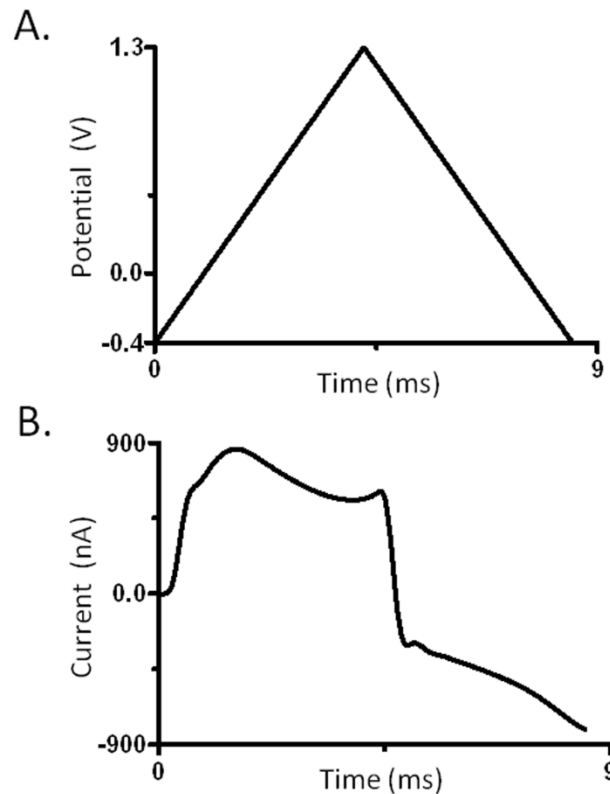


Figure 2.7 - Oscilloscope output. (A) Diagram of applied waveform. (B) Electrode response when circuit is completed in tissue or buffer.

2.3.6 Anesthetized Rat Experiment

Immediately following surgery, the stereotaxic frame is placed into the grounded Faraday cage. The electrodes (carbon fiber, stimulating, and Ag/AgCl reference) are lowered into the appropriate holes using the stereotaxic frame. There is no need to use screws and cranioplastic cement to secure the electrodes in an anesthetized experiment; however, the

reference can be secured in place for stability. The stimulating electrode is connected to the biphasic stimulus isolator and the working and reference electrodes are connected to the headstage. As described above, the carbon fiber microelectrode is lowered in small increments (0.1 mm) into a brain region rich in dopamine terminals. Dopamine neurons are electrically stimulated to illicit dopamine release at the terminals in a time-locked fashion (see Note 3).

2.3.7 After the Experiment

Upon completion of the experiment(s), there are two options depending on the objective of the experiment and the investigator's primary interest. These two options are described below.

2.3.7.1 Verification of Electrode Placement

The electrode tip is too small to leave a visible mark in tissue, thus an electrical lesion is made at the carbon fiber tip by applying a high current to the microelectrode. This unequivocally shows the location of the electrode in the tissue; however, this renders the electrode useless and it cannot be calibrated. The rat is transcardially perfused with 0.9 % saline and 10 % formalin solution to fix brain tissue. Finally, the animal is decapitated and the brain is removed from the skull and stored in formalin solution at 4 °C, until it is sliced for histology.

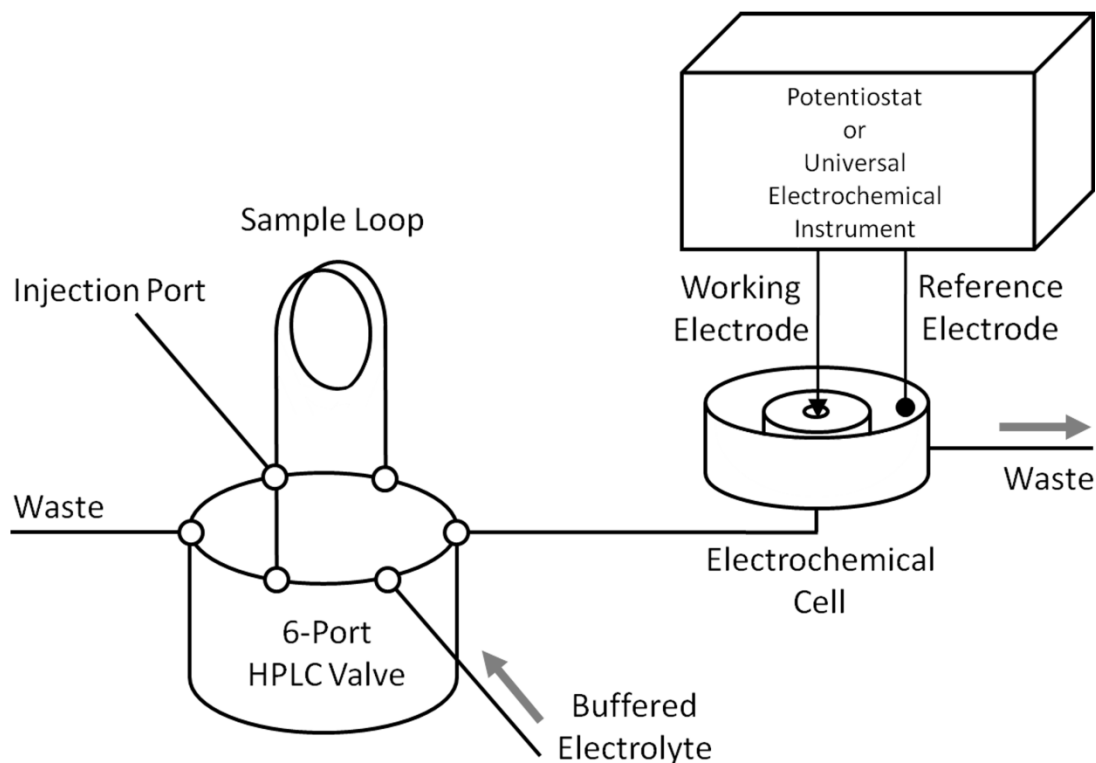


Figure 2.8. Flow injection analysis system. A syringe pump supplies a constant buffer flow across the working and reference electrodes. An HPLC valve controls the introduction of an analyte to the working electrode surface.

2.3.7.2 Electrode Postcalibration

Alternatively, the microelectrode is carefully removed from the brain, replaced with a sacrificial carbon fiber microelectrode, and an electrical lesion is made as described above. The electrode for calibration is rinsed in water and calibrated *in vitro* on a flow injection apparatus using known physiological concentrations of dopamine (usually between 200 and 1,000 nM). This system consists of a custom made electrochemical cell and a sample loop by which small volumes of analyte are rapidly injected into the cell using a six-port HPLC valve and a computer controlled pneumatic actuator. A syringe pump is used to continuously

supply physiological buffer at a constant flow rate through the electrochemical cell (Figure 2.8). The working electrode is lowered with a micromanipulator into the stream of buffer flowing at 1-3 mL/min. The Ag/AgCl reference electrode is submerged in the buffer as well and both are connected to the headstage. The same waveform used for the *in vivo* experiment is applied for the calibration of the electrode. Concentrations of the analyte of interest are loaded into the sample loop and introduced into the electrochemical cell with the digitally controlled pneumatic actuator. The injection is software controlled. Each concentration of dopamine is sampled at least in triplicate and the averaged peak oxidative current is plotted against concentration. The resulting calibration plot is used to relate the current collected *in vivo* to corresponding dopamine concentrations.

2.3.8 Data Analysis

TH-1 (ESA, Chelmsford, MA) software is commercially available and can be used for data analysis. Additionally, custom software written with Matlab (MathWorks, Inc., Natick, MA) can mathematically extract information from chemical data for quantitative analysis. The current method of multivariate statistical analysis involves the use of principle component regression (PCR) (16, 26). PCR has the ability to separate intensity based data into relevant components and noise, so that noise can be discarded. A training (calibration) set is used that includes individual cyclic voltammograms for the major species (typically dopamine and pH shifts, depending on the local microcircuitry) at various concentrations. Principle components that best describe the data are chosen. A principle component can be described as a vector that passes through the data that includes the most information. These

principle components are then used to predict unknown concentrations from individual cyclic voltammograms collected *in vivo*, as long as the unknown concentrations fit within the training set.

2.3.9 FSCV Combined with Electrophysiology

FSCV can be combined with more traditional neuroscience tools such as electrophysiology, a technique that uses an electrode to measure action potentials (12, 18, 27). With this combined approach, the microelectrode employed for electrochemical detection is also used to monitor local synaptic activity. Between scans the holding potential is abbreviated and the electrode is allowed to float, thereby adopting the potential of its local environment, which is digitally recorded. The use of this method has allowed dopamine release to be correlated with changes in the firing of specific neurons in the vicinity of the electrode, shedding light on dopamine function in discrete brain microcircuits.

2.3.10 FSCV Combined with Intracranial Self-Stimulation

The behavioral paradigm of intracranial self-stimulation (ICSS) is an intensely rewarding experimental model (28). It has also been combined with FSCV (10, 12, 29). In ICSS a stimulating electrode is implanted into a specific brain nucleus and the animal is taught to use a lever to deliver a mild electrical stimulation to the chosen region. This serves as a powerful operant reinforcer and is often used in studies of motivated behavior. The use of ICSS in combination with FSCV has led to the association of rapid dopamine signaling with learned cues (such as audio or visual cues) that precede an electrical stimulation or

reward availability (10, 12). This technique reveals information on the chemical mechanisms underlying reward based learning.

2.3.11 FSCV and Methods of Localized Pharmacological Manipulation

Microinjection and iontophoresis are two methods that have been implemented for administering small quantities of a compound into a specific region of the brain. While systemic application of drugs affects global brain circuitry, localized drug delivery techniques allow the experimenter to pharmacologically manipulate one discrete brain region. Microinjection involves the placement of a small needle into the desired brain location, and the subsequent pressure-driven infusion of a compound. Intracranial self-administration using microinjection has been used to elucidate the reinforcing action of specific agents in precise brain nuclei (30-32). Additionally, microinjection combined with FSCV has established that dopamine transients recorded in the nucleus accumbens shell require phasic neuronal activity in the ventral tegmental area (7), linking the activity of these two regions.

Iontophoresis can be used to locally apply compounds in an ionic solution using an applied current (33). When combined with FSCV (17, 34), capillary barrels are attached to a working electrode to deliver small quantities of a compound into tissue (Figure 2.9). This approach enables drug administration to the same site as the working electrode. While it has its advantages, iontophoresis is a largely non-quantitative technique. However, recent advances have allowed researchers to accurately quantify the amount of drug delivered during an iontophoretic ejection by use of an electroosmotic flow marker (17, 34). This

marker allows quantitative analysis by taking into account the variability due to inconsistent barrel dimensions that affect electroosmosis, which in turn affects the observed iontophoretic ejection.

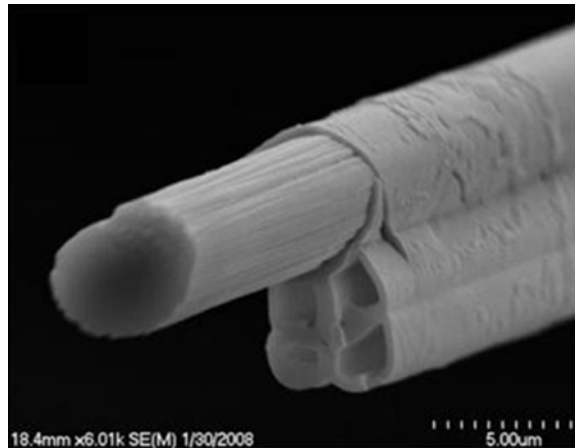


Figure 2.9. Iontophoresis probe. Scanning electron micrograph of a five barrel probe coupling FSCV with iontophoresis, using a carbon fiber microelectrode. Reprinted with permission from ref. 36. Copyright 2008 American Chemical Society.

2.3.12 Recent Advances

One drawback to the use of FSCV in freely-moving experiments has been the cable which tethers the animal. The introduction of wireless integrated circuits has created new opportunities for studying dopamine function in freely-moving animals (35). Advantages of this technology include the ability to perform measurements during multiple animal social interactions, investigation of more natural behaviors and more complex environments, and fewer artifacts introduced during movement of electrical connections. Another recent development has been the incorporation of analog background subtraction to enable

recordings over 30 minute time intervals before distortion of dopamine signals occurs due to background drift (36). Other developments such as microelectrode arrays (Figure 2.10), allow multiple electrodes to be used in a single experiment (37-39). This has opened up the opportunity for researchers to simultaneously measure dopamine release at spatially discrete brain locations (37, 39). This approach also allows for the simultaneous detection of multiple signaling agents at various locations (38), and allows for more representative data to be obtained because of the increased number of recordings that can be acquired in a given experiment. Another recent advance has enabled chronic implantation of microelectrodes, enabling recording at the same electrode over months, rather than hours (40, 41). Finally, as an alternative to electrical stimulation, optogenetics can be used to stimulate specific neuronal populations using light-activated ion channels (42).

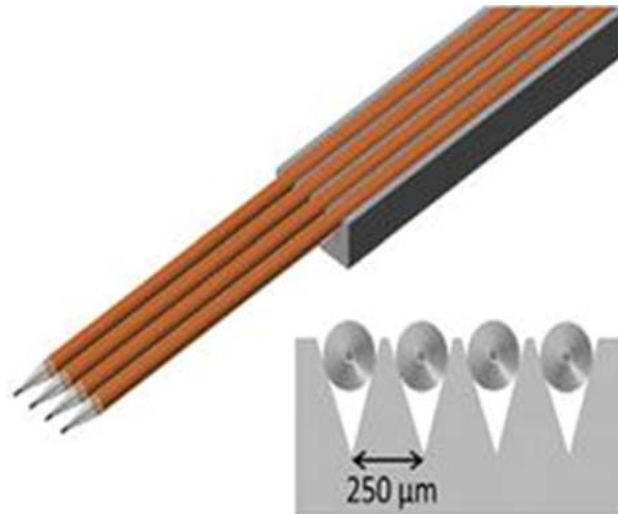


Figure 2.10. Microelectrode array. An array of four carbon fiber microelectrodes, with fused silica insulation, secured with a fixed separation of 250 μm . Reprinted with permission from ref. 41. Copyright 2010 Elsevier.

2.4 Notes

1. Optimal electrode length is determined by instrument limitations and experimental goals.
2. Many experiments monitor naturally-occurring dopamine fluctuations, or transients. These dopamine release events are evident at some, but not all sites that support electrically evoked dopamine release (43). Also, after several days of implantation, the reference electrode may drift by about 0.2 V, requiring the applied potential to be offset by 0.2 V.
3. Naturally-occurring transient dopamine release events have not been detected in anesthetized animals, unless pharmacologically evoked (44).

2.5 References

1. Day, J. J., Roitman, M. F., Wightman, R. M., and Carelli, R. M. (2007) Associative learning mediates dynamic shifts in dopamine signaling in the nucleus accumbens, *Nat Neurosci* 10, 1020-1028.
2. Schultz, W. (2007) Behavioral dopamine signals, *Trends Neurosci* 30, 203-210.
3. Obeso, J. A., Rodriguez-Oroz, M. C., Goetz, C. G., Marin, C., Kordower, J. H., Rodriguez, M., Hirsch, E. C., Farrer, M., Schapira, A. H., and Halliday, G. (2010) Missing pieces in the Parkinson's disease puzzle, *Nat Med* 16, 653-661.
4. Grace, A. A. (1991) Phasic versus tonic dopamine release and the modulation of dopamine system responsivity: a hypothesis for the etiology of schizophrenia, *Neuroscience* 41, 1-24.
5. Carelli, R. M., and Wightman, R. M. (2004) Functional microcircuitry in the accumbens underlying drug addiction: insights from real-time signaling during behavior, *Curr Opin Neurobiol* 14, 763-768.
6. Di Chiara, G., and Bassareo, V. (2007) Reward system and addiction: what dopamine does and doesn't do, *Curr Opin Pharmacol* 7, 69-76.
7. Sombers, L. A., Beyene, M., Carelli, R. M., and Wightman, R. M. (2009) Synaptic overflow of dopamine in the nucleus accumbens arises from neuronal activity in the ventral tegmental area, *Journal of Neuroscience* 29, 1735-1742.
8. Cheer, J. F., Wassum, K. M., Sombers, L. A., Heien, M. L., Ariansen, J. L., Aragona, B. J., Phillips, P. E., and Wightman, R. M. (2007) Phasic dopamine release evoked by abused substances requires cannabinoid receptor activation, *Journal of Neuroscience* 27, 791-795.
9. Phillips, P. E., Stuber, G. D., Heien, M. L., Wightman, R. M., and Carelli, R. M. (2003) Subsecond dopamine release promotes cocaine seeking, *Nature* 422, 614-618.
10. Owesson-White, C. A., Cheer, J. F., Beyene, M., Carelli, R. M., and Wightman, R. M. (2008) Dynamic changes in accumbens dopamine correlate with learning during intracranial self-stimulation, *Proc Natl Acad Sci U S A* 105, 11957-11962.
11. Roitman, M. F., Stuber, G. D., Phillips, P. E., Wightman, R. M., and Carelli, R. M. (2004) Dopamine operates as a subsecond modulator of food seeking, *J Neurosci* 24, 1265-1271.

12. Cheer, J. F., Aragona, B. J., Heien, M. L., Seipel, A. T., Carelli, R. M., and Wightman, R. M. (2007) Coordinated accumbal dopamine release and neural activity drive goal-directed behavior, *Neuron* 54, 237-244.
13. Justice, J. B., Jr. (1993) Quantitative microdialysis of neurotransmitters, *J Neurosci Methods* 48, 263-276.
14. Lu, Y., Peters, J. L., and Michael, A. C. (1998) Direct comparison of the response of voltammetry and microdialysis to electrically evoked release of striatal dopamine, *J Neurochem* 70, 584-593.
15. Michael, A. C., and Borland, L. M., (Eds.) (2007) *Electrochemical Methods for Neuroscience*, Vol. 1, 1 ed., CRC Press, Boca Raton.
16. Heien, M. L. A. V., Johnson, M. A., and Wightman, R. M. (2004) Resolving neurotransmitters detected by fast-scan cyclic voltammetry, *Analytical Chemistry* 76, 5697-5704.
17. Herr, N. R., Belle, A. M., Daniel, K. B., Carelli, R. M., and Wightman, R. M. (2010) Probing Presynaptic Regulation of Extracellular Dopamine with Iontophoresis, *ACS Chemical Neuroscience* 1, 627-638.
18. Kuhr, W. G., Wightman, R. M., and Rebec, G. V. (1987) Dopaminergic neurons: simultaneous measurements of dopamine release and single-unit activity during stimulation of the medial forebrain bundle, *Brain Res* 418, 122-128.
19. Millar, J., Stamford, J. A., Kruk, Z. L., and Wightman, R. M. (1985) Electrochemical, pharmacological and electrophysiological evidence of rapid dopamine release and removal in the rat caudate nucleus following electrical stimulation of the median forebrain bundle, *Eur J Pharmacol* 109, 341-348.
20. Robinson, D. L., Hermans, A., Seipel, A. T., and Wightman, R. M. (2008) Monitoring rapid chemical communication in the brain, *Chemical Reviews* 108, 2554-2584.
21. Phillips, P. E. M., and Wightman, R. M. (2003) Critical guidelines for validation of the selectivity of in-vivo chemical microsensors, *Trac-Trends in Analytical Chemistry* 22, 509-514.
22. Arbuthnott, G. W., and Wickens, J. (2007) Space, time and dopamine, *Trends Neurosci* 30, 62-69.
23. Bath, B. D., Michael, D. J., Trafton, B. J., Joseph, J. D., Runnels, P. L., and Wightman, R. M. (2000) Subsecond adsorption and desorption of dopamine at carbon-fiber microelectrodes, *Analytical Chemistry* 72, 5994-6002.

24. Bard, A. J., and Faulkner, L. R. (2001) *Electrochemical Methods: Fundamentals and Applications*, 2nd ed., John Wiley, New York.
25. Wightman, R. M., Amatore, C., Engstrom, R. C., Hale, P. D., Kristensen, E. W., Kuhr, W. G., and May, L. J. (1988) Real-time characterization of dopamine overflow and uptake in the rat striatum, *Neuroscience* 25, 513-523.
26. Keithley, R. B., Heien, M. L., and Wightman, R. M. (2009) Multivariate concentration determination using principal component regression with residual analysis, *Trends Analyt Chem* 28, 1127-1136.
27. Williams, G. V., and Millar, J. (1990) Concentration-dependent actions of stimulated dopamine release on neuronal activity in rat striatum, *Neuroscience* 39, 1-16.
28. Olds, J., and Milner, P. (1954) Positive reinforcement produced by electrical stimulation of septal area and other regions of rat brain, *J Comp Physiol Psychol* 47, 419-427.
29. Garris, P. A., Kilpatrick, M., Bunin, M. A., Michael, D., Walker, Q. D., and Wightman, R. M. (1999) Dissociation of dopamine release in the nucleus accumbens from intracranial self-stimulation, *Nature* 398, 67-69.
30. Ikemoto, S., Qin, M., and Liu, Z. H. (2005) The functional divide for primary reinforcement of D-amphetamine lies between the medial and lateral ventral striatum: is the division of the accumbens core, shell, and olfactory tubercle valid?, *Journal of Neuroscience* 25, 5061-5065.
31. Ikemoto, S., Qin, M., and Liu, Z. H. (2006) Primary reinforcing effects of nicotine are triggered from multiple regions both inside and outside the ventral tegmental area, *Journal of Neuroscience* 26, 723-730.
32. Ikemoto, S., and Sharpe, L. G. (2001) A head-attachable device for injecting nanoliter volumes of drug solutions into brain sites of freely moving rats, *J Neurosci Methods* 110, 135-140.
33. Rebec, G. V., and Bashore, T. R. (1984) Critical issues in assessing the behavioral effects of amphetamine, *Neurosci Biobehav Rev* 8, 153-159.
34. Herr, N. R., Kile, B. M., Carelli, R. M., and Wightman, R. M. (2008) Electroosmotic flow and its contribution to iontophoretic delivery, *Analytical Chemistry* 80, 8635-8641.
35. Garris, P. A., Ensman, R., Poehlman, J., Alexander, A., Langley, P. E., Sandberg, S. G., Greco, P. G., Wightman, R. M., and Rebec, G. V. (2004) Wireless transmission of

- fast-scan cyclic voltammetry at a carbon-fiber microelectrode: proof of principle, *J Neurosci Methods* 140, 103-115.
36. Hermans, A., Keithley, R. B., Kita, J. M., Sombers, L. A., and Wightman, R. M. (2008) Dopamine detection with fast-scan cyclic voltammetry used with analog background subtraction, *Analytical Chemistry* 80, 4040-4048.
 37. Zachek, M. K., Park, J., Takmakov, P., Wightman, R. M., and McCarty, G. S. (2010) Microfabricated FSCV-compatible microelectrode array for real-time monitoring of heterogeneous dopamine release, *Analyst* 135, 1556-1563.
 38. Zachek, M. K., Takmakov, P., Moody, B., Wightman, R. M., and McCarty, G. S. (2009) Simultaneous Decoupled Detection of Dopamine and Oxygen Using Pyrolyzed Carbon Microarrays and Fast-Scan Cyclic Voltammetry, *Analytical Chemistry* 81, 6258-6265.
 39. Zachek, M. K., Takmakov, P., Park, J., Wightman, R. M., and McCarty, G. S. (2010) Simultaneous monitoring of dopamine concentration at spatially different brain locations in vivo, *Biosens Bioelectron* 25, 1179-1185.
 40. Clark, J. J., Sandberg, S. G., Wanat, M. J., Gan, J. O., Horne, E. A., Hart, A. S., Akers, C. A., Parker, J. G., Willuhn, I., Martinez, V., Evans, S. B., Stella, N., and Phillips, P. E. (2010) Chronic microsensors for longitudinal, subsecond dopamine detection in behaving animals, *Nat Methods* 7, 126-129.
 41. Garris, P. A. (2010) Advancing neurochemical monitoring, *Nat Methods* 7, 106-108.
 42. Stuber, G. D., Hnasko, T. S., Britt, J. P., Edwards, R. H., and Bonci, A. (2010) Dopaminergic terminals in the nucleus accumbens but not the dorsal striatum corelease glutamate, *J Neurosci* 30, 8229-8233.
 43. Wightman, R. M., Heien, M. L., Wassum, K. M., Sombers, L. A., Aragona, B. J., Khan, A. S., Ariansen, J. L., Cheer, J. F., Phillips, P. E., and Carelli, R. M. (2007) Dopamine release is heterogeneous within microenvironments of the rat nucleus accumbens, *European Journal of Neuroscience* 26, 2046-2054.
 44. Venton, B. J., and Wightman, R. M. (2007) Pharmacologically induced, subsecond dopamine transients in the caudate-putamen of the anesthetized rat, *Synapse* 61, 37-39.

CHAPTER 3

Specific Oxygen-Containing Functional Groups on the Carbon Surface Underlie an Enhanced Sensitivity to Dopamine at Electrochemically Pretreated Carbon Fiber Microelectrodes

The following work was reprinted with permission from: James G. Roberts, Benjamin P. Moody, Gregory S. McCarty, and Leslie A. Sombers, *Langmuir*, 2010, 26, 9116-9122., Copyright 2010 American Chemical Society.

3.1 Introduction

Carbon fiber microelectrodes are commonly employed to quantify rapid dopamine fluctuations both *in vitro* (1-3) and *in vivo* (4, 5). These electrodes have proven to be particularly useful for biological applications due to their biocompatibility, high tensile strength, low cost, wide potential window and inert nature (6-8). Although carbon materials have been extensively investigated for their distinct electronic and chemical properties, carbon fibers are significantly less well characterized than macro carbon electrode materials including highly ordered pyrolytic graphite and glassy carbon electrodes (8).

The manufacturing of carbon fibers generally results in graphitic sheets that radiate out from the center of the fiber (radial type), align in concentric circles (onion type), or distribute randomly (random type) throughout the fiber (8). The basal plane forms the backbone of the graphitic lattice, and the edge plane contains a significant population of oxygen containing functional groups (8). Importantly, the final orientation of the graphitic structure largely determines the electrochemical performance. Since the edge plane of the

graphitic sheet is more reactive than the basal plane, the desired shape of an electrode dictates the appropriate carbon fiber for a given application.

Many types of signal improvement schemes have previously been used to enhance the electrochemical properties of carbon including laser activation (9-11), surface cleaning (12, 13), flame etching (14), and electrochemical conditioning (15-19). Of these, electrochemical methods are particularly common due to the facile and practical nature of this type of enhancement strategy. The sensitivity and selectivity of carbon fiber microelectrodes conditioned with extended wavelimits have been demonstrated in several published studies, both in vitro (17, 19) and in vivo (19-21), in which dopamine has been detected in the presence of multiple interferences. A variety of spectroscopic techniques including x-ray photoelectron spectroscopy (XPS) (22), thermal desorption mass spectrometry (23), enzyme immobilized fluorescence microscopy (24-26), and optical spectroscopy (27) have provided a general understanding of carbon surface functionality after electrochemical pretreatment of macro carbon electrode materials. Overall, the data suggest that electrochemical conditioning improves the response of the electrode by increasing the population of oxygen-containing functional groups on the carbon surface. However, the complex and dynamic nature of carbon surfaces precludes generalization across carbon materials, and the specific chemical mechanisms underlying electrochemical enhancement strategies remain poorly understood.

In this work, we describe a specific chemical mechanism underlying the enhanced adsorbance and sensitivity of carbon fiber microelectrodes conditioned with extended voltage scans prior to detection of endogenous catecholamines using FSCV. AFM and Raman

spectroscopy were used to demonstrate that electrochemical conditioning with a commonly used waveform increases carbonyl and hydroxyl group surface coverage without increasing nanoscale surface roughness. Upon conditioning with extended wavelimits to optimize sensitivity, the hydroxyl groups on the carbon surface were more extensively developed. The conditioning treatment described herein can be used to generate microdisc electrodes with a sensitivity approaching that of much larger, cylindrical microelectrodes. This treatment provides a viable means to achieve improved spatial resolution for measurements in discrete microenvironments such as in brain tissue, with an electrode geometry that can be more easily multiplexed into compact carbon arrays for simultaneous measurements at multiple channels.

3.2 Experimental Section

3.2.1 Chemicals

All chemicals were purchased from Sigma-Aldrich Co., (St. Louis, MO) unless specified and used without additional processing. All electrochemical experiments were done in physiological pH 7.4 buffer solution (15 mM Tris, 3.25 mM KCl, 1.20 mM CaCl₂, 1.2 mM MgCl₂, 2 mM Na₂SO₄, 1.25 mM NaH₂PO₄, 145 mM NaCl,). All aqueous solutions were made using doubly distilled deionized water (Barnstead EasyPure II, Dubuque, IA).

3.2.2 Electrode Fabrication

Elliptical disc microelectrodes with a polished angle of 15° were fabricated using P-55s pitch-based carbon fibers and cylindrical microelectrodes were fabricated using T-650

carbon fibers (Cytec Industries, Inc., Woodland Park, NJ) as previously described (13). A Ag/AgCl reference electrode was employed (World Precision Instruments, Inc., Sarasota, FL).

3.2.3 Flow Injection

A syringe pump (New Era Pump Systems, Inc., Wantagh, NY) supplied a continuous buffer flow of 1 mL/minute across the working and reference electrodes. Single two second bolus injections were accomplished with a six-port HPLC valve and air actuator controlled by a digital valve interface (Valco Instruments Co., Inc, Houston, TX). The working electrode was positioned in a custom electrochemical cell using a micromanipulator (World Precision Instruments, Inc., Sarasota, FL). The flow injection apparatus was housed within a custom Faraday cage.

3.2.4 Electrochemical Data Acquisition

The triangular detection waveform ranged from -0.4 to +1.3 V (28-31) and the electrochemical pretreatment waveform ranged from -0.5 to +1.8 V. These were output using a custom built instrument for potential application to the electrochemical cell and current transduction (University of North Carolina at Chapel Hill, Department of Chemistry, Electronics Facility). TH-1 software (ESA, Chelmsford, MA) was used for waveform output with a DAC/ADC card (NI 6251 M). A second card (NI 6711) was used for triggering the DACs and ADCs and for synchronization of the electrochemical experiment with flow

injection. Signal processing (background subtraction, signal averaging, and digital filtering (4-pole Bessel Filter, 2 KHz) was software-controlled.

Simulations of cyclic voltammograms were generated using DigiSim Version 3 (Bioanalytical Systems, Inc., West Lafayette, IN).

3.2.5 Surface Analysis

AFM of the carbon surface was carried out with a Veeco D3000 microscope (Plainview, NY) using tips from Nanosensors (PPP-HCH, Neuchatel, Switzerland) with a nominal resonance of 280 kHz. Raman experiments were performed with a previously described custom built spectrometer (29). Spectra with a collection time of 120 seconds were obtained with a dry 100x objective while the electrode surface was submerged within physiological pH 7.4 Tris buffer solution.

3.2.6 Chemical Derivatization

Surface derivatization of electrochemically pretreated electrodes with 2,4-dinitrophenylhydrazine (DNPH) (Alfa Aesar, Ward Hill, MA) was accomplished following the procedure of Fryling et. al. (27, 32). An equal molar ratio of concentrated HCl and KOH (Thermo Fisher Scientific, Inc., Pittsburgh, PA) were used for a Lucas test reagent (33). Electrochemically pretreated electrodes were saturated for one minute in the Lucas test solution. Structures were drawn using ChemDraw Ultra v11.0.

3.2.7 Statistics

Data are presented as the mean \pm standard error of the mean. A one-tailed Student's *t* tests were used to determine significance of means. Analysis of covariance (ANCOVA) was used for the comparison of linear regression results. In Figure 3.6, data were analyzed using a one-way ANOVA with Tukey's post hoc test for repeated measures. In all cases, statistical significance is designated as $p < 0.05$. Statistical and graphical analysis was carried out using GraphPad Prism 5 (GraphPad Software, Inc., La Jolla, CA).

3.3 Results and Discussion

3.3.1 Electrochemical Pretreatment Enhances Electrode Sensitivity

A freshly polished electrode was used to detect various concentrations of dopamine before and after application of a facile electrochemical pretreatment with FSCV. This experimental design allowed for the comparison of data at a single electrode, thus eliminating confounds resulting from electrode-to-electrode variability.

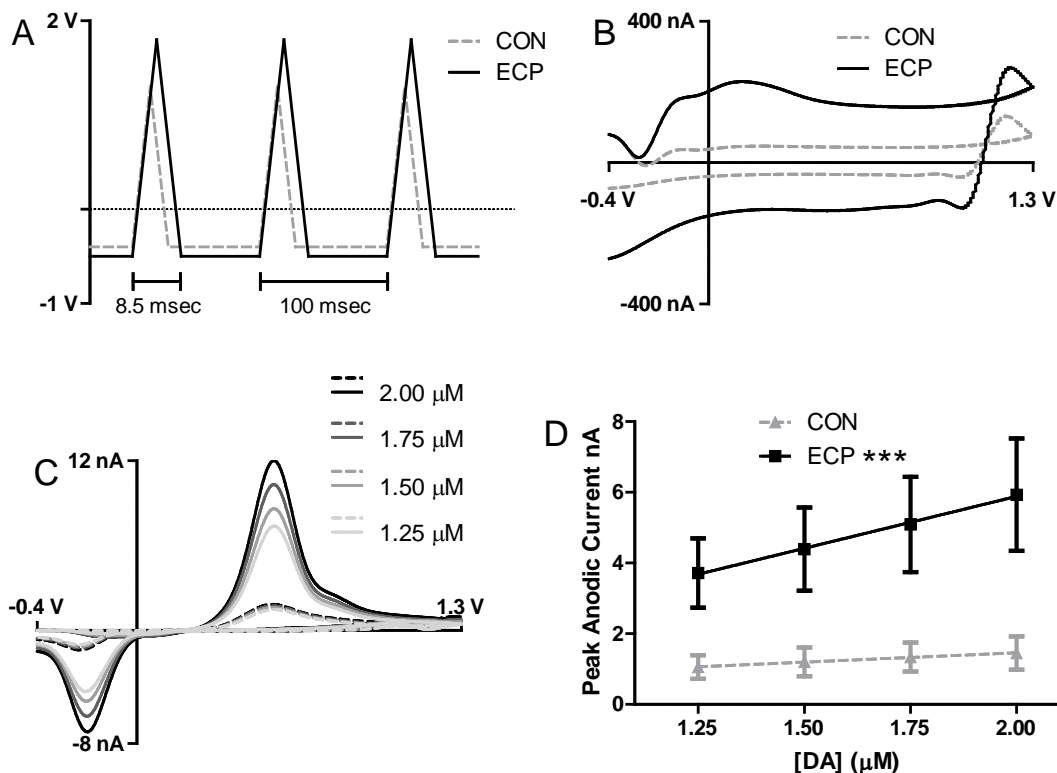


Figure 3.1 - Electrochemical pretreatment enhances electrode sensitivity. (A) A comparison of the electrochemical waveforms, applied at 400 V/s every 100 msec. The electrochemical pretreatment waveform ranged from -0.5 to +1.8 V. The control waveform used for electrochemical detection ranged from -0.4 to +1.3 V. (B) Representative background cyclic voltammograms collected at a single electrode, demonstrating the change in nonfaradaic charging current that results in response to electrochemical pretreatment. (C) Representative background-subtracted cyclic voltammograms collected at one electrode in response to varying concentrations of DA, before (dashed lines) and after (solid lines) electrochemical pretreatment. (D) Calibration curve that demonstrates increased sensitivity after pretreatment ($n = 6$, $p < 0.001$, ANCOVA).

Figure 3.1A illustrates the waveforms used for detection and pretreatment, applied with a scan rate of 400 V/s and a frequency of 10 Hz. A waveform that is regularly used *in vivo*, ranging from -0.4 to +1.3 V, was applied for approximately 10 min until the electrode stabilized. Herein, this waveform will be termed the control waveform (CON), which was

used for the initial detection of dopamine. A pretreatment waveform (ECP), ranging from -0.5 to +1.8 V, was subsequently applied for five minutes as a treatment which was intended to build surface oxides for improved electrochemical performance. Finally, the control waveform was again applied for at least 10 minutes to reestablish a stable background current prior to the final detection of dopamine. Figure 3.1B reveals the non-faradaic background current generated in response to the application of each of these waveforms, showing a 3.6 fold increase in the capacitive charge upon the pretreatment process. Figure 3.1C demonstrates representative CVs for the detection of various dopamine concentrations at a single electrode before (dashed lines) and after (solid lines) electrochemical pretreatment. Obvious increases in the peak anodic and cathodic currents are evident after pretreatment. In Figure 3.1D, peak anodic currents were plotted against a range of physiological dopamine concentrations and the 5.6-fold increase in the slope demonstrates that the electrochemical pretreatment significantly ($p < 0.001$, ANCOVA) increased sensitivity for the detection of dopamine ($n = 6$). The normalized sensitivities (accounting for electrode area) were $0.17 \pm 0.01 \text{ mA} \cdot \mu\text{M}^{-1} \cdot \text{cm}^{-2}$ prior to pretreatment and $0.97 \pm 0.04 \text{ mA} \mu\text{M}^{-1} \text{ cm}^{-2}$ after conditioning. The sensitivity for the more commonly used cylindrical carbon fiber microelectrode was $0.621 \text{ mA} \cdot \mu\text{M}^{-1} \cdot \text{cm}^{-2}$ ($n = 4$), a value not significantly different from that of the pretreated disk electrode ($p > 0.05$, ANCOVA).

To rule out the possibility that the increased signal inherent to an ECP-conditioned electrode was due solely to an increased electrochemical cycling time (rather than to the extended wavelimits of the ECP waveform), a control experiment was conducted in a separate set of electrodes ($n = 4$). For this group, the ECP conditioning period was

substituted with a period of conditioning using the control waveform; however, the wavelimits were not extended. An average signal of 0.9 ± 0.1 nA was measured for 1 μ M dopamine both before and after this conditioning, demonstrating that this additional cycling time did not improve sensitivity to this analyte ($p > 0.05$, one-tailed paired t test). Thus, it was concluded that signal enhancement after ECP conditioning resulted from the extended wavelimits of the applied ECP waveform.

3.3.2 Atomic Force Microscopy

Because the electrochemical background current scales with electrode area, and application of the electrochemical pretreatment waveform increased the capacitive background current (Figure 3.1B), the enhanced electrochemical sensitivity may have resulted from an increase in electrode surface area. However, no obvious differences in the electrode surface area or fiber diameter were detected with optical or scanning electron microscopy (SEM) when control electrodes were compared to those that were pretreated with the ECP waveform (data not shown). Thus, contact AFM of the carbon electrode surface was carried out in order to determine if the nanoscale surface roughness was altered by electrochemical pretreatment. The first sample set ($n = 4$) established a baseline roughness for polished electrodes prior to the application of any waveform. The second sample set ($n = 4$) comprised of polished electrodes that were cycled with the ECP waveform for 5 minutes.

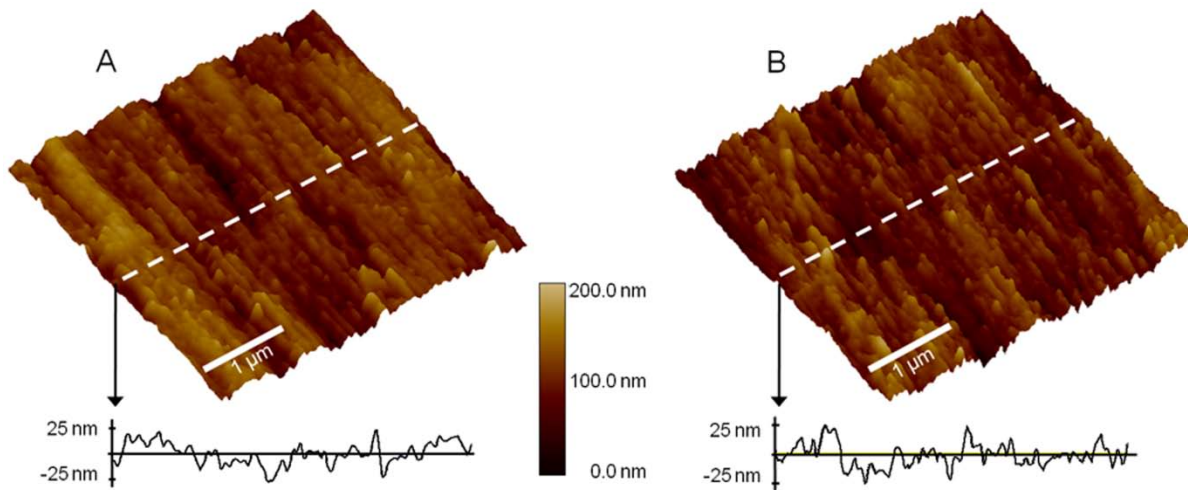


Figure 3.2 - Electrochemical conditioning does not alter surface roughness. Representative AFM images collected at (A) an unconditioned carbon microdisc electrode and (B) an electrode conditioned with the ECP waveform, with associated line plots. Surface roughness values were not significantly different between the two groups ($n = 4$, $p > 0.05$, Student's t test).

Figure 3.2A,B show representative AFM images and line plots from these sample sets. Quantitative analysis of these data indicated that the rms roughness values for the two surface treatments were 13.8 ± 0.6 nm for a polished electrode and 13.9 ± 0.2 nm for an ECP-cycled electrode. These values were not significantly different ($p > 0.05$, one-tailed t test). Thus, electrode surface topography at this size scale did not play a significant role in enhancing the electrochemical signal.

3.3.3 Adsorption Isotherm

It has been previously reported that during voltammetric detection of dopamine at carbon fiber microelectrodes, dopamine adsorbs to oxide groups on the carbon surface (12, 19). Thus, the increase in sensitivity resulting from electrochemical pretreatment may have

been due to an increase in the number of adsorption sites on the carbon surface for dopamine. Therefore, the amount of adsorbed analyte on the carbon surface was determined before and after the electrochemical pretreatment. The equation for peak current due to an adsorbing species:

$$i_p = (9.36 \times 10^5)n^2\nu A\Gamma_{DA} \quad (1)$$

defines how the peak anodic current (i_p) is proportional to both the surface coverage of the analyte (Γ_{DA}) and the surface area of the electrode ($A = 3 \times 10^{-6} \text{ cm}^2$) (34). Given that the surface area of the electrode was not significantly altered by the pretreatment process, the number of electrons transferred ($n = 2$), and the unchanged scan rate ($\nu = 400 \text{ V/s}$), it follows that the adsorbing qualities increased due to the electrochemical pretreatment. To further investigate this, a Langmuir isotherm was constructed to quantify surface coverage of adsorbed dopamine. An adsorption isotherm is a method of relating the concentration of analyte in the bulk solution around an electrode, the coverage of the analyte adsorbed to the electrode surface, and the electrical state of the system at a given temperature (34).

Langmuir isotherms are governed by the equation:

$$\frac{\Gamma_{DA}}{\Gamma_s - \Gamma_{DA}} = \beta[DA] \quad (2)$$

where β is a constant, $[DA]$ is the concentration of dopamine in the bulk solution, and Γ_s is the saturation coverage of dopamine on the electrode surface. This equation reduces the number of variables by assuming no interactions between adsorbed species, a homogenous electrode surface, and at high concentrations the ability to form a monolayer (34). It has been shown that at low concentrations the equation for the Langmuir isotherm can be further

reduced to a simplified form, where $b = \beta\Gamma_S$, by assuming that the Γ_{DA} is small in comparison to the Γ_S (19, 35).

$$\Gamma_{DA} = b[DA] \quad (3)$$

The peak anodic currents for varying concentrations of dopamine were measured before and after electrochemical pretreatment. These experimentally measured currents are attributed to the sum of the diffusive and adsorptive currents at the electrode surface (12). Thus, a purely diffusion-controlled environment was digitally simulated, and the current due to diffusion was subtracted from the experimental current to resolve the contribution from adsorption alone. Using eq 1, the surface coverage of adsorbed dopamine was extracted from the diffusion-corrected experimental data and plotted versus concentration (Figure 3.3).

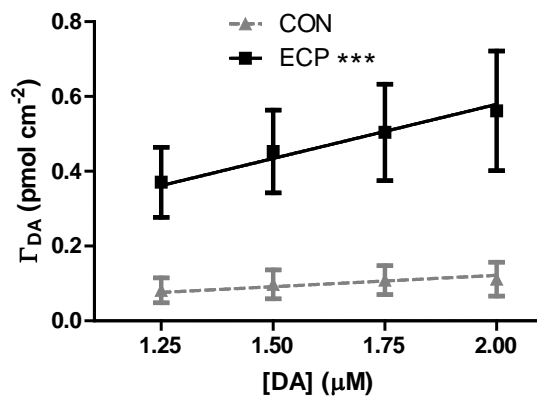


Figure 3.3 - Electrochemical pretreatment increases adsorption of dopamine to the carbon microelectrode surface. The Langmuir isotherms show increased surface coverage of DA at electrochemically pretreated electrodes, as compared to those conditioned with the control waveform ($n = 6$, $p < 0.001$, ANCOVA).

The 8-fold increase in the slope after application of ECP indicates that increased adsorption of dopamine to the electrode surface significantly ($p < 0.001$, ANCOVA) contributes to the enhanced electrochemical signal ($n = 6$). These data are consistent with previous reports demonstrating that increased adsorption at electrode surface increases sensitivity (35, 36).

3.3.4 Raman Spectroscopy of Carbon-Fiber Microelectrode Surface

The population of oxide-containing functional groups on the electrode surface may have been altered by application of the electrochemical waveform. Indeed, carbon surfaces are prone to reactions with O_2 and H_2O to form various oxygen-containing functional groups (8), and the application of an extended electrochemical waveform to a bundle of carbon fibers has been shown to increase the oxygen-to-carbon ratio, as observed with XPS (37). Here, Raman spectroscopy was used to determine the specific surface species responsible for enhanced dopamine adsorption to the carbon fiber surface. This method, which relies on the inelastic scattering of monochromatic light to provide information on molecular structure, was chosen for the exquisitely sensitive and nondestructive nature of the visible laser along with the ability to make measurements *in situ* through physiologically buffered solution (38).

McCreery et. al. have done extensive work using Raman spectroscopy to investigate graphitic and glassy carbon electrode surface structure, contributing greatly to the fundamental characterization of these carbon surfaces (8). However, carbon subtypes are highly variable in bulk and surface chemical properties, and cannot be generalized. In this work, spectra were collected to investigate the surface functional groups that develop on the

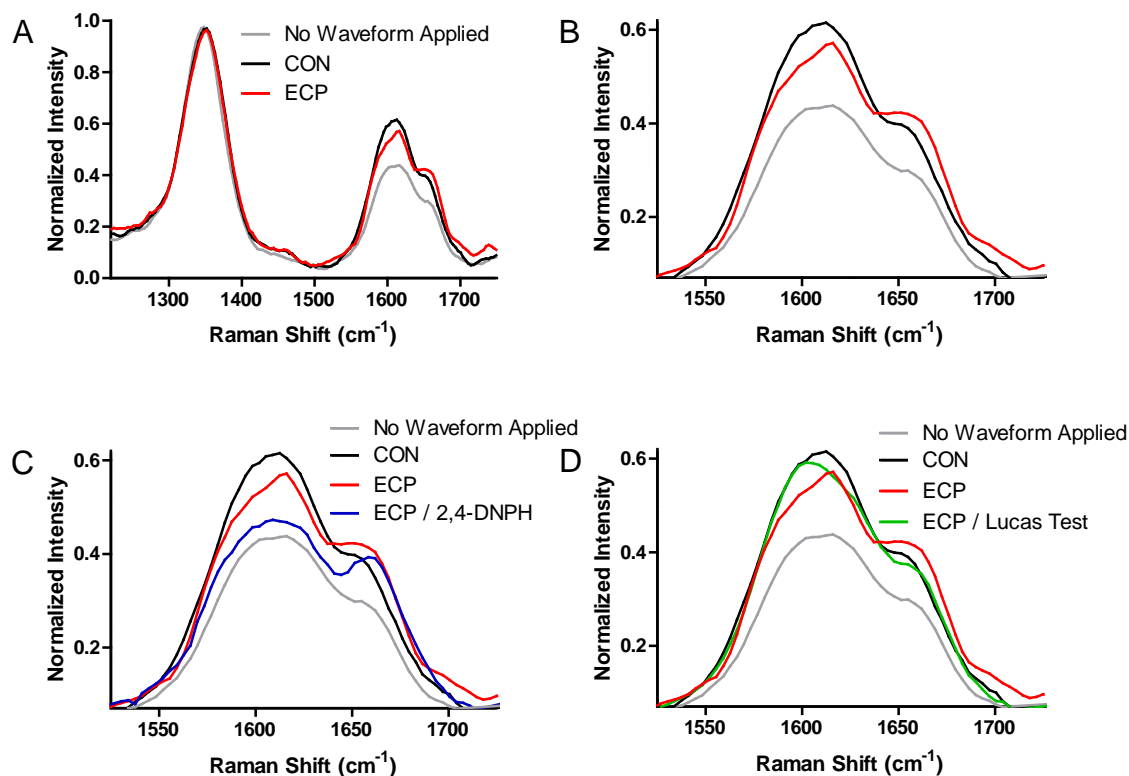


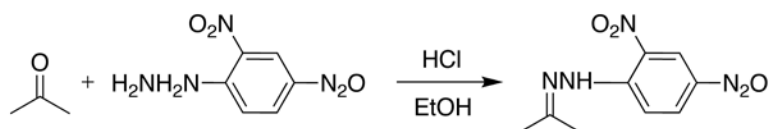
Figure 3.4 - Electrochemical conditioning increases surface carbonyl and hydroxyl groups. Averaged Raman spectra collected at the surface of carbon fiber microelectrodes, normalized to the 1340 cm⁻¹ peak. (A) Three prominent peaks of interest were noted in spectra collected from all sample sets: electrodes that had not been conditioned, electrodes conditioned with the control waveform (CON) and those conditioned with the electrochemical pretreatment (ECP) waveform. (B) Expanded view of a portion of (A) demonstrating the variation in the 1610 and 1655 cm⁻¹ peaks that results upon electrochemical conditioning. (C and D) Spectra collected after specific derivatization of surface oxygen-containing functional groups. (n = 6 for all spectra).

surface of P-55 carbon fiber microelectrodes in response to electrochemical pretreatment.

All measurements were performed in buffer solution. Consistent with previously published spectra for highly ordered pyrolytic graphite electrodes, three prominent Raman peaks were noted at 1340, 1610, and 1655 cm⁻¹ (Figure 3.4A) (39). The peak at 1340 cm⁻¹ was used in

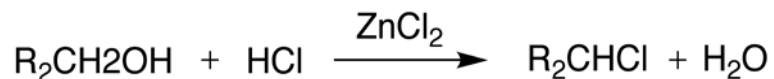
data normalization as this band is reliably stable and inherent to the graphitic lattice (39). Figure 3.4A shows the averaged spectra for freshly polished electrodes ($n = 3$, gray), and for electrodes conditioned with the control CON ($n = 3$, black), and ECP ($n = 3$, red) electrochemical waveforms. Figure 3.4B is an enlargement of the $1500 - 1750 \text{ cm}^{-1}$ range. Application of the control waveform increased the intensity of the peaks at 1610 and 1655 cm^{-1} as compared to an electrode that had no waveform applied. Electrodes conditioned with the ECP waveform exhibited a modest increase in the Raman intensity at 1610 cm^{-1} as compared to an electrode that had no conditioning; however, the intensity did not reach the value measured at electrodes conditioned with the control waveform. In contrast, the intensity of the 1655 cm^{-1} peak exceeded that collected at a control electrode conditioned with the control waveform, and this peak shifted to a slightly higher wavenumber. This distinct shift is likely due to increased intercalation of small anions, cations, and neutrals between graphite layers as the surface oxides are increased (40). A similar band has previously been observed for intercalation compounds and oxidized sp^2 carbon, due to an altered electronic environment as a result of increased asymmetry at the carbon surface (41-47).

Because XPS studies have shown that carbonyl and hydroxyl groups are the predominate surface oxide functionalities on carbon (48, 49), Raman spectroscopy was used to investigate electrochemically pretreated electrodes after selective derivatization of the surface. DNPH was used to target carbonyl groups selectively, forming a hydrazone derivative on the carbon surface (33). The following condensation reaction illustrates the product of the addition of DNPH.



The resulting spectra showed a marked reduction in the 1610 cm^{-1} peak, but the 1655 cm^{-1} peak remained relatively unchanged (Figure 3.4C, blue, $n = 6$), as compared to nonderivatized, ECP conditioned electrodes (red). This suggests that the 1610 cm^{-1} peak is largely due to the presence of surface carbonyl groups, and the selective removal of these groups allows the shoulder at 1655 cm^{-1} to become more apparent.

A classic condensation reaction was used to selectively target hydroxyl functionalities on the carbon surface. Organic chemistry dictates that an acid anhydride forms a covalent ester bond with alcohols, but not with carbonyl groups (33). Thus, the final sample set consisted of ECP conditioned electrodes that had subsequently undergone the Lucas test for hydroxyl groups according to the following condensation reaction.



This modification was designed to remove the surface hydroxyl groups from an electrochemically pretreated electrode (Figure 3.5).

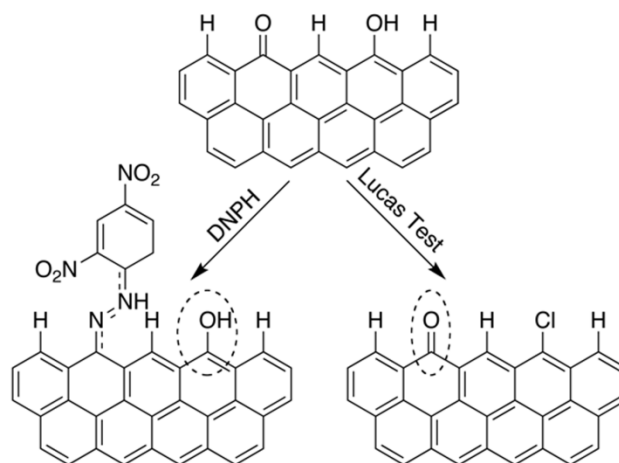


Figure 3.5 - Chemical derivatization of oxidized, edge-plane graphitic carbon at a microelectrode surface. Derivatization using DNPH specifically targets carbonyl groups (left). Condensation of the surface hydroxyl group using the Lucas test (right). Dashed ovals highlight the oxygen functionalities remaining after chemical modification.

The Raman spectra for this sample set (Figure 3.4D, green, $n = 6$) showed a marked reduction in the 1655 cm^{-1} peak when compared to nonderivatized, ECP-conditioned electrodes. This resulted in a spectrum that was strikingly similar to that acquired at the set of electrodes conditioned with the control waveform alone. Thus, the 1610 and 1655 cm^{-1} peak intensities were largely attributed to the surface carbonyl and hydroxyl groups, respectively. The data are consistent with previously reported XPS spectra collected at a bundle of carbon fibers demonstrating that the carbonyl surface functionality dominated with application of lower potentials; however, the hydroxyl group population developed as the applied potential increased to approximately 3.0 V (37). Overall, these data indicate that the application of the ECP waveform selectively increases surface hydroxyl group coverage and the formation of these hydroxyl functionalities significantly contributes to the enhanced electrochemical sensitivity to dopamine.

3.3.5 Electrochemical Characterization of Chemically Modified Electrodes

To verify this hypothesis electrochemically, electrodes were initially conditioned using the control waveform. Next, dopamine and ferrocenecarboxylic acid (FCA) were detected using background-subtracted FSCV before and after electrochemical pretreatment and again after subsequent derivatization of surface hydroxyl groups. FCA was chosen because it undergoes a well-characterized and highly reversible oxidation. The detection of the more adsorbing species, dopamine, should be enhanced to a greater extent by oxide functionalities on the carbon surface.

Figure 3.6 illustrates the results of the detection of 1 μ M dopamine (Figures 3.6A,C) and 1 mM FCA (Figures 3.6B,D). As expected, the electrochemical pretreatment significantly ($p < 0.001$) increased the electrochemical signal for dopamine ($n = 7$). Subsequent derivatization of the hydroxyl functionalities on the electrode surface significantly attenuated the signal enhancement; however, enhancement was not fully abolished. This is most likely due to the regeneration of surface hydroxyl groups upon renewed electrochemical cycling using the control waveform (19). The electrochemical pretreatment process did not significantly improve the signal in response to FCA ($p > 0.05$, $n = 7$), a species whose electrochemical detection is largely diffusion controlled (Figures 3.6C,D). The heterogeneous electron transfer rate constants (k^0) for the electrochemical detection of dopamine and FCA at pH 7.4, before and after pretreatment, were determined by digital simulation. For dopamine, there was a 2-fold increase in the k^0 for the electrochemical pretreatment process. For FCA, there was no significant change in the rate constant. This finding is in agreement with the results of previous studies that demonstrate

enhanced electron transfer at electrochemically treated, versus freshly cleaved, carbon fiber microdisk electrodes, particularly in the oxidation of cationic catechols (18, 50).

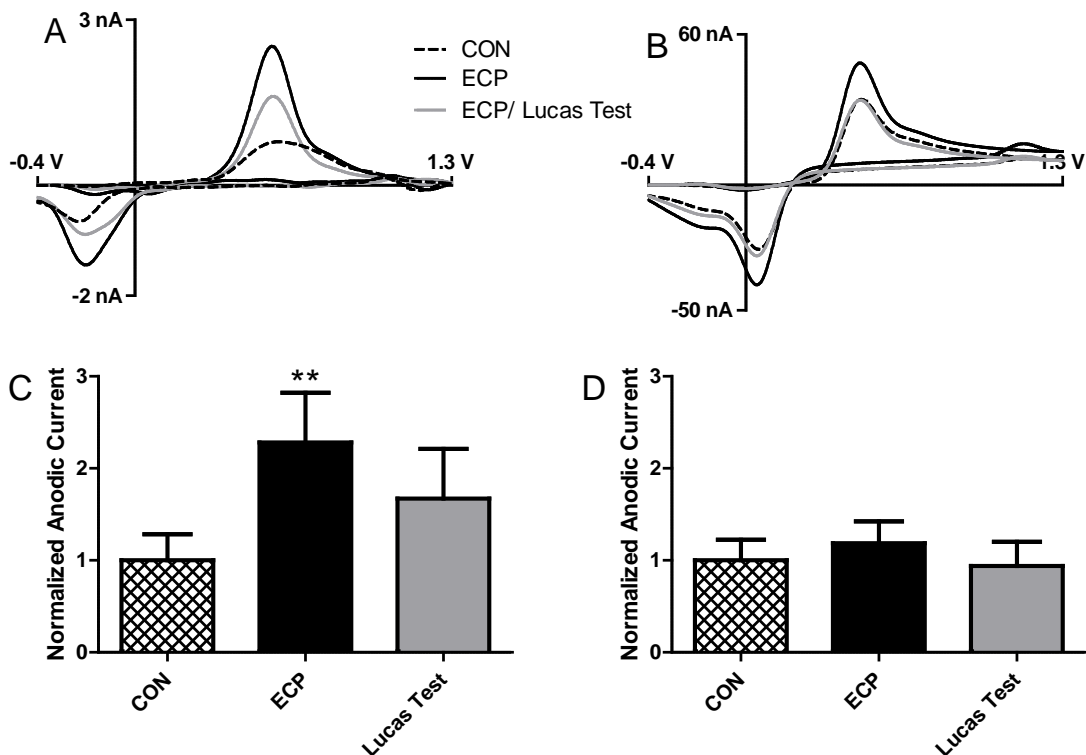


Figure 3.6 - Hydroxyl groups on the carbon fiber surface gained by electrochemical pretreatment with extended wavelimits underlie signal enhancement in the detection of DA. (A, B) Representative cyclic voltammograms for 1 μ M DA and 1 mM FCA respectively, before and after removal of hydroxyl groups using the Lucas test. (C, D) Normalized peak anodic currents for 1 μ M DA and 1 mM FCA, respectively, before and after Lucas test. (n = 7, p < 0.001, ANOVA).

3.4 Conclusions

The results show that electrochemical pretreatment of a pitch-based P-55s carbon fiber microelectrode can be used to increase electrode sensitivity, creating an improved tool for electrochemical measurements in small microdomains. The electrochemical pretreatment described herein results in an increased population of surface oxides consisting largely of carbonyl and, particularly at higher pretreatment potentials, hydroxyl functional groups that underlie an improved adsorptivity of dopamine on the carbon surface. Boasting a 5-fold increase in peak anodic current, nearly a 6-fold increase in sensitivity, and faster electron-transfer kinetics for the detection of dopamine, a pretreated carbon microdisk electrode offers a competitive alternative to a larger, cylindrical carbon fiber microelectrode for single channel measurements, and an optimized geometry that permits multiplexing into closely-spaced, multiple electrode arrays.

3.5 References

1. Staal, R. G., Mosharov, E. V., and Sulzer, D. (2004) Dopamine neurons release transmitter via a flickering fusion pore, *Nat Neurosci* 7, 341-346.
2. Sombers, L. A., Hanchar, H. J., Colliver, T. L., Wittenberg, N., Cans, A., Arbault, S., Amatore, C., and Ewing, A. G. (2004) The effects of vesicular volume on secretion through the fusion pore in exocytotic release from PC12 cells, *Journal of Neuroscience* 24, 303-309.
3. Heien, M. L., and Ewing, A. G. (2009) Quantitative chemical analysis of single cells, *Methods Mol Biol* 544, 153-162.
4. Robinson, D. L., Venton, B. J., Heien, M. L., and Wightman, R. M. (2003) Detecting subsecond dopamine release with fast-scan cyclic voltammetry in vivo, *Clin Chem* 49, 1763-1773.
5. Robinson, D. L., Hermans, A., Seipel, A. T., and Wightman, R. M. (2008) Monitoring rapid chemical communication in the brain, *Chemical Reviews* 108, 2554-2584.
6. Cahill, P. S., Walker, Q. D., Finnegan, J. M., Mickelson, G. E., Travis, E. R., and Wightman, R. M. (1996) Microelectrodes for the measurement of catecholamines in biological systems, *Anal Chem* 68, 3180-3186.
7. Wightman, R. M. (2006) Detection technologies. Probing cellular chemistry in biological systems with microelectrodes, *Science* 311, 1570-1574.
8. McCreery, R. L. (2008) Advanced carbon electrode materials for molecular electrochemistry, *Chemical Reviews* 108, 2646-2687.
9. Hershenhart, E., McCreery, R. L., and Knight, R. D. (1984) In situ Cleaning and Activation of Solid Electrode Surfaces by Pulsed Laser-Light, *Analytical Chemistry* 56, 2256-2257.
10. Poon, M., McCreery, R. L., and Engstrom, R. (1988) Laser Activation of Carbon Electrodes - Relationship between Laser-Induced Surface Effects and Electron-Transfer Activation, *Analytical Chemistry* 60, 1725-1730.
11. Strein, T. G., and Ewing, A. G. (1994) Laser Activation of Microdisk Electrodes Examined by Fast-Scan Rate Voltammetry and Digital-Simulation, *Analytical Chemistry* 66, 3864-3872.

12. Bath, B. D., Michael, D. J., Trafton, B. J., Joseph, J. D., Runnels, P. L., and Wightman, R. M. (2000) Subsecond adsorption and desorption of dopamine at carbon-fiber microelectrodes, *Analytical Chemistry* 72, 5994-6002.
13. Kawagoe, K. T., Zimmerman, J. B., and Wightman, R. M. (1993) Principles of voltammetry and microelectrode surface states, *J Neurosci Methods* 48, 225-240.
14. Strand, A. M., and Venton, B. J. (2008) Flame etching enhances the sensitivity of carbon-fiber microelectrodes, *Analytical Chemistry* 80, 3708-3715.
15. Engstrom, R. C. (1982) Electrochemical Pretreatment of Glassy-Carbon Electrodes, *Analytical Chemistry* 54, 2310-2314.
16. Engstrom, R. C. (1984) Spatial-Resolution of Electrode Heterogeneity Using Iontophoresis, *Analytical Chemistry* 56, 890-894.
17. Gonon, F. G., Fombarlet, C. M., Buda, M. J., and Pujol, J. F. (1981) Electrochemical Treatment of Pyrolytic Carbon-Fiber Electrodes, *Analytical Chemistry* 53, 1386-1389.
18. Saraceno, R. A., and Ewing, A. G. (1988) Electron-Transfer Reactions of Catechols at Ultrasmall Carbon Ring Electrodes, *Analytical Chemistry* 60, 2016-2020.
19. Heien, M. L. A. V., Phillips, P. E. M., Stuber, G. D., Seipel, A. T., and Wightman, R. M. (2003) Overoxidation of carbon-fiber microelectrodes enhances dopamine adsorption and increases sensitivity, *Analyst* 128, 1413-1419.
20. Gonon, F., Buda, M., Cespuglio, R., Jouvet, M., and Pujol, J. F. (1980) In vivo electrochemical detection of catechols in the neostriatum of anaesthetized rats: dopamine or DOPAC?, *Nature* 286, 902-904.
21. Hafizi, S., Kruk, Z. L., and Stamford, J. A. (1990) Fast cyclic voltammetry: improved sensitivity to dopamine with extended oxidation scan limits, *J Neurosci Methods* 33, 41-49.
22. Langley, L. A., Villanueva, D. E., and Fairbrother, D. H. (2006) Quantification of surface oxides on carbonaceous materials, *Chemistry of Materials* 18, 169-178.
23. Fagan, D. T., and Kuwana, T. (1989) Thermal-Desorption Mass Analysis of Carbon-Fiber Surfaces - Surface Oxygen Complexes, *Analytical Chemistry* 61, 1017-1023.
24. Pantano, P., and Kuhr, W. G. (1991) Characterization of the Chemical Architecture of Carbon-Fiber Microelectrodes .1. Carboxylates, *Analytical Chemistry* 63, 1413-1418.

25. Pantano, P., and Kuhr, W. G. (1993) Characterization of the Chemical Architecture of Carbon-Fiber Microelectrodes .2. Correlation of Carboxylate Distribution with Electron-Transfer Properties, *Analytical Chemistry* 65, 2452-2458.
26. Pantano, P., and Kuhr, W. G. (1993) Dehydrogenase-modified carbon-fiber microelectrodes for the measurement of neurotransmitter dynamics. 2. Covalent modification utilizing avidin-biotin technology, *Anal Chem* 65, 623-630.
27. Ray, K. R., and McCreery, R. L. (1999) Characterization of the surface carbonyl and hydroxyl coverage on glassy carbon electrodes using Raman spectroscopy, *J Electroanal Chem* 469, 150-158.
28. Heien, M. L. A. V., Johnson, M. A., and Wightman, R. M. (2004) Resolving neurotransmitters detected by fast-scan cyclic voltammetry, *Analytical Chemistry* 76, 5697-5704.
29. Zachek, M. K., Takmakov, P., Moody, B., Wightman, R. M., and McCarty, G. S. (2009) Simultaneous Decoupled Detection of Dopamine and Oxygen Using Pyrolyzed Carbon Microarrays and Fast-Scan Cyclic Voltammetry, *Analytical Chemistry* 81, 6258-6265.
30. Sombers, L. A., Beyene, M., Carelli, R. M., and Wightman, R. M. (2009) Synaptic overflow of dopamine in the nucleus accumbens arises from neuronal activity in the ventral tegmental area, *Journal of Neuroscience* 29, 1735-1742.
31. Hermans, A., Keithley, R. B., Kita, J. M., Sombers, L. A., and Wightman, R. M. (2008) Dopamine detection with fast-scan cyclic voltammetry used with analog background subtraction, *Analytical Chemistry* 80, 4040-4048.
32. Fryling, M. A., Zhao, J., and McCreery, R. L. (1995) Resonance Raman Observation of Surface Carbonyl Groups on Carbon Electrodes Following Dinitrophenylhydrazine Derivatization, *Analytical Chemistry* 67, 967-975.
33. Shriner, R. L., and Fuson, R. C. (1979) *The systematic identification of organic compounds; a laboratory manual*, 6d ed., J. Wiley, New York,.
34. Bard, A. J., and Faulkner, L. R. (2001) *Electrochemical Methods: Fundamentals and Applications*, 2nd ed., John Wiley, New York.
35. Zachek, M. K., Hermans, A., Wightman, R. M., and McCarty, G. S. (2008) Electrochemical dopamine detection: Comparing gold and carbon fiber microelectrodes using background subtracted fast scan cyclic voltammetry, *J Electroanal Chem* 614, 113-120.

36. Bath, B. D., Martin, H. B., Wightman, R. M., and Anderson, M. R. (2001) Dopamine adsorption at surface modified carbon-fiber electrodes, *Langmuir* 17, 7032-7039.
37. Proctor, A., and Sherwood, P. M. A. (1983) X-Ray Photoelectron Spectroscopic Studies of Carbon-Fiber Surfaces .2. The Effect of Electrochemical Treatment, *Carbon* 21, 53-59.
38. Ray, K., and McCreery, R. L. (1997) Spatially resolved Raman spectroscopy of carbon electrode surfaces: Observations of structural and chemical heterogeneity, *Analytical Chemistry* 69, 4680-4687.
39. Wang, Y., Alsmeyer, D. C., and McCreery, R. L. (1990) Raman-Spectroscopy of Carbon Materials - Structural Basis of Observed Spectra, *Chemistry of Materials* 2, 557-563.
40. Dresselhaus, M. S., Dresselhaus, G., and Fischer, J. E. (1977) Graphite Intercalation Compounds - Electronic Properties in Dilute Limit, *Physical Review B* 15, 3180-3192.
41. Nakamizo, M., and Tamai, K. (1984) Raman-Spectra of the Oxidized and Polished Surfaces of Carbon, *Carbon* 22, 197-198.
42. Nemanich, R. J., and Solin, S. A. (1979) 1st-Order and 2nd-Order Raman-Scattering from Finite-Size Crystals of Graphite, *Physical Review B* 20, 392-401.
43. Dresselhaus, M. S., and Dresselhaus, G. (1981) Intercalation Compounds of Graphite, *Advances in Physics* 30, 139-326.
44. Bowling, R. J., Packard, R. T., and McCreery, R. L. (1989) Activation of Highly Ordered Pyrolytic-Graphite for Heterogeneous Electron-Transfer - Relationship between Electrochemical Performance and Carbon Microstructure, *Journal of the American Chemical Society* 111, 1217-1223.
45. Aljishi, R., and Dresselhaus, G. (1982) Lattice-Dynamical Model for Graphite, *Physical Review B* 26, 4514-4522.
46. Underhill, C., Leung, S. Y., Dresselhaus, G., and Dresselhaus, M. S. (1979) Infrared and Raman-Spectroscopy of Graphite-Ferric Chloride, *Solid State Communications* 29, 769-774.
47. Aljishi, R., and Dresselhaus, G. (1982) Lattice-Dynamical Model for Alkali-Metal Graphite-Intercalation Compounds, *Physical Review B* 26, 4523-4538.

48. Tougas, T. P., and Collier, W. G. (1987) Determination of Surface Carbonyl Groups on Glassy-Carbon with X-Ray Photoelectron-Spectroscopy Preceded by Derivatization with Pentafluorophenylhydrazine, *Analytical Chemistry* 59, 2269-2272.
49. Collier, W. G., and Tougas, T. P. (1987) Determination of Surface Hydroxyl-Groups on Glassy-Carbon with X-Ray Photoelectron-Spectroscopy Preceded by Chemical Derivatization, *Analytical Chemistry* 59, 396-399.
50. Kovach, P. M., Ewing, A. G., Wilson, R. L., and Wightman, R. M. (1984) In vitro comparison of the selectivity of electrodes for in vivo electrochemistry, *J Neurosci Methods* 10, 215-227.

CHAPTER 4

Voltammetric Detection of Hydrogen Peroxide at Carbon Fiber Microelectrodes

The following work was reprinted with permission from: Audrey L. Sanford, Stephen W. Morton, Kelsey L. Whitehouse, Hannah M. Oara, Leyda Z. Lugo-Morales, James G. Roberts, and Leslie A. Sombers, *Analytical Chemistry*, 2010, 82, 5205-5210., Copyright 2010 American Chemical Society. This work was part of a collaborative effort and only a portion constitutes the author's personal dissertation research; however, all results are shown to allow for a complete interpretation of the findings.

4.1 Introduction

Hydrogen peroxide (H_2O_2) is an important, membrane permeable, reactive oxygen species (ROS) in the brain that is most often regarded as a potential toxin because, under certain conditions, it can form highly reactive hydroxyl radicals that can irreversibly alter DNA, lipid and protein structure (1). Thus, an imbalance between H_2O_2 generation and metabolism could result in pathological oxidative stress and neuronal degeneration in disease states and aging (2-4). However, H_2O_2 is also an important player in reductive-oxidative-based signal transduction cascades and thus is essential for normal cell function, especially in the brain (4-6). Furthermore, H_2O_2 is gaining increasing recognition as a rapid neuromodulatory signaling molecule. Recent studies in brain slices have demonstrated that the classical neurotransmitters, glutamate and γ -aminobutyric acid (GABA), regulate dopamine (DA) release on a subsecond timescale by way of transient H_2O_2 signaling in the dorsal striatum, a key brain region in motor control (7, 8).

Despite a growing interest in H_2O_2 , there are few experimental tools available to directly measure dynamic H_2O_2 fluctuations in intact tissue. Molecular imaging with H_2O_2 -

responsive fluorophores is a powerful, and commonly used, approach for examining the diverse roles that H_2O_2 plays in complex biological environments (9). However, conventional fluorescent probes lack selectivity for H_2O_2 over other ROS. They are difficult (if not impossible) to use for dynamic *in vivo* measurements, and calibration of the fluorescence intensity of these dyes is not possible, precluding their use in quantitative analyses. In contrast, electrochemical techniques are especially useful for quantifying rapid chemical changes *in vivo*, because small probe sizes and fast sampling rates can be employed (10). However, the electron transfer kinetics for the irreversible oxidation of H_2O_2 are slow (11, 12), thus limiting the development and application of electroanalytical methods for the direct detection of this molecule.

The electrochemical detection of H_2O_2 is of widespread interest to bioanalytical scientists because it is often enzymatically generated at biosensors to serve as an electroactive reporter molecule in the indirect detection of nonelectroactive biomolecules such as glucose, glutamate, and acetylcholine (13-19). Because the electrochemical oxidation of H_2O_2 is electrocatalyzed (12, 20), Pt electrodes are widespread in the construction of these sensors, which normally utilize amperometric detection. However Pt electrodes readily biofoul and, although amperometry provides an accurate measure of the local flux of electroactive species, it lacks selectivity. Thus, when used *in vivo* these devices require several selective exclusion layer coatings in addition to enzymatic coatings. This is a significant drawback because coated electrodes exhibit increased response times due to the time required for analyte to diffuse through the coating, and they are difficult to reproducibly fabricate (21). Furthermore, the stability and selectivity is dependent on coating integrity.

Another electrochemical technique, background-subtracted, fast-scan cyclic voltammetry (FSCV), provides chemical selectivity in addition to temporal resolution and high sensitivity (10). With this approach, a cyclic voltammogram is generated to serve as a chemical signature for the analyte of interest, allowing discrimination from other electroactive species in the brain (22). This technique is commonly used for *in vivo* measurements with carbon fiber microelectrodes, which are advantageous due to their biocompatibility, small size, and ease of fabrication (23). In this work, we present the first voltammetric recordings of H₂O₂ at single, uncoated carbon-fiber microelectrodes. To overcome the kinetic limitations, the carbon surface is electrochemically conditioned on the anodic scan and H₂O₂ is irreversibly oxidized on the cathodic scan. We verify the identity of our signal by monitoring the selective enzymatic degradation of H₂O₂ in the presence of catalase. Various scan rates are investigated to optimize the detection, and the limits of detection and detectable range of H₂O₂ are established. We demonstrate that H₂O₂ can be reliably quantified in the presence of multiple electroactive species that are commonly found in the brain. Finally, we establish that this approach can be used at microelectrodes to detect enzymatically-generated H₂O₂ upon consumption of non-electroactive enzyme substrate.

4.2 Experimental Section

4.2.1 Chemicals

All chemicals were purchased from Sigma-Aldrich (Milwaukee, WI), unless otherwise noted, and used as received. A physiological buffer solution (15 mM Trisma HCl, 3.25 mM KCl, 1.2 mM CaCl₂, 1.2 mM MgCl₂, 2.0 mM Na₂SO₄, 1.25 mM NaH₂PO₄, 145 mM

NaCl) at pH 7.4 was used in all flow injection analysis experiments. All aqueous solutions were made using doubly distilled deionized water (Barnstead EasyPure II, Dubuque, IA).

4.2.2 Electrode Fabrication

Carbon-fiber microelectrodes were fabricated by aspirating a single 7 μm diameter T-650 carbon fiber (Cytec Industries, West Patterson NJ) into a single borosilicate glass capillary (0.60 mm x 0.40 mm, A-M Systems, Carlsburg, WA). A micropipette puller (Narishige, Tokyo, Japan) was used to taper the glass and form two sealed microelectrodes. The exposed length of carbon fiber was cut to approximately 100 μm . An electrical connection was made by backfilling the capillary with an ionic solution (4 M potassium acetate, 150 mM KCl).

4.2.3 Data Acquisition

All data was collected in an *in vitro*, flow injection system unless otherwise specified. In most experiments, a triangular waveform ranging from -0.4 to +1.4 V with a holding potential of -0.4 V versus Ag/AgCl was applied at a scan rate of 400 $\text{V}\cdot\text{s}^{-1}$ and a frequency of 10 Hz using a custom built instrument for potential application to the electrochemical cell and for current transduction (University of North Carolina at Chapel Hill, Department of Chemistry, Electronics Facility). TH-1 software (ESA, Chelmsford, MA) was used for waveform output with a DAC/ADC card (NI 6251 M). A second card (NI 6711) was used for triggering the DACs and ADCs and for synchronization of the electrochemical

experiment with flow injection. Signal processing (background subtraction, signal averaging, and digital filtering (4-pole Bessel Filter, 2 KHz) was software-controlled.

4.2.4 Flow Injection

The working electrode was positioned in a custom electrochemical cell using a micromanipulator (World Precision Instruments, Inc., Sarasota, FL). A syringe pump (BS-8000, Braintree Scientific, Braintree, MA) supplied a continuous buffer flow of 3 mL/min across the working and reference electrodes. Five second bolus injections of analyte to the microelectrode surface were accomplished with a six-port HPLC valve mounted on a two-position air actuator controlled by a digital pneumatic solenoid valve kit (Valco Instruments, Houston TX). The entire apparatus was housed within a custom-built Faraday cage. All experiments were performed at room temperature.

4.2.5 Enzyme Coating of Microelectrodes

A total of 0.10 g of bovine serum albumin (BSA) was dissolved in 985 μL ddH₂O by manual agitation at room temperature. 5 microliters of glutaraldehyde solution (25%) was added and the mixture was allowed to set for 5 minutes. 1 μL of glucose oxidase (from *Aspergillus niger*) stock solution (2 U/ μL) was added to 9 μL of the BSA/glutaraldehyde solution in a 500 μL microcentrifuge tube and mixed by pipette agitation giving a final concentration of 0.1% BSA and 0.125% glutaraldehyde. Fabricated microelectrodes were then coated by dipping the microelectrode tip into the enzyme solution three times with 1-

minute dry times between dips. Finally, electrode tips were immersed in TRIS buffer (pH 7.4) at room temperature for one hour to allow the enzyme matrix to set.

4.2.6 Brain Slice Experiment

Male Sprague-Dawley rats (n = 4, 250-300 g, Charles River Laboratories, Raleigh, NC) were decapitated after being deeply anesthetized with urethane (1.5 g/kg, i.p.). The brain was rapidly removed and kept in cold Tris buffer at pH 7.4 while 400 μm thick coronal slices containing the striatum were prepared with a vibratome (World Precision Instruments, Sarasota, FL). Slices were subsequently placed in a recording chamber and superfused with buffer maintained at 37°C. A bare microelectrode (n = 4) was placed at least 100 μm below the surface of the slice, and a glass micropipette pulled from borosilicate glass capillary (1.2 mm x 0.68 mm, A-M Systems, Carlsburg, WA) with an outer tip diameter of 15-20 μm was positioned in the tissue about 1 mm from the recording electrode. Electrode and injector placements were made with the aid of a microscope (Nikon Instruments Inc., Melville, NY). Buffered solution containing 50 μM H_2O_2 was injected for 1 second at 5 psi with a Picospritzer III (Parker Hannifin Corp., Fairfield, NJ). Animal care was in accordance with institutional guidelines.

4.2.7 Statistics

All values are given as the mean \pm standard error of the mean (SEM). One-tailed paired Student's *t* tests were used to determine statistical differences, designated at $p < 0.05$. Mixtures were resolved with principal component regression using MATLAB (The

MathWorks, Natick, MA) (22). Statistical and graphical analysis was carried out using GraphPad Prism 5 (GraphPad Software, Inc., La Jolla, CA).

4.3 Results and Discussion

4.3.1 H_2O_2 Cyclic Voltammetry

Cyclic voltammograms were collected in the *in vitro* flow injection system by ramping the potential applied to the carbon fiber electrode from a holding potential of -0.4 V versus Ag/AgCl to 1.4 V and back at $400 \text{ V}\cdot\text{s}^{-1}$ every 100 ms, as shown in Figure 4.1A. The fast scan rate resulted in a non-faradaic background current, shown in Figure 4.1B (solid line), that was relatively stable over time. The current at the electrode increased slightly upon introduction of a 5 s bolus of $100 \mu\text{M}$ H_2O_2 to the electrode surface using the flow injection system (dashed line). The non-faradaic background current was subtracted to produce the analyte-specific cyclic voltammograms shown in Figure 4.1C,D. The oxidation peak for the two-electron, irreversible process was observed at an overpotential on the reverse scan.

Previous voltammetric studies using slow scan rates at carbon, Pt, or Pt + Ir electrodes in physiological buffer solution have established that the electrode must acquire an oxidized surface to accommodate H_2O_2 oxidation (12, 20, 24). Electrochemical conditioning of a carbon fiber microelectrode in aqueous solution using fast scan rates and similar potential limits specifically increases the population of carbonyl and hydroxyl functional groups on the carbon surface (25) in an oxidative etching process that constantly renews the electrochemically active surface (26). Thus, our finding that the H_2O_2 did not oxidize until

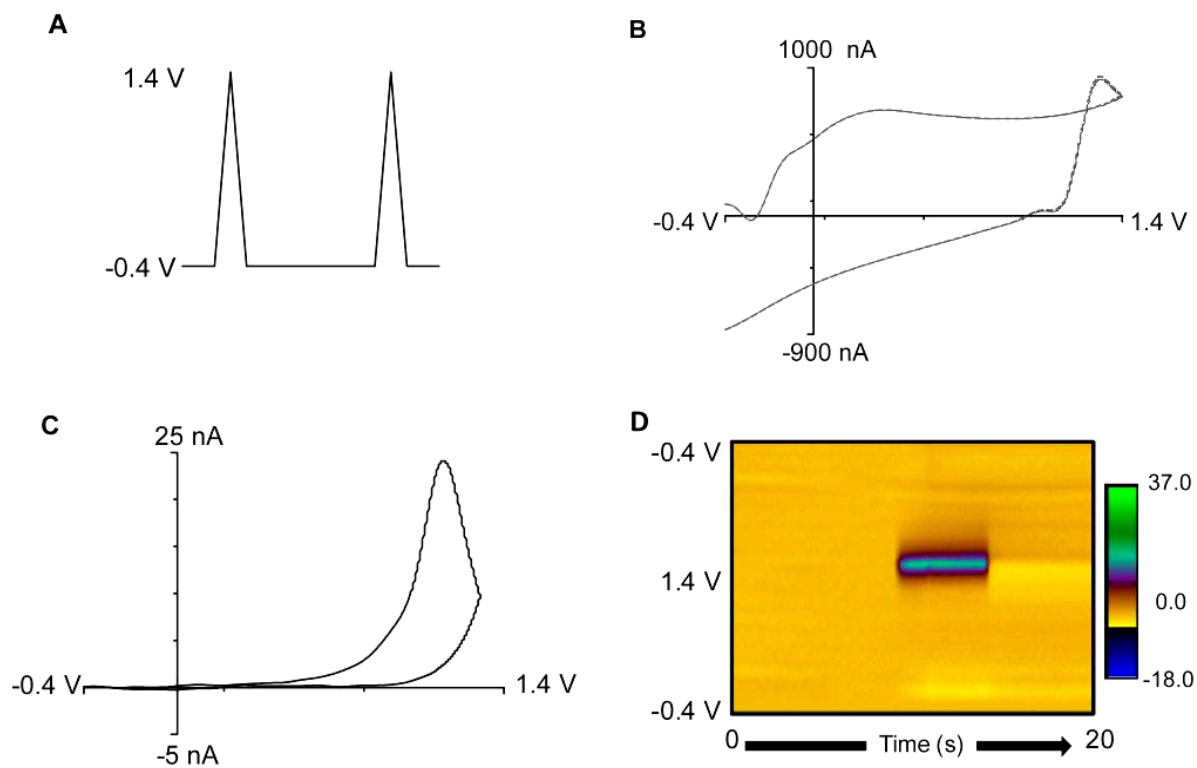


Figure 4.1 - Fast-scan cyclic voltammetry of H₂O₂. (A) The applied potential was scanned from -0.4 V to 1.4 V and back at 400 V·s⁻¹ every 100 msec. (B) Background current at the carbon surface produced by the rapid scan (solid line). This changed only slightly after 100 μM H₂O₂ was added (dashed line). (C) Background-subtracted cyclic voltammogram of 100 μM H₂O₂ at pH 7.4. At this scan rate the oxidation peak is detected at 1.2 V on the cathodic scan. (D) Color plot containing 200 background-subtracted cyclic voltammograms recorded over 20 sec. The ordinate is the applied potential to the carbon-fiber electrode, the abscissa is time, and the current (nA) is depicted in false color.

after the electrode was rapidly scanned to a moderately high anodic potential is not unexpected. To determine the potential limit required to sufficiently oxidize the electrode surface for the oxidation of H₂O₂, the switching potential was varied from 0.8 V to 1.4 V (Figure 4.2). A significant oxidation peak was observed only at switching potentials greater than 1.2 V. The amplitude of the oxidation current increased as the potential limit was

extended, with maximum sensitivity observed using a potential limit of 1.4 V. Thus, this waveform was selected for further characterization.

The scan rate was varied between 100 and 800 $\text{V}\cdot\text{s}^{-1}$, typical scan rates for *in vivo* measurements (Figure 4.3). At the slowest scan rate, the peak oxidation current for 100 μM H_2O_2 occurred at the switching potential, suggesting that oxidation was incomplete prior to switching to the cathodic scan. The cyclic voltammogram is similar to those published previously for the voltammetric detection of H_2O_2 on carbon at slow scan rates (27, 28). When the scan rate was increased the peak oxidation potential, E_p , shifted to the cathodic scan and the peak became well defined. The peak oxidation current was maximized at 400 $\text{V}\cdot\text{s}^{-1}$; thus, this scan rate was considered optimum.

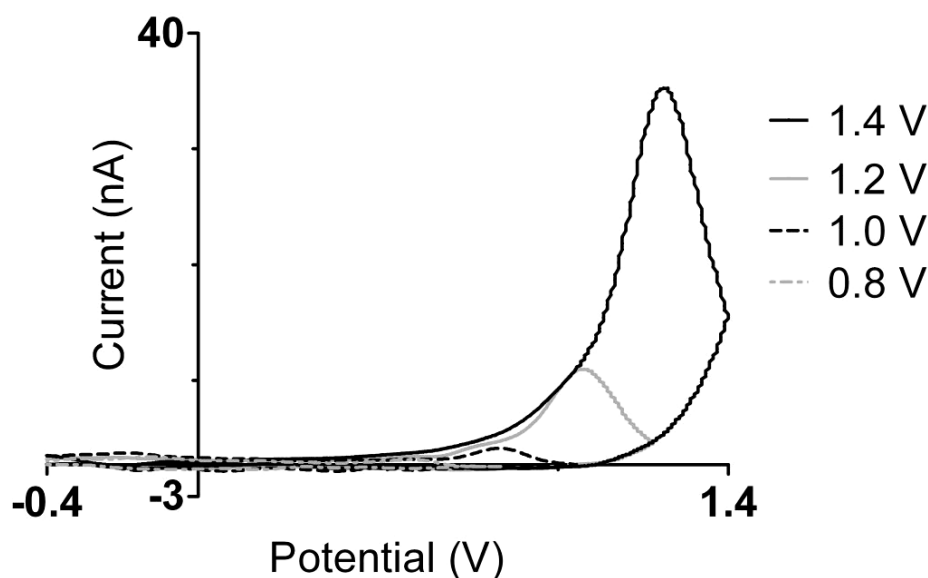


Figure 4.2 - An oxidized electrode surface is required to accommodate the irreversible oxidation of H_2O_2 . A significant H_2O_2 oxidation peak was observed only at switching potentials greater than 1.2 V. The amplitude of the oxidation current increased as the potential limit was extended, with maximum sensitivity observed using a potential limit of 1.4 V.

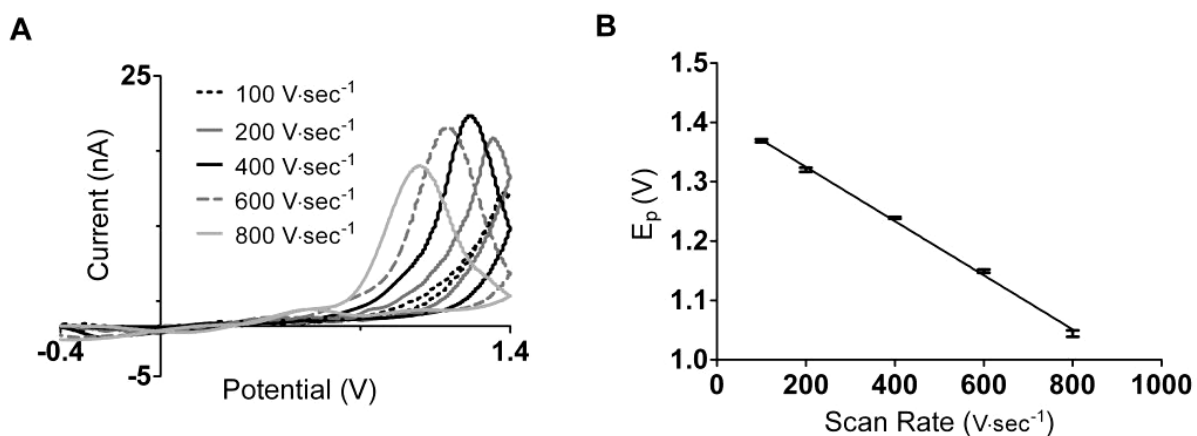


Figure 4.3 - Effect of various scan rates ($\text{V}\cdot\text{s}^{-1}$) on H_2O_2 cyclic voltammetry. (A) Cyclic voltammograms for $100\ \mu\text{M}$ H_2O_2 at typical scan rates for in vivo measurements. The oxidation current was maximized at $400\ \text{V}\cdot\text{s}^{-1}$. (B) Peak oxidation potential, E_p (V), versus scan rate ($\text{V}\cdot\text{s}^{-1}$). $r^2 = 0.99$. Error bars are the SEM ($n = 4$ electrodes).

4.3.2 Signal Validation

To pharmacologically verify that the observed current was due to the oxidation of H_2O_2 , cyclic voltammograms were collected for $100\ \mu\text{M}$ H_2O_2 before and after the addition of $1\ \text{U}/\text{mL}$ catalase (from *Aspergillus niger*), a common enzyme that catalyzes the decomposition of H_2O_2 to water and oxygen. Cyclic voltammograms collected at a representative electrode are presented in Figure 4.4. Five minutes after the addition of catalase, the peak oxidative current was significantly reduced to $6 \pm 2\%$ of the initial current ($p < 0.001$, Student's t test, $n = 3$). The representative cyclic voltammogram for the catalase-containing H_2O_2 solution (dashed line) shows a reduction of the H_2O_2 signal and no other significant current peaks produced by products of the reaction. Twenty minutes after the addition of catalase the current was completely abolished (data not shown). The cyclic voltammogram for a fresh bolus of $100\ \mu\text{M}$ H_2O_2 was identical to that initially obtained,

demonstrating that the catalase solution did not simply abolish the current by fouling the electrode.

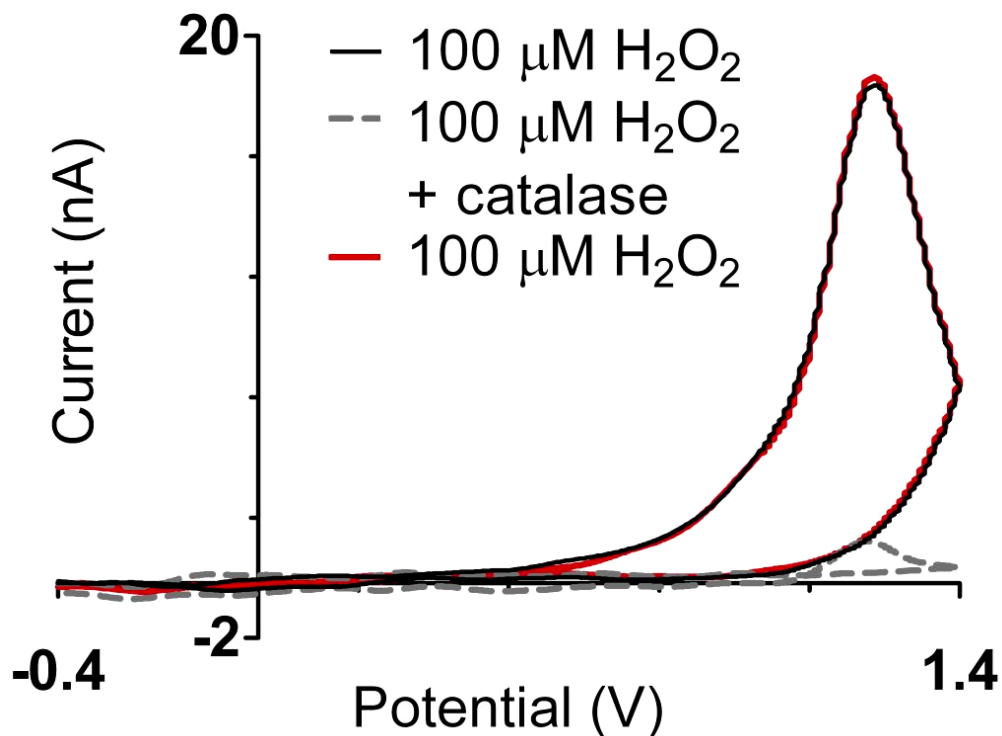


Figure 4.4 - Enzymatic degradation of H₂O₂. Cyclic voltammograms for H₂O₂ (100μM) before (solid black) and 5 min. after (dashed) the addition of catalase (1U/mL) to the sample. A fresh sample of 100 μM H₂O₂ (red) demonstrates that the integrity of the electrode was not compromised.

4.3.3 Characterization of H₂O₂ Electrochemistry

Varying concentrations of H₂O₂ were used to characterize the linear relationship between peak current and solution concentration. Figure 5A shows five representative cyclic voltammograms of physiological concentrations at regular intervals (50 μM to 250 μM). The current versus time traces for these data are presented in Figure 4.5B. The response time for

the detection of 100 μM H_2O_2 , defined as the time required to go from 10% to 90% of the peak current, was 0.75 ± 0.05 sec ($n = 5$). The linear plot of peak current versus concentration shown in Figure 4.5C was compiled from four repetitions of each concentration at six electrodes ($r^2 = 0.95$). Assuming a detection limit of three times the noise, the limit of detection was 1.9 ± 0.1 μM ($n = 5$). Figure 4.5D shows good linearity up to 1 mM ($r^2 = 0.98$, $n = 4$).

In the brain, other endogenous electroactive neurotransmitters can contribute to the current collected at the carbon fiber surface, thus it is important to be able to distinguish H_2O_2 from potential interferents. The characteristic voltammograms of different neurotransmitters obtained with FSCV are multiple point measures of the species detected, providing qualitative information that enables identification. Dopamine, ascorbate and basic pH shifts are well-characterized at carbon fiber electrodes (22) and these signals are present in discrete brain regions where H_2O_2 might also be detected. To demonstrate that H_2O_2 could be discriminated from these signals, dopamine, ascorbate and H_2O_2 were evaluated at five different concentrations chosen based on estimates of their *in vivo* concentrations (29, 30). Five basic pH shifts were also evaluated, as these signals are often measured in living brain tissue (31, 32). The background-subtracted cyclic voltammograms (Figure 4.6A-D) were used to construct a calibration set. Mixtures of the four compounds were analyzed using principal component regression (PCR), as described previously (22). Figure 4.6E shows the predicted H_2O_2 concentration plotted versus the actual concentration of H_2O_2 in the mixtures at $n = 6$ electrodes. The slope of the regression line was 0.99 ± 0.03 ($r^2 = 0.97$), indicating appropriate identification and quantification of H_2O_2 .

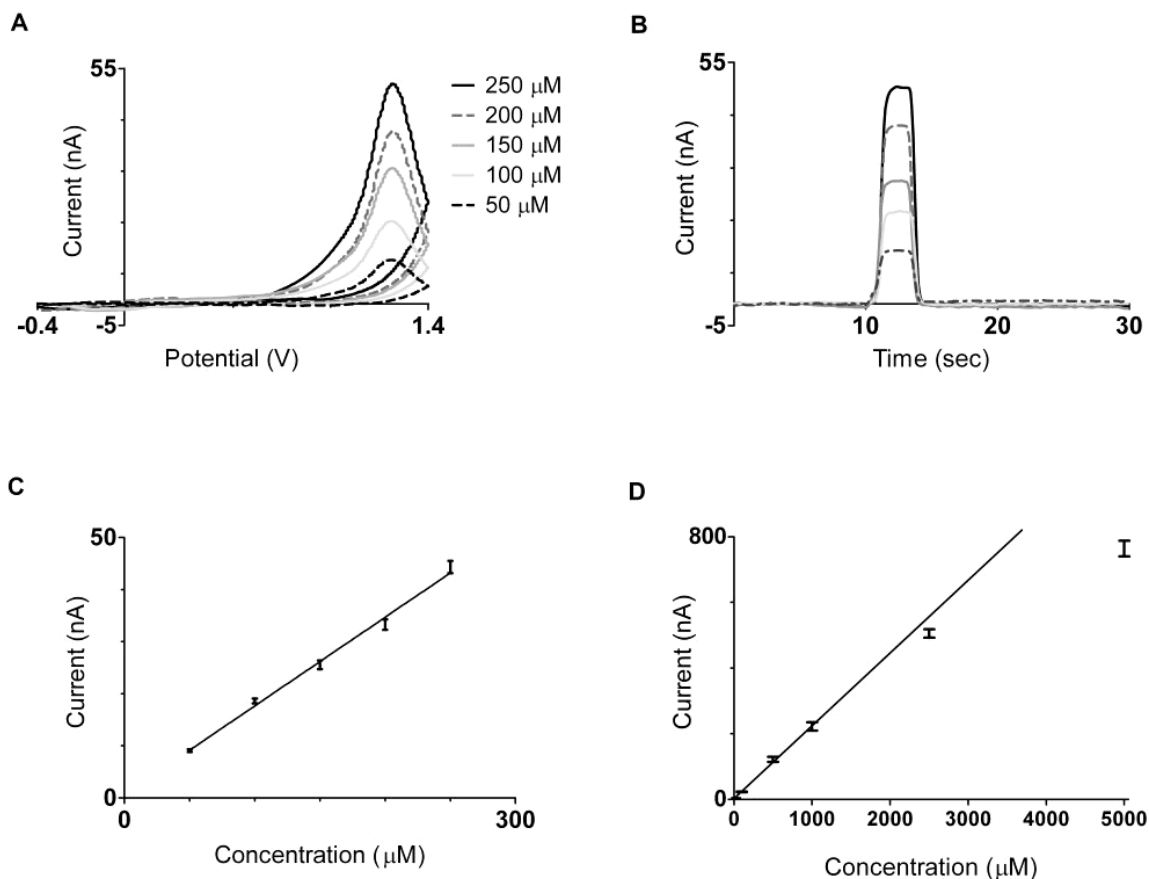


Figure 4.5 - Characterization of H₂O₂ electrochemistry. (A) Cyclic voltammograms for H₂O₂ solutions ranging from 50 μM to 250 μM. All peak currents occur at 1.2 V. (B) Current (nA) versus time (sec) plot of the same five samples, demonstrating the rapid response time of the electrode. (C) Linear relationship between peak current (nA) versus H₂O₂ concentration (μM). $r^2 = 0.95$, $n = 6$ electrodes. (D) Current (nA) versus concentration (μM) plot to show linear range. Deviation from linearity occurs at concentrations greater than 1 mM.

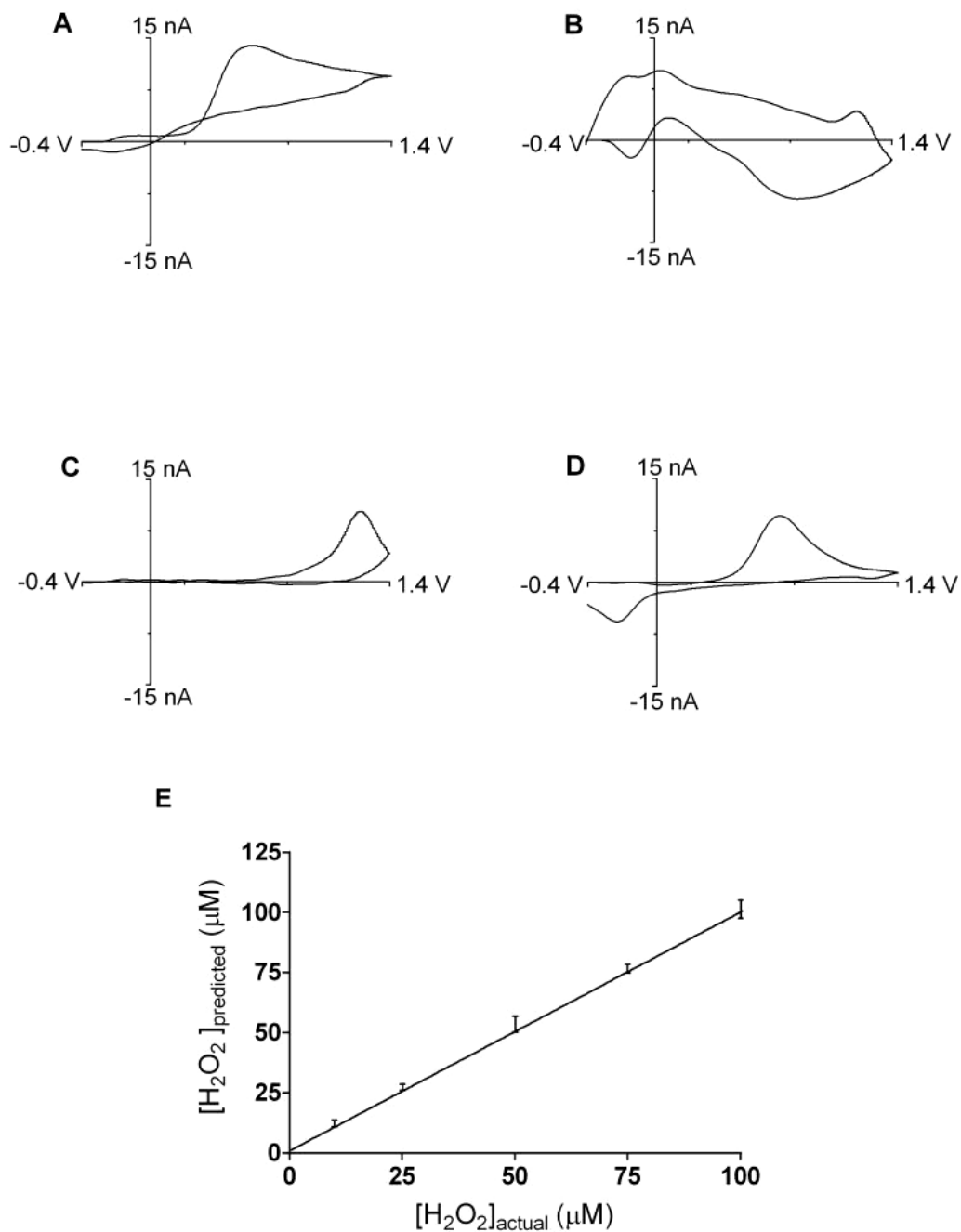


Figure 4.6 - Selectivity and sensitivity in the presence of multiple interferents. (A-D) Cyclic voltammograms of possible in vivo interferents. (A) 50 μM ascorbate (B) 0.2 basic pH shift (7.6) (C) 50 μM H_2O_2 (D) 500 nM dopamine. (E) Predicted concentrations of H_2O_2 as evaluated by PCR compared to known sample concentrations. The diagonal line represents a regression line of 1 to show data variance. The data regression line (not shown) is 0.99 ± 0.03 ($r^2 = 0.97$). Error bars represent the mean \pm SEM ($n = 6$ electrodes).

4.3.4 Voltammetric Detection of H₂O₂ in a Brain Slice

To demonstrate that the electrode can distinguish H₂O₂ when implanted in tissue, background-subtracted cyclic voltammograms for the oxidation of H₂O₂ were recorded in a brain slice. The microelectrode was inserted at least 100 μm into a section of brain tissue that encompassed the striatum, a region with nerve terminals containing the electroactive transmitter dopamine (a potential interferent). A glass micropipette containing 50 μM H₂O₂ was also positioned in the tissue approximately 1 mm from the carbon fiber electrode. A 1 s pressure ejection was used to introduce the exogenous H₂O₂ to the electrode surface. Example voltammetric recordings are shown in Figure 4.7. Chemical changes were not recorded until the onset of the pressure ejection. The individual, background-subtracted voltammograms corresponded to those collected for H₂O₂ *in vitro* as judged by the correlation coefficient ($r > 0.86$).

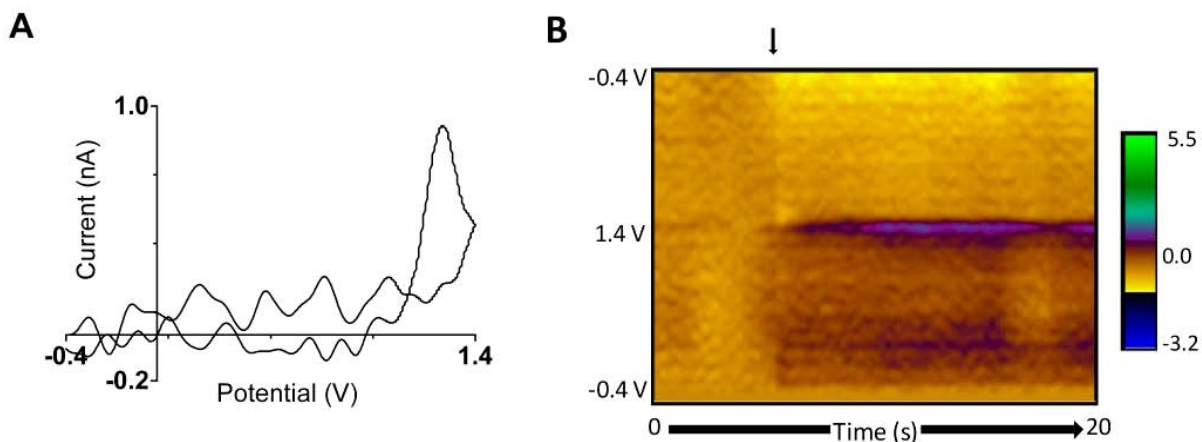


Figure 4.7 - H_2O_2 detection in a brain slice containing the striatum. A) A background-subtracted cyclic voltammogram collected at the maximum of the current response. The signal corresponds to those collected for H_2O_2 in the *in vitro* flow cell ($r > 0.86$). B) The color plot contains 200 background-subtracted cyclic voltammograms recorded over 20 sec, and allows visualization of interfering species. The ordinate is the applied potential to the carbon-fiber electrode, the abscissa is time, and the current is depicted in false color.

4.3.5 Enzymatic Production of H_2O_2

To establish whether FSCV could be used to detect enzymatically generated H_2O_2 , a carbon fiber microelectrode was modified with glucose oxidase, an oxidoreductase that reduces molecular oxygen to H_2O_2 as a by-product in the highly specific conversion of glucose to gluconolactone. Glucose is a nonelectroactive species and thus it cannot be directly detected by FSCV at a bare electrode, as shown in Figure 4.8 (dashed black line). However, when a glucose sample (125 μM) was introduced to the enzyme-modified microelectrode, a cyclic voltammogram was detected with an oxidation peak occurring at 1.2 V on the cathodic scan (solid black line), consistent with the cyclic voltammogram for H_2O_2 at a bare carbon electrode (solid gray line). This demonstrates that the voltammetric

detection of H_2O_2 can be used at enzyme-modified carbon fiber microelectrodes to indirectly monitor non-electroactive species.

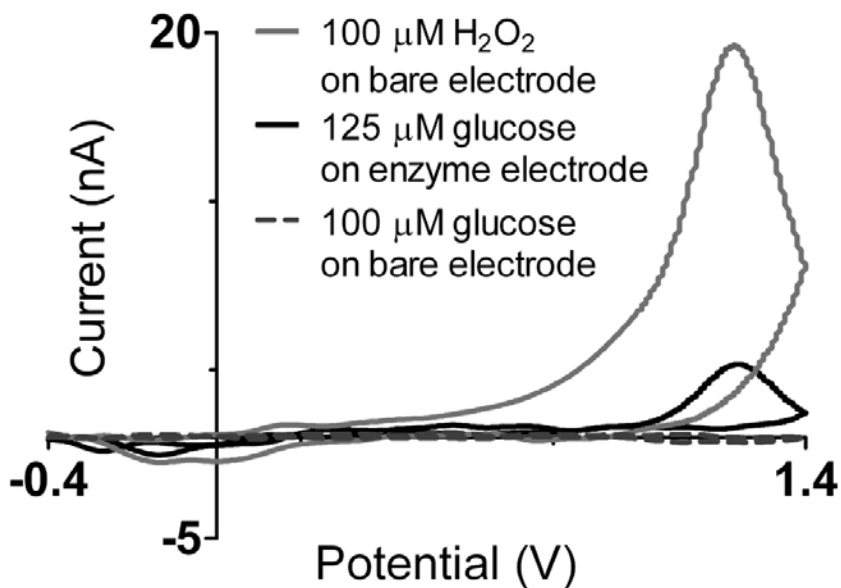


Figure 4.8 - Enzymatic production of H_2O_2 at a glucose-oxidase modified carbon-fiber electrode. Cyclic voltammograms of H_2O_2 (grey) and glucose (black, dashed) on a bare carbon-fiber electrode compared to the detection of H_2O_2 produced by enzymatic degradation of glucose (black, solid) at an enzyme-modified electrode.

4.4 Conclusions

The voltammetric detection of H_2O_2 at carbon electrodes is challenging due to the slow electron transfer kinetics associated with the irreversible oxidation of peroxide. By using the anodic scan as an electrochemical pretreatment, a rapid, sensitive and selective voltammetric method has been developed for the detection of physiological concentrations of H_2O_2 at uncoated carbon fiber microelectrodes. This strategy will allow for the development of improved biosensors with wide applicability for a variety of biological analytes.

4.5 References

1. Halliwell, B. (2006) Oxidative stress and neurodegeneration: where are we now?, *J Neurochem* 97, 1634-1658.
2. Mattson, M. P., and Liu, D. (2002) Energetics and oxidative stress in synaptic plasticity and neurodegenerative disorders, *Neuromolecular Med* 2, 215-231.
3. Zhang, Y., Dawson, V. L., and Dawson, T. M. (2000) Oxidative stress and genetics in the pathogenesis of Parkinson's disease, *Neurobiol Dis* 7, 240-250.
4. Kishida, K. T., and Klann, E. (2007) Sources and targets of reactive oxygen species in synaptic plasticity and memory, *Antioxid Redox Signal* 9, 233-244.
5. Smythies, J. (2000) Redox aspects of signaling by catecholamines and their metabolites, *Antioxid Redox Signal* 2, 575-583.
6. Rhee, S. G. (2006) Cell signaling. H₂O₂, a necessary evil for cell signaling, *Science* 312, 1882-1883.
7. Avshalumov, M. V., Chen, B. T., Marshall, S. P., Pena, D. M., and Rice, M. E. (2003) Glutamate-dependent inhibition of dopamine release in striatum is mediated by a new diffusible messenger, H₂O₂, *J Neurosci* 23, 2744-2750.
8. Avshalumov, M. V., Patel, J. C., and Rice, M. E. (2008) AMPA receptor-dependent H₂O₂ generation in striatal medium spiny neurons but not dopamine axons: one source of a retrograde signal that can inhibit dopamine release, *J Neurophysiol* 100, 1590-1601.
9. Miller, E. W., Tulyathan, O., Isacoff, E. Y., and Chang, C. J. (2007) Molecular imaging of hydrogen peroxide produced for cell signaling, *Nat Chem Biol* 3, 263-267.
10. Wightman, R. M. (2006) Detection technologies. Probing cellular chemistry in biological systems with microelectrodes, *Science* 311, 1570-1574.
11. Hall, S. B., Khudaish, E. A., and Hart, A. L. (1998) Electrochemical oxidation of hydrogen peroxide at platinum electrodes. Part II: effect of potential, *Electrochimica Acta* 43, 2015-2024.
12. Hall, S. B., Khudaish, E. A., and Hart, A. L. (1998) Electrochemical oxidation of hydrogen peroxide at platinum electrodes. Part 1. An adsorption-controlled mechanism, *Electrochim Acta* 43, 579-588.

13. Burmeister, J. J., and Gerhardt, G. A. (2001) Self-referencing ceramic-based multisite microelectrodes for the detection and elimination of interferences from the measurement of L-glutamate and other analytes, *Analytical chemistry* 73, 1037-1042.
14. Hascup, K. N., Rutherford, E. C., Quintero, J. E., Day, B. K., Nickell, J. R., F., P., Huettl, P., Burmeister, J., and Gerhardt, G. A. (2007) Second-by-Second Measures of Glutamate and Other Neurotransmitters Using Enzyme-Based Microelectrode Arrays, In *Electrochemical Methods for Neuroscience* (Michael, A. C., and Borland, L. M., Eds.), pp 407-450, CRC Press, Boca Raton.
15. Parikh, V., Kozak, R., Martinez, V., and Sarter, M. (2007) Prefrontal acetylcholine release controls cue detection on multiple timescales, *Neuron* 56, 141-154.
16. Wassum, K. M., Tolosa, V. M., Wang, J., Walker, E., Monbouquette, H. G., and Maidment, N. T. (2008) Silicon Wafer-Based Platinum Microelectrode Array Biosensor for Near Real-Time Measurement of Glutamate in Vivo, *Sensors Basel Sensors* 8, 5023-5036.
17. Wilson, G. S., and Johnson, M. A. (2008) In-vivo electrochemistry: what can we learn about living systems?, *Chem Rev* 108, 2462-2481.
18. Updike, S. J., and Hicks, G. P. (1967) The enzyme electrode, *Nature* 214, 986-988.
19. Robinson, D. L., Hermans, A., Seipel, A. T., and Wightman, R. M. (2008) Monitoring rapid chemical communication in the brain, *Chem Rev* 108, 2554-2584.
20. Zhang, Y., and Wilson, G. S. (1993) Electrochemical Oxidation of H₂O₂ on Pt and Pt + Ir Electrodes in Physiological Buffer and Its Applicability to H₂O₂-Based Biosensors, *J Electroanal Chem* 345, 253-271.
21. Martin, C. R., and A.F., C. (1996) Chemically Modified Electrodes, In *Laboratory Techniques in Electroanalytical Chemistry* (Kissinger, P. T., and Heineman, W. R., Eds.) 2nd ed., pp 403-442, Marcel Dekker, Inc., New York.
22. Heien, M. L., Johnson, M. A., and Wightman, R. M. (2004) Resolving neurotransmitters detected by fast-scan cyclic voltammetry, *Anal Chem* 76, 5697-5704.
23. Huffman, M. L., and Venton, B. J. (2009) Carbon-fiber microelectrodes for in vivo applications, *Analyst* 134, 18-24.
24. Aoki, K., Ishida, M., Tokuda, K., and Hasebe, K. (1988) Electrode-Kinetics of the Oxidation of Hydrogen-Peroxide at Pretreated Glassy-Carbon and Carbon-Fiber Electrodes, *J Electroanal Chem* 251, 63-71.

25. Roberts, J. G., Moody, B. P., McCarty, G. S., and Sombers, L. A. (2010) Specific Oxygen-Containing Functional Groups on the Carbon Surface Underlie an Enhanced Sensitivity to Dopamine at Electrochemically Pretreated Carbon Fiber Microelectrodes, *Langmuir Epub, ASAP*.
26. Takmakov, P., Zachek, M. K., Keithley, R. B., Walsh, P. L., Donley, C., McCarty, G. S., and Wightman, R. M. (2010) Carbon Microelectrodes with a Renewable Surface, *Analytical chemistry Epub, ASAP*.
27. Florescu, M., and Brett, C. M. A. (2005) Development and evaluation of electrochemical glucose enzyme biosensors based on carbon film electrodes, *Talanta* 65, 306-312.
28. Nowall, W. B., and Kuhr, W. G. (1997) Detection of hydrogen peroxide and other molecules of biological importance at an electrocatalytic surface on a carbon fiber microelectrode, *Electroanal* 9, 102-109.
29. Gonon, F., Buda, M., Cespuglio, R., Jouvet, M., and Pujol, J. F. (1980) In vivo electrochemical detection of catechols in the neostriatum of anaesthetized rats: dopamine or DOPAC?, *Nature* 286, 902-904.
30. Kulagina, N. V., Shankar, L., and Michael, A. C. (1999) Monitoring glutamate and ascorbate in the extracellular space of brain tissue with electrochemical microsensors, *Analytical chemistry* 71, 5093-5100.
31. Venton, B. J., Michael, D. J., and Wightman, R. M. (2003) Correlation of local changes in extracellular oxygen and pH that accompany dopaminergic terminal activity in the rat caudate-putamen, *Journal of neurochemistry* 84, 373-381.
32. Cheer, J. F., Wassum, K. M., and Wightman, R. M. (2006) Cannabinoid modulation of electrically evoked pH and oxygen transients in the nucleus accumbens of awake rats, *Journal of neurochemistry* 97, 1145-1154.

CHAPTER 5

Comparison of Electrode Materials for the Detection of Rapid Hydrogen Peroxide Fluctuations Using Background-Subtracted Fast Scan Cyclic Voltammetry

The following work was reprinted with permission from: James G. Roberts, Keri L. Hamilton, and Leslie A. Sombers, *Analyst*, 2011, 136, 3550-3556., Copyright 2011 The Royal Society of Chemistry.

5.1 Introduction

Hydrogen peroxide (H_2O_2) is an important, naturally-occurring, reactive oxygen species that has been gaining recognition in the biological sciences as a rapid neuromodulatory (1) and subcellular signaling molecule (2, 3). The accurate and reliable detection of H_2O_2 has also been critically important in the field of biosensing since the development of the first enzyme electrode in 1962, which detected glucose by the amperometric detection of H_2O_2 produced in the presence of glucose and oxygen by a thin layer of glucose oxidase on the electrode surface (4). Since then, enzyme-based electrodes have become one of the most active areas of analytical research (5). Of the common electrode materials, carbon and platinum are most frequently used to construct microelectrodes for biological applications. Carbon-fiber microelectrodes have proven most useful for biological applications due to their low cost, wide potential window, and renewable surface (6-8). However, the electrochemical oxidation of H_2O_2 is kinetically slow and this material offers little by way of catalytic activity. Platinum electrodes are typically used for the detection of H_2O_2 , because the platinum surface is electrocatalytic (9-14).

However, transition metal electrodes exhibit unstable electrochemical backgrounds when used *in vivo*, due to non-specific adsorption of biological molecules to the electrode surface. Furthermore, they are traditionally coupled with constant-potential amperometry, a technique that offers no chemical selectivity. Thus, these devices require selective exclusion layer coatings, such as Nafion[®], which reduce interferences but slow the electrode response time (15, 16).

Fast-scan cyclic voltammetry (FSCV) offers both sensitivity and selectivity, making it ideal for monitoring molecular fluctuations *in vivo* (17-19). With this approach, the voltammogram is characteristic of the analyte, allowing it to be distinguished from many other electroactive species. Multiple groups have studied the voltammetry of H₂O₂ on platinum using more traditional (slow) scan rates; however, the precise mechanism of oxidation is still debated (9-14, 20-22). The excellent set of papers by Hall and co-workers make clear that for electrocatalysis to occur, a layer of platinum II oxide must form on the electrode surface. This also explains the poor response to H₂O₂ that is typically seen on carbon electrodes. The voltammetric detection of H₂O₂ at carbon electrodes requires electrochemical pretreatment of the carbon surface (23, 24); however, the complex mechanism underlying the kinetically slow redox chemistry remains elusive. To date, mechanistic studies have been limited to slow scan rates, and direct comparisons of the electrode materials under identical experimental conditions are largely lacking.

The voltammetric detection of rapid H₂O₂ fluctuations at carbon-fiber microelectrodes in living tissue was recently reported by our group, using background-subtracted fast-scan cyclic voltammetry (24). With this novel approach, the forward scan

serves to electrochemically condition the electrode, and the irreversible oxidation of physiological levels of H₂O₂ is detected on the return scan. The complex mechanism underlying this atypical electrochemical signal remains undetermined. Nonetheless, this novel fast-scan approach could potentially revolutionize H₂O₂ detection in the field of biosensing. The experiments presented herein comparatively characterize the background-subtracted, fast-scan voltammetry of H₂O₂ on carbon-fiber and platinum microdisc electrodes, using a rapid scan rate (400 V·s⁻¹) that is optimum for studies of rapid H₂O₂ dynamics (24). The fundamental differences between data collected on these substrates shed light on the chemical mechanisms underlying the redox chemistry at the electrode surface. Carbon fibers were found to be the best choice for rapid voltammetric measurements of H₂O₂ when both sensitivity and selectivity are required.

5.2 Experimental

5.2.1 Chemicals

All chemicals were purchased from Sigma-Aldrich (St. Louis, MO) and used as received, unless otherwise noted. A physiologically buffered solution (Tris Buffer: 15 mM Tris-HCl, 3.25 mM KCl, 1.2 mM CaCl₂, 1.2 mM MgCl₂, 2.0 mM Na₂SO₄, 1.25 mM NaH₂PO₄, and 145 mM NaCl) at pH 7.4 was used in all flow injection analysis experiments. All aqueous solutions were made using doubly deionized water (Barnstead EasyPure II, Dubuque, IA).

5.2.2 Electrode Fabrication

Carbon-fiber disc microelectrodes with a polished angle of 30° were fabricated using $10\ \mu\text{m}$ diameter P-55s pitch-based carbon fibers (Cytex Industries, Woodland Park, NJ) as previously described (25). In brief, a single carbon fiber was inserted into a glass capillary tube (A-M Systems, Sequim, WA), sealed with a micropipette puller (Narishige, Tokyo, Japan), dipped in epoxy (Epoxy Technologies, Billerica, MA), dried, then polished (Sutter Instrument Co., Novato, CA). Platinum disc microelectrodes with a polished angle of 30° were constructed using $25\ \mu\text{m}$ diameter hard platinum wire (Goodfellow, Huntingdon England), following the same procedure. A Ag/AgCl pellet reference electrode (World Precision Instruments, Sarasota, FL) was employed to complete the two electrode electrochemical cell.

5.2.4 Data Acquisition

All data were collected in a custom flow injection system unless otherwise specified. In most experiments, a triangular waveform ranging from $+0.2$ to $+1.3\ \text{V}$ with a holding potential of $+0.2\ \text{V}$ versus Ag/AgCl was applied at a scan rate of $400\ \text{V}\cdot\text{s}^{-1}$ and at a frequency of $10\ \text{Hz}$ using a custom built instrument for potential application to the electrochemical cell and for current transduction (University of North Carolina at Chapel Hill, Department of Chemistry, Electronics Facility). TH-1 software (ESA, Chelmsford, MA) was used for waveform output and data collection with a DAC/ADC card (6251, National Instruments, Austin, TX). A second card (6711) was used for triggering the DACs and ADCs and for synchronization of the electrochemical experiment with the flow injection system. Signal

processing including background subtraction, signal averaging, and digital filtering (low-pass filtered at 2 KHz) was software-controlled.

5.2.5 Flow Injection System

A syringe pump (New Era Pump Systems, Wantagh, NY) supplied a continuous buffer flow of $1 \text{ mL}\cdot\text{min}^{-1}$ across the working and reference electrodes. The working electrode was positioned in a custom electrochemical cell using a micromanipulator (World Precision Instruments, Sarasota, FL). Two second bolus injections of analyte to the microelectrode surface were accomplished with a six-port HPLC valve mounted on a two-position air actuator controlled by a digital pneumatic solenoid valve (Valco Instruments, Houston TX). The entire apparatus was housed within a custom-built grounded Faraday cage. All experiments were performed at room temperature.

5.2.6 Statistics

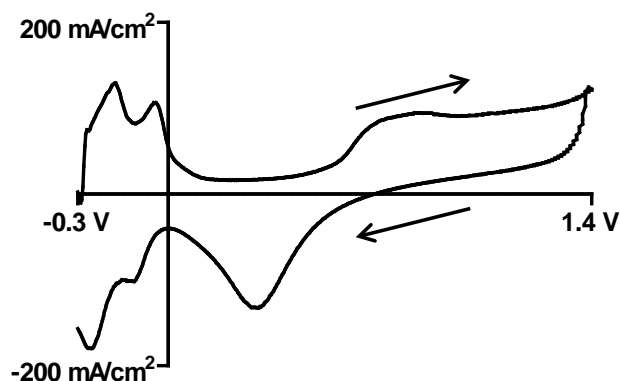
All values are given as the mean \pm standard error of the mean (SEM), unless otherwise noted. Two-tailed paired Student's *t* tests and one-way analysis of variance (ANOVA) with Tukey's test were used to determine statistical differences, with significance designated as $p < 0.05$. Mixtures of analytes were resolved with principal component regression using MATLAB (MathWorks, Natick, MA) (26). Analysis of covariance (ANCOVA) was used for the comparison of linear regression results. Limit of detection was defined as three times the noise. Statistical and graphical analysis was accomplished using GraphPad Prism 5 (GraphPad Software, Inc., La Jolla, CA).

5.3 Results and Discussion

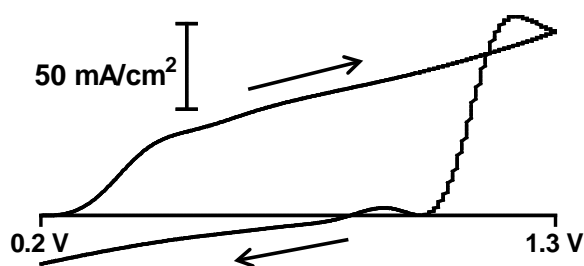
5.3.1 Waveform Optimization

We previously reported on the detection of rapid H_2O_2 fluctuations at carbon-fiber microelectrodes in living tissue using FSCV at cylindrical electrodes (24). In order to directly compare carbon with a platinum microdisc electrode substrate, a common waveform was determined that could be used at both platinum and carbon-fiber microdisc electrodes. Initially, the bare platinum microdisc electrodes were cathodically conditioned in 0.1 M H_2SO_4 by holding the potential at -2.0 V vs. Ag/AgCl for one minute. To ensure that the procedure had sufficiently prepared the electrode surface, cyclic voltammograms were collected in 0.5 M H_2SO_4 at a scan rate of $40 \text{ V}\cdot\text{s}^{-1}$. Figure 5.1(A) shows the resulting voltammogram from an applied waveform of -0.3 to +1.4 V vs. Ag/AgCl which highlights the hydrogen and oxygen adsorption/desorption regions, demonstrating a clean platinum surface (27). Voltammograms of the background charging current were then collected in Tris buffer at $40 \text{ V}\cdot\text{s}^{-1}$, which subsequently overloaded (data not shown). Thus, the potential limits were reduced and a waveform of +0.2 to +1.3 V vs. Ag/AgCl applied at $400 \text{ V}\cdot\text{s}^{-1}$ was used. This abbreviated waveform is completed in 5.5 msec, and was used for all experiments herein in order to enable a direct comparison between electrode substrates. With these modifications, the sensitivity of the carbon microdisc electrode was severely decreased by ~94% when compared to the larger potential window previously used at the larger cylindrical carbon microelectrode (24); however, the voltammograms are qualitatively unchanged and a direct comparison to the platinum substrate was enabled.

A. Platinum, 0.5 M H₂SO₄, 40 V/s



B. Platinum, Tris Buffer, 400 V/s



C. Carbon, Tris Buffer, 400 V/s

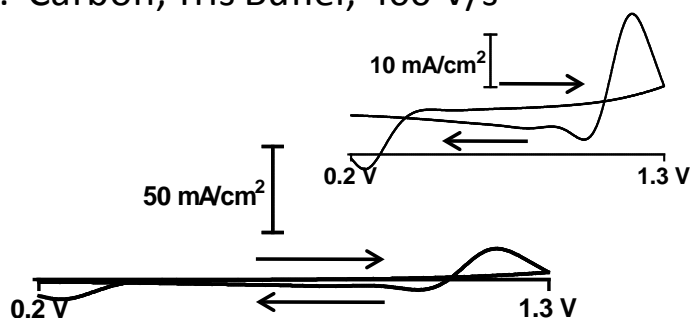


Figure 5.1 - Background current. Cyclic voltammograms collected on platinum microdisc electrodes in either (A) 0.5 M H₂SO₄ or (B) Tris buffer. (A) The potential was scanned from -0.3 to +1.4 V vs. Ag/AgCl at 40 V·s⁻¹, then reduced to (B) +0.2 to +1.3 V due to overloading at higher scan rates. Voltammograms for (C) carbon-fiber microdisc electrodes using the waveform ranging from +0.2 to +1.3 V vs. Ag/AgCl at 400 V·s⁻¹ in Tris buffer shown at the same scale. The inset in (C) is the same voltammogram enlarged for enhanced visibility.

Figure 5.1(B and C) plots the background current collected at platinum and carbon-fiber microdisc electrodes scanned at $400 \text{ V}\cdot\text{s}^{-1}$, respectively. The differences in the shape of the voltammograms can be attributed to the inherent differences between the substrates. The data have been normalized for surface area (e.g. current density) because the platinum electrode is larger than the carbon electrode (geometric surface area = $9.82 \times 10^{-6} \text{ cm}^2$ and $1.57 \times 10^{-6} \text{ cm}^2$, respectively).

5.3.2 FSCV of H_2O_2 on Carbon and Platinum Electrodes

Background-subtracted FSCV was used to detect concentrations of H_2O_2 ranging from 0.25 to 1.0 mM at bare carbon, bare platinum, and Nafion[®]-coated microdisc electrodes under identical experimental conditions. Since platinum is susceptible to biofouling and chlorine contamination, platinum electrodes are generally coated with exclusion layer coatings for use in biological applications. Such coatings have also been used on carbon electrodes, and have proven to be effective deterrents of biological interferents that can foul the electrode surface and/or mask the desired signal. However, they increase electrode response time as H_2O_2 exhibits a decreased diffusion coefficient within the membrane (28), and are challenging to reproducibly fabricate. Nafion[®], a cation exchange polymer, has been used extensively to exclude the contribution of negatively charged species, such as ascorbic acid, and to reduce the rate of biofouling (15, 16, 18, 29-33). Thus, Nafion[®] was electrodeposited on the surface of platinum and carbon microdisc electrodes following a previously published procedure (18). In brief, a conditioned electrode was held at +1.0 V vs.

Ag/AgCl for 30 seconds in a 5% Nafion[®] solution in methanol, then allowed to oven dry at 70 °C for 10 minutes.

The shape of the cyclic voltammograms varied significantly between electrode substrates. Figure 5.2(A) shows a representative response for several concentrations of H₂O₂ at a bare platinum microdisc electrode. A rise in current is evident at approximately +0.3 V on the forward scan. This current cannot be directly attributed to changes in dissolved oxygen, as voltammograms collected for O₂ saturated samples were identical (data not shown).

Interestingly, at this high scan rate the peak current is generated after the switching potential, similar to the detection of H₂O₂ using FSCV on carbon (24). This observation corresponds well to previous voltammetric studies demonstrating that the oxidation of H₂O₂ is favored on oxidized surfaces (14, 21, 22). The representative cyclic voltammograms for various concentrations of H₂O₂ collected on Nafion[®]-coated platinum microdisc electrodes are shown in Figure 5.2(B). There was a slight change in the shape of anodic current in comparison to uncoated platinum. Additionally, there was a marked reduction in the current collected on both the forward and reverse scans (~28% decrease in sensitivity). This is attributed to a decreased diffusion coefficient for H₂O₂ in Nafion[®]. The H₂O₂ diffusion coefficient in a Nafion[®] membrane has been estimated to be $3.4 \times 10^{-10} \text{ cm}^2 \cdot \text{s}^{-1}$, which is 4 orders of magnitude smaller than in aqueous solution (28). Representative voltammograms collected at a bare carbon-fiber microdisc electrode are shown in Figure 5.2(C). These data are qualitatively similar to those published previously that were collected both *in vitro* and in tissue at cylindrical carbon-fiber microelectrodes using a larger waveform ranging from

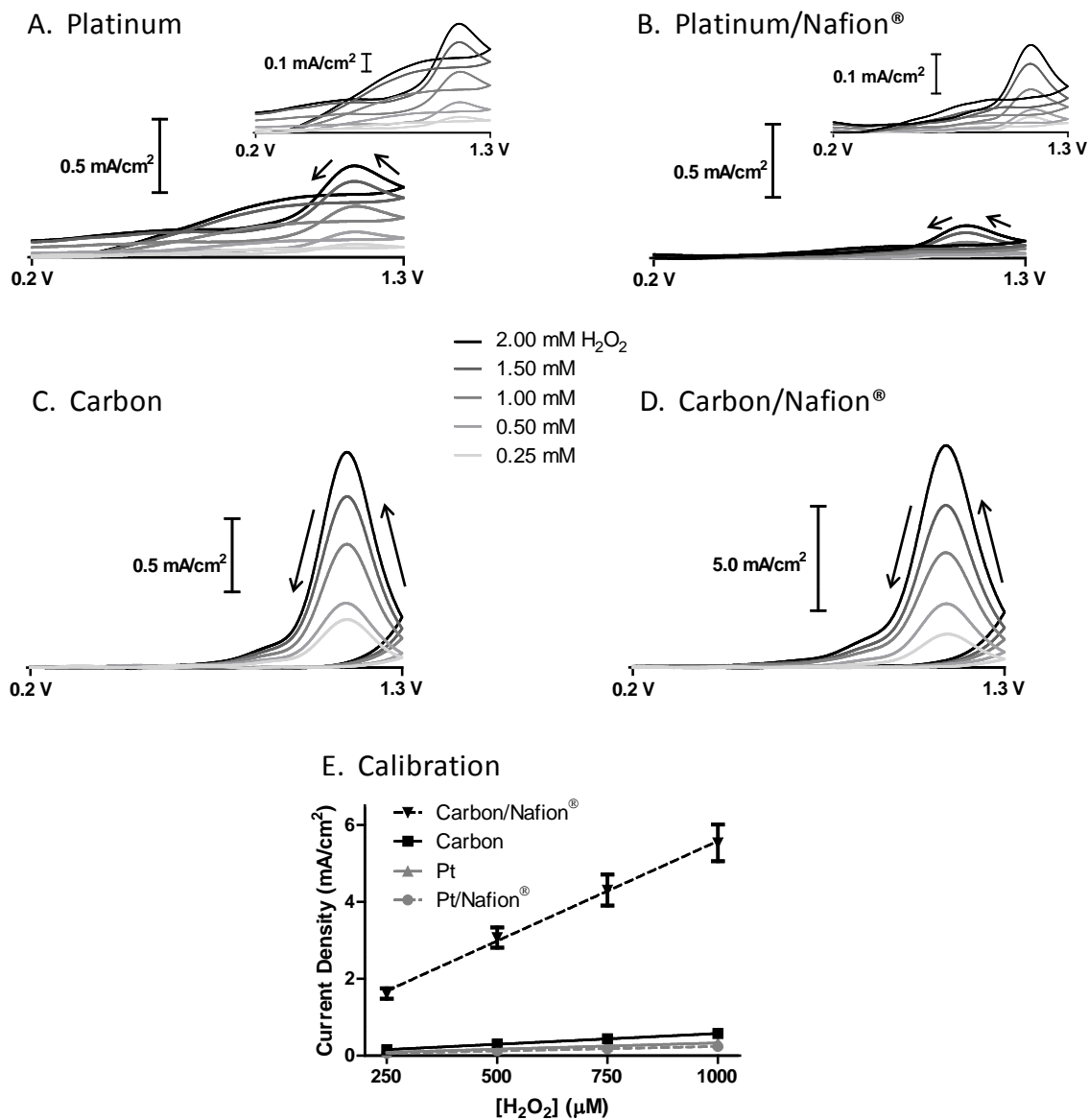


Figure 5.2 - Electrochemical response to H_2O_2 . Representative background-subtracted cyclic voltammograms for various concentrations of H_2O_2 (ranging from 0.25 to 2.0 mM) at (A) platinum, (B) Nafion[®]-coated platinum, and (C) carbon-fiber (D) Nafion[®]-coated carbon-fiber microdisc electrodes. Note that in (D) the scale was increased to accommodate the enhanced sensitivity of the Nafion[®]-coated carbon electrode. The inset in (A) and (B) provide enlarged voltammograms for enhanced visibility. (E) The sensitivities to changes in H_2O_2 concentration for all electrode substrates, within the linear range. All slopes are significantly different (error bars are present, ANCOVA, $p < 0.0001$) ($n = 4$).

-0.4 to +1.4 V at $400 \text{ V}\cdot\text{s}^{-1}$ (24). Interestingly, these voltammograms are also similar to those collected on platinum in that the peak current is generated on the reverse scan; however, little to no current is observed on the forward scan. It is important to note that the edge plane of carbon has established oxygen containing functional groups (8, 34), not dissimilar to oxides that form on the platinum surface. Furthermore, it has been shown that the current density for peroxide oxidation is about 50 times smaller on the basal plane of stress-annealed pyrolytic graphite than on the edge orientation, which is significantly more oxidized (35). The representative cyclic voltammograms for various concentrations of H_2O_2 collected on Nafion®-coated carbon microdisc electrodes are shown in Figure 5.2(D). The voltammetric shape for a coated carbon electrode is identical to the uncoated version, except for the ~9 fold increase in amplitude. This response was unexpected and reveals that distinctly different chemical mechanisms underlie the redox chemistry occurring at platinum and carbon. It can also be noted that the Nafion® membrane effectively increased the noise inherent to the measurements on carbon, and decreased the noise on platinum electrodes. The sensitivities to H_2O_2 for all electrode substrates ($n = 4$) are plotted in Figure 5.2(E) and all slopes are significantly different (ANCOVA, $p < 0.0001$). The values for these sensitivities and limits of detection are listed in Table 5.1. When normalized for surface area, carbon exhibited the highest sensitivity to H_2O_2 ; however, it falls short of the sensitivity that can be achieved at a polypyrrole-coated platinum electrode operated amperometrically (36).

It is important to note that there is little consensus on the normal range of H_2O_2 concentrations in the brain, either intra- or extracellularly, largely due to the lack of a sensitive and specific methodology for the quantitative and dynamic assessment of H_2O_2 in

live tissue (37). The advent of second generation imaging dyes (38, 39), fluorescent protein-based probes (40), and novel, real-time electrochemical methods, such as that described herein, promise to help definitively resolve this question. Nonetheless, several lines of evidence suggest that levels of H₂O₂ for normal, physiologically relevant signaling are in the range of 15-150 μM (41-44) (for a comprehensive review, see Rice, M.E., 2011) (45). Using FSCV, both bare and Nafion[®]-coated carbon microdisc electrodes exhibit a limit of detection that is sufficient to detect these levels of H₂O₂ (Table 5.1); however, platinum offers little electrocatalytic advantage when coupled with FSCV. A significant lower limit of detection can be achieved using an optimized waveform at a carbon-fiber microelectrode with a cylindrical geometry (2 μM) (24) or using a mesoporous platinum electrode with amperometric detection (4.5 μM) (46).

Table 5.1 - Sensitivities and limits of detection for various electrode substrates for H₂O₂ detection. All slopes are significantly different (ANCOVA, p < 0.0001)

Sensitivity ± SEM (n = 4)	Carbon	Platinum	Nafion [®] Coated Platinum	Nafion [®] Coated Carbon
(nA·mM ⁻¹)	0.877 ± 0.011	3.21 ± 0.11	2.30 ± 0.42	8.15 ± 0.943
(μA·mM ⁻¹ ·cm ⁻²)	559.0 ± 7.6	327.0 ± 10.9	234.0 ± 4.3	5190 ± 600
Limit of Detection ± STD (μM)	51.2 ± 15.6	416 ± 148	504 ± 221	64.7 ± 34.1

5.3.3 Enzymatic Verification

In order to unequivocally verify that the current generated was in response to H₂O₂, cyclic voltammograms were collected before and after addition of the natural enzyme catalase, which rapidly and selectively decomposes H₂O₂ to water and molecular oxygen.

Figure 5.3 shows representative voltammograms that were collected for 1 mM H₂O₂ on platinum and carbon before (solid line) and at various time points after (dashed lines) the addition of 1 U/mL of catalase (from *A. niger*) to the stock solution. Catalase effectively eliminated the signal.

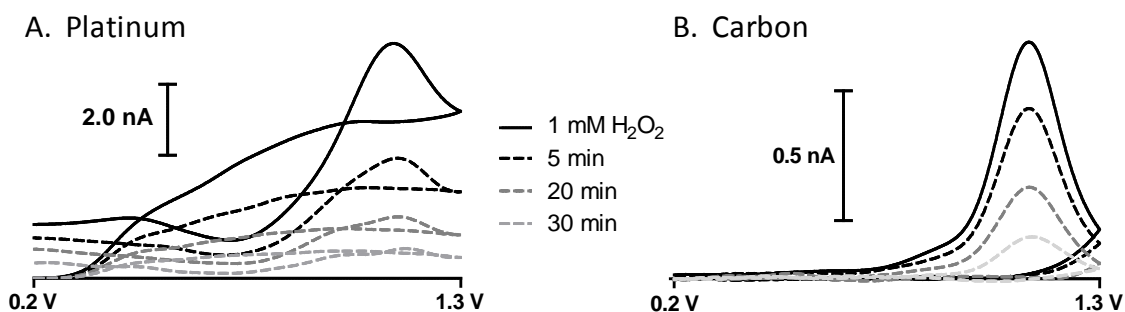


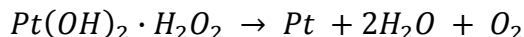
Figure 5.3 - Enzymatic verification of H₂O₂ oxidation. Representative background-subtracted cyclic voltammograms for the detection of 1 mM H₂O₂ at (A) platinum and (B) carbon-fiber electrodes (solid line). The addition of 1 U/mL catalase to 1mM H₂O₂ samples effectively reduced the electrochemical response over time (dashed lines).

5.3.4 Mechanistic Insights

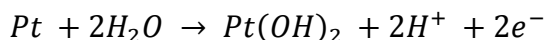
The precise mechanism for the oxidation of H₂O₂ at these substrates is currently undetermined, although several groups have studied this process, revealing important information (9-14, 21-23). In general, noble metals such as platinum have an electrocatalytic surface that facilitates the kinetically sluggish oxidation of H₂O₂ (47). Normalized voltammograms for the oxidation of H₂O₂ at bare carbon and platinum electrodes have been overlaid in Figure 5.4(A) to enable direct comparison. Interestingly, the peak current is

generated at a comparable potential on both materials, demonstrating that the electrocatalytic properties of the platinum surface are not readily apparent when using rapid scan rates.

Figure 5.4(B and C) overlays averaged voltammograms ($n = 3$) that were collected on a given substrate with switching potentials of +1.1 and +1.3 V. It is evident that on both platinum and carbon the signal is due to a combination of a non-faradaic contributor and some intermediate faradaic process on the electrode surface. Several investigators have suggested that on platinum, the primary electron transfer reaction is due to the re-oxidation of platinum to platinum oxides after the oxide film has been reduced by H_2O_2 (9-14, 20-22). Hall and Hart (10) have proposed that H_2O_2 can adsorb to oxidized sites on the Pt electrode surface and that the adsorbed complex then undergoes internal electron transfer with the regeneration of zero oxidation state platinum and the release of H_2O and O_2 according to the following equation:



Finally, the platinum is re-oxidized.



Through this process, the oxide layer is stripped from the Pt surface, which is immediately re-oxidized. In contrast to this stripping process, etching of oxidized carbon surfaces has been shown on carbon-fiber electrodes and pyrolyzed photoresist films, by applying anodic potentials above +1.3 V for extended periods of time (7). Adsorbed oxygen at a carbon surface is thermally broken down as CO and CO_2 , rather than removed via swift desorption (47).

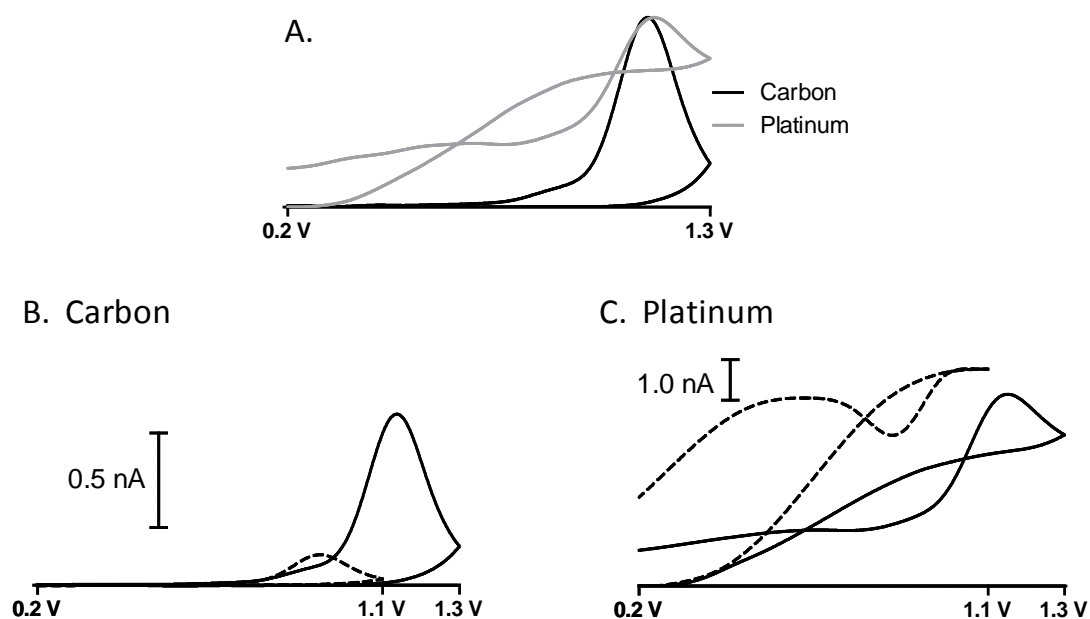


Figure 5.4 - Comparison of background-subtracted cyclic voltammograms collected on carbon and platinum. (A) Voltammograms were normalized by dividing each data point by the peak current. The electrocatalytic properties of the platinum surface are not readily apparent at this scan rate ($400 \text{ V}\cdot\text{s}^{-1}$). The switching potential was varied from +1.1 V (dashed line) to +1.3 V (solid line) on both (B) carbon and (C) platinum microdisc electrodes. Figures show averaged background-subtracted voltammograms for 2 mM H_2O_2 ($n = 3$).

5.3.5 Interfering Species

In contrast to amperometric approaches, FSCV provides qualitative information, allowing researchers to distinguish between multiple electroactive species (17). Since the electrode materials investigated herein are commonly used as substrates for biosensors to make measurements in complex biological preparations, selectivity is particularly important.

For this reason, the influence of interfering species was assessed at each electrode substrate. Two commonly encountered electroactive molecules in living brain tissue are ascorbic acid and dopamine. Both are present at relatively high physiological concentrations (26, 48, 49) (depending on the local microcircuitry) and either can pose a problem as a potential interferent at a biosensor that voltammetrically quantifies H₂O₂ fluctuations. Figure 5.5 presents representative cyclic voltammograms collected on each electrode substrate for these interfering analytes, as well as for H₂O₂, at physiologically relevant concentrations. Ideal detection of these species at any electrode would generate non-overlapping peaks, such that the formal reduction potential ($E^{\circ'}$) is sufficiently unique (separated by at least 118 mV) to distinguish between chemical species that are involved in diffusion controlled processes (50). As shown in Figure 5.5, the voltammograms for H₂O₂, ascorbic acid, and dopamine overlap considerably at all electrode substrates. The dopamine signal here is small compared to prior reports because the electrode is not being held at a negative potential between scans, which would allow for preconcentration of the positively charged analyte at the electrode surface (51, 52). The ability of Nafion® to reduce the contribution of negatively charged ascorbic acid can be seen by comparing the voltammograms collected at the coated electrodes to those collected at the bare electrodes (Figure 5.5).

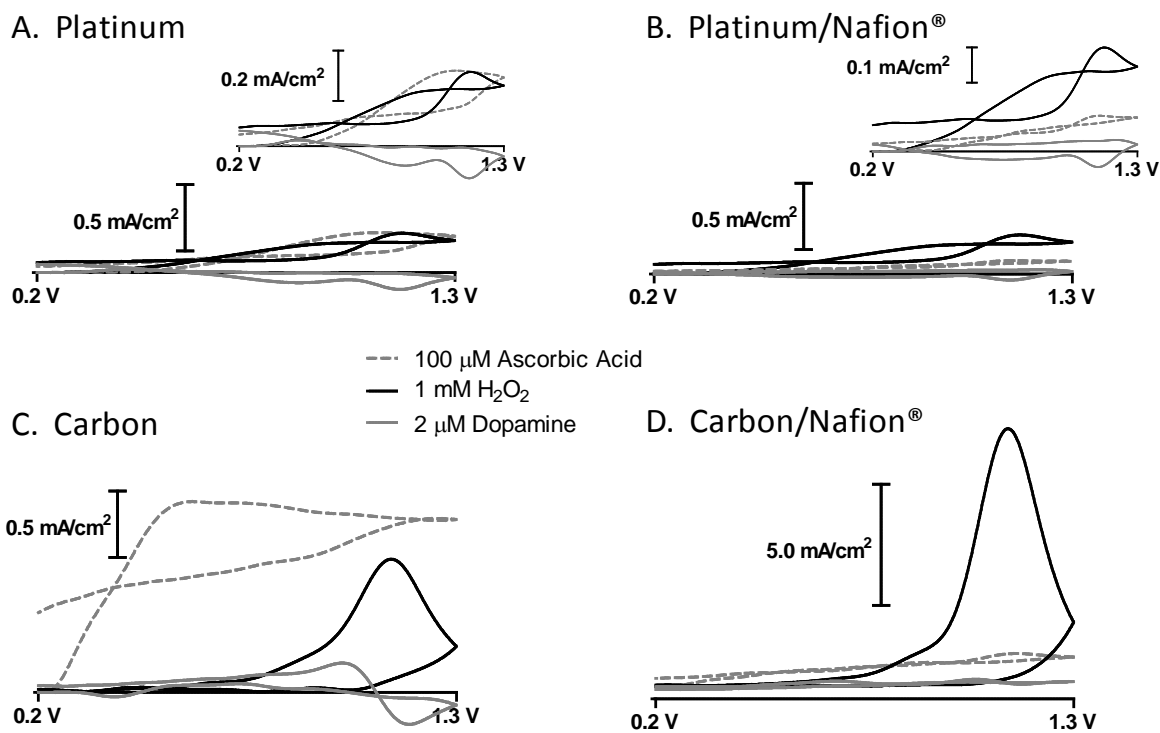


Figure 5.5 - Background-subtracted cyclic voltammograms for interfering species. Representative electrochemical response to ascorbic acid (dashed grey line), H_2O_2 (black line) and dopamine (grey line) at (A) platinum, (B) Nafion[®]-coated platinum, (C) carbon-fiber, and (D) Nafion[®]-coated carbon-fiber electrodes. (B and D) The cation exchange polymer reduces the current generated from negatively charged ascorbic acid.

In order to quantitatively assess the selectivity of an electrode substrate for H_2O_2 in the presence of interfering species, principle component regression (PCR) was used to evaluate concentrations of individual components in known mixtures. This manner of multivariate statistics can be used to completely separate the contributions of each analyte in a complex sample, such as living tissue (26, 53). Training sets were established for various physiological concentrations of ascorbic acid (50 - 150 μM), dopamine (1 - 2 μM), and H_2O_2 (250 - 2000 μM). These sets were used to predict known concentrations of H_2O_2 from a mixture of all three species (100 μM ascorbic acid, 1.5 μM dopamine, and varied

concentrations of H_2O_2). The known concentrations for H_2O_2 were plotted versus the PCR predicted concentrations, as shown in Figure 5.6. These data demonstrate that the carbon-fiber microdisc electrodes are most accurate in selectively quantifying H_2O_2 in this complex mixture. It should also be noted that coating the platinum surface effectively decreased the variability of the electrochemical data for the platinum substrate.

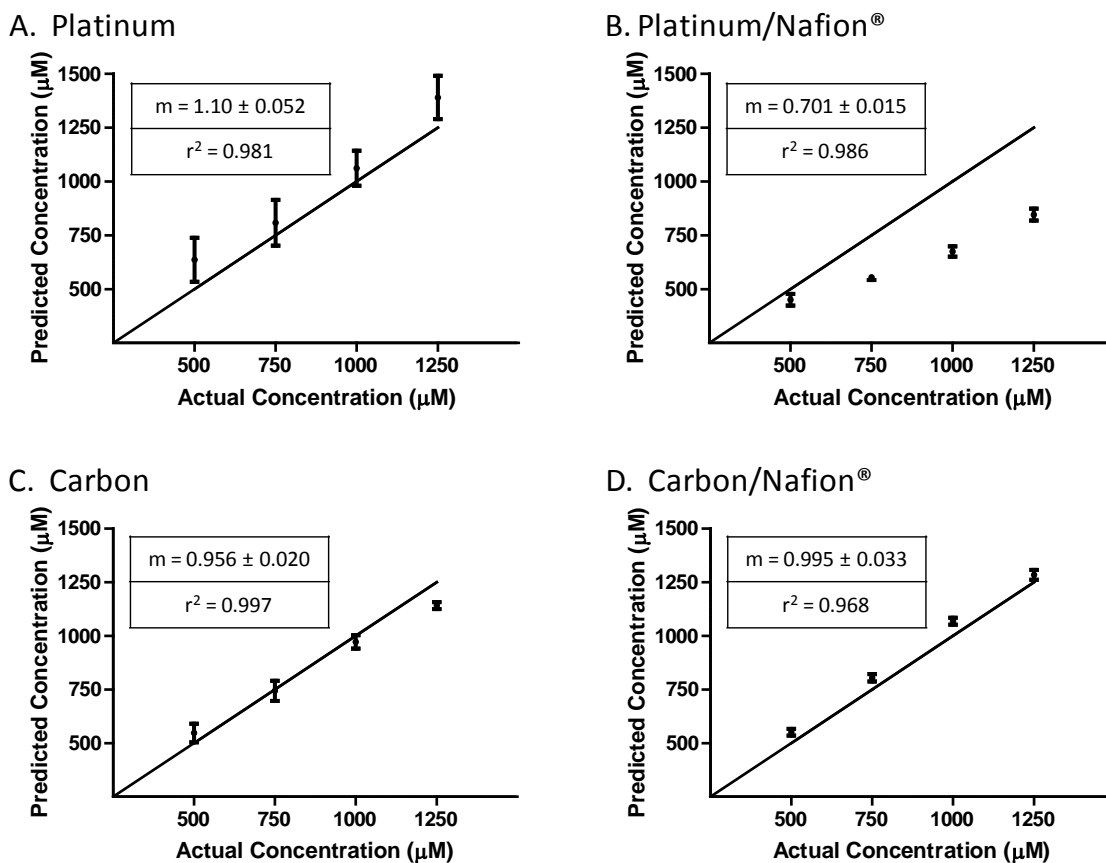


Figure 5.6 - Selectivity of electrode substrates. The known concentration of H_2O_2 was plotted against the PCR predicted concentration of H_2O_2 in the presence of 100 μM ascorbic acid and 1.5 μM dopamine, for (A) platinum, (B) Nafion[®]-coated platinum, (C) carbon-fiber, and (D) Nafion[®]-coated carbon-fiber electrode substrates. The solid line was plotted to demonstrate unity slope. Insets provide the correlation coefficient (r^2) and the slope (m) of the prediction line, with unity indicating an exact prediction ($n = 4$).

5.4 Conclusions

These results demonstrate that there are fundamental differences between electrode substrates that may provide clues to the complicated mechanism underlying the electrochemical oxidation of H_2O_2 at these electrode surfaces. The direct comparison of voltammograms collected at platinum and carbon microelectrodes reveals that platinum offers little electrocatalytic advantage compared to carbon-fiber microdisc electrodes when coupled with FSCV. Furthermore, carbon electrodes provide more selectivity and sensitivity for the rapid detection of H_2O_2 . These advantageous properties of carbon, coupled with its renewable surface, promise to provide the best performance for the *in vivo* voltammetric detection of H_2O_2 , and thus to significantly advance the field of biosensing.

5.5 References

1. Bao, L., Avshalumov, M. V., Patel, J. C., Lee, C. R., Miller, E. W., Chang, C. J., and Rice, M. E. (2009) Mitochondria are the source of hydrogen peroxide for dynamic brain-cell signaling, *Journal of Neuroscience* 29, 9002-9010.
2. Stone, J. R., and Yang, S. (2006) Hydrogen peroxide: a signaling messenger, *Antioxid Redox Signal* 8, 243-270.
3. Rhee, S. G. (2006) Cell signaling. H₂O₂, a necessary evil for cell signaling, *Science* 312, 1882-1883.
4. Clark, L. C., Jr., and Lyons, C. (1962) Electrode systems for continuous monitoring in cardiovascular surgery, *Ann N Y Acad Sci* 102, 29-45.
5. Wilson, G. S., and Johnson, M. A. (2008) In-vivo electrochemistry: what can we learn about living systems?, *Chem Rev* 108, 2462-2481.
6. Wightman, R. M. (2006) Detection technologies. Probing cellular chemistry in biological systems with microelectrodes, *Science* 311, 1570-1574.
7. Takmakov, P., Zachek, M. K., Keithley, R. B., Walsh, P. L., Donley, C., McCarty, G. S., and Wightman, R. M. (2010) Carbon microelectrodes with a renewable surface, *Anal Chem* 82, 2020-2028.
8. McCreery, R. L. (2008) Advanced carbon electrode materials for molecular electrochemistry, *Chem Rev* 108, 2646-2687.
9. Hall, S. B., Khudaish, E. A., and Hart, A. L. (1998) Electrochemical oxidation of hydrogen peroxide at platinum electrodes. Part II: effect of potential, *Electrochim Acta* 43, 2015-2024.
10. Hall, S. B., Khudaish, E. A., and Hart, A. L. (1998) Electrochemical oxidation of hydrogen peroxide at platinum electrodes. Part 1. An adsorption-controlled mechanism, *Electrochim Acta* 43, 579-588.
11. Hall, S. B., Khudaish, E. A., and Hart, A. L. (1999) Electrochemical oxidation of hydrogen peroxide at platinum electrodes. Part IV: phosphate buffer dependence, *Electrochim Acta* 44, 4573-4582.
12. Hall, S. B., Khudaish, E. A., and Hart, A. L. (1999) Electrochemical oxidation of hydrogen peroxide at platinum electrodes. Part III: Effect of temperature, *Electrochim Acta* 44, 2455-2462.

13. Hall, S. B., Khudaish, E. A., and Hart, A. L. (2000) Electrochemical oxidation of hydrogen peroxide at platinum electrodes. Part V: inhibition by chloride, *Electrochim Acta* 45, 3573-3579.
14. Zhang, Y., and Wilson, G. S. (1993) Electrochemical Oxidation of H₂O₂ on Pt and Pt + Ir Electrodes in Physiological Buffer and Its Applicability to H₂O₂-Based Biosensors, *J Electroanal Chem* 345, 253-271.
15. Burmeister, J. J., Pomerleau, F., Huettl, P., Gash, C. R., Werner, C. E., Bruno, J. P., and Gerhardt, G. A. (2008) Ceramic-based multisite microelectrode arrays for simultaneous measures of choline and acetylcholine in CNS, *Biosens Bioelectron* 23, 1382-1389.
16. Hu, Y., and Wilson, G. S. (1997) Rapid changes in local extracellular rat brain glucose observed with an in vivo glucose sensor, *J Neurochem* 68, 1745-1752.
17. Robinson, D. L., Hermans, A., Seipel, A. T., and Wightman, R. M. (2008) Monitoring rapid chemical communication in the brain, *Chemical Reviews* 108, 2554-2584.
18. Hashemi, P., Dankoski, E. C., Petrovic, J., Keithley, R. B., and Wightman, R. M. (2009) Voltammetric detection of 5-hydroxytryptamine release in the rat brain, *Analytical Chemistry* 81, 9462-9471.
19. Sombers, L. A., Beyene, M., Carelli, R. M., and Wightman, R. M. (2009) Synaptic overflow of dopamine in the nucleus accumbens arises from neuronal activity in the ventral tegmental area, *Journal of Neuroscience* 29, 1735-1742.
20. Hickling, A., and Wilson, W. H. (1951) The Anodic Decomposition of Hydrogen Peroxide, *J Electrochem Soc* 98, 425-433.
21. Lingane, J. J. (1961) Chronopotentiometric study of oxygen reduction at a platinum wire cathode, *J Electroanal Chem* 2, 296-309
22. Lingane, J. J., and Lingane, P. J. (1963) Chronopotentiometry of hydrogen peroxide with a platinum wire electrode, *J Electroanal Chem* 5, 411-419.
23. Aoki, K., Ishida, M., Tokuda, K., and Hasebe, K. (1988) Electrode-Kinetics of the Oxidation of Hydrogen-Peroxide at Pretreated Glassy-Carbon and Carbon-Fiber Electrodes, *J Electroanal Chem* 251, 63-71.
24. Sanford, A. L., Morton, S. W., Whitehouse, K. L., Oara, H. M., Lugo-Morales, L. Z., Roberts, J. G., and Sombers, L. A. (2010) Voltammetric Detection of Hydrogen Peroxide at Carbon Fiber Microelectrodes, *Analytical Chemistry* 82, 5205-5210.

25. Zachek, M. K., Hermans, A., Wightman, R. M., and McCarty, G. S. (2008) Electrochemical dopamine detection: Comparing gold and carbon fiber microelectrodes using background subtracted fast scan cyclic voltammetry, *J Electroanal Chem* 614, 113-120.
26. Heien, M. L. A. V., Johnson, M. A., and Wightman, R. M. (2004) Resolving neurotransmitters detected by fast-scan cyclic voltammetry, *Analytical Chemistry* 76, 5697-5704.
27. Bard, A. J., and Faulkner, L. R. (2001) *Electrochemical Methods: Fundamentals and Applications*, 2nd ed., John Wiley, New York.
28. Prakash, P. A., Yogeswaran, U., and Chen, S. M. (2009) Direct electrochemistry of catalase at multiwalled carbon nanotubes-nafion in presence of needle shaped DDAB for H₂O₂ sensor, *Talanta* 78, 1414-1421.
29. Cui, J., Kulagina, N. V., and Michael, A. C. (2001) Pharmacological evidence for the selectivity of in vivo signals obtained with enzyme-based electrochemical sensors, *J Neurosci Methods* 104, 183-189.
30. Wiedemann, D. J., Basse-Tomusk, A., Wilson, R. L., Rebec, G. V., and Wightman, R. M. (1990) Interference by DOPAC and ascorbate during attempts to measure drug-induced changes in neostriatal dopamine with Nafion-coated, carbon-fiber electrodes, *J Neurosci Methods* 35, 9-18.
31. Gerhardt, G. A., and Hoffman, A. F. (2001) Effects of recording media composition on the responses of Nafion-coated carbon fiber microelectrodes measured using high-speed chronoamperometry, *J Neurosci Methods* 109, 13-21.
32. Wassum, K. M., Tolosa, V. M., Wang, J., Walker, E., Monbouquette, H. G., and Maidment, N. T. (2008) Silicon Wafer-Based Platinum Microelectrode Array Biosensor for Near Real-Time Measurement of Glutamate in Vivo, *Sensors Basel Sensors* 8, 5023-5036.
33. Gerhardt, G. A., Oke, A. F., Nagy, G., Moghaddam, B., and Adams, R. N. (1984) Nafion-coated electrodes with high selectivity for CNS electrochemistry, *Brain Res* 290, 390-395.
34. Roberts, J. G., Moody, B. P., McCarty, G. S., and Sombers, L. A. (2010) Specific Oxygen-Containing Functional Groups on the Carbon Surface Underlie an Enhanced Sensitivity to Dopamine at Electrochemically Pretreated Carbon Fiber Microelectrodes, *Langmuir* 26, 9116-9122.
35. Morcos, I., and Yeager, E. (1970) Kinetic Studies of Oxygen-Peroxide Couple on Pyrolytic Graphite, *Electrochim Acta* 15, 953-&.

36. Debiemme-Chouvy, C. (2010) A very thin overoxidized polypyrrole membrane as coating for fast time response and selective H₂O₂ amperometric sensor, *Biosens Bioelectron* 25, 2454-2457.
37. Avshalumov, M. V., Bao, L., Patel, J. C., and Rice, M. E. (2007) H₂O₂ signaling in the nigrostriatal dopamine pathway via ATP-sensitive potassium channels: issues and answers, *Antioxid Redox Signal* 9, 219-231.
38. Jin, H., Heller, D. A., Kalbacova, M., Kim, J. H., Zhang, J., Boghossian, A. A., Maheshri, N., and Strano, M. S. (2010) Detection of single-molecule H₂O₂ signalling from epidermal growth factor receptor using fluorescent single-walled carbon nanotubes, *Nat Nanotechnol* 5, 302-309.
39. Miller, E. W., Tulyathan, O., Isacoff, E. Y., and Chang, C. J. (2007) Molecular imaging of hydrogen peroxide produced for cell signaling, *Nat Chem Biol* 3, 263-267.
40. Srikun, D., Albers, A. E., Nam, C. I., Iavarone, A. T., and Chang, C. J. (2010) Organelle-targetable fluorescent probes for imaging hydrogen peroxide in living cells via SNAP-Tag protein labeling, *Journal of the American Chemical Society* 132, 4455-4465.
41. Avshalumov, M. V., Chen, B. T., Marshall, S. P., Pena, D. M., and Rice, M. E. (2003) Glutamate-dependent inhibition of dopamine release in striatum is mediated by a new diffusible messenger, H₂O₂, *Journal of Neuroscience* 23, 2744-2750.
42. Avshalumov, M. V., Patel, J. C., and Rice, M. E. (2008) AMPA receptor-dependent H₂O₂ generation in striatal medium spiny neurons but not dopamine axons: one source of a retrograde signal that can inhibit dopamine release, *J Neurophysiol* 100, 1590-1601.
43. Chen, B. T., Avshalumov, M. V., and Rice, M. E. (2001) H₂O₂ is a novel, endogenous modulator of synaptic dopamine release, *J Neurophysiol* 85, 2468-2476.
44. Chen, B. T., Avshalumov, M. V., and Rice, M. E. (2002) Modulation of somatodendritic dopamine release by endogenous H₂O₂: susceptibility in substantia nigra but resistance in VTA, *J Neurophysiol* 87, 1155-1158.
45. Rice, M. E. (2011) *H₂O₂: A Dynamic Neuromodulator*, *The Neuroscientist*, in press.
46. Evans, S. A., Elliott, J. M., Andrews, L. M., Bartlett, P. N., Doyle, P. J., and Denuault, G. (2002) Detection of hydrogen peroxide at mesoporous platinum microelectrodes, *Anal Chem* 74, 1322-1326.
47. Bard, A. J., and Lund, H. (1973) *Encyclopedia of electrochemistry of the elements*, M. Dekker, New York,.

48. Gonon, F., Buda, M., Cespuglio, R., Jouvet, M., and Pujol, J. F. (1980) In vivo electrochemical detection of catechols in the neostriatum of anaesthetized rats: dopamine or DOPAC?, *Nature* 286, 902-904.
49. Kulagina, N. V., and Michael, A. C. (2003) Monitoring hydrogen peroxide in the extracellular space of the brain with amperometric microsensors, *Analytical Chemistry* 75, 4875-4881.
50. Kissinger, P. T., and Heineman, W. R. (1996) *Laboratory techniques in electroanalytical chemistry*, 2nd ed., Marcel Dekker, Inc., New York.
51. Bath, B. D., Michael, D. J., Trafton, B. J., Joseph, J. D., Runnels, P. L., and Wightman, R. M. (2000) Subsecond adsorption and desorption of dopamine at carbon-fiber microelectrodes, *Analytical Chemistry* 72, 5994-6002.
52. Heien, M. L. A. V., Phillips, P. E. M., Stuber, G. D., Seipel, A. T., and Wightman, R. M. (2003) Overoxidation of carbon-fiber microelectrodes enhances dopamine adsorption and increases sensitivity, *Analyst* 128, 1413-1419.
53. Keithley, R. B., Heien, M. L., and Wightman, R. M. (2009) Multivariate concentration determination using principal component regression with residual analysis, *Trends Analyt Chem* 28, 1127-1136.

CHAPTER 6

The Role of Hydroxyl Radical Generation in the Voltammetric Detection of Hydrogen Peroxide

This work was completed in collaboration with: Maxim Voynov, Tatyana Smirnova, and Leslie A. Sombers, and is in preparation for submission to the Journal of the American Chemical Society.

6.1 Introduction

Quantitatively detecting molecules within biological samples has been a particularly important advancement for clinical diagnostics, environmental monitoring, and other research areas spanning multiple scientific disciplines. Oxidase-based electrochemical sensors are a subclass of the biosensing field that combines the inherent bioselectivity of hydrogen peroxide (H_2O_2)-producing enzymes with the response time and low detection limits of electrochemistry. This results in a powerful analytical tool that has transformed the sensing community. The driving force for this research was to meet a critical end-user demand to make rapid measurements of H_2O_2 whether endogenous or enzymatically-generated, within discrete micro-environments. Since the establishment of H_2O_2 as a cellular signal transducer, there has been a growing interest in defining the role of this diffusible messenger in mammalian systems (1). Previous studies have defined a functional role for mitochondrial generated H_2O_2 that modulates dopamine release via potassium sensitive adenosine-5'-triphosphate channels, yet direct monitoring of H_2O_2 was not available (2). We have successfully developed a technique to voltammetrically monitor real-time fluctuations

in H_2O_2 concentration within brain tissue with electrochemical selectivity (3), and have further investigated methods to increase the sensitivity, lower the limits of detection, and identify the most appropriate electrochemical sensor substrate for *in vivo* applications (4). Our approach utilizes background-subtracted fast-scan cyclic voltammetry (FSCV) with biologically-compatible carbon-fiber microelectrodes to generate a characteristic voltammogram for H_2O_2 with peak oxidative current evident near the switching potential, on the cathodic scan. The atypical location of the oxidative peak is an advantageous consequence of data filtering, resulting in a predictable and well-resolved peak, allowing rapid qualitative identification and accurate quantitation.

In this work, the mechanism of electron transfer was investigated to elucidate any possible intermediates and take advantage of this knowledge to advance the sensitivity, selectivity, and utility of these sensors. Electron paramagnetic resonance (EPR) spectroscopy was used to demonstrate the presence of hydroxyl radicals upon the electrochemical oxidation of H_2O_2 , on both platinum and carbon microelectrodes. These radicals were found to contribute to the current collected during the electrochemical oxidation of H_2O_2 . These results will benefit research fields that investigate uses for radical generation and detection, and will aid in the development of superior electrochemical sensors.

6.2 Materials and Methods

6.2.1 Chemicals

All chemicals were purchased from Sigma-Aldrich (St. Louis, MO) and used as received, unless otherwise noted. A physiologically buffered solution (Tris Buffer: 15 mM Trisma HCl, 3.25 mM KCl, 1.2 mM CaCl₂, 1.2 MgCl₂, 2.0 mM Na₂SO₄, 1.25 mM NaH₂PO₄, and 145 mM NaCl) at pH 7.4 was used in all flow injection analysis. Tris buffer and phosphate buffered saline (0.1 M PBS) were used for electron paramagnetic resonance (EPR) spectroscopy experiments. All aqueous solutions were made using doubly deionized water (Millipore, Billerica, MA).

6.2.2 Electrode Fabrication

Carbon-fiber disc microelectrodes with a polished angle of 30° were fabricated using 10 µm P-55s pitch-based carbon fibers (Cytec Industries, Woodland Park, NJ) as previously described.⁽⁵⁾ In brief, a single carbon fiber was inserted into a glass capillary tube (A-M Systems, Sequim, WA), pulled with a micropipette puller (Narishige, Tokyo, Japan), exposed carbon was trimmed, dipped in epoxy (Epoxy Technologies, Billerica, MA), oven dried, then polished (Sutter Instrument Co., Novato, CA). Platinum disc microelectrodes with a polished angle of 30° were constructed using 25 µm hard platinum wire (Goodfellow, Huntingdon, England), following the same procedure. Carbon-fiber cylindrical microelectrodes were fabricated by aspirating a single 7 µm diameter T-650 carbon fiber (Cytec Industries, West Patterson, NJ) into a glass capillary. A micropipette puller was used to seal the microelectrodes and the exposed length of carbon fiber was cut to 400 µm. Electrical

connections to the working electrode were made by backfilling the capillary with an ionic solution (4 M potassium acetate and 150 mM potassium chloride) and inserting a lead. A Ag/AgCl pellet reference electrode (World Precision Instruments, Sarasota, FL) was employed to complete the two electrode electrochemical cell.

6.2.3 Data Acquisition

All electrochemical data was collected in a custom flow injection system. In most experiments, a triangular cyclic waveform ranging from +0.2 to +1.3 V with a holding potential of +0.2 V versus Ag/AgCl was applied at a scan rate of $400 \text{ V}\cdot\text{s}^{-1}$ and at a frequency of 10 Hz using a custom built instrument for potential application to the electrochemical cell and for current transduction (University of North Carolina at Chapel Hill, Department of Chemistry, Electronics Facility). TH-1 software (ESA, Chelmsford, MA) was used for waveform output with DAC/ADC cards and for synchronization of the electrochemical experiment with the flow injection system (National Instruments, Austin, TX). Signal processing including background subtraction, signal averaging, and digital filtering was software-controlled (low-pass filtered, 2 KHz).

6.2.4 Flow Injection System

A syringe pump (New Era Pump Systems, Wantagh, NY) supplied a continuous buffer flow of 1 mL/min across the working and reference electrodes. The working electrode was positioned within a custom electrochemical cell using a micromanipulator (World Precision Instruments, Sarasota, FL). Two second bolus injections of analyte to the

microelectrode surface were accomplished with a six-port HPLC valve mounted on a two-position air actuator controlled by a digital pneumatic solenoid valve (Valco Instruments, Houston TX). The entire apparatus was housed within a grounded Faraday cage. All experiments were performed at room temperature.

6.2.5 Spin-Trapping Experiments

A solution containing 5 mM 5,5-dimethyl-1-pyrroline-N-oxide (DMPO) along with a mixed solution containing 5 mM hydrogen peroxide (H_2O_2) and 5 mM DMPO was prepared in pH 7.4 PBS. 200 μL of either solution was placed in a custom polypropylene microliter electrochemical cell, which included a Ag/AgCl reference electrode. A platinum microdisc or carbon-fiber microelectrode was lowered into the solution and a waveform from +0.2 to +1.3 V at $400 \text{ V}\cdot\text{s}^{-1}$ was applied at 100 Hz. This waveform was applied for 30 minutes, and the solution was immediately transferred to a polytetrafluoroethylene (PTFE) 0.81 x 1.12 mm diameter tubing (NewAge Industries, Southampton, PA) for EPR measurements.

6.2.6 EPR Measurements

All measurements were taken at room temperature with a Varian (Palo Alto, CA) Century Series E-109 spectrometer. In the experiments, the sample was drawn into PTFE tubing (NewAge Industries, Southampton, PA), the tubing was folded twice and inserted into a standard 3 x 4 mm diameter quartz EPR tube (Wilmaad-LabGlass, Vineland, NJ). Data acquisition parameters were set as follows: 0.8 G modulation amplitude; 2 mW microwave

power; 100 G scan width; 30 sec sweep time; 32 msec time constant. All spectra represent 100 integrated scans.

6.2.7 Digital Simulations

Digital simulations of voltammograms were performed with DigiSim V3 (Bioanalytical Systems, West Lafayette, IN). Since DigiSim cannot model irreversible reactions, so two reactions were simulated: the heterogeneous reaction of hydrogen peroxide oxidation and a homogenous reaction that rapidly depleted the oxidized species. Filtering of simulated voltammograms was accomplished with Matlab (The MathWorks, Natick, MA).

6.2.8 Digital Simulation Parameters

Reactions: $B + e^- = A$, $B = C$; Waveform: -0.4 to +1.4 to -0.4 at $400 \text{ V}\cdot\text{s}^{-1}$; Electrode: Planer $3\text{E-}6 \text{ cm}^2$; Semi-infinite linear diffusion; Butler-Volmer kinetics; Room temperature; Initial concentration of H_2O_2 : 1 mM; E^0 : 0.85 V; α/λ : 0.5 eV; k_s : $1\text{E-}5 \text{ cm}\cdot\text{s}^{-1}$; D (all species): $1\text{E-}5 \text{ cm}^2\cdot\text{s}^{-1}$; Homogenous reaction rates: K_{eq} : 300, K_f : $1\text{E+}4$, K_b : 33.33.

6.2.9 Statistics

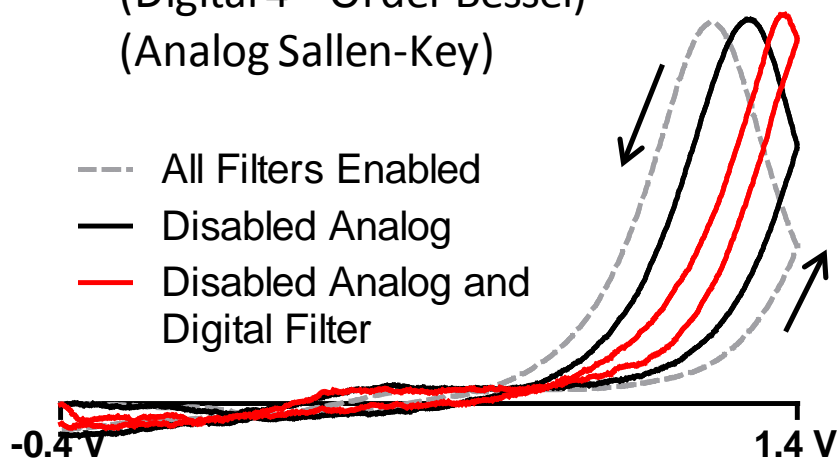
All values are given as the mean \pm standard deviation, unless otherwise noted. Two-tailed paired Student's t tests were used, with significance designated as $p < 0.05$. Multiple linear regression was used to extract concentration values from complex mixtures (Matlab, The MathWorks, Natick, MA). Statistical and graphical analysis was accomplished using GraphPad Prism 5 (GraphPad Software, Inc., La Jolla, CA).

6.3 Results and Discussion

We previously reported that on the detection of rapid H_2O_2 fluctuations using background-subtracted fast-scan cyclic voltammetry (FSCV) with carbon-fiber microelectrodes (3). This method results in peak oxidative current near the switching potential, on the cathodic scan. This location of the oxidative peak is a consequence of data filtering. This phenomenon is demonstrated experimentally (Figure 6.1.A), as well as digitally simulated (Figure 6.1.B). Voltammograms for $100\ \mu\text{M}\ \text{H}_2\text{O}_2$ were collected with both a 2 kHz analog and digital lowpass filter enabled (Figure 6.1.A, grey dashed line). As filters were individually removed, the oxidative peak shifted toward the switching potential. To further demonstrate this, a theoretical voltammogram was simulated for the oxidation of H_2O_2 (Figure 6.1.B, grey dashed line) using the parameters listed in the supporting information. Briefly, two reactions were simulated (E° : 0.85 V, k_s : $1\text{E-}5\ \text{cm}\cdot\text{s}^{-1}$, K_{eq} : 300, K_f : $1\text{E+}4$) including a heterogeneous reaction for H_2O_2 oxidation and a homogenous reaction that rapidly depleted the oxidized species to generate an irreversible voltammogram. A digital lowpass filter applied to the simulated voltammogram (Figure 6.1.B, black line) shifted the peak and altered the shape to resemble one experimentally collected, with filters enabled.

A) 2 kHz Lowpass Filters

(Digital 4th Order Bessel)
(Analog Sallen-Key)



B)

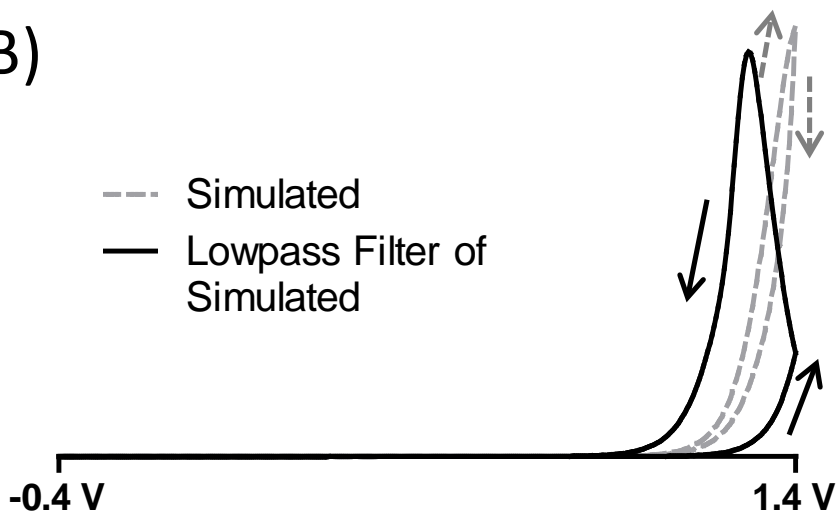


Figure 6.1 - Representative voltammograms. (A) 100 μM H_2O_2 with all filters enabled (grey dashed line), the 2 kHz analog lowpass filter disabled (black line), and both the 2 kHz digital and analog lowpass filter disabled (red line). (B) Simulated voltammogram for H_2O_2 (grey dashed line) and lowpass filtering of the simulated data (black line).

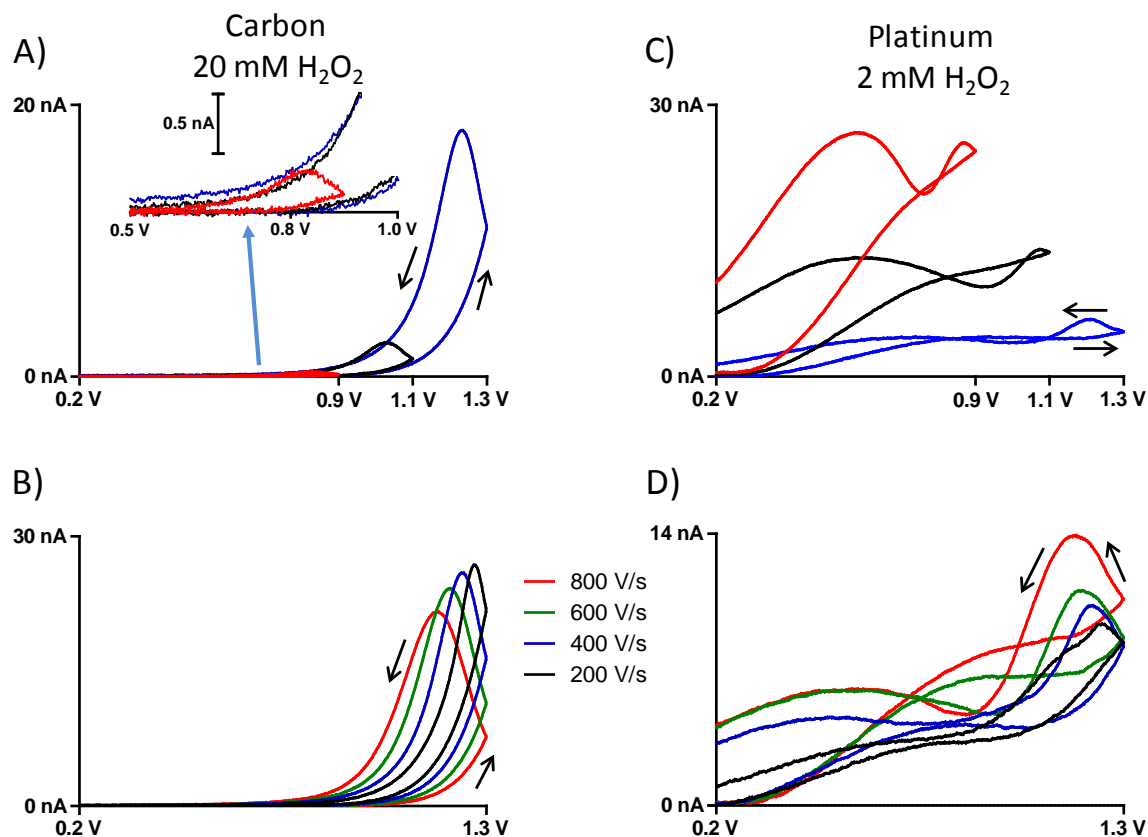


Figure 6.2 - Representative voltammograms for H₂O₂ on both carbon (A,B) and platinum (C,D) electrodes. Highlighting the differences with changing the anodic limits and scan rates of the waveform.

Previously, we have reported that the oxidation of H₂O₂ on both carbon and platinum microelectrodes generates similar voltammograms when using fast scan rates, suggesting a similar mode of electron transfer (4). When comparing the two substrates, a common waveform was established that prevented the larger platinum microdisc electrode from overloading the circuitry; however, this was not optimal for the carbon electrode as it reduced the sensitivity. This cyclic waveform ranged from +0.2 to +1.3 V at a scan rate of

400 V·s⁻¹. Peak current was generated after the switching potential, at about +1.2 V. Figures 6.2.A-B show representative voltammograms for H₂O₂ oxidation on carbon, and Figures 6.2.C-D on a platinum substrate. The top figures demonstrate how altering the anodic limit (+0.9, +1.1, and +1.3 V) affects the voltammograms, and the lower figures show the effect of scan rate (200, 400, 600, and 800 V·s⁻¹). Peak current increases with increasing anodic wave limits for carbon electrodes, but decreases on platinum conversely. As scan rates were increased, peak current increased on platinum, but decreased on carbon. The principle oxidation is similar on both substrates, as peak current occurs at the same voltages; however, these trends suggest a different mechanism or rate limiting step for the two substrates.

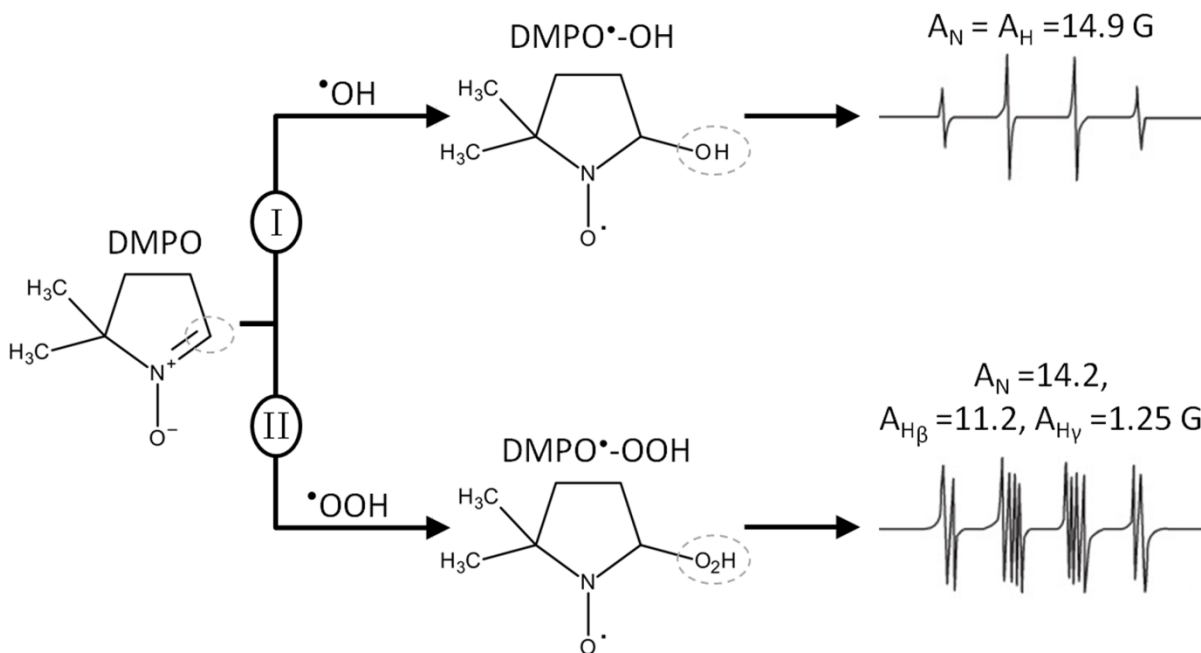


Figure 6.3 - Suspected radicals generated from the electrochemical oxidation of H₂O₂. Showing the formed adducts of DMPO with their respective EPR spectra and hyperfine coupling constants.

To investigate whether an intermediate step was involved in the oxidation of H_2O_2 , we elected to identify possible radical intermediates by including a commonly-used spin-trapping agent, 5,5-dimethyl-1-pyrroline-N-oxide (DMPO), in the H_2O_2 solution. Electron paramagnetic resonance (EPR) spectroscopy was used to determine the nature of any radicals formed in solution, due to its ability to selectively distinguish adducts of DMPO and resolve the structure of the trapped radical. DMPO itself is EPR silent. Figure 6.3 illustrates the reaction paths for two possible oxygen centered radicals bound to DMPO, and their respective spectra. Path 1 shows a hydroxyl radical binding to the alpha carbon of DMPO, to form the $\text{DMPO}^{\bullet}\text{-OH}$ adduct, while path 2 follows the trapping of a peroxy radical to form the $\text{DMPO}^{\bullet}\text{-OOH}$ adduct. The resulting spectra demonstrate the qualitative power of EPR, and further data analysis by least squares regression of experimental spectra generates hyperfine coupling constants, revealing adduct identity. A 200 μL electrochemical cell

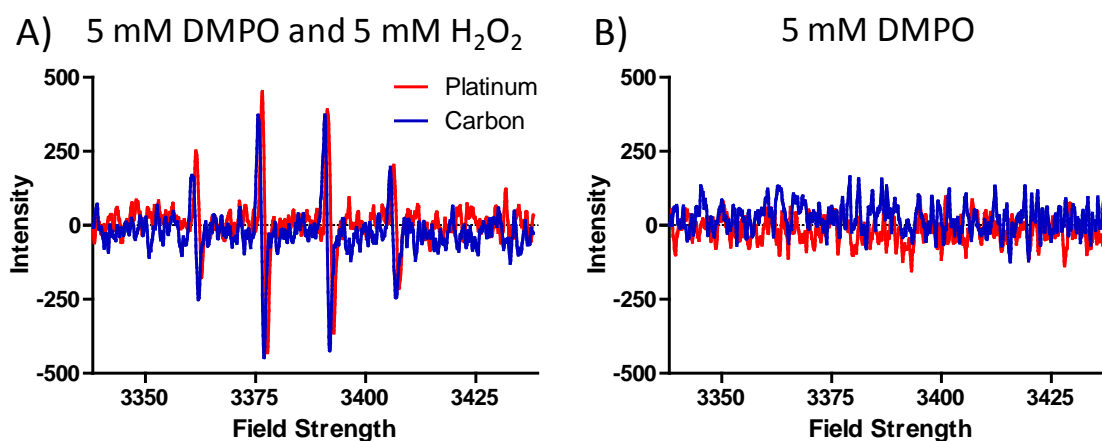


Figure 6.4 - Representative EPR spectra of solutions containing DMPO and H_2O_2 (A) or DMPO alone (B). The cyclic waveform was applied to either carbon (blue) or platinum (red) electrodes.

with a Ag/AgCl reference electrode was used to generate samples and facilitated transport to the spectrometer. Either a platinum disc or carbon-fiber cylindrical microelectrode was lowered into the cell, a cyclic waveform was applied for 30 minutes (+0.2 to +1.3 V, $400 \text{ V}\cdot\text{s}^{-1}$, 100 Hz), and samples were interrogated in the spectrometer. Spectra collected for samples that contained both 5 mM H_2O_2 and 5 mM DMPO shows a clear four line pattern indicative of the $\text{DMPO}^{\bullet}\text{-OH}$ adduct (Figure 6.4.A). These were generated using both carbon and platinum substrates. Samples that contained only 5 mM DMPO had no discernible signal above the noise (Figure 6.4.B). Following a previously published procedure for resolving hyperfine coupling constants (6), a 1:2:2:1 splitting pattern was calculated and resulted in $A_{\text{H}} = 15.24 \pm 0.03$, $A_{\text{N}} = 14.78 \pm 0.01$ for platinum electrodes, and $A_{\text{H}} = 15.15 \pm 0.04$, $A_{\text{N}} = 14.77 \pm 0.05$ for carbon ($n = 3$ electrodes). Literature values are $A_{\text{H}} = A_{\text{N}} = 14.9$ (7).

Since the electrochemical cell contained a Ag/AgCl reference electrode that could have been the site of radical formation, a control experiment was designed to exclude this possibility. A micro-agar salt bridge, constructed following a published method (8), enabled stable potentials and provided a diffusion barrier for the Ag/AgCl reference electrode to exclude its contribution. The resulting EPR spectra (data not shown) were identical to those for samples generated with the direct contact reference electrode, verifying that the site of radical formation was at the working electrode. An alternate source of an oxygen-centered radical could have originated from Trizma found in the buffered solution, which possesses three terminal hydroxyl groups. Tris buffer and PBS were compared to determine any contribution from Trizma on adduct formation. Equivalent spectra resulted for both buffer types (data not shown). One final control experiment consisted of placing all electrodes in a

solution of H_2O_2 and DMPO without applying a potential, and the spectra of the solution resulted in no observable signal over noise (data not shown). This EPR data demonstrate that hydroxyl radicals can be electrochemically generated in the oxidation of H_2O_2 , at both platinum and carbon electrodes under the expressed conditions. We then sought to determine if the voltammetric signal was radical dependant. Using carbon-fiber microelectrodes, a voltammogram for H_2O_2 was compared to a voltammogram for a mixture of a trapping agent and H_2O_2 , with DMPO in tenfold excess. In addition to DMPO, dimethyl sulfoxide (DMSO) is also capable of scavenging hydroxyl radicals (9, 10). Background-subtracted cyclic voltammograms were collected: 1 mM DMPO, 10 mM DMSO, 100 μM H_2O_2 , and mixtures of these species (Figure 6.5.A and 6.5.B). Voltammograms of the spin trapping agents demonstrate some current, which is likely due to a slight pH shift of the solution. In voltammetry, the currents for mixtures of multiple analytes should be additive, such that the sum of the voltammograms for each individual analyte comprise the voltammograms for the mixture, unless there is a chemical reaction that eliminates the redox activity of an analyte (11). This summation of current was generally observed and exhibited no chemical reaction, except at +1.2 V on the cathodic scan where the oxidation of H_2O_2 is evident. The sum of the currents here for the individual analytes totaled more than that of the current observed for the mixture, suggesting a chemical reaction has contributed to the loss in current for H_2O_2 oxidation.

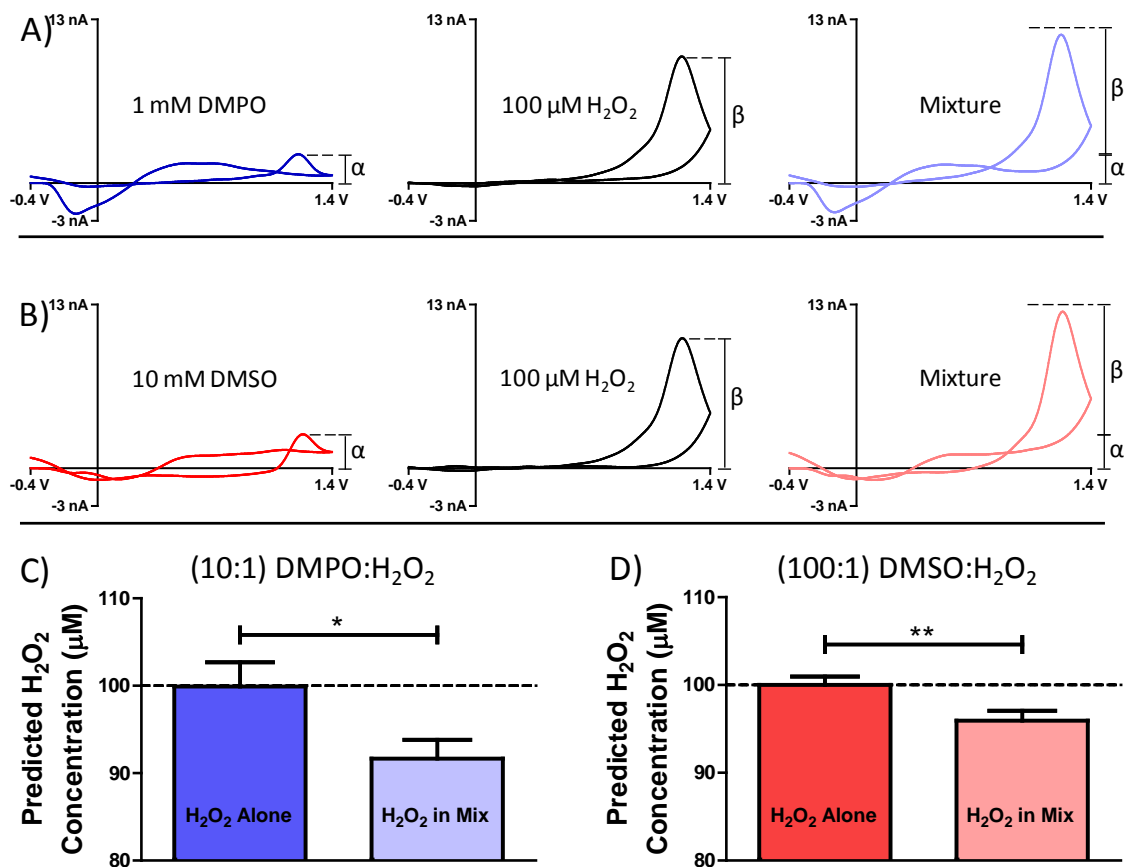


Figure 6.5 - (A and B) Representative voltammograms for individual analytes and a mixture of trapping agent and H₂O₂. (C and D) Bar graphs showing a significant difference between the predicted concentration of H₂O₂ within solutions of just H₂O₂ and mixed solutions of H₂O₂ and DMPO (n = 4 electrodes).

Since all analytes gave a predictable current response to concentration by themselves (data not shown), multiple linear regression (MLR) was used to solve for the concentration of H₂O₂ in each mixture (12, 13), following the equations:

$$\alpha(TrapCV) + \beta(H_2O_2CV) = (MixCV) \quad (1)$$

$$\frac{\beta}{\delta} \cdot (H_2O_2CV) = [H_2O_2]_{H_2O_2CV} \quad (2)$$

$$\frac{\beta}{\delta} = [H_2O_2]_{MixCV} \quad (3)$$

where TrapCV and H₂O₂CV are normalized voltammograms for each analyte, MixCV is a voltammogram for the mixed analyte solution, α and β are coefficients with units of nA, and δ is a calibration factor for each electrode describing sensitivity to H₂O₂ (nA· μ M⁻¹). The results are presented in Figures 6.5.C-D and are also listed in Table 6.1. There was a significant reduction in the predicted concentration of H₂O₂ within the DMPO-H₂O₂ mixture (p = 0.0105) and the DMSO-H₂O₂ mixture (p = 0.0057), when compared to H₂O₂ alone. One possibility for this result was that DMPO reduced electrode sensitivity to H₂O₂ oxidation.

Table 6.1 - Predicted concentration of H₂O₂ within a solution containing only H₂O₂, and within a solution containing H₂O₂ plus a trapping agent (DMPO or DMSO).

Solution	Predicted H ₂ O ₂ Concentration (μ M)
1 mM DMPO + 100 μ M H ₂ O ₂	91.87 \pm 2.13
100 μ M H ₂ O ₂	99.92 \pm 2.77
10 mM DMSO + 100 μ M H ₂ O ₂	95.99 \pm 1.11
100 μ M H ₂ O ₂	100.0 \pm 0.9
(n = 3 electrodes)	

To rule this out, an identical experiment was done performed using 1 μM histamine and 1 mM DMPO. 1 μM histamine was chosen because its voltammogram exhibits peak current intensity at a comparable potential to that of 100 μM H_2O_2 , and the molecule remains uncharged at physiological pH (Figure 6.6.A). MLR predicted equal concentrations of histamine in solutions of just histamine and histamine plus DMPO (Table 6.2). This result demonstrates that the loss in predicted H_2O_2 concentration is not a result of electrode fouling from spin trap exposure.

Table 6.2 - Predicted concentration of histamine within a solution containing only histamine, and within a solution containing histamine plus DMPO.

Solution	Predicted Histamine Concentration (μM)
1 mM DMPO + 1 μM histamine	0.99 ± 0.17
1 μM histamine	0.98 ± 0.18
(n = 4 electrodes)	

These voltammetric data reveal that the hydroxyl radical is a significant contributor to the voltammetric signal. Two other endogenous neuromodulators, adenosine (14) and histamine (15) have similar voltammetric signatures to that of H_2O_2 , where peak current is evident on the reverse scan at approximately +1.2 V using this waveform and filtering settings (Figure 6.6). We sought to determine if this common peak was also radical dependant. DMPO is an efficient trap of both nitrogen- and carbon-centered radicals, thus the EPR spectra would reveal the presence and identity of these species. The electrochemical trapping procedure

was replicated for these molecules, and the EPR spectra gave no significant signal over noise (data not shown). Although these data do not rule out the possibility of radical generation, the results suggest that the electrochemical detection of histamine and adenosine using FSCV does not generate oxygen- or nitrogen-centered radicals at the electrode surface.

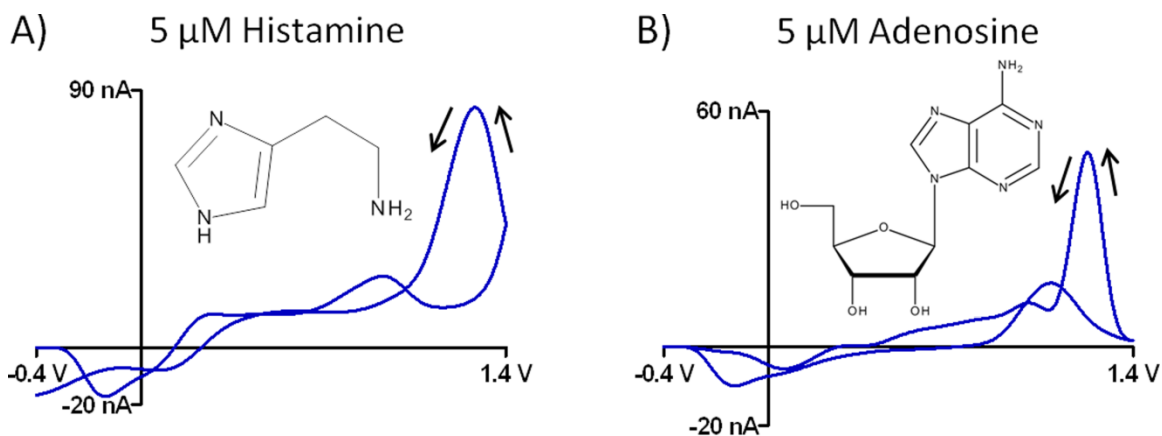


Figure 6.6 - Representative voltammograms for (A) histamine and (B) adenosine collected on cylindrical carbon-fiber microelectrodes.

6.4 Conclusions

This work suggests that this technique can be adapted as a real-time method for monitoring radical generation, and future work will evaluate this feasibility. The results presented here demonstrate a fundamental role for the hydroxyl radical in the oxidation and detection of H_2O_2 on both carbon and platinum substrates when using FSCV. Overall, these findings could be utilized to fulfill critical needs across many scientific disciplines by developing advanced electrochemical sensors or improving chemical functionalization methods.

6.5 References

1. Finkel, T. (1998) Oxygen radicals and signaling, *Curr Opin Cell Biol* 10, 248-253.
2. Rice, M. E. (2011) H₂O₂: A Dynamic Neuromodulator, *Neuroscientist* 17, 389-406.
3. Sanford, A. L., Morton, S. W., Whitehouse, K. L., Oara, H. M., Lugo-Morales, L. Z., Roberts, J. G., and Sombers, L. A. (2010) Voltammetric Detection of Hydrogen Peroxide at Carbon Fiber Microelectrodes, *Analytical Chemistry* 82, 5205-5210.
4. Roberts, J. G., Hamilton, K. L., and Sombers, L. A. (2011) Comparison of electrode materials for the detection of rapid hydrogen peroxide fluctuations using background-subtracted fast scan cyclic voltammetry, *Analyst* 136, 3550-3556.
5. Zachek, M. K., Hermans, A., Wightman, R. M., and McCarty, G. S. (2008) Electrochemical dopamine detection: Comparing gold and carbon fiber microelectrodes using background subtracted fast scan cyclic voltammetry, *J Electroanal Chem* 614, 113-120.
6. Voinov, M. A., Sosa Pagan, J. O., Morrison, E., Smirnova, T. I., and Smirnov, A. I. (2011) Surface-mediated production of hydroxyl radicals as a mechanism of iron oxide nanoparticle biotoxicity, *J Am Chem Soc* 133, 35-41.
7. Minotti, G., and Aust, S. D. (1987) The requirement for iron (III) in the initiation of lipid peroxidation by iron (II) and hydrogen peroxide, *J Biol Chem* 262, 1098-1104.
8. Shao, X. M., and Feldman, J. L. (2007) Micro-agar salt bridge in patch-clamp electrode holder stabilizes electrode potentials, *J Neurosci Methods* 159, 108-115.
9. Dixon, W. T., Norman, R. O. C., and Buley, A. L. (1964) Electron Spin Resonance Studies of Oxidation .2. Aliphatic Acids + Substituted Acids, *J Chem Soc*, 3625-3634.
10. Lagercrantz, C., and Forshult, S. (1969) Trapping of Short-Lived Free Radicals as Nitroxide Radicals Detectable by ESR Spectroscopy. Radicals Formed in Reaction between Oh-Radicals and Some Sulphoxides and Sulphones, *Acta Chem Scand* 23, 811-817.
11. Bard, A. J., and Faulkner, L. R. (2001) *Electrochemical Methods: Fundamentals and Applications*, 2nd ed., John Wiley, New York.
12. Brown, S. D., and Bear, R. S. (1993) Chemometric Techniques in Electrochemistry - a Critical-Review, *Crit Rev Anal Chem* 24, 99-131.

13. Bessant, C., and Saini, S. (2000) A chemometric analysis of dual pulse staircase voltammograms obtained in mixtures of ethanol, fructose and glucose, *J Electroanal Chem* 489, 76-83.
14. Ross, A. E., and Venton, B. J. (2012) Nafion-CNT coated carbon-fiber microelectrodes for enhanced detection of adenosine, *Analyst* 137, 3045-3051.
15. Chang, S. Y., Jay, T., Munoz, J., Kim, I., and Lee, K. H. (2012) Wireless fast-scan cyclic voltammetry measurement of histamine using WINCS--a proof-of-principle study, *Analyst* 137, 2158-2165.

CHAPTER 7

Analyte Specific Waveform for the Voltammetric Detection and Characterization of Met-Enkephalin in Brain Tissue

This work was part of a collaborative effort with: Andreas Schmidt and Leslie A. Sombers, and is in preparation for submission to ACS Neuroscience. Only a portion of the chapter constitutes the author's personal dissertation research; however, all results are shown to allow for a complete interpretation of the findings.

7.1 Introduction

Opioid peptides are a specific sub-group of neuropeptides composed of short amino acid sequences, and are a major class of signaling molecules in the brain. They are thought to play a key role in systems that modulate addiction, pain, and movement, often by way of their interactions with other neurochemical systems including the dopaminergic system (1-3). Opioid neuropeptides have been shown to bind to three principle types of opioid receptors mu, kappa, and delta (μ , δ , and κ) (4). Specifically, μ - and δ -agonists are reinforcing and are self-administered, while κ -agonists are not self-administered and are generally considered to be aversive (5). As such, opioid peptides are typically expressed in combination with fast-signaling neurotransmitters and messengers (6). These fast interactions require an analytical technique that can discriminately quantify neurotransmitters on a sub-second timescale in the complex environment of the brain. Background-subtracted fast-scan cyclic voltammetry (FSCV) is well suited to detecting low concentrations of electroactive neurotransmitters in real-time. It is an established technique that is often used to monitor fluctuating dopamine levels in living brain tissue, and more recently extended to other molecules such as

adenosine, hydrogen-peroxide, serotonin, local pH changes, and norepinephrine (7-13). Due to the range of possible interactions between opioid peptides and other neurotransmitters, FSCV could be instrumental in revealing a tremendous therapeutic potential for a variety of neuronal and cognitive disease states.

Opioid receptor regulation of mesolimbic dopamine neurons is the thought to be the pivotal underpinning of the opioid behavioral effects. Several animal studies have investigated the connection between the effects of alcohol, or other drugs of abuse, on the dopaminergic system and it is known that they also alter the opioid peptide concentration in relevant brain regions (14-17). To date, there have been no viable approaches to directly detecting opioid peptides in real-time. Some previous studies have primarily focused on establishing a behavioral role for methionine-enkephalin (mENK) and its interaction with dopamine rather than directly measuring the concentration of the peptide in specific brain regions. These studies have suggested that mENK caused a dose-dependent increase in locomotor activity, which was then indirectly attributed to increased dopamine levels in the striatum (3, 18). The most successful attempts at monitoring neuropeptides directly have been accomplished using solid-phase radioimmunoassay or microdialysis coupled to capillary liquid chromatography using either electrochemical detection or triple-stage mass spectrometry (14, 15, 19-22). Although microdialysis has low detection limits and high chemical selectivity, the spatial and temporal resolution required for monitoring rapid mENK fluctuations and dynamic interactions with other neurochemical systems is lacking. Sub-second temporal resolution is required to gain a better understanding of the neurochemical

fluctuations of neuropeptides that happen on a rapid timescale, their interactions with other neurochemical systems, and the molecular mechanisms underlying behavior.

FSCV fills the critical need for an approach that can not only measure rapid fluctuations of neurotransmitters, but also provides excellent spatial resolution when coupled to carbon-fiber microelectrodes. Due to the small size of the electrodes, tissue damage is minimized compared to other more invasive techniques, including microdialysis (23). FSCV also provides better chemical selectivity and resolution than other electrochemical techniques, such as chronoamperometry, by providing voltammograms composed of 1000 individual data points collected over a wide range of potentials. However, electrochemically detecting tyrosine-containing neuropeptides, like mENK, in living tissue is extremely challenging.

Neuropeptides are typically found in concentrations in the picomolar to nanomolar range, are present in the extracellular space for only short periods, and tend to foul the electrode surface upon oxidation, making it difficult to obtain reproducible measurements (20). Furthermore, these peptides oxidize at higher potentials than catecholamines causing possible interferent problems (20). Nonetheless, FSCV in conjunction with bare carbon-fiber microelectrodes can be adapted to measure neuropeptides in living tissue. To tailor FSCV for the detection of mENK, a waveform was developed that eliminated electrode fouling to allow reproducible measurements, while also increasing chemical resolution compared to other chemical interferents. This research presents the development of an analyte specific waveform for making reproducible measurements of acute mENK concentration changes in

the presence of *in vivo* interferents. The results of this research are broadly applicable towards the electrochemical detection of other tyrosine-containing peptides using FSCV.

7.2 Methods

7.2.1 Chemicals

All chemicals were purchased from Sigma-Aldrich (St. Louis, MO) and used as received, unless otherwise specified. Methionine-enkephalin, leucine-enkephalin, and neurotensin were obtained as acetate salts from LKT Laboratories (St. Paul, MN). Electrochemical experiments were carried out in phosphate buffered saline (0.1 M PBS) or Tris buffer (15 mM Tris, 3.25 mM KCl, 1.20 mM CaCl₂, 1.2 mM MgCl₂, 2 mM Na₂SO₄, 1.25 mM NaH₂PO₄, 145 mM NaCl), both at physiological pH 7.4. Brain slice experiments used artificial cerebral spinal fluid (aCSF) saturated with 95% O₂ and 5% CO₂, at physiological pH 7.4. aCSF consisted of 124 mM NaCl, 26 mM NaHCO₃, 3.7 mM KCl, 2.4 mM CaCl₂, 1.3 mM MgCl₂, 1.3 mM NaH₂PO₄, and 10 mM glucose. All aqueous solutions were made from double deionized water >18 MΩ·cm (Millipore, Billerica, MA).

7.2.2 Electrode Fabrication

All electrochemical experiments were carried out with T-650 carbon-fiber microelectrodes (Cytec Industries, West Patterson, NJ). These were fabricated by aspirating a single 7 μm diameter fiber into a single borosilicate glass capillary (1.0 mm x 0.5 mm, A-M Systems, Carlsburg, WA). Using a micropipette puller (Narishige, Tokyo, Japan), the glass was tapered to form sealed microelectrodes, which were then cut to the desired length.

Electrodes were cut to 300 μm for experiments involving calibration, reproducibility, and interferent studies. Electrodes cut to 100 μm were used for comparison between the -0.4 V to +1.4 V triangular and modified waveforms, as well as the brain slice experiments. To establish an electrical connection with the carbon fiber, the glass capillary was backfilled with ionic solution (4 M potassium acetate, 150 mM KCl) and a lead was inserted. All measurements were recorded against a Ag/AgCl reference electrode (World Precision Instruments, Inc., Sarasota, FL).

7.2.3 Flow Injection

All data, with the exception of brain slice experiments, were collected in a custom-built flow injection apparatus housed within a Faraday cage. A syringe pump (New Era Pump Systems, Inc., Wantagh, NY) supplied a continuous buffer flow of 1 $\text{mL}\cdot\text{min}^{-1}$ across both the working and reference electrode. The working electrode was lowered into the electrochemical cell via a micromanipulator (World Precision Instruments, Inc., Sarasota, FL). Two-second bolus injections of analyte were accomplished using a six-port HPLC valve and air actuator controlled by a digital valve interface (Valco Instruments Co., Inc., Houston, TX).

7.2.4 Electrochemical Waveforms and Data Acquisition

A novel waveform, referred to as a modified saw-horse waveform (MSW) herein, was applied at 10 Hz for peptide detection experiments (Figure 7.1.B). The potential was held at -0.2 V, then ramped to +0.6 V at 100 $\text{V}\cdot\text{s}^{-1}$, and then raised to +1.2 V at 400 $\text{V}\cdot\text{s}^{-1}$.

The potential was then held at +1.2 V for 3 msec before scanning back to the holding potential of -0.2 V at $100 \text{ V}\cdot\text{s}^{-1}$. A more traditional triangular waveform (TW) was used for performance comparisons to the MSW, which was applied from -0.2 V to +1.2 V and back at $400 \text{ V}\cdot\text{s}^{-1}$ (Figure 1A). These waveforms were output using a custom-built instrument for potential application to the electrochemical cell and current transduction (University of North Carolina at Chapel Hill, Department of Chemistry, Electronics Facility). TH-1 software (ESA, Chelmsford, MA) controlled waveform output and two PCI bus cards (National Instruments Corp., Austin, TX) were used for collecting data and synchronization of the electrochemical experiment with the flow injection system. Signal processing (background subtraction, signal averaging, and digital filtering (2-pole Sallen-Key Filter, 2 KHz)) was software-controlled.

7.2.5 Brain Slice Preparation

Male Sprague-Dawley rats (250-300 g, Charles River Laboratories, Raleigh, NC) were decapitated after being deeply anesthetized with urethane (1.5 g kg^{-1} , i.p.). The brain was rapidly removed, mounted, and placed in cold aCSF while $400 \mu\text{m}$ thick coronal slices containing the striatum were obtained with a vibratome (World Precision Instruments, Sarasota, FL). The slices were allowed to rest in buffer for at least one hour before the start of an experiment. Brain slices were subsequently placed in a recording chamber (Warner Instruments, Hamden, CT) and superfused with aCSF buffer maintained at $34 \text{ }^\circ\text{C}$ for at least 1.5 hours. Carbon-fiber microelectrodes were placed about $100 \mu\text{m}$ below the surface of the slice. For the sample injection experiments, a glass micropipette pulled from borosilicate

glass capillary (A-M Systems, Carlsburg, WA) with an outer tip diameter of 15 - 20 μm was positioned in the tissue approximately 1 mm from the recording electrode. Working electrode and microinjector placements were made with the aid of a microscope (Nikon Instruments, Inc., Melville, NY). Buffered solution containing 1 mM mENK was injected for 1 sec at 5 psi with a Picospritzer III (Parker Hannifin Corp., Fairfield, NJ). Animal care and use was in complete accordance with institutional guidelines.

7.2.6 Statistics

All data presented are shown as the mean \pm standard deviation (SD). One-tailed Student's *t* tests were used to determine the significance of means. Statistical and graphical analysis was carried out using GraphPad Prism 5 (GraphPad Software, Inc., La Jolla, CA).

7.3 Results

7.3.1 Met-Enkephalin Cyclic Voltammetry

Cyclic voltammograms (CVs) were initially collected *in vitro* using a standard triangular waveform applied at a scan rate of 400 $\text{V}\cdot\text{s}^{-1}$, ranging from -0.4 V to +1.4 V applied at 10 Hz to a 100 μm carbon-fiber microelectrode (9). Figure 7.1.C shows the background-subtracted CV, as well as the colorplot (24) for a two second bolus injection of 2 μM mENK. This sample was introduced to the electrode surface at the time indicated by the red bars. Currents generated at numerous potentials (*) are evident in Figure 7.1.C. This signal persists after the end of the 2 second analyte injection, indicating surface fouling highlighted by the white asterisks. This residual current lowers the sensitivity of the

electrode to the analyte for subsequent injections while also reducing sensitivity toward other detectable neurochemicals, making reproducible measurements difficult. It was determined experimentally that a wider potential window leads to significantly higher surface fouling; consequently, the potential range was decreased.

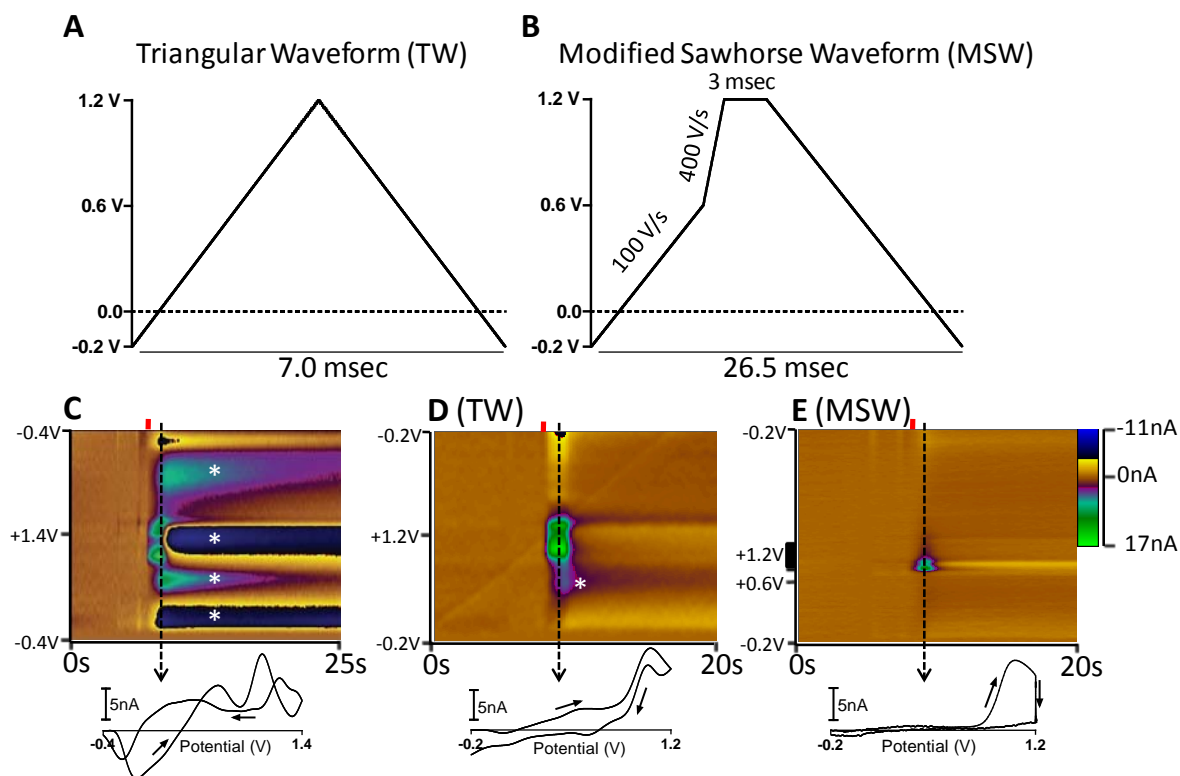


Figure 7.1 - Representative voltammetric data of 2 μM mENK on 100 μm cylindrical carbon-fiber microelectrodes, collected *in vitro*. (A) Traditional triangular waveform (TW) applied to electrode for performance comparisons to the analyte specific waveform. (B) Modified Sawhorse Waveform (MSW) developed for the detection of tyrosine-containing peptides. (C) Colorplot and CV extracted at dotted line when collecting using a large triangular waveform ranging from -0.4 V to +1.4 V scanned at $400 \text{ V}\cdot\text{s}^{-1}$. (D) Colorplot and CV extracted at dotted line when using the TW. (E) Colorplot and CV extracted at dotted line when using the MSW. The ordinate is the applied potential to the carbon-fiber electrode, the abscissa is time in seconds, and the current (nA) is depicted in false color. Red bars indicate time of sample introduction to electrode. Colorplots illustrate the rapid change in concentration of an analyte.

A triangular waveform (hereafter referred to as TW, Figure 7.1.A) from -0.2 V to +1.2 V at $400 \text{ V}\cdot\text{s}^{-1}$ was tested. A representative colorplot for data collected using this abbreviated cyclic waveform is shown in Figure 7.1.D. Though surface fouling was reduced, it was not completely eliminated. A modified saw-horse waveform (hereafter referred to as MSW, Figure 7.1.B) was developed to retain chemical selectivity and reproducibility, while maintaining adequate sensitivity and temporal resolution. Specifically, the potential was ramped from -0.2 V to +0.6 V at $100 \text{ V}\cdot\text{s}^{-1}$, then to +1.2 V at $400 \text{ V}\cdot\text{s}^{-1}$ and held for 3 msec at this potential. The potential was then ramped back to -0.2 V at $100 \text{ V}\cdot\text{s}^{-1}$ (Figure 7.1.B). A representative colorplot collected using this waveform is shown in Figure 7.1.E. This waveform takes 26.5 msec to apply, which allows measurements to be made at 10 Hz and maintains sub-second temporal resolution. Since current scales with scan rate, the faster rate was applied only in the potential range of oxidation for our analyte of interest. By using a slower scan rate before and after our oxidation potential of interest, the faradaic contributions of other analytes were reduced. The potential was held at +1.2 V for 3 msec because research has shown that the adsorption of tyrosine onto the electrode surface weakens above +1.1 V (25). The results indicate that the holding of the potential is sufficient to renew the electrode surface, thus eliminating signal loss from surface fouling. The results give a resolved peak at about +1.05 V and another smaller peak during the holding time at +1.2 V, suggesting that the two observed peaks could result from the oxidation of two separate amino acids.

7.3.2 Electrochemical Moiety

Given that mENK is composed of a five amino-acid chain, as shown in Figure 7.2.A (top), it was important to isolate which moiety was responsible for the electrochemical response. The redox activities of tyrosine and methionine have been demonstrated (26, 27). Conversely, glycine and phenylalanine were not expected to be redox active within the potential window. By comparing colorplots obtained using the MSW for tyrosine and mENK (Figure 7.2.A, left and center color plot, respectively), it was determined that the amino acid tyrosine was responsible for the first peak observed in the CV for mENK. Methionine was found to also be redox active (Figure 7.2.A, right color plot). The unfolded CV (Figure 7.2.B) for methionine suggests that the methionine group on mENK could be contributing to the second peak on mENKs CV. In Figure 7.2.B, the holding portion of the CV was plotted linearly with time and labeled with the potential of the electrode in the range of +0.6 V to +1.2 V and to +1.0 V on the return scan for the three analytes. Plotting the data using this method enables better visualization and comparison of the oxidation peaks. The first peak is always greater in magnitude than the second. This larger peak was chosen to be the peak used for calibration and analysis. This voltammetric data shows that mENK has two distinct peaks, the former due to the oxidation of tyrosine and the latter from methionine. With tyrosine being the principle contributor in the detection of mENK, the fouling effects of tyrosine were assessed.

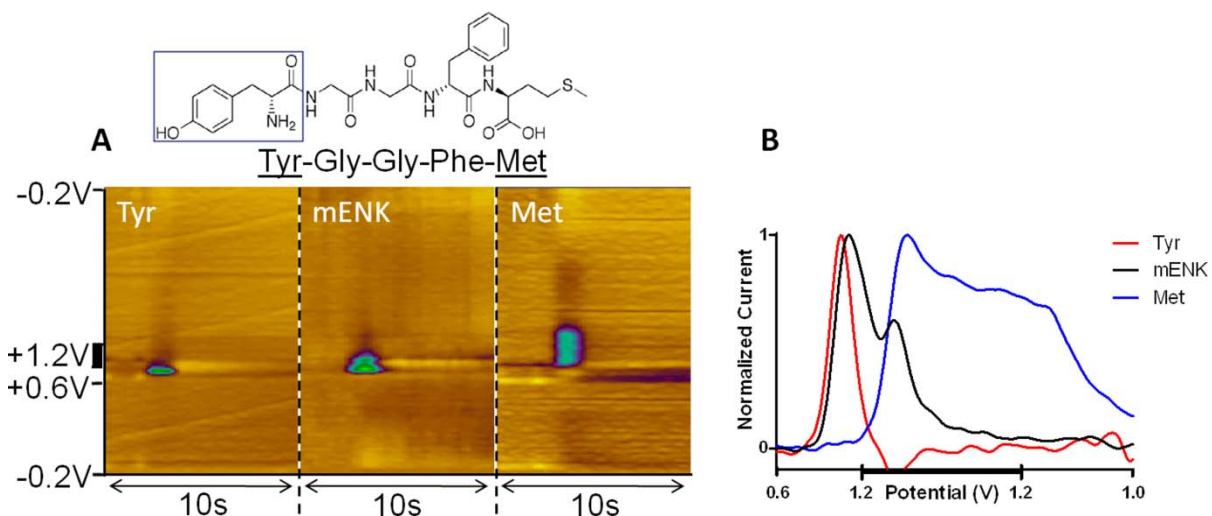


Figure 7.2 - Met-enkephalin is a five amino-acid peptide with terminating tyrosine and methionine groups (top). (A) Representative colorplots of 2 μM tyrosine (left), 1 μM mENK (center), and 30 μM methionine (right). The signal for tyrosine occurs at the same potential as the first signal for mENK. Methionine's peak occurs during the 3 msec hold of the potential and starts at a similar potential to mENK. (B) To better visualize the current response during the voltage hold, current and a portion of the potential range are plotted linearly rather than cyclically.

7.3.3 Reproducibility of Met-Enkephalin Electrochemistry

Tyrosine and tyrosine-containing peptides tend to foul the electrode surface upon oxidation. Consequently, the fouling characteristics of the MSW were compared to the more traditional TW and examined for reproducibility by introducing a 2 second bolus of 500 nM mENK onto a carbon-fiber electrode, repeated every 30 seconds for ten consecutive injections (Figure 7.3.A). The results demonstrate that after ten consecutive injections, the MSW showed no significant loss of measured current (Figure 7.3.A, red), and no change in the CV was evident (Figure 7.3.B). On the other hand, the TW showed significant deviations from baseline ($n = 5$ electrodes) after the sequence of injections (Figure 7.3.A, black), thus not providing reproducible means of detection. The results illustrate that holding the

potential at +1.2 V for 3 msec is sufficient to regenerate a clean electrode surface, suggesting that reproducible calibrations can be constructed for mENK. Interestingly, when increasing the maximum potential beyond +1.2 V, fouling of the electrode increased, thus making +1.2 V the experimental limit for which we could gather reproducible results (data not shown).

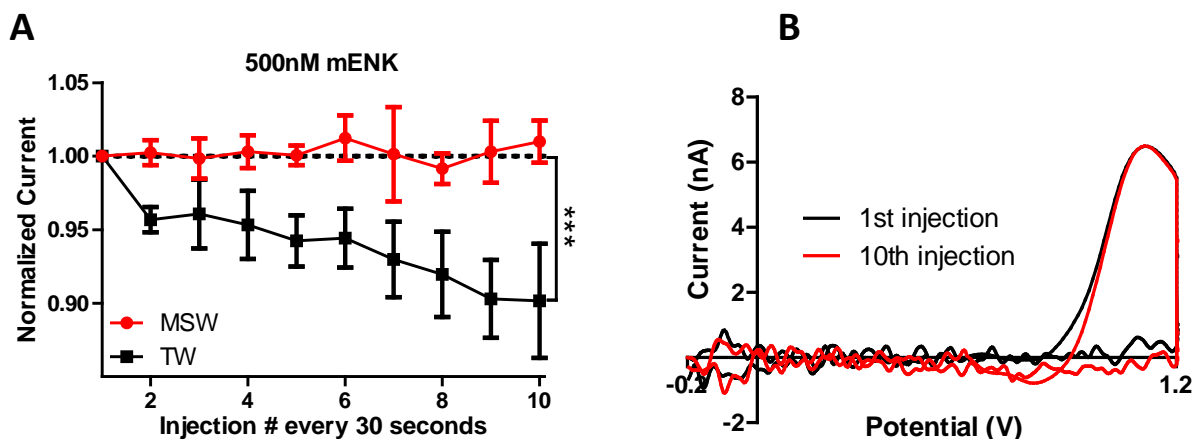


Figure 7.3 - Effects of tyrosine fouling of the electrode surface. (A) Ten consecutive injections were spaced 30 seconds apart, comparing the MSW and TW waveform performance. Peak oxidative currents were normalized to the first injections to demonstrated changes in sensitivity to analyte exposure ($n = 5$ electrodes). (B) Representative CV of a first and tenth injection using the MSW. Data shown are mean \pm SD, $n = 5$ electrodes, $p < 0.005$ for the 10th injection.

A calibration curve for mENK was created by plotting the linear relationship between peak current and concentration. Figure 7.4.A plots the peak oxidation current measured for four different concentrations of mENK ranging from 250 nM to 1000 nM ($n = 5$ electrodes, 3 injections per electrode, $r^2 = 0.99$), affording a sensitivity of $12.6 \pm 0.1 \text{ nA}\cdot\mu\text{M}^{-1}$. Representative CVs are shown in Figure 7.4.B for the various concentrations. When defining

the limit of detection as three times the standard deviation of the noise, the theoretical limit is 27.9 ± 3.5 nM. The results demonstrate that a reproducible calibration curve can be constructed for mENK, when there are no other analytes present.

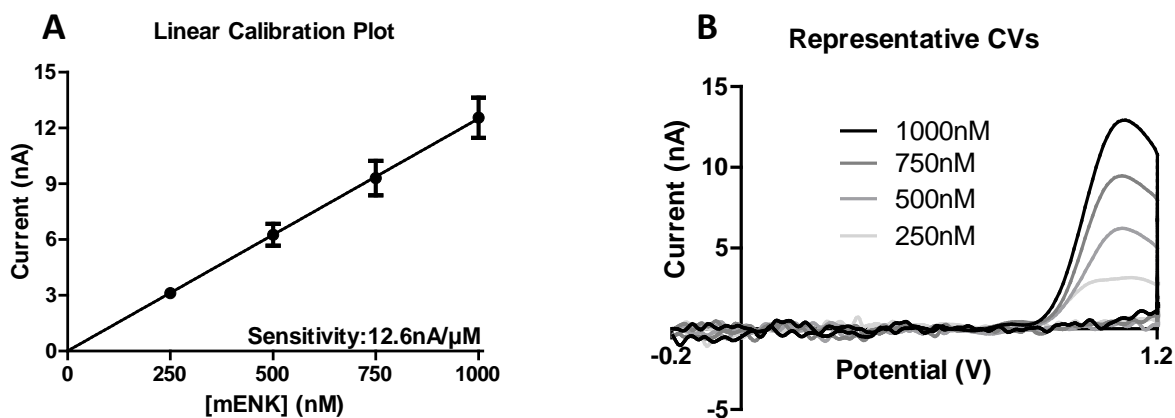


Figure 7.4 - (A) Calibration curve of mENK showing linear relationship between peak current (at +1.05 V) and concentration ($r^2 = 0.99$, $n = 5$ electrodes). (B) Representative CVs for mENK concentrations ranging from 250 to 1000 nM.

7.3.4 Selectivity Compared to Common Interferents

Since the brain is a complex matrix consisting of numerous electroactive molecules, the influence of a few interfering species commonly encountered in living brain tissue was quantitatively assessed to determine their impact on electrode selectivity and sensitivity, using principal component regression (PCR). PCR is a multivariate statistical analysis technique that first requires principal component analysis to identify the principle components that best describe the variance in the data and then uses linear regression on the selected components to deconvolute the data. Solutions containing varying concentrations of

mENK in the presence of physiological concentrations of ascorbic acid (AA), dopamine (DA), and pH shifts were tested (28-31). These common biological interferents were selected because they have a known electrochemical response in the potential window used to voltammetrically quantify mENK.

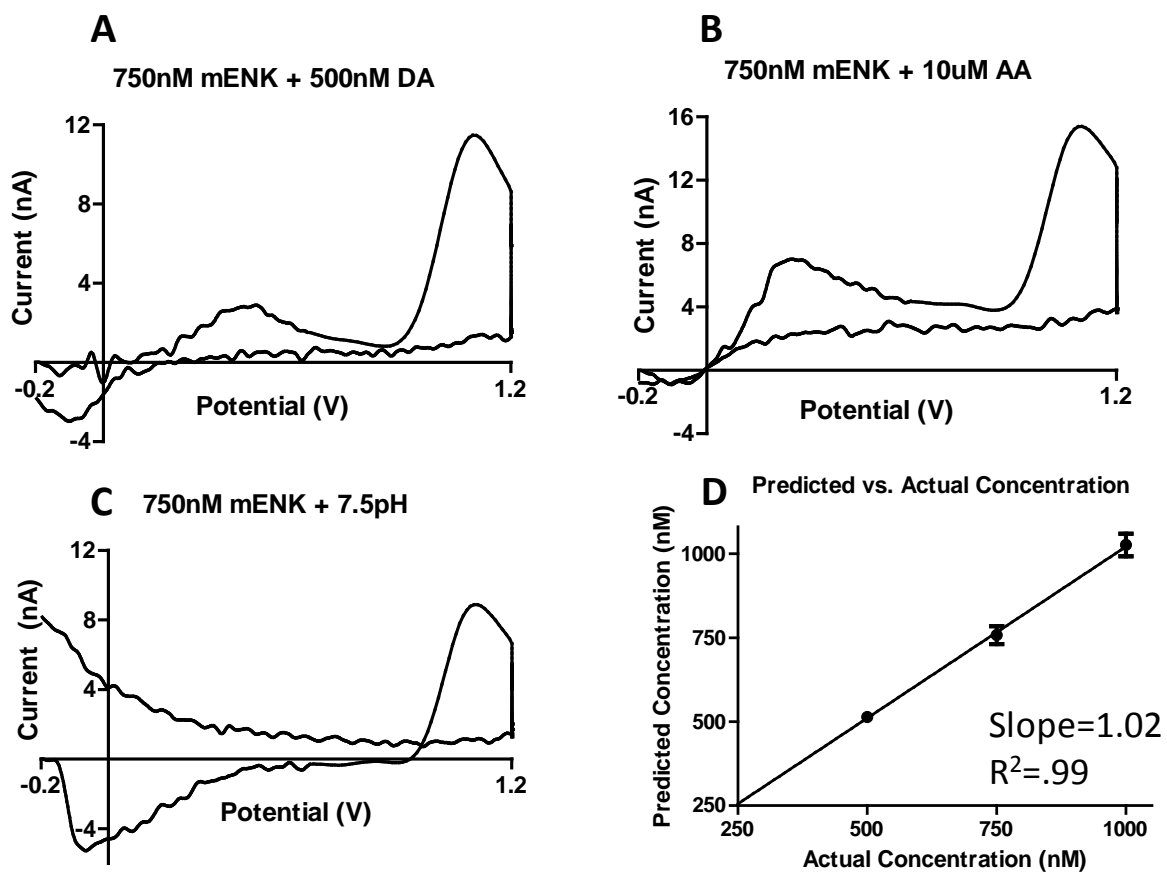


Figure 7.5 – (A-C) Selectivity and sensitivity in the presence of multiple interferents. 750 nM mENK mixed with physiologically relevant concentrations of possible interferents. (D) Predicted concentrations of ENK as evaluated by PCR compared to known sample concentrations. The diagonal line represents unity for a perfect prediction. The slope of the regressions line was 1.02 ± 0.01 ($r^2 = 0.99$, $n = 3$ electrodes).

Figure 7.5.A-C exhibits representative cyclic voltammograms for solutions containing a mixture of mENK and each electroactive interferent. Figure 5D shows the PCR-predicted concentration versus the actual concentration of mENK from mixed solutions that contained varying concentrations of mENK, AA, DA, and pH shift, where mENK was held at a constant concentration. The slope of the regression line for a perfect prediction would be unity, and our approach yielded a slope of 1.02 ± 0.01 ($r^2 = 0.99$, $n = 3$ electrodes), indicating that the combination of the waveform and PCR was able to appropriately identify and quantify mENK within a complex mixture. The results show successful separation of DA, AA, and pH shifts from mENK due to the distinct oxidation potentials of the involved species.

7.3.5 Comparing Other Tyrosine-Containing Peptides to mENK

Having demonstrated that tyrosine was the electrochemical moiety and that mENK can be quantified in the presence of common interferents, the electrochemical resolution against a few common neuropeptides was assessed. Leu-enkephalin (lENK) and mENK have the same four amino acid backbone (N-terminus) but differ in the C-terminus with a leucine or methionine group, respectively. Neurotensin is a 13-amino acid peptide containing two tyrosine groups. All three neuropeptides produced similar electrochemical responses with a principle oxidation peak at +1.05 V (Figure 7.6.A-C). Sensitivity was comparable across each of these analytes, and neurotensin showed considerably more electrode fouling than the other enkephalins, presumably due to the additional tyrosine group. Neither lENK nor NT exhibited the second peak evident in mENK. This second peak is more

obvious when viewing the CV with the change of potential plotted linearly and only focusing on the +0.6 V to +1.2 V to +1.0 V portion of the applied potential (Figure 7.6D). This observation further suggests that the second peak in mENK oxidation is due to the methionine group and provides a means of distinguishing other peptides from mENK. The results suggest that this novel waveform is appropriate for use in detecting a wide variety of tyrosine-containing compounds and can therefore be adapted for detection of other peptides in brain tissue.

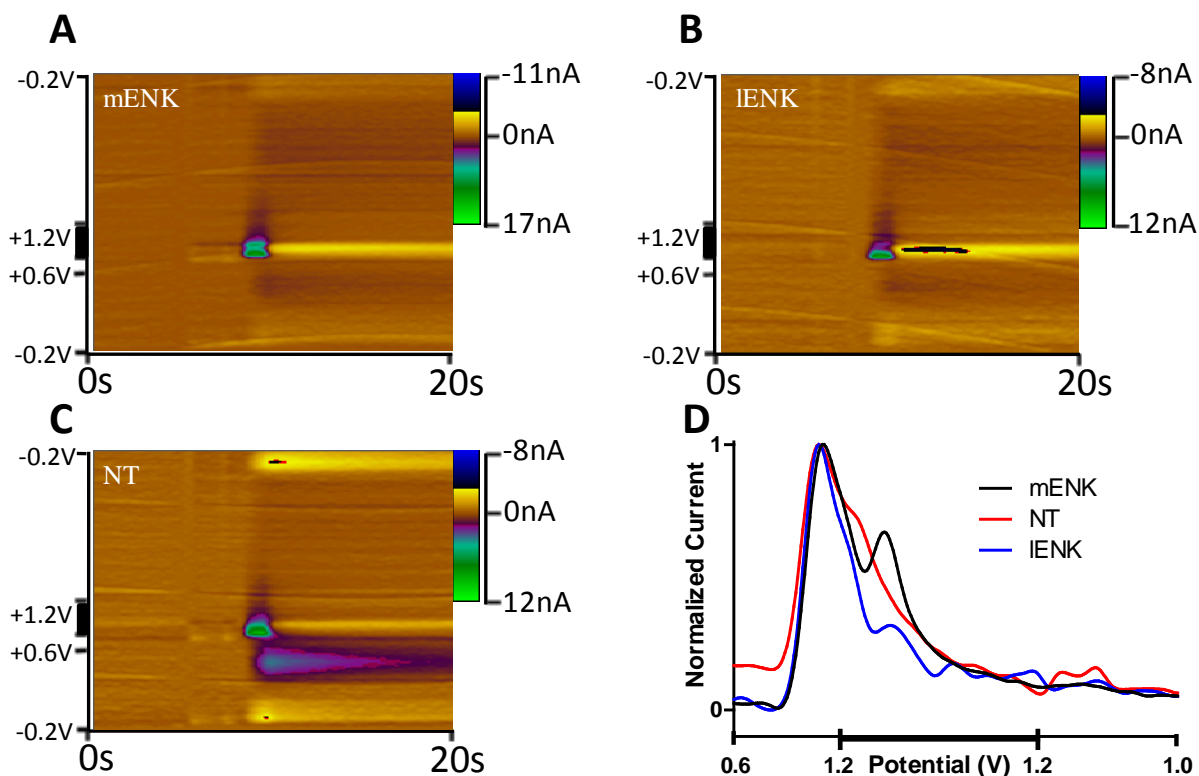


Figure 7.6 - Colorplots of 1 μ M mENK (A), 1 μ M leu-enkephalin (IENK) (B), and 1 μ M neurotensin (NT) (C). (D) Linear abbreviated CVs for the three neuropeptides demonstrating their similarities.

7.3.6 Detecting Met-Enkephalin in Living Brain Tissue

To demonstrate that the voltammetric detection of mENK is applicable in complex living tissue, CVs were collected for mENK microinfused into brain tissue slices. A carbon-fiber microelectrode was inserted at least 100 μm into a section of rat brain tissue (400 μm overall slice thickness) that encompasses the striatum, a region with nerve terminals containing mENK and the electroactive transmitter dopamine (a potential interferent). A glass micropipette containing 1 mM mENK was positioned into tissue approximately 1 mm from the working electrode. A 1 sec pressure ejection (5 psi) was used to introduce exogenous mENK into the vicinity of the carbon-fiber electrode. In Figure 7.7.A-B, representative voltammetric recordings are shown comparing the signal observed *in vitro* to that collected within tissue, respectively. The time course of the tissue data shows considerably slow clearance of the peptide within the tissue when compared to data collected with flow injection analysis. This result is expected and can be attributed to lower convection and a reduced diffusion coefficient for mENK within tissue.

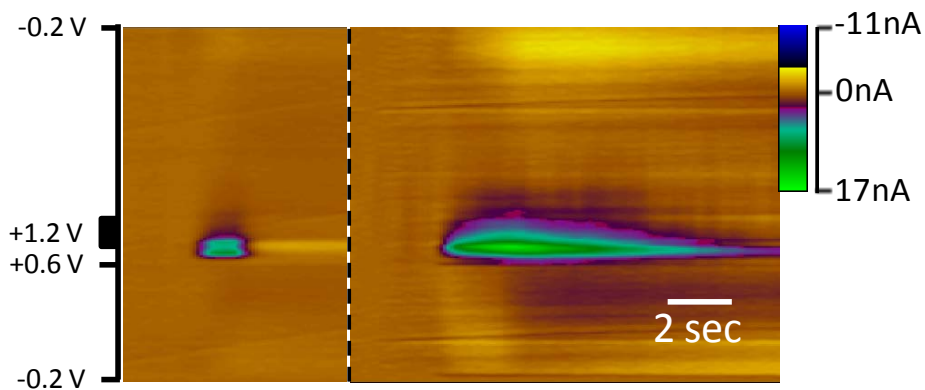


Figure 7.7 - mENK detection in rat brain slices containing the striatum. (A) A colorplot collected *in vitro*. (B) Data collected within a brain slice while 1 mM met-enkephalin was exogenously applied (1 sec injection, 1 mm distance from working electrode).

7.4 Conclusions

The analyte-specific waveform provides the necessary sensitivity, selectivity, reproducibility, and temporal resolution to make rapid, accurate and repeated measurements of mENK in complex mixtures. This detection method was extended to establish the feasibility of monitoring this peptide within living brain tissue. Though the actual limit of detection is currently below the expected concentration of mENK in brain tissue, this waveform was used to successfully measure exogenously applied mENK. In addition, it is expected that the procedures presented here can be adapted for detection of other tyrosine-containing peptides, some of which are present in higher concentrations. Therefore, this new waveform provides the necessary foundation for directly measuring opioid peptides in living tissue. This entire study will expand the capabilities of neuropeptide detection and their role in neurochemical signaling.

7.5 References

1. Cabot, P. J., Carter, L., Schafer, M., and Stein, C. (2001) Methionine-enkephalin-and Dynorphin A-release from immune cells and control of inflammatory pain, *Pain* 93, 207-212.
2. Gianoulakis, C. (2009) Endogenous Opioids and Addiction to Alcohol and other Drugs of Abuse, *Current Topics in Medicinal Chemistry* 9, 999-1015.
3. Kelley, A. E., Stinus, L., and Iversen, S. D. (1980) Interactions between D-ala-met-enkephalin, A10 dopaminergic neurones, and spontaneous behaviour in the rat, *Behav Brain Res* 1, 3-24.
4. Van Wimersma Greidanus, T. B., Maigret, C., Torn, M., Ronner, E., Van der Kracht, S., Van der Wee, N. J., and Versteeg, D. H. (1989) Dopamine D-1 and D-2 receptor agonists and antagonists and neuropeptide-induced excessive grooming, *European journal of pharmacology* 173, 227-231.
5. Herz, A. (1997) Endogenous opioid systems and alcohol addiction, *Psychopharmacology* 129, 99-111.
6. Hokfelt, T., Broberger, C., Xu, Z. Q. D., Sergeev, V., Ubink, R., and Diez, M. (2000) Neuropeptides - an overview, *Neuropharmacology* 39, 1337-1356.
7. Phillips, P. E. M., Robinson, D. L., Stuber, G. D., Carelli, R. M., and Wightman, R. M. (2003) Real-time measurements of phasic changes in extracellular dopamine concentration in freely moving rats by fast-scan cyclic voltammetry, *Methods in molecular medicine* 79, 443-464.
8. Robinson, D. L., Venton, B. J., Heien, M., and Wightman, R. M. (2003) Detecting subsecond dopamine release with fast-scan cyclic voltammetry in vivo, *Clin. Chem.* 49, 1763-1773.
9. Sanford, A. L., Morton, S. W., Whitehouse, K. L., Oara, H. M., Lugo-Morales, L. Z., Roberts, J. G., and Sombers, L. A. (2010) Voltammetric Detection of Hydrogen Peroxide at Carbon Fiber Microelectrodes, *Anal. Chem.* 82, 5205-5210.
10. Borue, X., Cooper, S., Hirsh, J., Condrón, B., and Venton, B. J. (2009) Quantitative evaluation of serotonin release and clearance in Drosophila, *J. Neurosci. Methods* 179, 300-308.
11. Swamy, B. E. K., and Venton, B. J. (2007) Subsecond detection of physiological adenosine concentrations using fast-scan cyclic voltammetry, *Anal. Chem.* 79, 744-750.

12. Park, J., Takmakov, P., and Wightman, R. M. (2011) In vivo comparison of norepinephrine and dopamine release in rat brain by simultaneous measurements with fast-scan cyclic voltammetry, *J. Neurochem.* 119, 932-944.
13. Takmakov, P., Zachek, M. K., Keithley, R. B., Bucher, E. S., McCarty, G. S., and Wightman, R. M. (2010) Characterization of Local pH Changes in Brain Using Fast-Scan Cyclic Voltammetry with Carbon Microelectrodes, *Anal. Chem.* 82, 9892-9900.
14. Marinelli, P. W., Bai, L., Quirion, R., and Gianoulakis, C. (2005) A microdialysis profile of met-enkephalin release in the rat nucleus accumbens following alcohol administration, *Alcoholism-Clinical and Experimental Research* 29, 1821-1828.
15. Lam, M., Marinelli, P., Bai, L., and Gianoulakis, C. (2008) Effects of acute ethanol on opioid peptide release in the central amygdala: an in vivo microdialysis study, *Psychopharmacology* 201, 261-271.
16. Hadjiconstantinou, M., and Neff, N. H. (2011) Nicotine and endogenous opioids: Neurochemical and pharmacological evidence, *Neuropharmacology* 60, 1209-1220.
17. Alburges, M. E., Keefe, K. A., and Hanson, G. R. (2001) Unique responses of limbic met-enkephalin systems to low and high doses of methamphetamine, *Brain Res.* 905, 120-126.
18. Kalivas, P. W., Widerlov, E., Stanley, D., Breese, G., and Prange, A. J., Jr. (1983) Enkephalin action on the mesolimbic system: a dopamine-dependent and a dopamine-independent increase in locomotor activity, *J Pharmacol Exp Ther* 227, 229-237.
19. Mabrouk, O. S., Li, Q., Song, P., and Kennedy, R. T. (2011) Microdialysis and mass spectrometric monitoring of dopamine and enkephalins in the globus pallidus reveal reciprocal interactions that regulate movement, *J. Neurochem.* 118, 24-33.
20. Shen, H., Lada, M. W., and Kennedy, R. T. (1997) Monitoring of met-enkephalin in vivo with 5-min temporal resolution using microdialysis sampling and capillary liquid chromatography with electrochemical detection, *J. Chromatogr. B* 704, 43-52.
21. Li, Q., Zubieta, J. K., and Kennedy, R. T. (2009) Practical Aspects of in Vivo Detection of Neuropeptides by Microdialysis Coupled Off-Line to Capillary LC with Multistage MS, *Anal. Chem.* 81, 2242-2250.
22. Lisi, T. L., and Sluka, K. A. (2006) A new electrochemical HPLC method for analysis of enkephalins and endomorphins, *J. Neurosci. Methods* 150, 74-79.
23. Jaquins-Gerstl, A., and Michael, A. C. (2009) Comparison of the brain penetration injury associated with microdialysis and voltammetry, *J. Neurosci. Methods* 183, 127-135.

24. Michael, D., Travis, E. R., and Wightman, R. M. (1998) Color images for fast-scan CV, *Anal. Chem.* *70*, 586A-592A.
25. Ogura, K., Kobayashi, M., Nakayama, M., and Miho, Y. (1999) In-situ FTIR studies on the electrochemical oxidation of histidine and tyrosine, *J. Electroanal. Chem.* *463*, 218-223.
26. Tan, W. T., and Goh, J. K. (2008) Electrochemical Oxidation of Methionine Mediated by a Fullerene-C(60) Modified Gold Electrode, *Electroanalysis* *20*, 2447-2453.
27. Harriman, A. (1987) Further Comments on the Redox Potentials of Tryptophan and Tyrosine, *J Phys Chem-US* *91*, 6102-6104.
28. Kulagina, N. V., Shankar, L., and Michael, A. C. (1999) Monitoring glutamate and ascorbate in the extracellular space of grain tissue with electrochemical microsensors, *Anal. Chem.* *71*, 5093-5100.
29. Venton, B. J., Michael, D. J., and Wightman, R. M. (2003) Correlation of local changes in extracellular oxygen and pH that accompany dopaminergic terminal activity in the rat caudate-putamen, *J. Neurochem.* *84*, 373-381.
30. Cheer, J. F., Wassum, K. M., and Wightman, R. M. (2006) Cannabinoid modulation of electrically evoked pH and oxygen transients in the nucleus accumbens of awake rats, *J. Neurochem.* *97*, 1145-1154.
31. Gonon, F., Buda, M., Cespuoglio, R., Jouvet, M., and Pujol, J. F. (1980) In vivo electrochemical detection of catechols in the neostriatum of anaesthetized rats: dopamine or DOPAC?, *Nature* *286*, 902-904.

CHAPTER 8

Eliminating Standard Electrode Calibration with a Novel Approach to Accurately Quantify *in vivo* Voltammetric Data

This work was completed in collaboration with: Vincent Toups, Eyob Eyualem, Gregory McCarty, and Leslie A. Sombers, and is in preparation for submission to the journal Analytical Chemistry.

8.1 Introduction

Over the past few decades, background-subtracted fast-scan cyclic voltammetry (FSCV) has been coupled with carbon-fiber microelectrodes to monitor chemical fluctuations in living tissue, with high spatiotemporal resolution (1). This method combines sensitivity, selectivity, and real-time measurements of electroactive molecules in discrete brain locations. When used in freely-moving animals and coupled with specific behavioral challenges, it has provided unprecedented information about the molecular mechanism underlying specific motivated behavior, significantly advancing studies focused on reward, drug abuse, and addiction (2).

To monitor dopamine release events, a triangular waveform is applied to the working electrode, at a scan rate of $400 \text{ V}\cdot\text{s}^{-1}$ and voltammograms are collected at a frequency of 10 Hz. The kinetics of dopamine events evoked by electrical stimulation, pharmacological manipulation, or external stimulation can be observed and quantified (3).

After collecting *in vivo* data, the electrode must be calibrated in a flow-injection system to quantitatively relate current to analyte concentration. This calibration scheme

assumes that a buffered electrolyte used *ex vivo* is comparable to the environment of living tissue, and that the electrode surface was not altered when removed from tissue. Importantly, if the electrode was damaged during removal, post-calibration is precluded. Additionally, the tip of a carbon-fiber microelectrode is too small to leave a track in the tissue, requiring that the electrode be used to lesion the recording site. This verifies the data collection site in the tissue, but requires that high currents are passed through the carbon electrode to create the lesion, which destroys the electrode and prevents post-calibration. Attempts have been made to generalize electrode sensitivity, but electrode variability brings about much error. FSCV has recently been used in human studies (4, 5); however, quantitation of the data was done using average calibration factors, because pre-calibration was prohibited by experimental protocol that requires sterilization of the electrode before implantation. Additionally, post-calibration was abandoned because the electrode is considered medical waste. Expanding FSCV to studies that use chronically-implanted electrodes or work in humans requires a novel method to quantitate the fluctuations measured in the *in vivo* environment without pre/post-calibration of the electrode is required.

We present a quantitative method that uses the inherent non-faradaic charging current and characteristics of the applied waveform as predictors of electrode sensitivity. In FSCV, the high scan rate generates a large capacitive current, which is significantly larger than faradaic currents resulting from redox processes at the microelectrode surface. These background currents are stable over tens of seconds (6), allowing background subtraction to reveal the interesting rapid faradaic responses. Since it is known that charging current is in part a function of electrode surface area and scan rate, and that faradaic current is in part a

function of surface area and analyte concentration (7), we sought to use the background current collected during a typical experiment to define the sensitivity of the electrode to a particular analyte.

This research shows that the total current of the background was proportional to the electrode size and could be used to generate a model predicting the sensitivity of the electrode to dopamine. Finally, the calibration factor obtained with this model were compared with factors obtained using the traditional calibration procedure and both demonstrated equal powers of predictability. This novel and facile method of data interpretation will allow researchers to obtain precise quantitative measurement without a post-calibration, once a proper intra-laboratory training set is established.

8.2 Materials and Methods

8.2.1 Chemicals

All chemicals were purchased from Sigma-Aldrich Co., (St. Louis, MO) unless otherwise specified and used without additional processing. All electrochemical experiments were done in physiological pH 7.4 buffer solution (15 mM Tris, 3.25 mM KCl, 1.20 mM CaCl₂, 1.2 mM MgCl₂, 2 mM Na₂SO₄, 1.25 mM NaH₂PO₄, 145 mM NaCl). All aqueous solutions were made using double-deionized water (Millipore, Billerica, MA).

8.2.2 Electrode Fabrication

Carbon-fiber cylindrical microelectrodes were fabricated using T-650 carbon fibers (Cytec Industries, Inc., Woodland Park, NJ) as previously described (8). In brief, a single

carbon fiber was inserted into a glass capillary tube (A-M Systems, Sequim, WA), sealed with a micropipette puller (Narishige, Tokyo, Japan), and cut to the desired length of 100 μm . A Ag/AgCl pellet reference electrode was employed (World Precision Instruments, Inc., Sarasota, FL) to complete the two electrode electrochemical cell.

8.2.3 Flow-Injection System

A syringe pump (New Era Pump Systems, Wantagh, NY) supplied a continuous buffer flow of 1 $\text{mL}\cdot\text{min}^{-1}$ across the working and reference electrodes. The working electrode was positioned in a custom electrochemical cell using a micromanipulator (World Precision Instruments, Sarasota, FL). Two second bolus injections of analyte to the microelectrode surface were accomplished with a six-port HPLC valve mounted on a two-position air actuator controlled by a digital pneumatic solenoid valve (Valco Instruments, Houston TX). The entire apparatus was housed within a custom-built grounded Faraday cage. All experiments were performed at room temperature.

8.2.4 Data Acquisition

All data was collected in a custom flow-injection system unless otherwise specified. In most experiments, a triangular waveform ranging from -0.4 to +1.3 V with a holding potential of -0.4 V versus Ag/AgCl was applied at a scan rate of 400 $\text{V}\cdot\text{s}^{-1}$ and at a frequency of 10 Hz using a custom built instrument for potential application to the electrochemical cell and for current transduction (University of North Carolina at Chapel Hill, Department of Chemistry, Electronics Facility). Some experiments investigated various wavelimits (+1.0,

1.1, 1.2, 1.3, and 1.4 V). TH-1 software (ESA, Chelmsford, MA) was used for waveform output and data analysis, along with data acquisition cards (National Instruments, Austin, TX) used for measuring currents and synchronization of the electrochemical experiment. Signal processing including background subtraction and signal averaging, and analog filtering was accomplished with a 2-pole Sallen-Key, low-pass filtered at 2 KHz. There was no digital filtering of the data.

8.2.5 Traditional Electrode Calibration

All calibration data was collected with the flow-injection system. A minimum of three different concentrations of analyte within the electrode's linear range were analyzed. These were as follows: dopamine (0.50, 0.75, 1.0 μM), hydrogen peroxide (250, 500, 1000 μM), ascorbic acid (50, 100, 200 μM), pH shift (+0.1, +0.2, +0.3, relative to pH 7.4). Peak currents were plotted versus concentration and the fitted slope was used as a calibration factor for predicting the *in vivo* concentration. When multiple waveforms were used on a single electrode, the applied waveform started with the lowest switching potential and ended with the highest. Pre-calibration was accomplished by performing an electrode calibration before the electrode was implanted within brain tissue. Post-calibration was defined as calibrating the electrode after it was removed from tissue, rinsed in deionized water, and soaked in isopropyl alcohol overnight.

8.2.6 Anesthetized Animal Experiments

Male Sprague-Dawley rats (n = 3, 250 - 300 g, Charles River Laboratories, Raleigh, NC) were urethane anesthetized ($4 \cdot \text{g kg}^{-1}$ intraperitoneally), placed in a stereotaxic frame (David Kopf Instruments, Tujunga, CA), and holes for electrodes were drilled in the skull precisely using stereotaxic coordinates (working electrode was placed +1.2 mm anterior-posterior and +3.0 mm medial-lateral relative to bregma, and the Ag/AgCl reference electrode was placed in the contralateral forebrain). The working electrode (positioned above the caudate putamen) was lowered to -5 mm relative to bregma. The animal's body temperature was maintained at 37 °C by a heating pad. Once the working electrode was lowered into position, the detection waveform was applied for 1 hour to obtain stable data collection. Animal care was in accordance with North Carolina State University Institutional Animal Care and Use Committee (IACUC) guidelines.

8.2.7 Statistics

Data are presented as the mean \pm standard deviation. One-way ANOVA with Tukey-Kramer post-test was used to compare significance between multiple groups. Statistical and graphical analysis was carried out using MATLAB, R2008a (The MathWorks, Natick, MA) and GraphPad Prism 5 (GraphPad Software, Inc., La Jolla, CA).

8.3 Results and Discussion

8.3.1 Electrochemical Properties and Sensitivity

To ascertain the affects of the applied waveform on electrode sensitivity and total background current, we tested 5 cyclic waveforms that differ only by switching potential. These chosen waveforms span a range that has traditionally been used to monitor dopamine fluctuations in living tissue (8, 9). All of the applied cyclic waveforms start at a holding potential of -0.4 V and ramp at $400\text{ V}\cdot\text{s}^{-1}$ to the switching potential and return to the holding potential at the same rate (Figure 8.1.A). This ramping is repeated at a frequency of 10 Hz ,

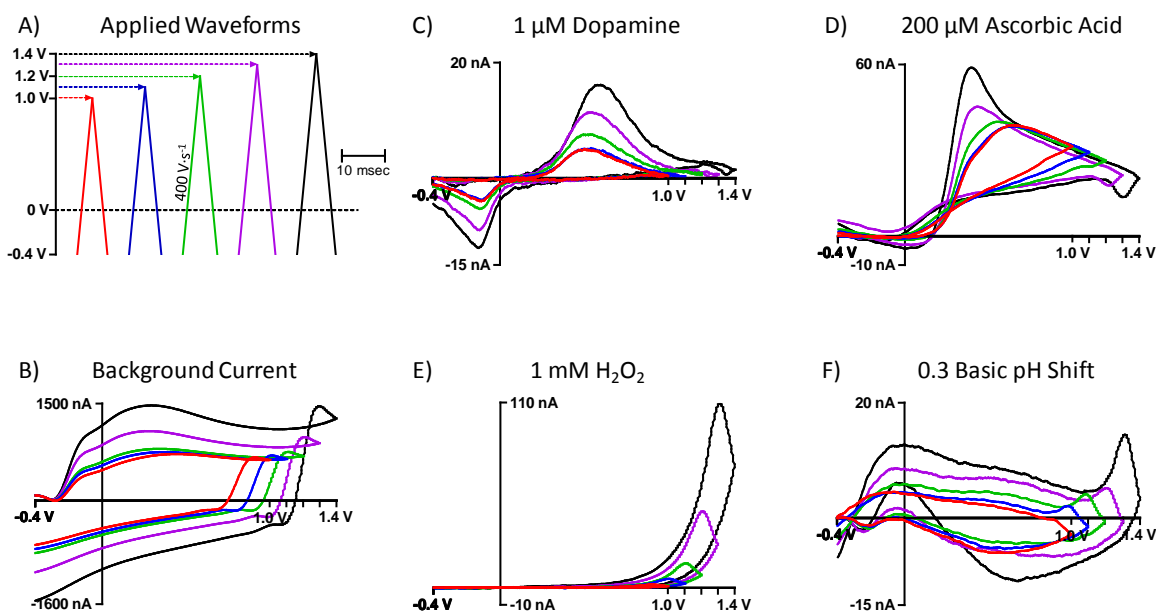


Figure 8.1 - Background-subtracted fast-scan cyclic voltammetry. (A) Five different waveforms were applied to each electrode. (B) Representative voltammograms resulting from waveform application to a carbon-fiber microelectrode. Representative background-subtracted voltammograms, collected at multiple waveforms for $1\text{ }\mu\text{M}$ dopamine (C), $200\text{ }\mu\text{M}$ ascorbic acid (D), $1\text{ mM H}_2\text{O}_2$ (E), and a basic pH shift to 7.7 (F).

so voltammograms take ≤ 9 ms to record and collection occurs every 100 ms ec. There was a two percent difference (2 msec) in the duration of the holding potential between the waveforms that had a 1.0 and a 1.4 V switching potential. Any differences in electrode sensitivity were not attributed to this minor deviation in holding time (10, 11). The method of background subtraction typically averages 10 consecutive voltammograms collected in a chemically quiet portion of the data to represent a baseline of the corpus of data and subtracts this baseline from all collected data. This approach effectively removes all current contributions from double-layer capacitance and redox processes inherent to the electrode surface. The power of the technique rests on the detection of rapid fluctuations in analyte concentration and subtracting out information on stable analytes that are often considered interferences.

Representative voltammograms of the background current are shown in Figure 8.1.B. As the switching potential increases, the amplitude of the background current also increases across all potentials. When the sum of the absolute value of all currents in the background voltammogram is plotted versus the switching potential, a non-linear relationship is evident, whereby total current increases by a second degree polynomial with respect to the switching potential (Figure 8.2). This illustrates that the total background current changes in a predictable manner, thus enabling it to be used in estimating electrode sensitivity.

Background-subtracted FSCV has also been utilized to quantitate rapid concentration fluctuations of many analytes within the complex environment that is biological tissue, including dopamine, hydrogen peroxide (H_2O_2), ascorbic acid, and pH shifts (8, 12-14). For instance, Figure 8.1.C-F shows representative background-subtracted voltammograms for all

wavelimits investigated at a single concentration of each of these analytes collected used in this study. Similar to non-faradaic background current, as the switching potential increases, peak faradaic current for the analytes also increases. This phenomenon is a factor of surface chemistry. As the anodic limit is increased, the oxygen-containing functional groups are formed on the graphitic-carbon surface, effectively increasing electrode sensitivity (15).

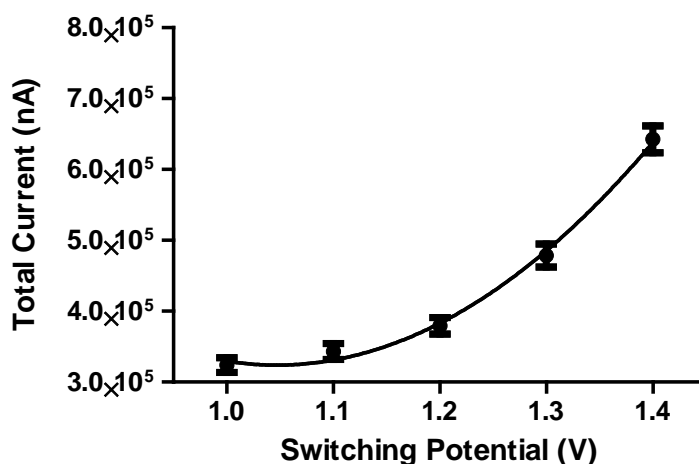


Figure 8.2 - Total background current plotted against the switching potential of the applied waveform. Total current was determined by summation of the absolute value of all currents within the voltammogram and exhibited a non-linear relationship with the switching potential ($n = 10$ electrodes).

In order to correlate the measured current to a concentration, electrode calibration is necessary. Traditionally, calibrations are performed by exposing known concentrations of analyte to the electrochemical sensor, collecting voltammograms, and extracting peak current from the background-subtracted voltammograms. This peak current is then plotted versus analyte concentration and the slope of a fitted line determines the sensitivity of the carbon electrode. In turn, the calculated slope can be used to predict analyte concentration from

peak currents extracted from unknown voltammograms. Many studies use multivariate statistical analysis, such as principle component regression, to extract analyte information from the experimental voltammograms. This procedure enables multiple species to be deconvoluted once a proper training set has been established (16). In Figure 8.3, data was collected with this calibration method for all five waveforms, for the analytes dopamine (Figure 8.3.A), ascorbic acid (Figure 8.3.B), H_2O_2 (Figure 8.3.C), and basic pH shift (Figure 8.3.D). All analytes exhibited linearity within the given concentration range and across all applied waveforms. It should be noted that for most analytes there were only slight differences in electrode sensitivity using the 1.0 and 1.1 wavelimits, but as the wavelimit increased there were marked increases in sensitivity. As such, plotting the traditionally calculated sensitivity versus the applied waveform switching potential resulted in a non-linear relationship (Figure 8.4), reminiscent of Figure 8.2.

Since both sensitivity and total background current increased as the switching potential increased, sensitivity was plotted versus total background current to determine if there was a linear correlation. Figure 8.5 plots analyte sensitivity versus background current, where ten electrodes tested at five different waveforms resulted in 50 data points. A line was fitted through the cluster and the correlation coefficient was inset within each panel. A linear relationship was evident.

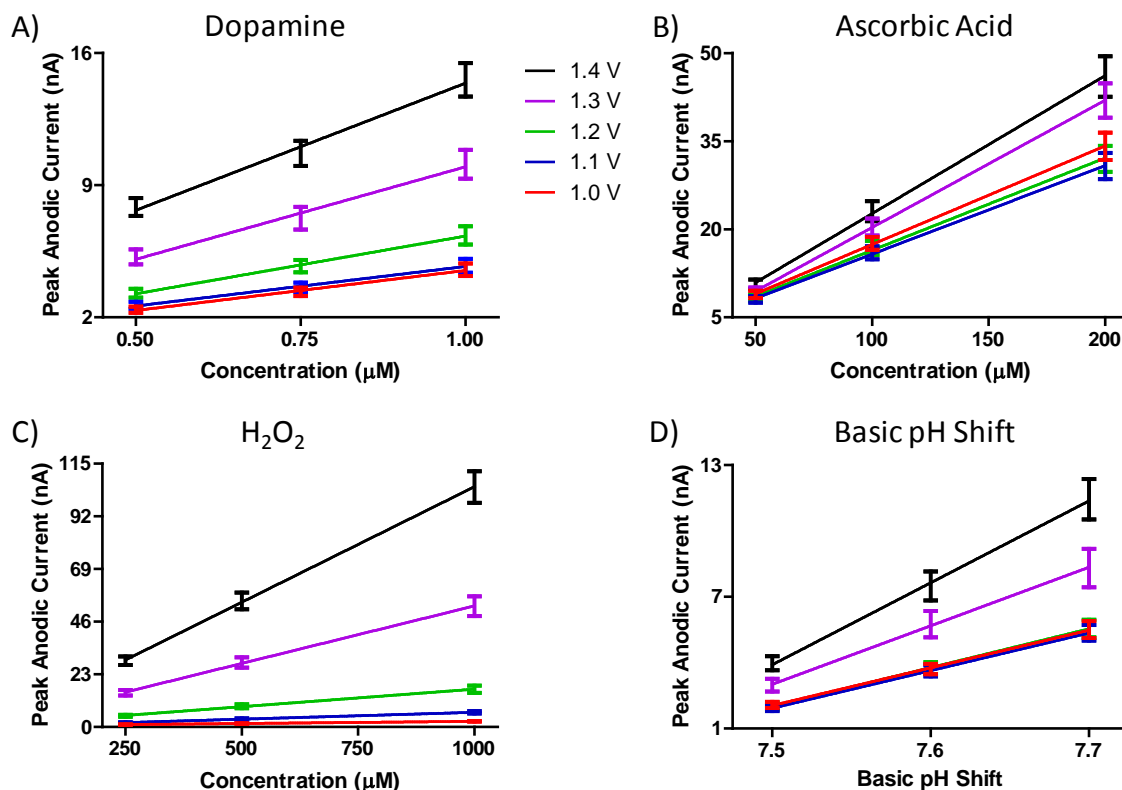


Figure 8.3 - Traditional method of determining electrode sensitivity. Peak current was plotted versus analyte concentration, for all applied waveforms. A linear relationship was found for dopamine (A), ascorbic acid (B), H_2O_2 (C), and basic pH shifts (D), where the slope of the fitted line represents the sensitivity of the electrode at a particular applied waveform ($n = 10$ electrodes).

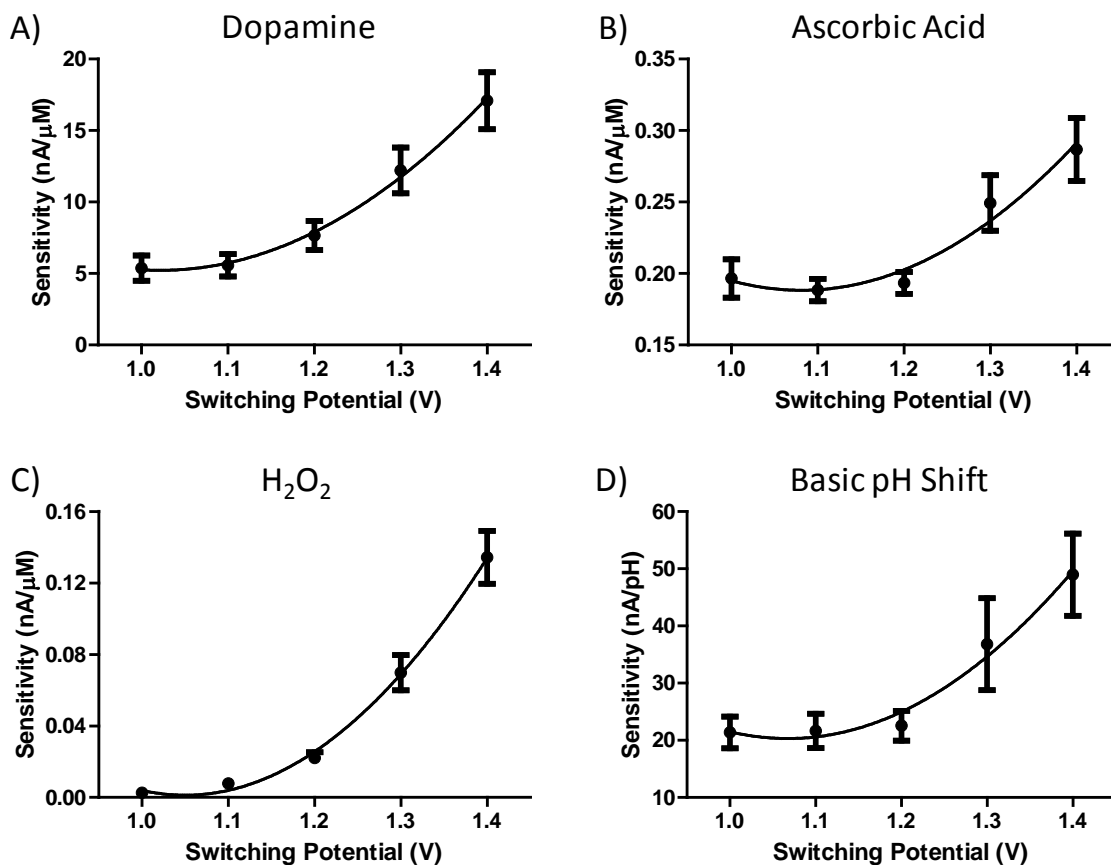


Figure 8.4 - Electrode sensitivity plotted against the switching potential of the applied waveform. Sensitivity was determined by the traditional calibration method and exhibited a non-linear relationship with switching potential for dopamine (A), ascorbic acid (B), H₂O₂ (C), and basic pH shifts (D). (n = 10 electrodes)

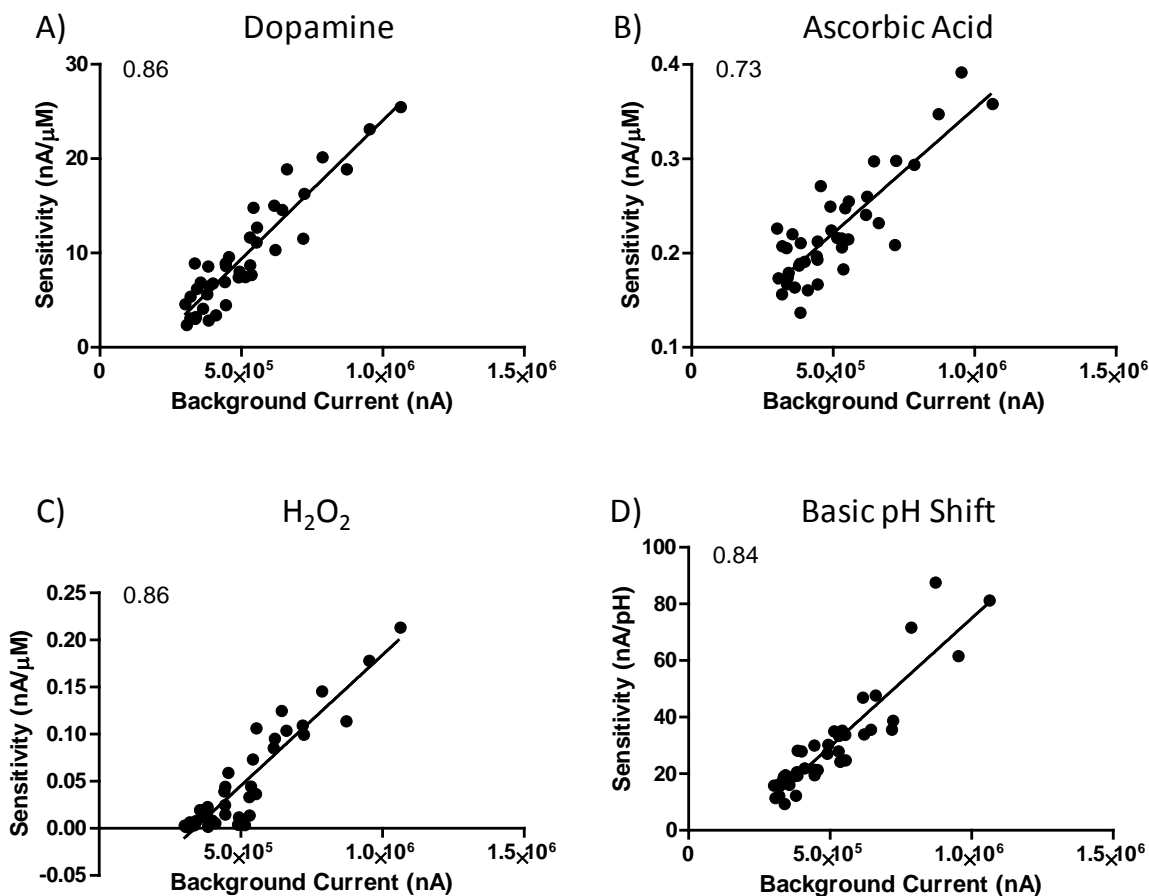


Figure 8.5 - Electrode sensitivity plotted against the total background current for each waveform. Sensitivity was determined by the traditional calibration method and exhibited a linear relationship with background current for dopamine (A), ascorbic acid (B), H_2O_2 (C), and basic pH shifts (D). Correlation coefficients for each fitted line are inset within the respective panel ($n = 10$ electrodes).

8.3.2 Calibration Model

Since it was found that background current alone did not capture all of the variability and the waveform limit exhibited a stable non-linear relationship with sensitivity, the data were fit to the following model to predict electrode sensitivity:

$$\text{Sensitivity} = \alpha C + \beta S + \gamma S^2 + \delta \quad (1)$$

$$\sum_i^{\text{electrode}} ((\alpha C_i + \beta S_i + \gamma S_i^2 + \delta_i) - \text{Sensitivity}_i)^2 = 0 \quad (2)$$

where electrode sensitivity for a given analyte is a function of both total background current (C) and the switching potential (S). Multiple linear regression was used to solve for electrode sensitivity, by determining the coefficients α , β , γ , and δ , minimized with Equation 2. The calculated values for these regression coefficients are listed in Table 8.1.

Table 8.1 - Coefficients determined by multiple linear regression on Equation 1 for the training set (n = 10 electrodes).

Coefficients	Dopamine	Ascorbic Acid	H ₂ O ₂	pH
α	-0.0829	2.55x10 ⁻⁵	-0.122	7.79
β	0.438	2.55x10 ⁻⁷	-0.589	0.248
γ	0.604	1.62x10 ⁻⁷	-1.26	0.598
δ	-0.825	1.10x10 ⁻⁴	128.0	-66.7

This model was used to determine the sensitivity of ten electrodes, for all analytes, and across all waveforms. This predicted sensitivity was then plotted versus the sensitivity determined by the traditional calibration method (Figure 8.6). The slope of linear regression is inset within each corresponding panel, where a slope of 1.0 would demonstrate a perfect match between our background calibration and the traditional method. The extent of electrode sensitivity should be noted for all analytes. This further demonstrates the futility of assuming an average electrode sensitivity to equate currents collected *in vivo* to detected concentration.

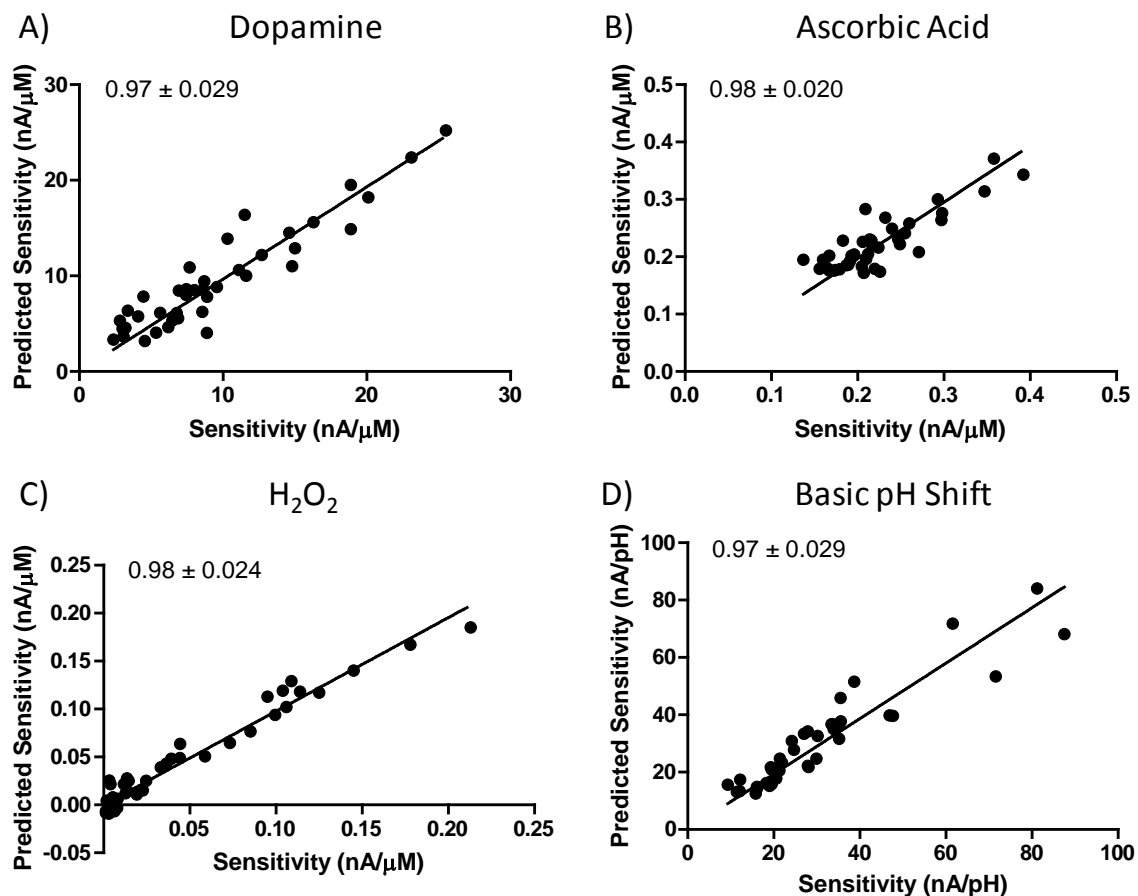


Figure 8.6 - Predicted electrode sensitivity plotted against electrode sensitivity. Predicted sensitivity was found by utilizing Equation 1 and sensitivity was determined by the traditional calibration method. Fitting a line through the data points gave a slope at unity for dopamine (A), ascorbic acid (B), H₂O₂ (C), and basic pH shifts (D), demonstrating the validity of the model. Actual slopes for each fitted line are inset within the respective panel (n = 10 electrodes).

8.3.3 Testing the Model

Since the intention of this research is to eliminate traditional calibration methods to afford researchers more experimental flexibility and safeguard data, we sought to evaluate the effectiveness of this prediction model by testing the method in comparison to the

traditional methods for data collection within living tissue. For this experiment, dopamine sensitivity was assessed before the electrode was implanted in brain tissue (pre-calibration) and then after removal (post-calibration). Dopamine calibrations were performed by traditional means using concentrations ranging from 250 to 1000 nM, and applying a 400 $\text{V}\cdot\text{s}^{-1}$, -0.4 V to +1.3 V cyclic waveform. An electrode was pre-calibrated in a flow-injection system. This pre-calibrated electrode was then immediately lowered into the dorsal striatum, a brain region rich in dopaminergic terminals. After the electrode exhibited a stable electrochemical response in brain tissue, voltammograms were collected and this data was used with the prediction model to determine electrode sensitivity. The electrode was then removed from the animal and stored in isopropyl alcohol overnight, following traditional protocol (17, 18). The following day, post-calibration of the electrode was performed.

Electrode sensitivity was calculated using Equation 1, along with the coefficients of α , β , γ , and δ for the dopamine calibration model, and the characteristics of the background current collected while the electrode was inside living tissue. This approach is compared with the traditional pre- and post-calibration methods, and is shown in Figure 8.7, pre-calibration sensitivity ($13.74 \pm 1.07 \text{ nA}\cdot\mu\text{M}^{-1}$) was significantly greater than either post-calibration sensitivity ($9.659 \pm 1.287 \text{ nA}\cdot\mu\text{M}^{-1}$) or that predicted utilizing our model ($9.248 \pm 0.774 \text{ nA}\cdot\mu\text{M}^{-1}$). These results are consistent with previous findings of decreased electrode sensitivity after tissue exposure (19). Importantly, there was no significant difference between the sensitivity calculated using the traditional post-calibration method and the model presented herein, verifying the efficacy of this approach.

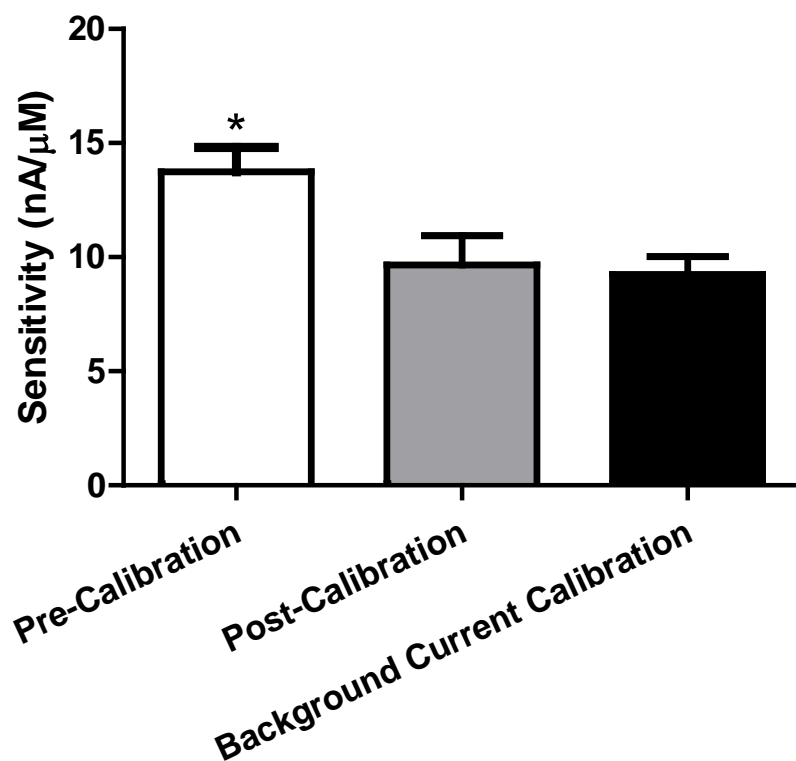


Figure 8.7 - Comparison of electrode calibration methods. Sensitivity was determined by the traditional calibration method before implantation (pre-calibration), after implantation (post-calibration), and using background voltammograms collecting in tissue along with Equation 1 (background current calibration). Pre-calibration was the only method found to be significantly different ($p = 0.011$, one-way ANOVA, Tukey-Kramer test, $n = 18$ electrodes). -0.4 V to $+1.3$ V at 400 $\text{V}\cdot\text{s}^{-1}$ waveform was applied.

It should be noted that this model is not only a means to obtain a calibration factor after the experiment. Simply using a calibration factor after the experiment assumes an average sensitivity of the sensor during the course of an experiment, which is inaccurate as the electrode may lose sensitivity during the course of an *in vivo* experiment. The power of the model lies in the fact that the electrode can be calibrated at any point during the

experiment, to determine the real-time sensitivity of the electrode, to accurately relate current to analyte concentration. Furthermore, it is important to accurately quantitate neurotransmitter concentration, rather than relying on an approximate value, as the D₁ thru D₅ dopamine receptor subtypes bind dopamine with various affinities ranging from nanomolar to micromolar concentrations (20, 21). The amount of dopamine in the extracellular space will determine which receptor subtypes will be activated, and thus the functional effects of the dopamine release.

8.4 Conclusions

We describe a model that uses the background current and switching potential to accurately predict electrode sensitivity, eliminating the need for traditional post-calibration procedures. This tool will be particularly valuable in cases where calibration is difficult, such as following human studies, when lesioning is required to mark the recording site, and in research that implements chronically-implanted electrodes that cannot be removed. This research fills a critical need in electrode calibration to allow researchers more freedom in experimental design. Furthermore this calibration method will permit real-time electrode calibration to enable accurate quantification of dopamine concentrations monitored in tissue, which is necessary to make correct descriptions about the molecular mechanisms underlying behavior.

8.5 References

1. Stamford, J. A., Kruk, Z. L., Millar, J., and Wightman, R. M. (1984) Striatal dopamine uptake in the rat: in vivo analysis by fast cyclic voltammetry, *Neurosci Lett* 51, 133-138.
2. Rebec, G. V., Christensen, J. R., Guerra, C., and Bardo, M. T. (1997) Regional and temporal differences in real-time dopamine efflux in the nucleus accumbens during free-choice novelty, *Brain Res* 776, 61-67.
3. Sombers, L. A., Beyene, M., Carelli, R. M., and Wightman, R. M. (2009) Synaptic overflow of dopamine in the nucleus accumbens arises from neuronal activity in the ventral tegmental area, *Journal of Neuroscience* 29, 1735-1742.
4. Chang, S. Y., Kim, I., Marsh, M. P., Jang, D. P., Hwang, S. C., Van Gompel, J. J., Goerss, S. J., Kimble, C. J., Bennet, K. E., Garris, P. A., Blaha, C. D., and Lee, K. H. (2012) Wireless fast-scan cyclic voltammetry to monitor adenosine in patients with essential tremor during deep brain stimulation, *Mayo Clin Proc* 87, 760-765.
5. Kishida, K. T., Sandberg, S. G., Lohrenz, T., Comair, Y. G., Saez, I., Phillips, P. E., and Montague, P. R. (2011) Sub-second dopamine detection in human striatum, *PLoS One* 6, e23291.
6. Heien, M. L., Khan, A. S., Ariansen, J. L., Cheer, J. F., Phillips, P. E., Wassum, K. M., and Wightman, R. M. (2005) Real-time measurement of dopamine fluctuations after cocaine in the brain of behaving rats, *Proc Natl Acad Sci U S A* 102, 10023-10028.
7. Bard, A. J., and Faulkner, L. R. (2001) *Electrochemical Methods: Fundamentals and Applications*, 2nd ed., John Wiley, New York.
8. Sanford, A. L., Morton, S. W., Whitehouse, K. L., Oara, H. M., Lugo-Morales, L. Z., Roberts, J. G., and Sombers, L. A. (2010) Voltammetric Detection of Hydrogen Peroxide at Carbon Fiber Microelectrodes, *Analytical Chemistry* 82, 5205-5210.
9. Garris, P. A., and Wightman, R. M. (1994) In vivo voltammetric measurement of evoked extracellular dopamine in the rat basolateral amygdaloid nucleus, *J Physiol* 478 (Pt 2), 239-249.
10. Bath, B. D., Michael, D. J., Trafton, B. J., Joseph, J. D., Runnels, P. L., and Wightman, R. M. (2000) Subsecond adsorption and desorption of dopamine at carbon-fiber microelectrodes, *Analytical Chemistry* 72, 5994-6002.

11. Kile, B. M., Walsh, P. L., McElligott, Z. A., Bucher, E. S., Guillot, T. S., Salahpour, A., Caron, M. G., and Wightman, R. M. (2012) Optimizing the Temporal Resolution of Fast-Scan Cyclic Voltammetry, *ACS Chem Neurosci* 3, 285-292.
12. Takmakov, P., Zacek, M. K., Keithley, R. B., Bucher, E. S., McCarty, G. S., and Wightman, R. M. (2010) Characterization of local pH changes in brain using fast-scan cyclic voltammetry with carbon microelectrodes, *Anal Chem* 82, 9892-9900.
13. Wilson, R. L., Kamata, K., Bigelow, J. C., Rebec, G. V., and Wightman, R. M. (1986) Crus cerebri lesions abolish amphetamine-induced ascorbate release in the rat neostriatum, *Brain Res* 370, 393-396.
14. Ariansen, J. L., Heien, M. L., Hermans, A., Phillips, P. E., Hernadi, I., Bermudez, M. A., Schultz, W., and Wightman, R. M. (2012) Monitoring extracellular pH, oxygen, and dopamine during reward delivery in the striatum of primates, *Front Behav Neurosci* 6, 36.
15. Roberts, J. G., Moody, B. P., McCarty, G. S., and Sombers, L. A. (2010) Specific Oxygen-Containing Functional Groups on the Carbon Surface Underlie an Enhanced Sensitivity to Dopamine at Electrochemically Pretreated Carbon Fiber Microelectrodes, *Langmuir* 26, 9116-9122.
16. Keithley, R. B., and Wightman, R. M. (2011) Assessing principal component regression prediction of neurochemicals detected with fast-scan cyclic voltammetry, *ACS Chem Neurosci* 2, 514-525.
17. Robinson, D. L., and Wightman, R. M. (2007) *Rapid Dopamine Release in Freely Moving Rats*, CRC Press, Boca Raton
18. Roberts, J. G., Lugo-Morales, L. Z., Loziuk, P. L., and Sombers, L. A. (2013) Real-time chemical measurements of dopamine release in the brain, *Methods Mol Biol* 964, 275-294.
19. Logman, M. J., Budygin, E. A., Gainetdinov, R. R., and Wightman, R. M. (2000) Quantitation of in vivo measurements with carbon fiber microelectrodes, *J Neurosci Methods* 95, 95-102.
20. Beaulieu, J. M., and Gainetdinov, R. R. (2011) The Physiology, Signaling, and Pharmacology of Dopamine Receptors, *Pharmacol Rev* 63, 182-217.
21. Missale, C., Nash, S. R., Robinson, S. W., Jaber, M., and Caron, M. G. (1998) Dopamine receptors: from structure to function, *Physiol Rev* 78, 189-225.

CHAPTER 9

Trace Metal Complexation by the Triscatecholate Siderophore protochelin: Structure and Stability

The following work was reprinted with kind permission from Springer Science and Business Media: James M. Harrington, John Barger, Andrzej A. Jarzecki, James G. Roberts, Leslie A. Sombers, and Owen W. Duckworth, *Biometals*, 2011, 22, 393-412., Copyright 2011 Springer. This work was part of a collaborative effort and only a portion constitutes the author's personal dissertation research; however, all results are shown to allow for a complete interpretation of the findings. Supplemental information is found in Appendix D.

9.1 Introduction

Specific trace metals are essential to the metabolic activity of all organisms, and scarcity of metals may be an important factor in limiting organism growth. One strategy that plants and microbes use to obtain these trace metals is the production and exudation of biomolecules that solubilize metals, return them to the cell, and facilitate their uptake for use by the organism (1-5). Siderophores, a class of biogenic ligands that are traditionally associated with the mobilization and uptake of Fe(III), have a high degree of structural variability in terms of their binding groups and backbone structure (6). Despite this structural diversity, these molecules broadly make use of large binding affinities and relatively slow exchange kinetics to bind and solubilize metals.

One feature that contributes to the structural variability of siderophores and plays a significant role in determining the reactivity of siderophores is the identity of the donor groups that bind the metal ion. The majority of siderophores achieve selective complexation

of hard metal ions, as well as stabilization of higher oxidation states, through coordination by hard donor atoms (viz. charged oxygen in specific moieties, such as catechol moieties), which are contained in numerous bacterial siderophores such as enterobactin, petrobactin, and azotochelin (Figure 9.1). Catechol donor groups bind Fe(III) through the conjugated central ring system, which delocalizes electron density (7). Catecholate siderophores are produced by many soil and pathogenic bacteria and may also be produced by marine organisms (4, 8, 9).

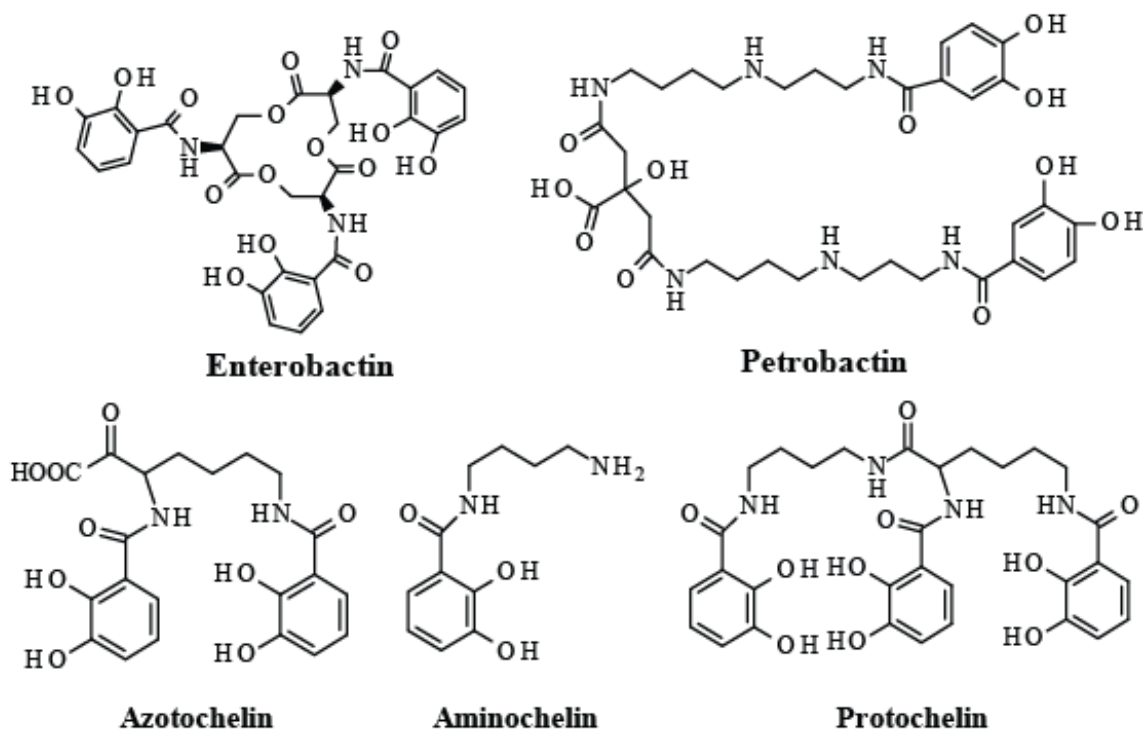


Figure 9.1 - Structures of the catecholate siderophores enterobactin, petrobactin, azotochelin, aminochelin, and protochelin.

An environmentally important catecholate siderophore is protochelin (Figure 9.1), which is produced by the free-living diazotroph *Azotobacter vinelandii* (10). Catecholate siderophores are one of the few ligands that bind molybdate at circumneutral pH, although these complexes have significantly lower stability constants than those of the ligand with Fe(III) (11-14). Protochelin has been implicated in the specific transport of Mo and V (in addition to Fe) in *A. vinelandii* (15, 16), which uses these metals in nitrogenase enzymes (17). Protochelin is also associated with the specific rejection of toxic W (18), and the ability to form complexes with many metals coupled with selectivity of the uptake may function as a detoxification mechanism to exclude toxic metals (19). Coupled with a growing body of work that has explored the geochemistry and biology of non-ferric metal interactions with other siderophores (20-31), work with protochelin has led to the suggestion that siderophores may be involved with the transport of non-ferric metals (19) and have a diverse chemistry with a variety of environmentally relevant metals (32).

Despite the proposed role that siderophores play in the cycling of non-ferric metals in the environment and the observed interactions of Mo and V with protochelin, very little work has been done to characterize the binding reactions of common non-ferric metals with catecholate siderophores. In this study, we investigated the fundamental solution properties of the bacterial siderophore, protochelin, and the binding characteristics of Fe(III) protochelin complexes. Additionally, we explored the structure and stability of its complexes with common first-row transition metals that may form strong complexes with siderophores (viz. Mn, Co, and Cr) by using spectroscopic and computational methods (32, 33). The

results will then be discussed in terms of the role of protochelin and catecholate siderophores in the environmental cycling of metals and the cellular uptake of metals.

9.2 Materials and Methods

9.2.1 Materials

All solutions were prepared in Type I deionized water. Protochelin was prepared synthetically by the Small Molecule Synthesis Facility (SMSF) at Duke University using a previously reported procedure (34), and was used as received. The purity of the sample was verified by nuclear magnetic resonance spectroscopy and liquid chromatography-mass spectrometry at the SMSF (data not shown). Desferrioxamine B mesylate (DFOB; 95%) was purchased from Sigma-Aldrich and used as obtained. The preparation of metal-protochelin complexes was performed as described in the Supporting Information. Buffers used will be noted where appropriate. For electrochemical studies, all chemicals were purchased from Sigma-Aldrich (St. Louis, MO) and used as received, unless otherwise noted.

Solution pH was measured with an Accumet XL20 pH meter (Fisher Scientific) equipped with a 410 Micro-combination pH probe (Microelectrodes, Inc). Solution pH was controlled through addition of measured volumes of standardized 0.10 M HCl and 0.10 M NaOH, purchased from Sigma-Aldrich, unless otherwise noted. Electrodes were standardized by using commercial buffers (Fisher) at pH 4.0, 7.0, and 10.0. UV-visible spectra were measured using an Ocean Optics Jaz spectrophotometer equipped with an external dip probe for pH-dependent spectrophotometric titrations and a fiber-optic 1 cm path length cell for competition titrations.

9.2.2 Ligand Characterization

Ligand solubility was characterized by preparing two solutions of protochelin dissolved in buffer solutions. The first solution was prepared by massing 50.0 mg of solid protochelin and adding 50 mL of a buffer solution of 0.10 M HEPES in 0.10 M NaCl at pH 7.0. The second solution was prepared by massing 50.0 mg of solid protochelin and adding 50 mL of a buffer solution of 0.10 M MOPS in 0.10 M NaCl at pH 8.0. Both solutions were sonicated for 15 minutes, and the solution was filtered through a 0.22 μm filter into a cuvet to remove any undissolved particulate matter. The UV-visible absorbance of the solution was measured and the molar absorbance at the measured $\lambda_{\text{max}} = 316 \text{ nm}$ was used to determine the concentration of the ligand in solution.

Ligand stability was characterized by spectrophotometric kinetic measurement of the degradation reaction. Solutions were prepared by adding the ligand to aqueous solutions of 0.10 M NaCl at a pH below that is required to dissolve the ligand. To these solutions, a measured volume of buffer in 0.10 M NaCl was added to adjust the solution pH, followed by rapid dilution to the final volume and measurement of the initial spectrum. Subsequent spectra were measured regularly to monitor the degree of ligand degradation. Reaction temperature was controlled at 25°C with a temperature-controlled water bath. The concentration of buffer used in all experiments was 0.010 M. At pH 8.0, the buffer used was MOPS, whereas all other experiments at pH 8.5, 9.0, 9.5, and 10.0 contained CHES.

9.2.3 Fe(III)-Protochelin Spectrophotometric Titration

To characterize the binding mode of the Fe(III) with protochelin, a pH-dependent UV-visible spectrophotometric titration was performed. A solution of 4.1×10^{-5} M Fe(III) and protochelin was prepared at pH = 9.1 as described in the Supplemental Material. The Fe(III) and protochelin solution was titrated with measured volumes of 0.10 M HCl with stirring. At each addition, the final pH was recorded and the UV-visible spectrum over the range of 250–800 nm was measured. The reaction temperature was controlled at 25°C using a temperature-controlled water bath.

9.2.4 Mass Spectrometry Analysis of the Degradation Products of Protochelin and the Metal-Protochelin Complexes

Mass spectrometry of samples was performed using Electrospray Ionization (ESI) on an Agilent Technologies (Santa Clara, California) 6210 LC-TOF mass spectrometer. Solutions of protochelin and of the Mn-Proto and Co-Proto complexes were prepared at a concentration of 1.0 mM as described above and in the Supplemental Material. Samples were diluted in methanol and analyzed via a 1 μ L flow injection at 300 μ L \cdot min⁻¹ in a water:methanol mixture (25:75 v/v) with 0.1% formic acid. The mass spectrometer was operated in negative-ion mode with a capillary voltage of 3.5 kV, nebulizer pressure of 50 psig, and a drying gas flow rate of 10 L \cdot min⁻¹ at 350°C. The fragmentor and skimmer voltages were 110 and 65 V respectively. Reference ions of purine at m/z 112.9855 and HP-0921 at m/z 966.0007 were simultaneously introduced via a second orthogonal sprayer, and

used as internal calibrants. Mass spectra of the protochelin solution, the Mn-Proto solution, and the Co-Proto solution are shown in the Supplemental Material.

9.2.5 Computations of Metal-Protochelin Complexes

All structure and frequency calculations reported here were carried out by the Gaussian 09 program package (35). Molecular structures were found by full geometry optimization at the B3LYP/6-31G* exchange-correlation hybrid of density functional (36, 37). Computed frequencies of all structures are positive, indicating that the optimized structures are at real minima of their ground-state potential energy surfaces. To simulate complexes in aqueous solutions, density functional theory (DFT) calculations were embedded in the polarizable cavity with a static dielectric constant ($\epsilon = 78.355$) and by making the solvent reaction field self-consistent with the solute electrostatic potential, commonly referred to as the Polarizable Continuum Model (PCM) implemented in Gaussian 09 (38).

9.2.6 X-ray Spectroscopy of Metal-Protochelin Complexes

K-edge X-ray fluorescence-yield (FY) spectra of the metal centers in solutions containing Fe(III) and protochelin (5 mM; pH = 7.5 and 10 mM; pH = 4) were measured at Stanford Synchrotron Radiation Lightsource (SSRL) Beamline 11-2 [Si (220) variable-exit monochromator] at room temperature using a 30-element Ge fluorescence detector. Mn(III)Proto³⁻ (5 mM; pH = 9.3) and Co-Proto (5 mM; pH = 8.0) FY spectra were measured in a liquid helium cryostat (7-13°K) using a 30-element Ge fluorescence detector to retard the

rate of photolytic degradation of these complexes. Frozen samples contained 40% glycerol to reduce formation of ice crystals (39). Cr-Proto (5 mM; pH = 8) FY spectra were measured at SSRL Beamline 4-3 [Si (111) variable-exit monochromator] using a Lytle-type ionization-chamber detector. Harmonics were rejected using Rh-coated mirrors and/or by detuning the monochromators. In all cases, spectra were collected using Soller slits and Z-1 X-ray filters to reduce the intensity elastic scattering received by the detectors. For the Fe-, Co-, and Cr-siderophore complexes, energy calibration was maintained using metal foils; for the Mn-siderophore complex, calibration was accomplished by adjusting the E_0 of potassium permanganate (KMnO_4). In the measurements of the Fe(III)-Proto samples, at least five spectra were averaged for each sample to improve signal-to-noise ratio. The Mn(III)Proto³⁻ complex exhibited slight beam damage after the initial scan (shown in Figure D.1) and thus only one scan was used. Spectra were dead-time corrected, energy calibrated, averaged, background-subtracted, splined, and fit in R -space (40) using the SixPACK interface (41), which makes use of the IFEFFIT code (42).

The relative fraction of Mn(II) in the initial and successive scans of the Mn(III)Proto³⁻ sample (i.e., due to photolytic beam reduction) was assessed by (a) comparing the first Mn(III)Proto³⁻ scan to spectra from the more Mn(II)HDFOB⁰ and Mn(III)HDFOB⁺ complexes (by linear combination fitting over the energy range 6400 to 6800 eV) (43), and (b) by fitting the successive Mn(III)Proto³⁻ scans as a linear combination of XANES (X-ray Absorption Near-Edge Structure) from Mn(II)Cl₂ and Mn(III)Proto³⁻ (first scan).

Amplitude and phase functions calculated using FEFF 9 [Dirac-Hara exchange potentials (44)] and structural models for Mn(III)Proto³⁻, Fe(III)Proto³⁻, and Fe(III)H₃Proto

complexes obtained from DFT calculations. EXAFS data were fit using a common value of the parameter ΔE_0 , which was allowed to float during optimization. The amplitude reduction factor (S_0^2) was fixed at 0.87 for Fe and 0.835 for Mn based on prior work (45 , 46). The Debye-Waller disorder parameter (σ^2) and the interatomic distance (R) for each shell were floated freely during optimization. Development of the structural models used to fit spectra is described in detail in the Supplemental Material.

9.2.7 Competition of Fe(III) and Mn(III) for Protochelin and Desferrioxamine B

For determination of the Mn(III)Proto^{3-} stability constant, a competition experiment was performed between the Fe(III)Proto^{3-} complex and the Mn(III)HDFOB^+ complex. A solution of 0.4 mM Fe(III)Proto^{3-} was prepared as described in the Supplemental Material. A second solution of 2.0 mM Mn(III)HDFOB^+ was prepared using previously established air-oxidation procedures and was used in experiments (21). Solution pH was controlled with a final concentration of 0.050 M HEPES at pH = 9.05. The Fe(III)Proto^{3-} solution was separated into 5.0 mL aliquots, and varying volumes of the Mn(III)HDFOB^+ solution were added to produce a concentration range from 0 equivalents of Mn(III) to 25 equivalents of Mn(III). After allowing 5 days equilibration time, the solution spectra were measured. The spectra were measured a second time a day later to ensure that no change was taking place in the solution speciation. The computer program HYPERQUAD was used to determine the relative concentrations of each species in solution and the equilibrium constant of the Mn(III)Proto^{3-} complex from each addition (47). HYPERQUAD used an input of the spectra of all species in solution to determine the relative concentrations of the four species involved

in the equilibrium. Using the determined concentrations of the species, the program is able to calculate the equilibrium constant (K_{obs}) of the following reaction:



The program then uses the known $\log \beta_{110}$ of Fe(III)Proto^{3-} , the known stability constant of Mn(III)HDFOB^+ and the known stability constant of Fe(III)HDFOB^+ to determine the stability constant of Mn(III)Proto^{3-} (Eq. 2), using Eq. 3.



$$\beta_{110, \text{Mn(III)Proto}} = \frac{K_{obs} \beta_{110, \text{Fe(III)Proto}} \beta_{110, \text{Mn(III)HDFOB}}}{\beta_{110, \text{Fe(III)HDFOB}}} \quad (3)$$

Analysis of the UV-visible spectra was performed in 1.0 nm increments over the wavelength range of 310–750 nm. For the determination of the Mn(III)Proto^{3-} formation constant, protonation constants of protochelin and Fe(III) complex stability constants were taken from the literature (34). Protonation constants, Fe(III) complex formation constants, and Mn(III) complex formation constants for DFOB were also taken from the literature (21, 48). For solution of equilibrium concentrations, reference spectra were loaded for Mn(III)Proto^{3-} , Fe(III)Proto^{3-} , Mn(III)HDFOB^+ , and Fe(III)HDFOB^+ .

9.2.8 Background-Subtracted Fast-Scan Cyclic Voltammetry (FSCV)

A physiologically buffered solution (phosphate buffered saline) at pH = 7.4 was used in all flow injection analysis experiments. All aqueous solutions were prepared using doubly deionized water (Barnstead EasyPure II, Dubuque, IA).

Carbon-fiber microelectrodes were fabricated as described previously (49). Briefly, a single 7 μm diameter T-650 carbon fiber (Cytec Industries, West Patterson NJ) was aspirated into a single borosilicate glass capillary (A-M Systems, Sequim, WA) and tapered using a micropipette puller (Narishige, Tokyo, Japan) to form two sealed microelectrodes. The exposed length of carbon fiber was cut to approximately 100 μm , and an electrical connection was made by backfilling the capillary with an ionic solution and inserting a lead. A Ag/AgCl pellet reference electrode (World Precision Instruments, Sarasota, FL) was employed to complete the two electrode electrochemical cell.

A syringe pump (New Era Pump Systems, Wantagh, NY) supplied a continuous buffer flow of 1 mL/min across the working and reference electrodes. The working electrode was positioned in a custom electrochemical cell using a micromanipulator (World Precision Instruments, Sarasota, FL). Two second bolus injections of analyte to the microelectrode surface were accomplished with a six-port HPLC valve mounted on a two-position air actuator controlled by a digital pneumatic solenoid valve (Valco Instruments, Houston TX). The entire apparatus was housed within a custom-built grounded Faraday cage. In most experiments, an inverted triangular waveform ranging from +0.8 to -0.8 V with a holding potential of +0.8 V versus Ag/AgCl was applied at a scan rate of 100 $\text{V}\cdot\text{s}^{-1}$, and at a frequency of 10 Hz using a custom built instrument for potential application to the electrochemical cell and for current transduction (University of North Carolina at Chapel Hill, Department of Chemistry, Electronics Facility). Complete cyclic voltammograms of protochelin were collected in ~50 msec. All experiments were performed at room temperature. TH-1 software (ESA, Chelmsford, MA) was used for waveform output and data

collection with a DAC/ADC card (6251, National Instruments, Austin, TX). A second card (6711) was used for triggering the DACs and ADCs and for synchronization of the electrochemical experiment with the flow injection system. Signal processing including background subtraction, signal averaging, and digital filtering (low-pass filtered at 2 KHz) was software-controlled. Statistical and graphical analysis was accomplished using GraphPad Prism 5 (GraphPad Software, Inc., La Jolla, CA).

9.3 Results and Discussion

9.3.1 Solubility of Protochelin

Previous reports on the ligand protochelin have generally focused on the production of the ligand and its Fe or Mo binding properties (10, 14, 16, 34, 50). In these reports, there is very little mention of the solution properties of free protochelin. To address this basic knowledge gap, we conducted a characterization of the solubility and stability of protochelin. A semi-quantitative determination of protochelin found that its solubility at pH = 7.0 is approximately 2.4×10^{-4} M; at pH = 8.0, the solubility of the molecule is significantly higher (> 1.0 mM). It is impractical to determine the exact solubility of the ligand at this pH due to the large masses of ligand required for such an experiment. Between pH of 7.0 and 8.0, the ligand undergoes a spectral shift consistent with protonation of the catechol donor groups, making characterization of the solubility in this range difficult. The low solubility of the protonated form (neutral) of protochelin can easily be rationalized from a simple analysis of the structure of the molecule (Figure 9.1). The backbone of the molecule features very few hydrogen bond donor or acceptor sites, and the catechol donor groups of the molecule are

likely protonated at $\text{pH} < 7.5$ (51), resulting in a neutral charge and highly hydrophobic donor groups at low solution pH (52). The limited solubility of protochelin at circumneutral to acidic pH may affect laboratory experiments; however, it is unlikely to constrain protochelin mobility and efficacy in an environmental setting, where ligand concentrations are significantly lower than those utilized in the studies presented here (53, 54). Although concentrations of protochelin in soils and natural waters have not been measured, environmental concentrations of individual siderophore are typically on the order of picomolar to 10's of nanomolar (55-58) as compared to the millimolar concentrations used here.

9.3.2 Degradation of Protochelin and Metal-Protochelin Complexes

Soluble protochelin degrades slowly over time. At the low end of the experimental pH range (< 7.5), the ligand was found to be stable in solution over extended periods of time, as long as 5 days in solution. However, as the solution pH increased, the ligand was found to be unstable, as evidenced by the gradual increase in solution turbidity and changes in the UV-visible absorbance spectra (Figure 9.2). Attempts to quantify the rate of degradation as a function of pH (not shown) exhibited a high degree of variability, preventing a detailed analysis of the pH-dependent reaction mechanism.

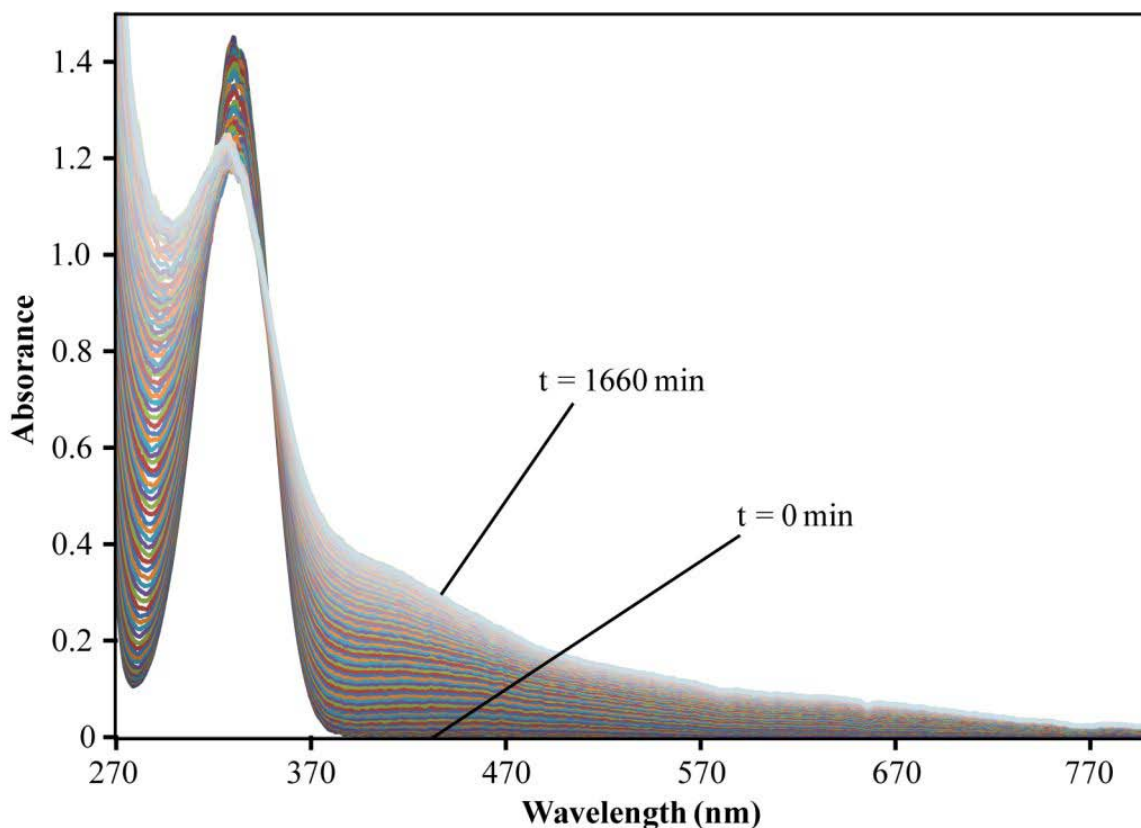


Figure 9.2 - Plot of the change in absorbance spectrum of a solution of protochelin over time as ligand degradation occurs. Conditions: [Ligand] = 6.4×10^{-5} M, pH = 9.5, μ = 0.10 M (NaCl), 0.10 M CHES, T = 25°C.

The degradation of the ligand over time was confirmed by reduction of the parent peak in mass spectra of aged solutions (cf. Supplemental Material, Figs. D.2 and D.3). In addition to the M^- peak (623.23 m/z ratio), peaks are observed at lower m/z ratios, suggesting degradation of the ligand. Mass spectral analysis of solutions of the Mn-Proto complex and of the Co-Proto complex (see Supplemental Material, Figs. D.4-7) exhibits a number of peaks at lower m/z ratios than the M^- peak at 623.23 m/z ratio, suggesting that the ligand degrades both in the presence and in the absence of metals. Further, after reaction times

greater than 2 hours, a peak is gradually observed at 982.99 m/z ratio in all samples and at 1282.97 in the presence of Co(II), suggesting the possibility of phenol coupling of the ligands (59). Attempts to assign the mass spectral signals observed in the degradation experiments were unsuccessful, including assignment with the predicted hydrolytic products, azotochelin and aminochelin. It is interesting to note additionally that at longer reaction times, the mass spectral signal corresponding to the M^- peak of protochelin disappears in the presence of Co, further supporting the idea of metal-catalyzed ligand degradation. Finally, it should be noted that although mass spectral signals that appeared in the solutions of protochelin alone (146 m/z peak, 197 m/z peak) were also observed in the mass spectra measured for the M-Proto³⁻ systems, a number of novel low m/z peaks were observed in the presence of the metals.

Collectively, these observations suggest that the ligand decomposes by a number of pathways. Such degradation pathways could potentially include hydrolysis and oxidation, and result in the formation of benzoquinone groups, coupled hydroxylated aromatic compounds, or a number of other organic molecules (60). Because some masses representing degradation products that are observed in the presence of metals are not observed in the absence of metals, metals may promote the formation of novel degradation products. Mass spectral peaks corresponding to expected hydrolysis products of the ligand were not observed, further suggesting that redox reactions may be involved in the presence of Mn and Co. In previous studies, redox degradation reactions have been shown to be more likely to occur in the presence of oxidizing agents (61). This process may explain degradation of the complexes studied herein over extended periods of time in the presence of Mn, and rapidly in the presence of Co, both of which are oxidizing agents in the 3+ oxidation state.

9.3.3 Formation of Metal-Protochelin Complexes

In the case of stable 3+ metal ions, such as Fe, direct complex formation is possible by simple adjustment of the pH (see Supplemental Material). However, in the case of metal ions that obtain the 3+ oxidation state through redox reactions, a less direct route of complex formation must be taken. Manganese(II) oxidation in the environment, even under oxic conditions, is typically slow unless the process is mediated by bacteria or fungi (62). However, complexation of a metal by hard donor groups such as the catechol donors of protochelin may increase the rate of oxidation and stabilize the oxidation product (63, 64). This type of reaction has been observed for Mn(III) complexes with other siderophores, namely DFOB, coprogen, and pyoverdine GB-1 (21, 22, 31). Although the oxidation rate of Mn(II) in the presence of protochelin was not quantified, at pH = 8.5 the complex concentration reaches a steady-state, as indicated by stability in the UV-visible spectrum after 2 h.

Like manganese, Co(II) air-oxidation does not typically occur under environmental conditions, but can be promoted by the presence of strong complexing agents (viz. ethylene diamine). In the case of the Co(III)-Proto complex, mixture of Co(II) in solution with the ligand, followed by an increase in the solution pH results in a change in the solution color that suggests that air oxidation of the metal is taking place. However, the solution gradually shifts from a green color that likely corresponds to a Co(III)-siderophore complex (43) to a dark brown solution with a turbid appearance. Additionally, X-ray spectroscopy of a sample analyzed approximately 30 min after synthesis revealed a XANES white line position consistent with the presence of Co(II), and no evidence in the EXAFS spectrum of any

second shell structure in the FT magnitude plot (not shown). This observation suggests that oxidation of Co(II) resulted in an unstable Co(III) complex that degraded by internal electron transfer, resulting in reaction with the catechol donor groups (60, 61). A similar behavior was observed in experiments performed with the Mn-enterobactin complex, where Mn(II) oxidation over the course of 2 h at pH = 9 in the presence of enterobactin resulted in a cloudy black solution containing Mn(II) (65). Previous work with Co(III)HDFOB⁺ noted that, despite a high stability constant, a fraction of the complex in solution degrades to Co(II) at all pH values investigated (43). In addition, Carrano et al. (1996) noted that rhizoferrin, an α -hydroxycarboxylate siderophore, does not form a stable complex with Co(III).

Attempts were made to synthesize the Cr(III)Proto³⁻ complexes for structural analysis. However, it is difficult to synthesize these complexes by methods used for Mn or Fe because of slow rate of ligand exchange for Cr(III) (66). The FT magnitude of EXAFS spectrum for Cr-Proto synthesized by exchange reaction (data not shown) exhibited no second shell structure, suggesting that no complex had formed.

9.3.4 Determination of Mn(III)Proto³⁻ Stability Constant

The absorbance spectra measured during the exchange reaction of Fe(III)Proto³⁻ with Mn(III)HDFOB⁺ are shown in Figure 9.3. The initial spectrum (labeled 0:1 in Figure 9.3) exhibits a spectral handle consistent with formation of triscatecholate-coordinated Fe(III) ($\lambda_{\text{max}} = 492 \text{ nm}$), suggesting that Fe(III) is completely coordinated by protochelin. Addition of Mn(III)HDFOB⁺ results in an increase in absorbance in the UV region, a result of a large excess of unreacted Mn(III)HDFOB⁺ in solution ($\lambda_{\text{max}} = 310 \text{ nm}$). The isosbestic point

evident at 490 nm indicates conversion of the Fe(III)Proto^{3-} complex to the Fe(III)HDFOB^+ complex as the concentration of added Mn(III)HDFOB^+ increases. The maximum degree of exchange observed during these experiments was 90% exchange. As determined by fitting in HYPERQUAD, the stability constant from three replicate titrations was found to be $\log \beta_{110} = 41.6 \pm 0.3$.

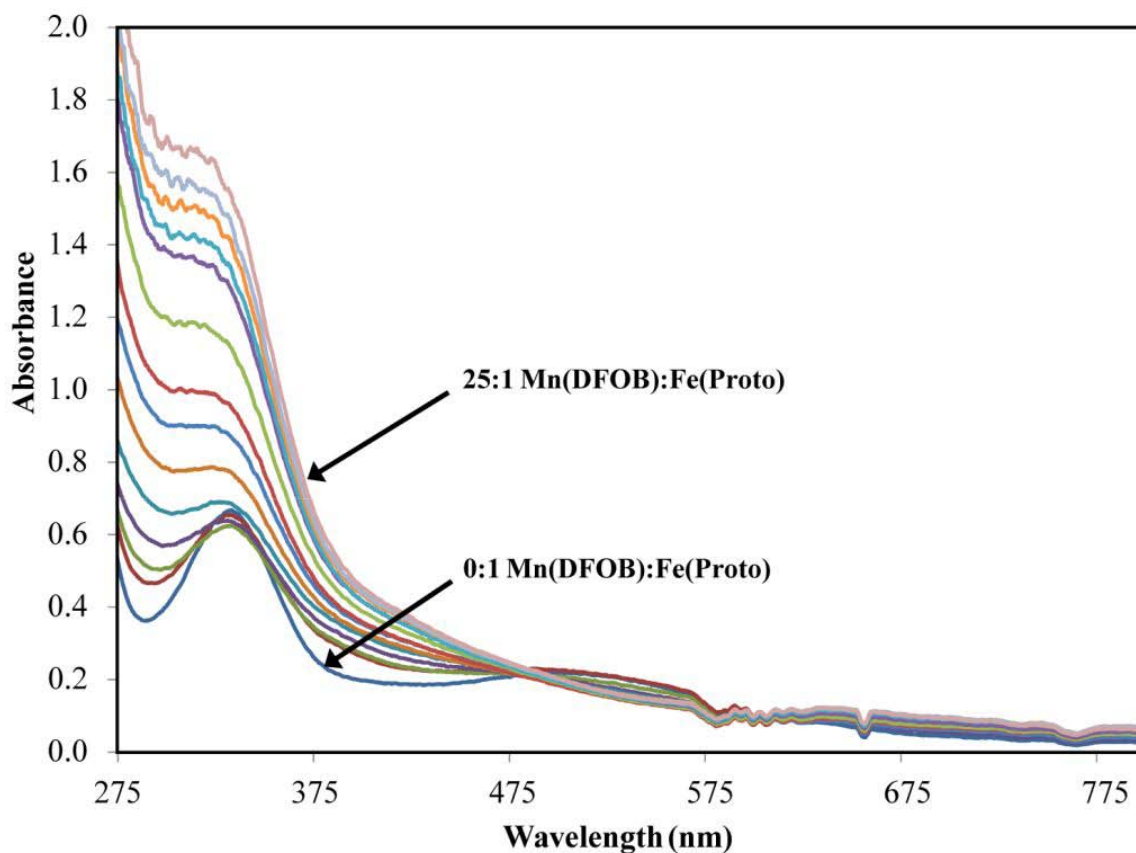


Figure 9.3 - UV-visible spectra obtained from the competition experiment between the Fe(III)Proto^{3-} complex and the Mn(III)HDFOB^+ complex. The concentration ratio of Mn(III)HDFOB^+ to Fe(III)Proto^{3-} ranges from 0 equivalents Mn(III)HDFOB^+ to 25 equivalents Mn(III)HDFOB^+ . Experiment was performed in HEPES buffer at pH = 9.05, T = 25°C and $\mu = 0.10$ M (NaCl).

The Mn(III)Proto³⁻ stability constant can be compared to Mn(III)HDFOB⁺ and Fe(III)Proto³⁻ (Table 1). The Mn(III)Proto³⁻ complex is higher than that of the Mn(III)HDFOB⁺, which is consistent with trends for Fe(III) complexes. Fe(III) exhibits high stability with protochelin due to electron resonance in the conjugated ring system of the catechol donor groups (7), and this phenomenon may also be responsible for the high stability of Mn(III)Proto³⁻. However, the value determined here for the metal stability constant of Mn(III)Proto³⁻ is somewhat lower than that of Fe(III)Proto³⁻, with a three order of magnitude difference in stability (34). The trend in stability constants observed for the protochelin system is consistent with that of DFOB, where the Mn(III)HDFOB⁺ (log β₁₁₀ = 29.9) was found to have a stability constant just over two orders of magnitude lower than that of the Fe(III)HDFOB⁺ complex (log β₁₁₀ = 32.02) (21, 67). The significant difference between the stability constants of the Mn(III) complexes of DFOB and protochelin (Δlog β = 11.7) is also consistent with the difference observed between the Fe(III) complexes of DFOB and protochelin (Δlog β = 12.6).

Table 9.1 - Log of the stability constant of the metal complexes of a number of siderophores (T = 25°C).

Equilibrium	Mn(III)	Fe(III)
HDFOB ⁺ + M(III) ⇌ M(III)HDFOB ⁺	29.9 ^a	32.02 ^b
Ent ⁶⁻ + M(III) ⇌ M(III)Ent ³⁻	N/A	49 ^c
Proto ⁶⁻ + M(III) ⇌ M(III)Proto ³⁻	41.6 ± 0.3 ^d	44.6 ^e

Structures of Ent and Proto siderophores are shown in Figure 9.1.

^a μ = 0 M, (21)

^b μ = 0 M, (68)

^c μ = 0.1 M, (51)

^d This work, μ = 0.1 M (NaCl)

^e μ = 0.1 M, (34).

A similar comparison may be made between the pM values of protochelin with Mn(III) and Fe(III). The pM values are calculated values of the free metal ions in solution (excluding hydrolysis products) at set conditions, usually 1×10^{-6} M metal, 1×10^{-5} M ligand, pH = 7.4, $\mu = 0.10$ M, and $T = 25^\circ\text{C}$ (69). As the complex stoichiometry is the same between the two complexes, the pMn value (25.34) and the pFe value (22.3) of protochelin also differ by 3 orders of magnitude, demonstrating the relatively lower stability of the Mn(III)Proto³⁻ complex compared to the Fe(III)Proto³⁻ complex. Comparison of the pM values to the known pFe of enterobactin (35.6) demonstrates the relatively lower complex stability of the protochelin complexes than that of enterobactin (70).

9.3.5 Fe(III)-Protochelin Complex Coordination Modes

The spectra measured during the spectrophotometric titration of Fe(III) in the presence of protochelin are shown in Figure 9.4. A gradual shift was observed in the spectral maximum over the course of the titration, from 492 nm at pH = 9.1 to 545 nm at pH = 4.4. The majority of the spectral shift was observed over the pH range of 7.0 to 4.4. An isosbestic point was observed at 547 nm, indicating the observation of a single equilibrium over the course of the titration. The initial wavelength is consistent with the formation of the Fe(III)Proto³⁻ complex (34). An additional shift in the λ_{max} of the peak located at lower wavelengths was observed from 333 nm at pH = 7.0 to 319 nm at pH = 4.4. Below pH = 4.4, the spectrum began to decrease in intensity until a gray precipitate was observed in solution at pH = 3.8. The spectra changed negligibly through pH = 10.2 (data not shown), suggesting no change in binding mode or speciation at basic conditions.

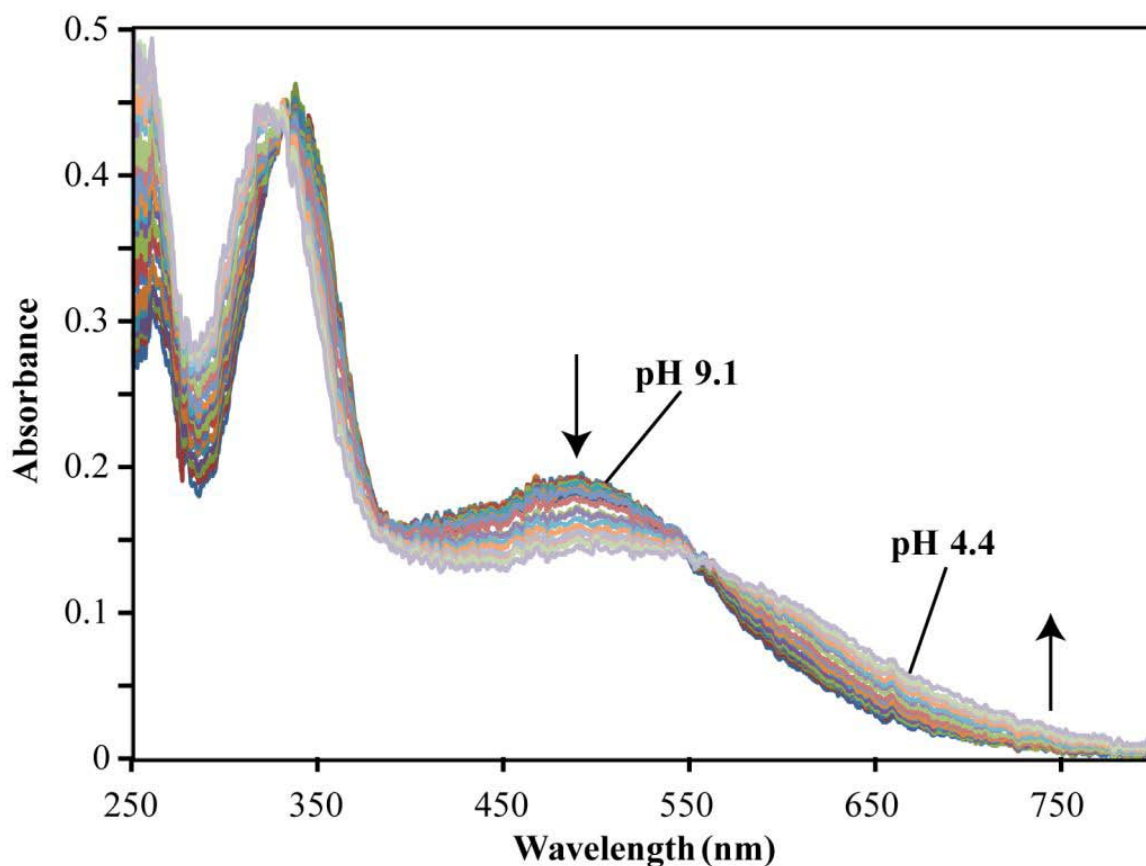
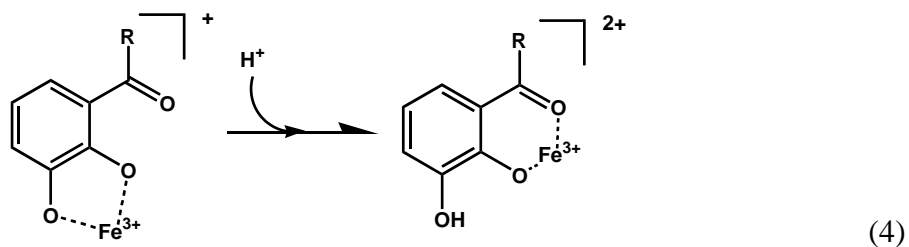


Figure 9.4 - Spectrophotometric titration of the Fe(III)Proto³⁻ system as a function of pH from pH 9.1 to 4.4. Conditions: [Fe³⁺]_{tot} = 4.0 x 10⁻⁵ M, [Proto]_{tot} = 4.1 x 10⁻⁵ M, T = 25°C, μ = 0.10 (NaCl). Arrows indicate the direction of spectral shifts with increasing pH.

Many siderophores feature ionizable donor groups, which play a strong role in determining the solution thermodynamics and speciation of siderophore complexes. Upon a decrease in solution pH, a high concentration of protons may compete with metals in solution for accepting electron density from the donor atoms. In donor groups such as hydroxamates or carboxylates, protonation of the donor atom generally results in dissociation of the donor group. In previous studies of catecholamide donor group siderophores, however, it has been

shown that a coordination shift in the binding mode of the catecholamide donor groups will occur upon decrease in the system pH, as shown in Eq. 4 (71).



Protonation occurs at the distal hydroxyl donor of each catecholamide donor group, and the binding mode shifts from the catecholate mode to the salicylate mode. In a previous study, the stability of the Fe(III)Proto³⁻ complex was determined; however, the protonation of the Fe(III)Proto³⁻ complex was not characterized (34). The spectrophotometric titration of the Fe(III)Proto³⁻ complex over the pH range of 7.0 to 2.8 shows a gradual shift in the observed λ_{\max} of the solution from 492 nm at pH = 7.0 to $\lambda_{\max} = 547$ nm at pH ≤ 4.4 , consistent with a shift in complex binding mode from catecholate to salicylate binding mode, as seen in Eq. 4 (71, 72).

A similar experiment was performed with the Mn(III)Proto³⁻ complex, but titration to solution pH ≤ 6.0 resulted in little shift in solution absorbance values before the ligand precipitated out of solution. In all likelihood, a decrease in solution pH results in destabilization of the Mn(III) oxidation state, leading to reduction of Mn to the 2+ oxidation state, as has been observed for Mn(III)HDFOB⁺ at pH < 7 (21). Due to the selectivity of protochelin for higher oxidation state metals, the Mn(II)Proto⁴⁻ and Mn(II)H₃Proto⁻ complexes should have markedly lower stability constants than Mn(III)-Proto complexes. This difference in stability between the two oxidation states may be compounded by the

salicylate shift, possibly making complexation at lower pH even less stable than at higher pH values.

9.3.6 Redox Chemistry of Protochelin and Metal Protochelin Complexes

A representative background-subtracted cyclic voltammogram for protochelin in the absence of a metal ion is shown in Figure 9.5 (black), using a waveform ranging from -0.4 to +1.3 V at $400 \text{ V}\cdot\text{s}^{-1}$. This waveform is optimal for detecting dopamine, a catecholamine that is commonly studied using carbon-fiber electrodes (73, 74). Because dopamine's structure contains a catechol group, it is an appropriate model for comparison to protochelin. Dopamine exhibits a 2-electron redox reaction via the catechol/*ortho*-quinone couple with a half-wave potential of $\sim +200 \text{ mV}$ vs. NHE (gray). Protochelin's voltammogram exhibits similar peaks, corresponding to the redox conversion of its catechol functional groups to *ortho*-quinones.

The redox chemistry of $10 \mu\text{M}$ protochelin was further studied using an inverted triangular waveform optimized for this molecule ranging from +0.8 to -1.2 V and scanned at $100 \text{ V}/\text{sec}$ (Figure 9.6a). Addition of a metal ($10 \mu\text{M}$ Mn, Fe, or Co) to protochelin slightly decreased the half-wave potential for the redox chemistry associated with the catecholate ligand, suggesting that the metal facilitates electron transfer (Figure 9.6b-d). Additionally, the overall redox current was reduced upon addition of metal, consistent with a structural change or distortion in the catechol ligand upon binding. This phenomenon was most evident in the case of Co. Interestingly, approximately one second into data collection, the voltammograms clearly shifted to indicate the development of a second redox process

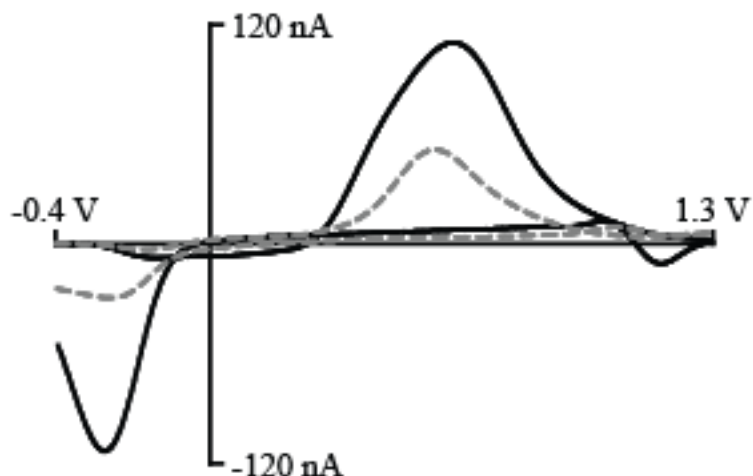


Figure 9.5 - Representative background-subtracted cyclic voltammograms measured for 20 μM protochelin (black) and 1 mM dopamine (gray dashed) using a waveform ranging from -0.4 to +1.3 V at $400 \text{ V}\cdot\text{s}^{-1}$. Dopamine is a well-studied catecholamine that exhibits a 2-electron transfer redox reaction via the catechol/*ortho*-quinone couple with a half-wave potential of $\sim +200 \text{ mV}$ vs. NHE. Protochelin's voltammogram exhibits similar peaks, corresponding to the redox conversion of its catechol functional groups to *ortho*-quinones.

centered at a more negative potential as current resulting from the first redox reaction simultaneously decreased (Figure 9.6b). In this case, adsorption of an initial layer of protochelin onto the carbon electrode may have altered the redox chemistry of protochelin molecules that were subsequently detected (see supporting information). Redox reactions of catechols at carbon fiber electrodes have been shown to be adsorption-controlled under similar experimental conditions (74, 75). Indeed, the current generated for the redox reaction of protochelin was found to be adsorption-controlled (rather than diffusion-controlled), by plotting cathodic peak current collected at -0.2 V as a function of scan rate ($r^2 = 0.978$, $n = 3$ electrodes, Figure D.8). These results may have interesting implications regarding the possibility of metal transport by siderophores, as will be discussed later.

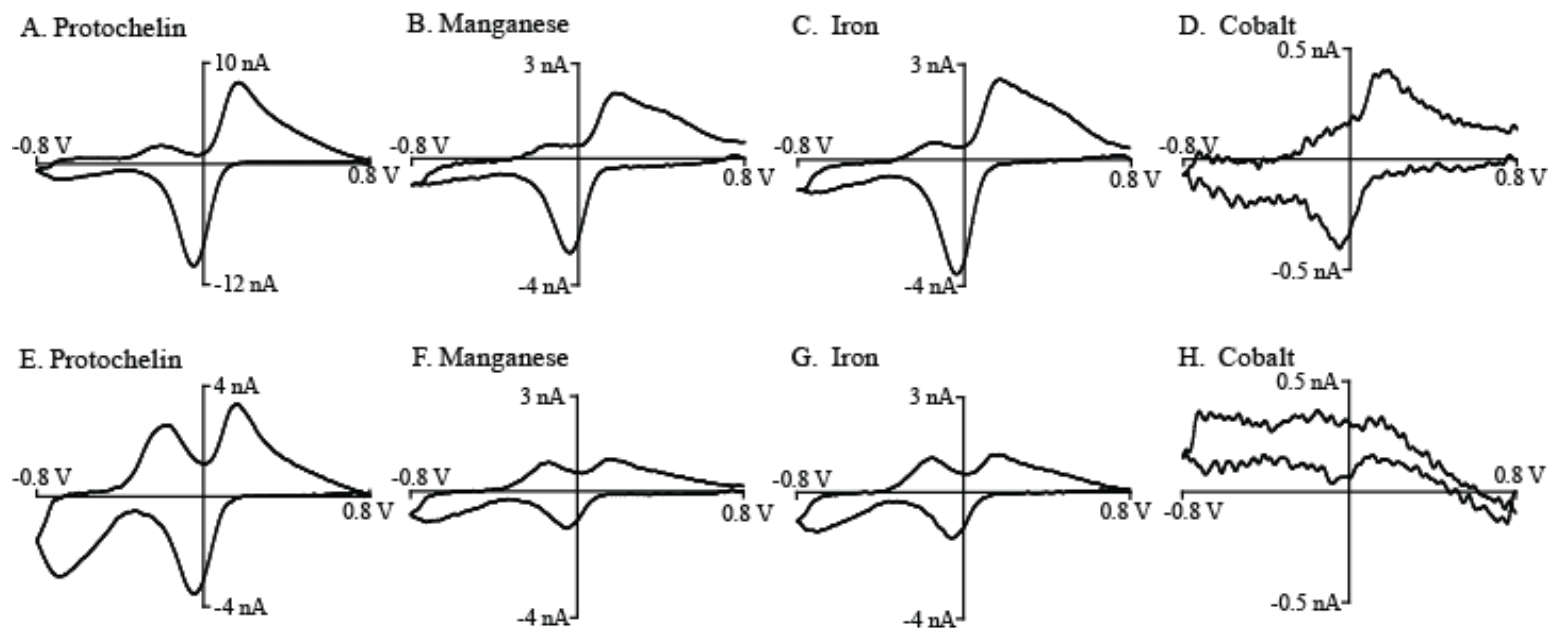


Figure 9.6 - Representative background-subtracted cyclic voltammograms measured for protochelin and metal-protochelin complexes of manganese(III), iron(III), and cobalt(III) (top, b-d). Interestingly, one second into data collection the voltammograms clearly shifted to indicate the presence of a second redox process developing as current resulting from the first redox reaction simultaneously decreased. Addition of a metal to protochelin reduced the overall redox current, consistent with a structural change or distortion in the catechol ligand upon binding. One second into data collection the voltammograms indicate the development of a second redox process as current resulting from the first redox reaction is simultaneously decreased (bottom, e-h).

9.3.7 Metal Protochelin Complex Computational Simulations

The DFT calculations produced theoretical models of the structures of the metal-protochelin complexes in aqueous solution. These include simulations of both the catecholate and protonated salicylate form. The calculated structure of the Mn(III)Proto³⁻ complex is shown in Figure 9.7. Consistent with the electrochemical data, all complexes were predicted to have a distorted octahedral configuration due to chelation through the three catechol donor groups. Selected bond lengths predicted by the computational simulation are shown in Table D.1 (Supplemental Material). Within a complex, the Fe-O bond lengths of the Fe(III)Proto³⁻ complex were fairly consistent. In contrast, the Mn(III)Proto³⁻ complex was found to exhibit heavy distortion, resulting in a difference between equatorial and axial Mn-O bonds (average distance of 0.31 Å). Mn(III) has a d⁴ electronic configuration, resulting in a distorted octahedral coordination sphere due to the Jahn-Teller effect. The axial bond lengths themselves are also separated by 0.18 Å, consistent with the known structure of solid phase MnOOH minerals (76).

The differences in the axial bond distances are reflected in bond angle distortion. There is minimal distortion of the cis O-M-O bond angles from their ideal values of 90° [average O-M-O bond angles of 91.4° for Mn(III)Proto³⁻, 90.2° for Mn(III)H₃Proto], although the average trans angles are somewhat distorted from the ideal measurement of 180° [average O-M-O bond angles 162.4° for Mn(III)Proto³⁻ and 165.9° for Mn(III)H₃Proto]. This displacement of axial atoms in the same direction with an approximately planar set of four equatorial atoms results in mild distortion of average cis- angles and pronounced distortion of trans angles. The reduced angular distortion of the theoretical Mn(III)H₃Proto complex [as

compared to Mn(III)Proto^{3-}] is consistent with assertion that 6-membered rings may be better able to accommodate the Jahn-Teller distortion of Mn(III)-complexes (77).

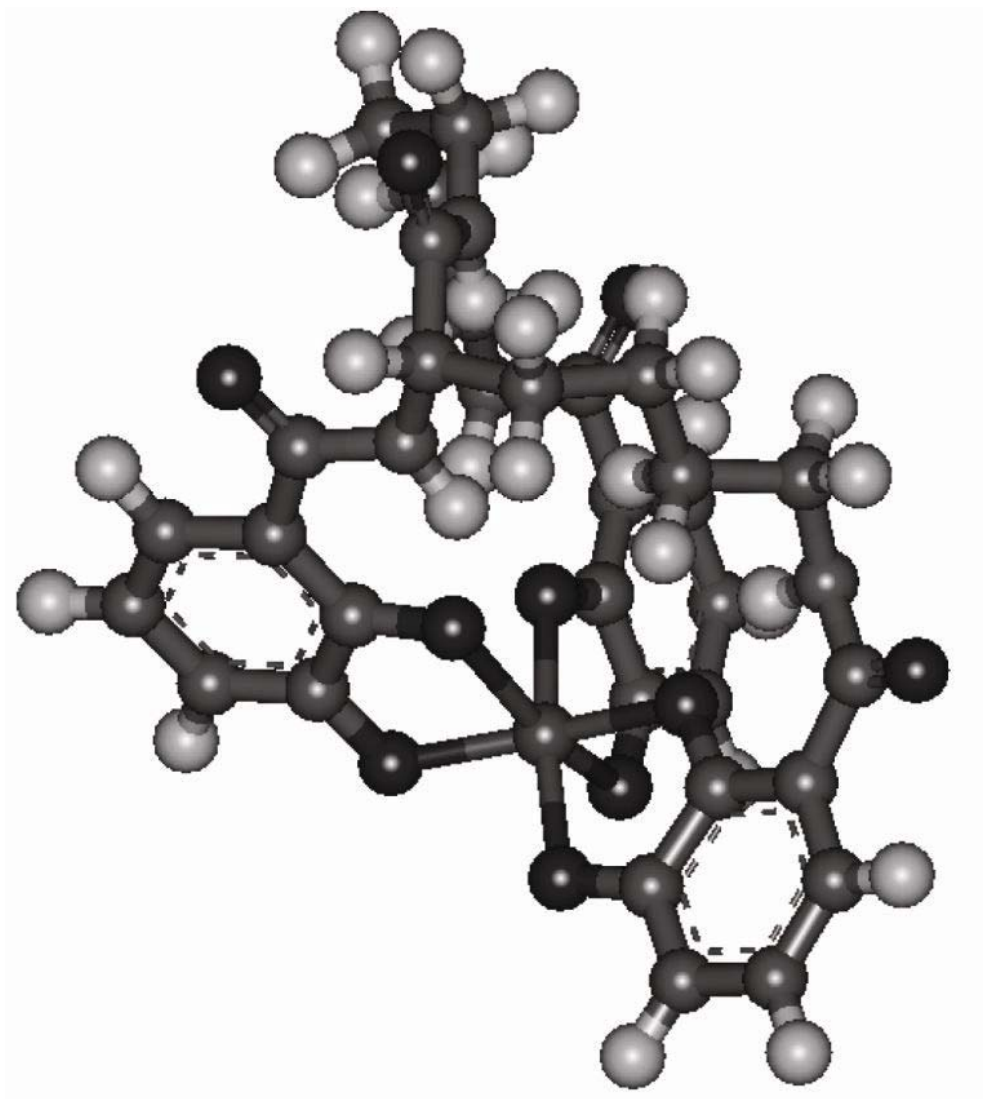
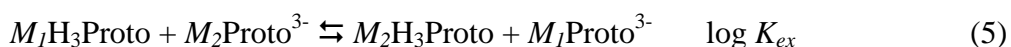


Figure 9.7 - Theoretical structure of the Mn(III)Proto^{3-} complex in aqueous solution calculated by density functional theory.

In addition to basic structural information, energy values for the $M(\text{III})\text{proto}^{3-}$ and $M\text{H}_3\text{Proto}$ complexes in aqueous solution were calculated for all complexes. The calculated energies for the $M(\text{III})\text{Proto}^{3-}$ complexes and their protonated $M(\text{III})\text{H}_3\text{Proto}$ forms are shown in Table D.2. Energy values can only be compared between systems that contain the same number of electrons and atoms. In order to obtain information regarding relative ease of protonation of metal-ligand complexes, the energy values of the complexes were set up in the form of a theoretical equilibrium, which took the form of:



where M_1 and M_2 are a first-row transition series, including Co(III), Mn(III), Cr(III), or Fe(III). To perform this comparison, the energy values (in Hartrees) on each side of the equilibrium were summed, and the difference between the two sides was taken as the difference in total strain energy of the reactants and products. The energy was converted to kJ mol^{-1} , and the resulting value was converted to an equilibrium constant ($\log K_{ex}$) to determine which protonated complex was the more stable of the two complexes using the Gibbs free energy equation. A positive calculated $\log K_{ex}$ value signifies that the protonated product complex ($M_2\text{H}_3\text{Proto}$ in Eq. 5) is favored. The resulting stability calculations demonstrate that the order of the relative ease of protonation of the four metal-protochelin complexes simulated here is $\text{Cr} > \text{Co} > \text{Mn} > \text{Fe}$. The energy values calculated for the $M(\text{III})\text{Proto}^{3-}$ complexes of Co(III), Cr(III), Fe(III), and Mn(III) are shown in Table D.2. Although it is not possible to observe all of the metal-protochelin complexes in solution, it can be informative to use theoretical simulations of the complexes to discern information

regarding their reactivity. Computational simulations, such as those obtained using DFT, provide theoretical estimations of the strain energy of complexes in solution, which can be used to predict which form of a complex may be the most stable. This approach thus can provide some insight into equilibria involving the calculated complexes. One example of a complex that can be studied using computational simulations is the protonated Mn(III)H₃Proto complex. Our results suggest that it is not possible to protonate the Mn(III)Proto³⁻ complex without resulting in reduction of the metal and subsequent dissociation of the complex, as discussed above; however, the protonation behavior may be significant to understanding complex breakdown.

The order described previously demonstrates that the Cr(III)Proto³⁻ complex is the easiest to protonate, followed by Co(III), Mn(III), and Fe(III). Protonation of the complex results in a shift in the coordination mode, as discussed above, to the salicylate binding mode. Such a shift in coordination mode results in a change from five-membered chelate rings to six-membered chelate rings, as well as a compression of bond lengths in the salicylate complex. Both factors may explain the trend in protonation that is observed in the theoretical calculations. Smaller metal ions form more stable complexes when six-membered chelate rings are formed with the donors of the chelators. Thus, Cr(III) and Co(III), which are the smaller of the four metals studied here (0.615 and 0.545 Å, respectively), may have a stronger preference for protonation of the catecholamide donor groups than Mn(III) and Fe(III), which are slightly larger metal ions (both 0.645 Å) (78). The relative increase in theoretical stability of Mn(III) to Fe(III) in six-membered rings is also consistent with a

recent report that noted that six-membered rings structures may be more stable with Mn(III) because they better accommodate Jahn-Teller distortion (77).

Mn(III) has a d^4 electronic configuration, which, as mentioned above, results in a distorted octahedral coordination sphere due to the Jahn-Teller effect. It can also be seen in the theoretical solution structure of the Mn(III)H₃Proto complex that one of the O-C-C-O dihedral angles is highly distorted from its ideal planar orientation, at 33°. This distorted dihedral angle may be necessary for the complex to accommodate the Jahn-Teller effect, and chelation of the metal through the catecholate binding mode will not allow the ligand the flexibility necessary to reach the lowest energy conformation. This may help to explain why a shift to the salicylate binding mode is more energetically favorable for the Mn(III) complex than the Fe(III) complex.

9.3.8 X-ray Spectroscopy of Metal-Protochelin Complexes

Mn K-edge XANES spectra of the Mn(III)Proto³⁻ complex are shown in Figure S9.1, Supplemental Material. In successive scans, the edge region of the spectrum changed shape, indicating beam-damage of the sample, even at ca. 10°K (liquid He cryostat). As beam damage occurred, the position and intensity of the white line shifted to lower energy, consistent with partial reduction of Mn to the 2+ oxidation state. The extent of reduction that occurred between the first and second scans is >7%, as determined by linear combination fit of the second scan with the first scan and aqueous Mn(II) [see Figure D.1, Supplemental Material]. Only the first scan was used for subsequent analysis. The edge position and intensity of the white line of the first scan of the complex spectrum is consistent with the 3+

oxidation state of the metal, as judged using linear combinations of Mn(III)HDFOB⁺ and Mn(II)HDFOB⁰ XANES spectra. Fits to the first Mn(III)Proto³⁻ spectrum yielded a best fit containing approximately 98.8 ± 0.03% Mn(III)HDFOB⁺, suggesting the complex predominantly contained Mn(III).

EXAFS spectra of the Fe(III)Proto³⁻, Fe(III)H₃Proto, and Mn(III)Proto³⁻ complexes were measured and fit to structural models to elucidate their structures in solution. The complexes discussed above were fit using SS (single scattering) paths for Me-O and Me-C (2nd and 3rd shells) (cf. Table 9.2). Multiple-scattering shells were also utilized, as described in the Supplemental Material and shown in Table 9.2. In the Fe(III)Proto³⁻ complex, the large FT peak at ca. 1.5 Å (R + ΔR) corresponds to EXAFS from the first O shell and exhibits $N = 5.3$ and $R = 2.000 \pm 0.006$ Å. This ca. 2.0 Å Fe-O distant is consistent with the expected structure of the Fe(III)Proto³⁻ complex, which is believed to be hexacoordinate in solution. The Fe-O bond length is consistent with a previous study of the EXAFS spectrum of the Fe(III)-enterobactin complex in catecholate coordination, which determined the same average Fe-O bond length (71). Based on DFT calculations, the Fe(III)Proto³⁻ shell corresponding to the 2.5 Å (R + ΔR) FT peak was fit using a 6-carbon shell at $R = 2.80 \pm 0.02$ Å. This result also agrees with the model proposed for enterobactin, where the second shell was found to be composed of 6 carbon atoms at a distance of 2.82 Å. A third shell of 6 proximal ring carbon atoms at 4.32 Å was needed for our fit.

The results of structural fitting of the EXAFS spectrum of the Mn(III)Proto³⁻ complex are also shown in Figure 9.8 and Table 9.2. For this complex, a similar model was used to fit the spectrum, although it was necessary to add a fourth shell to the fit to obtain a more

accurate fit. The first shell of the fit contained 4 oxygen atoms located at an average distance of $1.86 \pm 0.01 \text{ \AA}$, and the second shell of the fit corresponds to the remaining 2 oxygen atoms, which are found an average of $2.25 \pm 0.03 \text{ \AA}$ from the metal center of the complex. This result demonstrates that the coordination environment of the Mn center is a distorted octahedron, arising from the Jahn-Teller effect, as previously noted for other Mn(III)-siderophore complexes (32, 77).

Table 9.2 Amplitude reduction factors, coordination numbers, interatomic distances, and Debye-Waller factors for M-siderophore complexes investigated in this study

Complex	S_0^2	First Shell M-O			Second Shell M-C			Third Shell M-C			Multiple Scattering M-C-O		
		N_O	R_O (Å)	σ_O^2 (Å ²)	N_{C2}	R_{C2} (Å)	σ_{C2}^2 (Å ²)	N_{C3}	R_{C3} (Å)	σ_{C3}^2 (Å ²)	N_{C-O}	R_{C-O} (Å)	σ_{C-O}^2 (Å ²)
Fe-Ent (cat) ^a	0.87	6	2.00	0.0053	6	2.82	0.0052	ND	ND	ND	ND	ND	ND
Fe-Ent (sal) ^a	0.86	6	1.98	0.0076	6	2.83	0.0049	ND	ND	ND	ND	ND	ND
(III)Proto ³⁻ (cat)	0.87 ^b	5.3[5] ^d	2.000[6]	0.0077[8]	6 ^e	2.80[2]	0.010[2]	6 ^e	4.32[3]	0.013[3]	12 ^e	3.06[3]	0.005[4]
(III)H ₃ Proto (sal)	0.87 ^b	4.6[7] ^d	1.97[1]	0.009[1]	6 ^e	2.81[3]	0.015[3]	6 ^e	4.26[5]	0.018[7]	12 ^e	3.14[5]	0.03[1]
					3 ^e	3.34[5]	0.012[7]						
ι(III)Proto ³⁻ (cat)	0.835 ^c	4 ^{e,f}	1.86[1]	0.0055[7]	6 ^e	2.64[4]	0.010[3]	6 ^e	4.16[4]	0.003[3]	12 ^e	2.88[5]	0.006[5]
		2 ^{e,f}	2.25[3]	0.009[4]									

Numbers in brackets represent uncertainty of the last decimal place of their respective values.

^a Data for Ent complexes is from Abergel et al. 2006.

^{b,c} Amplitude reduction factors were obtained from (b) (Duckworth et al. 2008a), and (c) (Webb et al. 2005a).

^d ESD values are model-dependent standard deviations. If the atoms in this specific shell are non-normally distributed (as expected for Fe(III)H₃Proto and Fe(III)Proto³⁻ based on DFT, cf. Table S1), then the fit-derived N values may deviate significantly from physical reality, and this deviation may not be captured in the stated ESD.

^e Fixed coordination number.

^f N = 4 and N = 2 represent oxygen atoms located at axial (N = 2) and equatorial (N = 4) positions of a Jahn-Teller distorted complex.

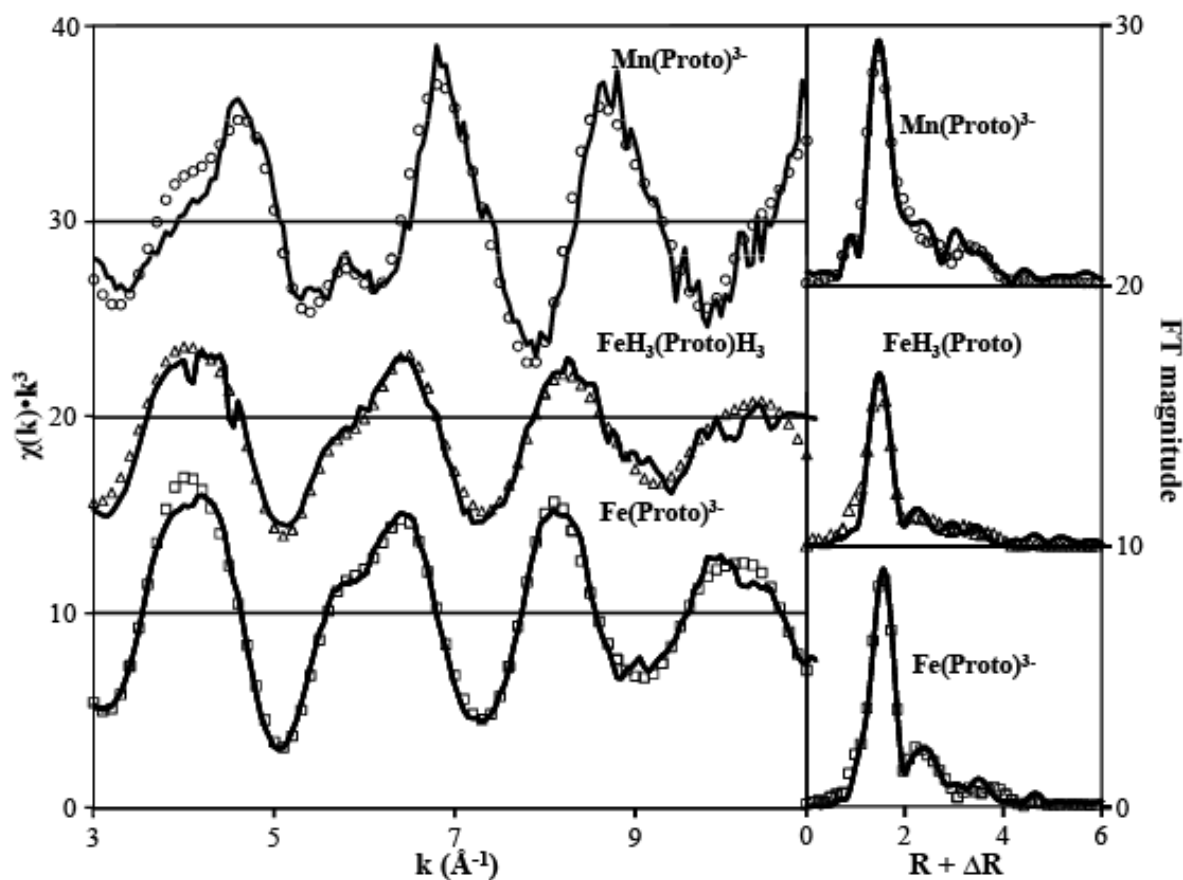


Figure 9.8 - K-edge EXAFS spectra of the Mn(III)Proto^{3-} complex, the Fe(III)Proto^{3-} complex bound through the catechol binding mode, and the $\text{Fe(III)H}_3\text{Proto}$ complex bound through the salicylate binding mode. Solid lines indicate experimental data, whereas points indicate the fit of a structural model. The optimized parameters used to produce the fit are shown in Table 2.

EXAFS measurements were also made of the protonated $\text{Fe(III)H}_3\text{Proto}$ complex. As discussed above, at lower solution pH values, the catechol groups are protonated, resulting in a shift in coordination modes to the salicylate binding mode. Upon protonation, the solubility of the complex decreases greatly due to the loss of its overall charge, and it precipitates out of solution as a neutral salt. As such, measurements of this complex were

performed on a colloidal suspension of Fe(III)H₃Proto. The salicylate binding mode complex was determined using a similar three-shell model as the catecholate binding mode complex. The number of O atoms found in the inner coordination sphere, however, was found to be 4.6, slightly less than the expected six O atoms. The average distance of the oxygen atoms, was found to be $1.97 \pm 0.01 \text{ \AA}$, agreeing with a previous study of the salicylate binding mode of enterobactin with Fe(III) ($R = 1.98 \text{ \AA}$). Additionally, the second shell was fit at an average distance of $2.81 \pm 0.03 \text{ \AA}$, compared to 2.83 \AA in the Fe(III)-enterobactin salicylate complex. These results demonstrate that the Fe-O bond lengths of the Fe(III)Proto³⁻ complex contract upon protonation. A similar observation was made in the Fe(III)-enterobactin system (71). This contraction likely arises due to a combination of the coordination geometry of the salicylate binding mode (six-membered chelate ring) and the nature of the hybridization of the orbitals involved in coordination (one sp² and one sp³ in salicylate binding mode and two sp³ orbitals in catecholate binding mode).

The fits of complexes in catecholate coordination [viz. Mn(III)Proto³⁻ and Fe(III)Proto³⁻] are improved by the inclusion of multiple scattering paths. Triangular multiple M-C-O paths were found to be at $2.88\text{-}3.14 \text{ \AA}$, consistent with the geometry of the complex from single scattering paths and DFT-calculated structures (as discussed below). The paths were significant for Fe(III)Proto³⁻ and Mn(III)Proto³⁻ as indicated by improvement of the R-factor at the 95% confidence level (79, 80). For Fe(III)H₃Proto in salicylate coordination, inclusion of this shell does not improve the fit, but is included for self-consistency of the structural model (see Supplemental Material).

Comparison of the theoretical structures of the Fe(III)-protochelin complex with the structures determined by EXAFS reveals strong agreement between the theoretical values and the experimentally-determined values (see Supplemental Material, Table D.1). For the Fe(III) complexes, the Fe-O bond lengths that are calculated ($R = 2.04 \pm 0.06 \text{ \AA}$) are slightly longer than the values determined from the EXAFS analysis of the complex in solution (ca. 2.0 \AA). The calculated Fe-O bond distances are not normally distributed (cf. Table D.1), an insight which may help to explain low coordination numbers seen in structural fits of the Fe(III)-Proto complexes (Table 9.2). A non-normal distribution of atoms may result in a systematically low N as determined by EXAFS fitting, as is observed in the first shell of our fits for these complexes.

The simulation of Mn(III)Proto³⁻ is also consistent with structures determined from EXAFS fits. Calculated Mn-O distances agree well with the average 1st and 2nd shell distance fits. The distortion in this complex was predicted to take place in two M-O bonds that are situated trans- from each other, which is accommodated in the case of the rigid catecholate donor group by a change in the angle of coordination and a concurrent shortening of the second M-O bond length on the donor group. Although Jahn-Teller distortion normally occurs in a trans-configuration, which facilitates breaking the degeneracy of the e_g orbitals in an octahedral complex, it is interesting that a complex with rigid conjugated donor groups is flexible enough to allow such a structural transition to occur.

9.3.9 Relating Complex Structure to Stability

Previous studies have shown that Mn(III)-siderophore complexes may have higher or lower stability constants than the corresponding Fe(III)-complexes (23, 32). A comparison of Mn(III)- and Fe(III)-siderophore complexes with DFOB and Proto (Table 9.1) suggests that catechol moieties have a larger preference for Fe(III) ($\Delta \log \beta_{110} = 3.0$) than hydroxamate groups ($\Delta \log \beta_{110} = 2.1$). It is possible that different siderophore moieties may favor the binding of specific metals. For example, catechol groups are particularly effective at binding Fe(III) (7), and may be slightly less effective at binding Mn(III). In contrast, carboxylate moieties may have a higher affinity for Mn(III) than Fe(III) (81). However, other structural factors may also affect the relative stability of complexes. Structural distortion of complexes away from ideal high-symmetry structures, as reflected in Debye-Waller factors and bond distances (32), and by distortion of complex angles (70), have been shown to be strongly related to siderophore-metal complex stability. Mn(III) has a d^4 electronic configuration, which, as mentioned above with regard to trans O-M-O and O-C-C-O dihedral angles, results in a highly distorted octahedral coordination sphere due to the Jahn-Teller effect. Thus, both the binding moieties and overall architecture may help to determine the relative affinities of siderophores for Fe(III) and Mn(III). A more in-depth discussion of this concept will be provided in a future report (77).

9.3.10 Implications for Metal Transport and Uptake

The results of the above experiments demonstrate that catecholate siderophores are able to form complexes with non-ferric metals Mn and Co, and that this chelation reaction

can promote the air-oxidation of Mn(II) to Mn(III). However, the results also suggest that the Mn(III) complex that is formed is unstable at environmental conditions on a time frame of hours, and that the complex formed between Co(II) and protochelin degrades rapidly at any pH. These results have interesting implications for the role of catecholate siderophores in environmental cycling of metals. The chelation and subsequent air oxidation of Mn(II) results in the formation of a Mn(III)-complex with presumably lower stability than that of Fe(III) complexes. Although the stability constants differ by three orders of magnitude, this difference in stability may still be small enough to allow interference with iron uptake and metabolism by siderophores in the environments that contain high concentrations of manganese, in a manner similar to what has been proposed for DFOB (Duckworth et al., 2009a).

The results of this study also have significant implications for the biological uptake of metals. In nature, some other catecholamide donor group siderophores have been observed to make use of hydrolysis reactions to assist in the intracellular release of complexed metals. The most notable example of this is enterobactin (Figure 9.1), the Fe(III) complex of which is taken into the bacterial cell, where the trilactone ring is broken into three dihydroxybenzyl subunits to assist in the removal of Fe(III) (82). A similar hydrolysis reaction is also observed in the bacterial siderophore brasilibactin A, which also contains an ester group in its backbone. However, it is unclear whether this reaction plays any role in the physiological function of the siderophore (83). Although it is not possible to say with any certainty whether the degradation of protochelin is utilized to facilitate intracellular release of Fe(III), the possibility does exist due to the relative instability of the molecule.

The electrochemistry of protochelin suggests that the redox chemistry of the catecholate ligand may play a significant role in the release of metals after uptake. A redox reaction centered on the catechol donor groups could facilitate dissociation of the metal from the complex. A previous study investigated the electrochemistry of Mn-catechol complexes and showed that upon oxidation of the catechol groups as those in protochelin to quinone groups, their affinity for chelating metals is significantly reduced (84), which may facilitate metal release. Ligand oxidation and metal release could be followed by reduction of the resulting quinone moieties back to catechol groups, regenerating the original siderophore. As mentioned above, some organisms make use of siderophore degradation to release Fe(III) from its complex. In the case of protochelin, however, it may be possible to release the metal from the siderophore through an electrochemical reaction without subsequent degradation of the ligand. This mechanism may allow the organism to avoid spending the metabolic cost associated with the production of a new molecule of the siderophore.

Protonation of the metal-ligand complex also can facilitate the removal of the metal from the complex. Although computational results predict Fe(III) to be the most difficult metal-protochelin complex to protonate, the complex undergoes a salicylate shift in coordination mode at circumneutral to acidic pH. This behavior has been proposed as having a role in the Fe(III) release mechanism of catecholamide siderophores; not only does the siderophore complex have lower affinity for binding 3+ metal ions in the salicylate binding mode, but there is also a drastic shift in the redox potentials of Fe(III) complexes, moving them into the range where Fe(III) can be reduced by biological reductants (71, 85).

The characteristics of metal selectivity that are suggested by this study as a result of ligand design may have broader implications for siderophore biogeochemistry. Another study is currently underway to systematically explore the role that donor group identity plays in metal selectivity of siderophores. The understanding that can be gained from such an analysis can provide a more thorough understanding of the roles of siderophores in trace metal cycling in the environment.

9.4 References

1. Crumbliss, A. L., and Harrington, J. M. (2009) Iron sequestration by small molecules: Thermodynamic and kinetic studies of natural siderophores and synthetic model compounds, In *Adv. Inorg. Chem.* (van Eldik, R., Ed.), pp 179-250.
2. Raymond, K. N., and Dertz, E. A. (2004) In *Iron Transport in Bacteria* (Crosa, J. H., Rey, A. R., and Payne, S. M., Eds.), p 3, ASM Press, Washington, D.C.
3. Renshaw, J. C., Robson, G. D., Trinci, A. P. J., Wiebe, M. G., Livens, F. R., Collison, D., and Taylor, R. J. (2002) Fungal siderophores: structures, functions and applications, *Mycol. Res.* 106, 1123.
4. Kraemer, S. M., Butler, A., Borer, P., and Cervini-Silva, J. (2005) Siderophores and the Dissolution of Iron-bearing Minerals in Marine Systems, In *Molecular Geomicrobiology* (Banfield, J. F., Cervini-Silva, J., and Nealson, K. H., Eds.), Mineralogical Society of America, Chantilly, VA.
5. Marschner, H., Romheld, V., and Kissel, M. (1986) Different strategies in higher plants immobilization and uptake of iron, *J. Plant Nutr.* 9, 695-713.
6. Hider, R. C., and Kong, X. (2010) Chemistry and biology of siderophores, *Nat. Prod. Rep.* 27, 637-657.
7. Albrecht-Gary, A. M., and Crumbliss, A. L. (1998) Coordination chemistry of siderophores: thermodynamics and kinetics of iron chelation and release, In *Metal Ions in Biological Systems* (Sigel, A., and Sigel, H., Ed.), M. Dekker, New York.
8. Clarke, E. T., Tari, L. W., and Vogel, H. J. (2001) Structural Biology of Bacterial Iron Uptake Systems, *Curr. Top. Med. Chem.* 1, 7.
9. Winkelmann, G. (2004) Ecology of Siderophores, In *Iron Transport in Bacteria* (Crosa, J. H., Rey, A. R., and Payne, S. M., Eds.), p 437, ASM Press, Washington, D.C.
10. Cornish, A. S., and Page, W. J. (1995) Production of the Triscatecholate Siderophore Protochelin by *Azotobacter vinelandii*, *BioMetals* 8, 332-338.
11. Duhme, A. K., Hider, R. C., Naldrett, M. J., and Pau, R. N. (1998) The stability of the molybdenum-azotochelin complex and its effect on siderophore production in *Azotobacter vinelandii*, *J. Biol. Inorg. Chem.* 3, 520-526.
12. Bellenger, J. P., Arnaud-Neu, F., Asfari, Z., Myneni, S. C. B., Stiefel, E. I., and Kraepiel, A. M. L. (2007) Complexation of oxoanions and cationic metals by the biscatecholate siderophore azotochelin, *J. Biol. Inorg. Chem.* 12, 367-376.

13. Khodr, H. H., Hider, R. C., and Duhme-Klair, A. K. (2002) The iron-binding properties of aminochelin, the mono(catecholamide) siderophore of *Azotobacter vinelandii*, *J. Biol. Inorg. Chem.* 7, 891-896.
14. Cornish, A. S., and Page, W. J. (2000) Role of molybdate and other transition metals in the accumulation of protochelin by *Azotobacter vinelandii*, *Appl. Environ. Microbiol.* 66, 1580-1586.
15. Bellenger, J. P., Wichard, T., and Kraepiel, A. M. L. (2008) Vanadium requirements and uptake kinetics in the dinitrogen-fixing bacterium *Azotobacter vinelandii*, *Appl. Environ. Microbiol.* 74, 1478-1484.
16. Bellenger, J. P., Wichard, T., Kustka, A. B., and Kraepiel, A. M. L. (2008) Uptake of molybdenum and vanadium by a nitrogen-fixing soil bacterium using siderophores *Nat. Geosci.* 1, 243-246.
17. Bellenger, J. P., Wichard, T., Xu, Y., and Kraepiel, A. M. L. (2011) Essential metals for nitrogen fixation in a free-living N₂-fixing bacterium: chelation, homeostasis and high use efficiency, *Environmental Microbiology* 13, 1395-1411.
18. Wichard, T., Bellenger, J. P., Loison, A., and Kraepiel, A. M. L. (2008) Catechol siderophores control tungsten uptake and toxicity in the nitrogen-fixing bacterium *Azotobacter vinelandii*, *Environ. Sci. Technol.* 42, 2408-2413.
19. Kraepiel, A. M. L., Bellenger, J. P., Wichard, T., and Morel, F. M. M. (2009) Multiple roles of siderophores in free-living nitrogen-fixing bacteria, *Biometals* 22, 573-581.
20. Duckworth, O. W., Sposito, G., and Bargar, J. R. (2008) Sorption of ferric iron from ferrioxamine B to synthetic and biogenic layer type manganese oxides, submitted.
21. Duckworth, O. W., and Sposito, G. (2005) Siderophore-manganese(III) interactions I. Air-oxidation of manganese(II) promoted by desferrioxamine B, *Environmental Science and Technology* 39, 6037-6044.
22. Parker, D. L., Morita, T., Mozafarzadeh, M. L., Verity, R., McCarthy, J. K., and Tebo, B. M. (2007) Inter-relationships of MnO₂ precipitation, siderophore-Mn(III) complex formation, siderophore degradation, and iron limitation in Mn(III)-oxidizing bacterial cultures, *Geochim. Cosmochim. Acta* 71, 5672.
23. Parker, D. L., Sposito, G., and Tebo, B. M. (2004) Manganese(III) binding to a pyoverdine siderophore produced by a manganese(II)-oxidizing bacterium, *Geochimica et Cosmochimica Acta* 68, 4809-4820.

24. Boukhalfa, H., Reilly, S. D., and Neu, M. P. (2007) Complexation of Pu(IV) with the natural siderophore desferrioxamine B and the redox properties of Pu(IV)(siderophore) complexes *Inorg. Chem.* *46*, 1018.
25. Boukhalfa, H., Reilly, S. D., Smith, W. H., and Neu, M. P. (2004) EDTA and mixed-ligand complexes of tetravalent and trivalent plutonium *Inorg. Chem.* *43*, 5816.
26. Neu, M. P., Icopini, G. A., and Boukhalfa, H. (2005) Plutonium speciation affected by environmental bacteria *Radiochim. Acta* *93*, 705.
27. Harris, W. R., Amin, S. A., Kuepper, F. C., Green, D. H., and Carrano, C. J. (2007) Borate binding to siderophores: Structure and stability *J. Am. Chem. Soc.* *129*, 12263.
28. Mishra, B., Haack, E. A., Maurice, P. A., and Bunker, B. A. (2009) Effects of the Microbial Siderophore DFO-B on Pb and Cd Speciation in Aqueous Solution *Environ. Sci. Technol.* *43*, 94-100.
29. Dahlheimer, S. R., Neal, C. R., and Fein, J. B. (2007) Potential mobilization of platinum-group elements by siderophores in surface environments *Environ. Sci. Technol.* *41*, 870-875.
30. Frazier, S. W., Kretzschmar, K., and Kraemer, S. M. (2005) Bacterial siderophores promote dissolution of UO₂ under reducing conditions *Environ. Sci. Technol.* *39*, 5709-5715.
31. Szabo, O., and Farkas, E. (2011) Characterization of Mn(II) and Mn(III) binding capability of natural siderophores desferrioxamine B and desferricoprogen as well as model hydroxamic acids, *Inorg. Chim. Acta* *376*, 500-508.
32. Duckworth, O. W., Bargar, J. R., and Sposito, G. (2009) Quantitative structure-activity relationships for aqueous metal-siderophore complexes, *Environ. Sci. Technol.* *43*, 343-349.
33. Hernlem, B. J., Vane, L. M., and Sayles, G. D. (1999) The application of siderophores for metal recovery and waste remediation: Examination of correlations for prediction of metal affinities, *Water Resources* *33*, 951-960.
34. Duhme, A. K., Hider, R. C., and Khodr, H. H. (1997) Synthesis and iron-binding properties of protochelin, the tris(catecholamide) siderophore of *Azotobacter vinelandii* *Chem. Ber. Recueil* *130*, 969-973.
35. Frisch, M. J., Trucks, G. W., Schlegel, H. B., Scuseria, G. E., Robb, M. A., Cheeseman, J. R., Scalmani, G., Barone, V., Mennucci, B., Petersson, G. A., Nakatsuji, H., Caricato, M., Li, X., Hratchian, H. P., Izmaylov, A. F., Bloino, J., Zheng, G., Sonnenberg, J. L., Hada, M., Ehara, M., Toyota, K., Fukuda, R.,

- Hasegawa, J., Ishida, M., Nakajima, T., Honda, Y., Kitao, O., Nakai, H., Vreven, T., Montgomery, J., J.A., Peralta, J. E., Ogliaro, F., Bearpark, M., Heyd, J. J., Brothers, E., Kudin, K. N., Staroverov, V. N., Kobayashi, R., Normand, J., Raghavachari, K., Rendell, A., Burant, J. C., Iyengar, S. S., Tomasi, J., Cossi, M., Rega, N., Millam, N. J., Klene, M., Knox, J. E., Cross, J. B., Bakken, V., Adamo, C., Jaramillo, J., Gomperts, R., Stratmann, R. E., Yazyev, O., Austin, A. J., Cammi, R., Pomelli, C., Ochterski, J. W., Martin, R. L., Morokuma, K., Zakrzewski, V. G., Voth, G. A., Salvador, P., Dannenberg, J. J., Dapprich, S., Daniels, A. D., Farkas, Ö., Foresman, J. B., Ortiz, J. V., Cioslowski, J., and Fox, D. J. (2009) Gaussian 09, B,01 ed., Gaussian, Inc, Wallingford, CT.
36. Becke, A. D. (1993) Density-functional thermochemistry. III. The role of exact exchange, *J. Chem. Phys.* *98*, 5648-5652.
 37. Lee, C., Yang, W., and Parr, R. G. (1988) Development of the Colle-Salvetti correlation-energy formula into a functional of the electron density, *Phys. Rev. B* *37*, 785-789.
 38. Tomasi, J., Mennucci, B., and Cammi, R. (2005) Quantum mechanical continuum solvation models, *Chem. Rev.* *105*, 2999-3094.
 39. Levina, A., Armstrong, R. S., and Lay, P. A. (2005) Three-dimensional structure determination using multiple-scattering analysis of XAFS: Applications to metalloproteins and coordination chemistry, *Coord. Chem. Rev.* *249*, 141-160.
 40. Kelly, S. D., Hesterberg, D., and Ravel, B. (2008) Analysis of Soils and Minerals Using X-ray Absorption Spectroscopy, In *Methods of Soil Analysis* (Ulery, A. L., and Drees, L. R., Eds.), Soil Science Society of America, Madison, WI.
 41. Webb, S. M. (2005) SIXPACK: A graphical user interface for XAS analysis using IFEFFIT, *Phys. Scr.*, 1011-1014.
 42. Newville, M. (2001) *IFEFFIT*: Interactive XAFS analysis and *FEFF* fitting, *J. Synchrotron Rad.* *8*, 322-324.
 43. Duckworth, O. W., Jarzecki, A. A., Bargar, J. R., Oyerinde, O., Spiro, T. G., and Sposito, G. (2009) An exceptionally stable cobalt(III)-desferrioxamine B complex, *Marine Chem.* *113*, 114–122.
 44. Rehr, J. J., Kas, J. J., Prange, M. P., Sorini, A. P., Takimoto, Y., and Vila, F. (2009) Ab initio theory and calculations of X-ray spectra, *Comptes Rendus Physique* *10*, 548-559.

45. Duckworth, O. W., Bargar, J. R., and Sposito, G. (2008) Sorption of ferric iron from ferrioxamine B to synthetic and biogenic layer type manganese oxides, *Geochim. Cosmochim. Acta* 72, 3371-3380.
46. Webb, S. M., Tebo, B. M., and Bargar, J. R. (2005) Structural characterization of biogenic Mn oxides produced in seawater by the marine *bacillus sp.* strain SG-1, *Am. Min.* 90, 1342-1357.
47. Gans, P., Sabatini, A., and Vacca, A. (1996) Investigation of equilibria in solution. Determination of equilibrium constants with HYPERQUAD suite of programs, *Talanta* 43, 1739-1753.
48. Schwarzenbach, G., and Schwarzenbach, K. (1963) Hydroxamatkomplexe I. Die Stabilität der Eisen(III)-Komplexe einfacher Hydroxamsäuren und des Ferrioxamins B, *Helv. Chim. Acta* 46, 1390-1400.
49. Sanford, A. L., Morton, S. W., Whitehouse, K. L., Oara, H. M., Lugo-Morales, L. Z., Roberts, J. G., and Sombers, L. A. (2010) Voltammetric Detection of Hydrogen Peroxide at Carbon Fiber Microelectrodes, *Anal. Chem.* 82, 5205-5210.
50. Taraz, K., Ehlert, G., Geisen, K., Budzikiewicz, H., Korth, H., and Pulverer, Z. (1990) Chemicals from bacteria. 40. Protocheline - A catechol siderophore from a bacterium (DMS no. 5746) *Z. Naturforsch.* 45b, 1327-1332.
51. Loomis, L. D., and Raymond, K. N. (1991) Solution equilibria of enterobactin and metal-enterobactin complexes, *Inorg. Chem.* 30, 906-911.
52. Harris, W. R., Carrano, C. R., Cooper, S. R., Sofen, S. R., Avdeef, A. E., McArdle, J. V., and Raymond, K. N. (1979) Coordination chemistry of microbial iron transport compounds. 19. Stability constants and electrochemical behavior of ferric enterobactin and model complexes, *J. Am. Chem. Soc.* 101, 6097-6104.
53. Winkelmann, G. (2007) Ecology of Siderophores with special reference to the fungi, *BioMetals* 20, 379-392.
54. Essén, S. A., Bylund, D., and Holmström, S. J. A. (2006) Quantification of hydroxamate siderophores in soil solutions of podzolic soil profiles in Sweden *BioMetals* 19, 269-282.
55. Holmström, S. J. A., Lundstrom, U. S., Finlay, R. D., and Van Hees, P. A. W. (2004) Siderophores in forest soil solution, *Biogeochemistry* 71, 247-258.
56. Duckworth, O. W., Holmström, S. J. M., Pena, J., and Sposito, G. (2009) Biogeochemistry of iron oxidation in a circumneutral freshwater habitat, *Chem. Geol.* 260, 149-158.

57. Mucha, P., Rekowski, P., Kosakowska, A., and Kupryszewski, G. (1999) Separation of siderophores by capillary electrophoresis, *J. Chromatog. A* 830, 183-189.
58. Mawji, E., Gledhill, M., Milton, J. A., Tarran, G. A., Ussher, S., Thompson, A., Wolff, G. A., Worsfold, P. J., and Achterbeg, E. P. (2008) Hydroxamate Siderophores: Occurrence and Importance in the Atlantic Ocean, *Environ. Sci. Technol.* 42, 8675-8680.
59. Selig, H., Keinath, T. M., and Weber, W. J. (2003) Sorption and Manganese-Induced Oxidative Coupling of Hydroxylated Aromatic Compounds by Natural Geosorbents, *Environ. Sci. Technol.* 37, 4122-4127.
60. Devlin, H. R., and Harris, I. J. (1984) Mechanism of the oxidation of aqueous phenol with dissolved oxygen, *Ind. Eng. Chem. Fundam.* 23, 387-392.
61. Schweigert, N., Zehnder, A. J. B., and Eggen, R. I. L. (2001) Chemical properties of catechols and their molecular modes of toxic action in cells, from microorganisms to mammals, *Environ. Microbiol.* 3, 81-91.
62. Tebo, B. M., Johnson, H. A., McCarthy, J. K., and Templeton, A. S. (2005) Geomicrobiology of manganese(II) oxidation, *Trends Microbiol.* 13, 421-428.
63. Buerge, I. J., and Hug, S. J. (1998) Influence of organic ligands on chromium(VI) reduction by iron(II), *Environ. Sci. Technol.* 32, 2092-2099.
64. Strathmann, T. J., and Stone, A. T. (2002) Reduction of the pesticides oxamyl and methomyl by Fe(II): Effect of pH and inorganic ligands, *Environ. Sci. Technol.* 36, 653-661.
65. Parker, D. L. (2010), Personal communication.
66. Hewkin, D. J., and Prince, R. H. (1970) The mechanism of octahedral complex formation by labile metal ions, *Coord. Chem. Rev.* 5, 45-73.
67. Martell, A. E., and Smith, R. M. (2003) *Critical Stability Constant Database*, National Institute of Science and Technology (NIST), Gaithersburg, MD.
68. Kraemer, S. M. (2004) Iron oxide dissolution and solubility in the presence of siderophores, *Aquat. Sci.* 66, 3-18.
69. Harris, W. R., Carrano, C. J., and Raymond, K. N. (1979) Coordination chemistry of microbial iron transport compounds. 16. Isolation, characterization, and formation constants of ferric aerobactin, *J. Am. Chem. Soc.* 101, 2722.

70. Hay, B. P., Dixon, D. A., Vargas, R., Garza, J., and Raymond, K. N. (2001) Structural Criteria for the Rational Design of Selective Ligands. 3. Quantitative Structure-Stability Relationship for Iron(III) Complexation by Tris-Catecholamide Siderophores, *Inorg. Chem.* *40*, 3922-3935.
71. Abergel, R. J., Warner, J. A., Shuh, D. K., and Raymond, K. N. (2006) Enterobactin protonation and iron release: structural characterization of the salicylate coordination shift in ferric enterobactin, *J. Am. Chem. Soc.* *128*, 8920-8931.
72. Hou, Z., Stack, T. D. P., Sunderland, C. J., and Raymond, K. N. (1997) Enhanced iron(III) chelation through ligand predisposition: syntheses, structures and stability of tris-catecholate enterobactin analogs, *Inorg. Chim. Acta* *263*, 341-355.
73. Heien, M., Johnson, M. A., and Wightman, R. M. (2004) Resolving neurotransmitters detected by fast-scan cyclic voltammetry, *Analytical Chemistry* *76*, 5697-5704.
74. Roberts, J. G., Moody, B. P., McCarty, G. S., and Sombers, L. A. (2010) Specific Oxygen-Containing Functional Groups on the Carbon Surface Underlie an Enhanced Sensitivity to Dopamine at Electrochemically Pretreated Carbon Fiber Microelectrodes, *Langmuir* *26*, 9116-9122.
75. Bath, B. D., Michael, D. J., Trafton, B. J., Joseph, J. D., Runnels, P. L., and Wightman, R. M. (2000) Subsecond adsorption and desorption of dopamine at carbon-fiber microelectrodes, *Analytical Chemistry* *72*, 5994-6002.
76. Kohler, T., Armbruster, T., and Libowitzky, E. (1997) Hydrogen bonding and Jahn-Teller distortion in groutite, α -MnOOH, and manganite, γ -MnOOH, and their relations to the manganese dioxides ramsdellite and pyrolusite, *J. Solid State Chem.* *133*, 486-500.
77. Harrington, J. M., Parker, D. L., Jarzecki, A. A., Bargar, J. R., Tebo, B. M., and Duckworth, O. W. (2011) Structural dependence of manganese chelation by siderophores: Donor group dependence of complex stability and reactivity, *Geochim. Cosmochim. Acta*, in preparation.
78. Shannon, R. D. (1976) Revised Effective Ionic Radii and Systematic Studies of Interatomic Distances in Halides and Chalcogenides, *Acta Cryst.* *A32*, 751-767.
79. Hamilton, W. C. (1965) Significance Tests on the Crystallographic R Factor, *Acta Cryst.* *18*, 502-510.
80. Downward, L., Booth, C. H., Lukens, W. W., and Bridges, F. (2006) A Variation of the F-Test for Determining Statistical Relevance of Particular Parameters in EXAFS Fits In *13th International Conference on X-Ray Absorption Fine Structure* (Hedman, B., and Pianetta, P., Eds.), Stanford Synchrotron Radiation Laboratory, Stanford, CA.

81. Ahrland, S., Dahlgren, A., and Persson, I. (1990) Stabilities and hydrolysis of some iron(II) and manganese(III) complexes with chelating ligands, *Acta Agric. Scand.* *40*, 101-111.
82. Abergel, R. J., Zawadzka, A. M., Hoette, T. M., and Raymond, K. N. (2009) Enzymatic Hydrolysis of Trilactone Siderophores: Where Chiral Recognition Occurs in Enterobactin and Bacillibactin Iron Transport, *J. Am. Chem. Soc.* *131*, 12682-12692.
83. Harrington, J. M., Park, H., Ying, Y., Hong, J., and Crumbliss, A. L. (2011) Characterization of Fe(III) sequestration by an analog of the cytotoxic siderophore brasilibactin A: Implications for the iron transport mechanism in mycobacteria, *Metallomics* *3*, 464-471.
84. Bodini, M., Osorio, C., Valle, M. A. d., Arancibia, V., and Munoz, G. (1995) Redox chemistry of 3,4-dihydroxy-2-benzoic acid, its oxidation products and their interaction with manganese(II) and manganese(III), *Polyhedron* *14*, 2933-2936.
85. Rodgers, S. J., Lee, C. W., Ng, C. Y., and Raymond, K. N. (1987) Ferric ion sequestering agents. 15. Synthesis, solution chemistry, and electrochemistry of a new cationic analogue of enterobactin, *Inorg. Chem.* *26*, 1622-1625.

APPENDICES

APPENDIX A

Supplemental Information to Chapter 1:

Introduction to Monitoring Neurotransmission with Voltammetric Methods and Approaches for Technique Optimization

A.1 Material and Methods

A.1.1 Chemicals

All chemicals were purchased from Sigma-Aldrich Co., (St. Louis, MO) unless specified and used without additional processing. Electrochemical experiments were done in physiological pH 7.4 buffered solutions; Tris buffer (15 mM Tris, 3.25 mM KCl, 1.20 mM CaCl₂, 1.2 mM MgCl₂, 2 mM Na₂SO₄, 1.25 mM NaH₂PO₄, 145 mM NaCl), and phosphate buffered saline (PBS) (0.01 M phosphate, 0.0027 M KCl, 0.138 M NaCl). All aqueous solutions were made using doubly distilled deionized water (Barnstead EasyPure II, Dubuque, IA).

A.1.2 Electrode Fabrication

Elliptical disc microelectrodes with a polished angle of 15° or 30° were fabricated using P-55s pitch-based carbon fibers (~10 μm diameter) and cylindrical microelectrodes were fabricated using T-650 carbon fibers (~7 μm diameter) (Cytec Industries, Inc., Woodland Park, NJ) as previously described (1). Electrodes were polishing on a microelectrode beveler (BV-10) with a rotating diamond abrasive plate (104D) (Sutter Instruments, Novato, CA). 25 μm platinum wire (Goodfellow Cambridge Ltd., Huntingdon,

England) was used to construct platinum microelectrodes, following the same procedure. A Ag/AgCl reference electrode was employed (World Precision Instruments, Inc., Sarasota, FL).

Multichannel electrodes were constructed by inserting two P-55s carbon fibers into separate barrels of multibore glass (Friedrich & Dimmock, Inc., Millville, NJ), with dimensions of 100 μm ID and 600 μm OD. The fabrication was done as previously described, except isolated 25 μm tungsten leads (Goodfellow Cambridge Ltd., Huntingdon, England) were inserted into the back of the electrode to make the electrical connection. The electrode surface was polished at 30° to expose two planer disc electrodes separated by ~ 15 μm .

A.1.3 Flow Injection

A syringe pump (New Era Pump Systems, Inc., Wantagh, NY) supplied a continuous buffer flow of 1 mL/minute across the working and reference electrodes. Single two-second bolus injections were accomplished with a six-port HPLC valve and air actuator controlled by a digital valve interface (Valco Instruments Co., Inc, Houston, TX). The working electrode was positioned in a custom electrochemical cell using a micromanipulator (World Precision Instruments, Inc., Sarasota, FL). The flow injection apparatus was housed within a custom Faraday cage.

A.1.4 Electrochemical-Data Acquisition

The triangular detection waveform ranged from -0.4 V to +1.3 V at 400 V·s⁻¹ (2-5). For comparison of carbon and platinum electrodes, the waveform was +0.2 to +1.3 V, at 400 V·s⁻¹ and repeated at 10 Hz. These waveforms were output using a custom instrument for potential application to the electrochemical cell and current transduction (University of North Carolina at Chapel Hill, Department of Chemistry, Electronics Facility). TH-1 software (ESA, Chelmsford, MA) was used with a DAC/ADC card (NI 6251 M). A second card (NI 6711) was used for triggering the DACs and ADCs and for synchronization of the electrochemical experiment with flow injection. Signal processing (background subtraction, signal averaging, and digital filtering (4-pole Bessel Filter, 2 KHz) was software controlled.

A.1.5 Statistics

Data are presented as the mean ± standard deviation. One-way ANOVA with Tukey's post-hoc test was used to determine significance. Analysis of covariance (ANCOVA) was used for the comparison of linear regression results. In all cases, statistical significance is designated as $p < 0.05$. Statistical and graphical analyses were carried out using GraphPad Prism 5 (GraphPad Software, Inc., La Jolla, CA).

A.2 Comparing Electrode Substrates for H₂O₂ Oxidation

To characterize the oxidation of H₂O₂ using fast-scan cyclic voltammetry (FSCV), three substrates were compared. The chosen materials were carbon, platinum, and platinized carbon disc electrodes. Carbon and platinum electrodes were constructed following the

procedure outlined in A.1.2. The platinized carbon electrode was made by starting with a carbon-fiber microdisc electrode constructed from a glass-insulated P-55 carbon fiber, polished at an angle of 15°. Platinization of the carbon surface was accomplished by reducing a solution of hexachloroplatinate (50 mg of K_2PtCl_6 in 1.5 mL of 0.1 M H_2SO_4) on the electrode for 60 s. A square waveform that stepped from 0 V, to + 0.1 V was held for 5 ms, stepped down to -0.2 V and held for 20 ms, and returned to 0 V for 15 ms before the next cycle (vs. Ag/AgCl).

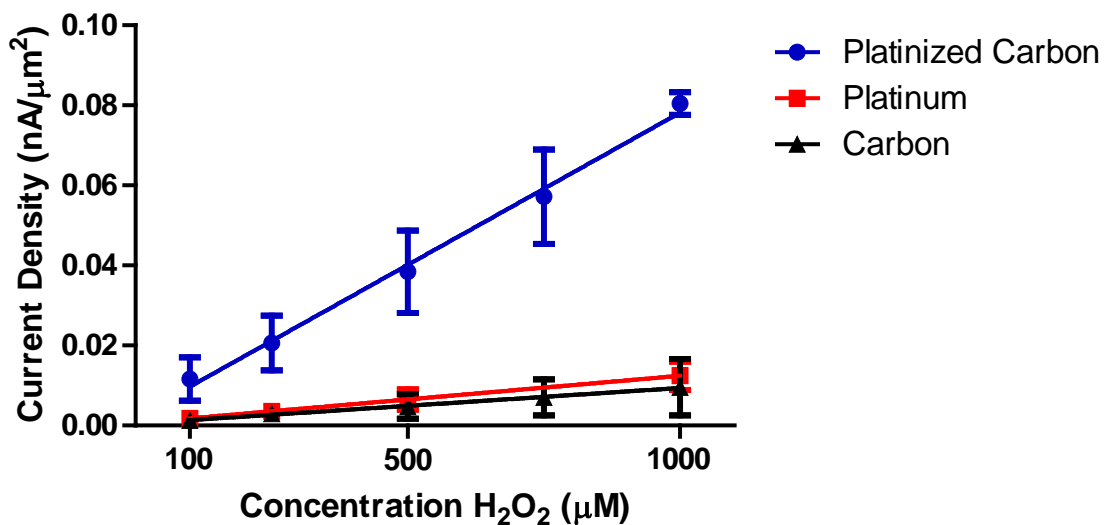


Figure A.1 - Comparison of electrode substrate sensitivity to hydrogen peroxide oxidation. Current density for the oxidation of H_2O_2 at carbon, platinum, and platinized carbon disc electrodes were plotted versus H_2O_2 concentration ($n = 5$ electrodes).

All platinum electrodes were electrochemically cleaned before use. This process required the electrode to be held at +2.0 V vs Ag/AgCl in 0.1 M H_2SO_4 for 30 sec. The electrodes were calibrated in the flow cell for H_2O_2 sensitivity, in pH 7.4 Tris buffer. After

normalizing for geometric surface area, the current density of the measurements indicated that platinized carbon electrodes were the most sensitive (Figure A.1). There was no significant difference in sensitivity between bare carbon and platinum. The enhanced sensitivity at the platinized surface was unexpected. It is possible that the enhanced sensitivity is a result of an increased real surface area over the geometric surface area (6). Platinization may have created a roughened surface. As current is proportional to surface area, the larger surface area of the platinized carbon electrode would result in an overestimation of sensitivity, because the real surface area was not corrected for in the current density normalization. The end result is a platinized electrode of similar geometric size to that of the other substrates, which could be adapted into a more sensitive neurochemical probe, without compromising spatial resolution.

A.3 Development of a Two-Channel, Carbon-Fiber, Microdisc-Electrode Array

When making neurochemical measurements, it is important to obtain as much chemical information as possible, while maintaining high spatial resolution. An electrode array would allow simultaneous electrochemical recording from multiple signaling molecules, to gain more chemical information. If the electrodes in the array are spaced close enough, the electrodes would be able to monitor the same microsphere, to retain the necessary spatial resolution to monitor a single signaling pathway. Arrays of carbon-fiber microelectrodes have been used to monitor a single neurotransmitter in spatially discrete locations (7). Conversely, the ability to monitor neurotransmitters in the same area would be more advantageous for determining centralized information. At some critical separation,

close spacing of the electrodes results in crosstalk (8) and the individual channels begin to act as one electrode (6). However, there are also benefits to having individual electrodes in close proximity. It has been shown that close spacing of parallel electrodes can induce redox cycling, which results in signal amplification (9, 10).

In order to design an electrode array with discrete channels, mass transport to the electrode surface must be considered. The diffusion layer thickness can be calculated and the electrode array will be constructed to minimize the overlap of the layers. Approximation of the diffusion layer thickness can be made with the following equation (6):

$$\delta_x(t) = \sqrt{\pi D_x t} \quad (1)$$

where δ is the diffusion layer thickness for the analyte, D is the diffusion coefficient for the analyte, and t is the time of electrolysis. However, determining the time of electrolysis is not that straightforward. The typical dopamine detection waveform (-0.4 to +1.3 V at 400 V·s⁻¹), is applied for 8.5 ms, while the period between scans that the electrode is held at -0.4 V is 91.5 ms. During this holding potential, dopamine concentrates at the surface, amplifying the signal (11). Using equation 1, calculations of the diffusion layer thickness resulted in 4 μm for a waveform duration of 8.5 ms and 14 μm for a duration of 100 ms.

Multichannel electrodes were constructed and an experiment was designed to test the performance of an array of two electrodes separated by ~15 μm . Figure A.2 is a representative scanning-electron micrograph of the electrode surface, showing the separation of the individually addressable channels.

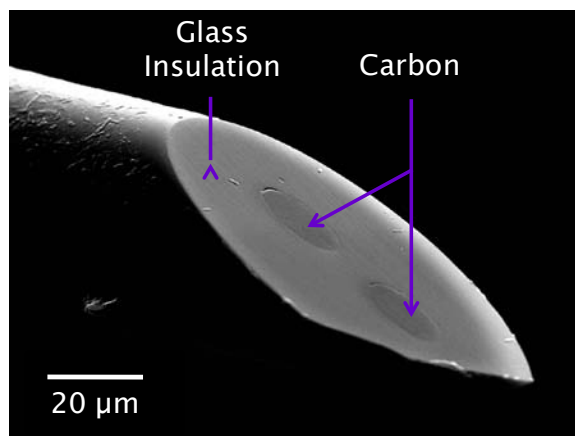


Figure A.2 - Representative scanning-electron micrograph of a dual-channel electrode.

The locally written LabView-based software can apply a distinct electrochemical waveform at each channel, enabling independent measurements. Data was collected with the dopamine waveform for 2 μM dopamine, in pH 7.4 Tris buffer. The two channels were addressed as either a single channel or dual channels. If the currents vary depending how the channels are addressed, then the operation of one channel is affecting the other. Figure A.3.A-B shows representative background-subtracted cyclic voltammograms for 2 μM dopamine for individual channels. The red voltammogram shows the response for dual channel measurements and the black voltammogram shows a single measurement. Figure A.3.C-D graphs the peak oxidative current. There is no significant difference between these groups (one-way ANOVA, Tukey's post-hoc test, $n = 4$ electrodes). These data show that this spacing permit separate neurochemical measurements within the same microsphere. The benefits of this electrode design will enable simultaneous monitoring of multiple signaling molecules that could not typically be monitored at a single electrode.

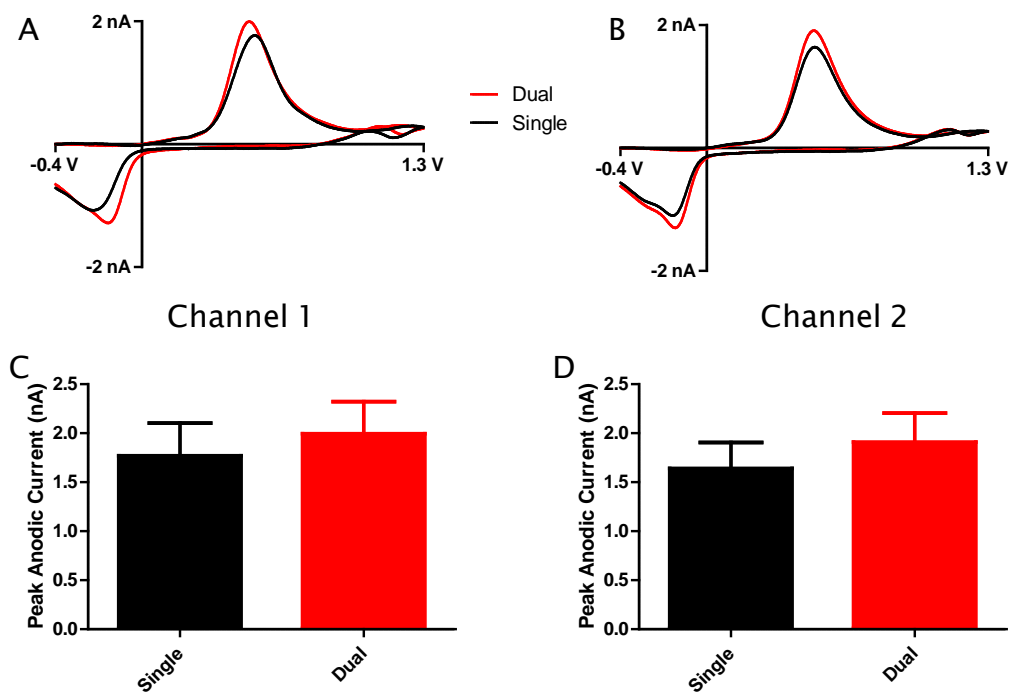


Figure A.3 - Analysis of multichannel electrodes for discrete information. (A and B) Averaged voltammograms for 2 μM dopamine, collected at channel 1 and 2 of a dual channel electrode, respectively. (C and D) Graphs the peak anodic current for channel 1 and 2 respectively (one-way ANOVA, Tukey post-hoc test, $n = 4$ electrodes).

A.4 pH Dependence of Charging Current and the Oxidation of H_2O_2 and Dopamine

The pH of brain tissue is tightly regulated and changes in this value are largely due to changes in metabolism and blood flow (12). Glucose metabolism produces carbon dioxide and lactic acid resulting in an acidic pH shift. This change in pH affects many biological processes. Shifts in pH have been shown to alter neurotransmitter uptake (13). Furthermore, dopamine redox chemistry is pH dependent (14). As such, shifts in physiological pH would alter both biological processes and the voltammogram for dopamine. Quantification of rapid

pH fluctuations in complex biological systems is vital to understanding neuronal activity and energy utilization. Background-subtracted fast-scan cyclic voltammetry coupled with carbon-fiber microelectrodes has this capability, as well as the ability to simultaneously monitor H_2O_2 and dopamine. To determine the effect of pH on charging current, voltammograms were collected using 100 μm cylindrical carbon-fiber microelectrodes, in Tris buffer at pH 7.0, 7.4, and 8.0. The applied waveform was -0.4 V to +1.3 V at $400 \text{ V}\cdot\text{s}^{-1}$ applied at a frequency of 10 Hz. Figure A.4.A presents representative voltammograms, demonstrating the dependence of the non-faradaic charging current on pH. To quantify, the sum of the absolute value of all currents in the voltammogram was calculated and the changes in this current, relative pH 7.4, was plotted versus the solution pH (Figure A.4.B). A linear relationship was observed, where basic shifts in solution pH lowered the total current in a voltammogram for the charging current. It was also observed that a peak at $\sim +0.25 \text{ V}$ (*) shifted to a higher potential as the pH of the solution increased. This peak has been suggested to be the result of the oxidation and reduction of quinone functional groups on the electrode surface (15). The shift in potential of peak current was plotted versus the solution pH (Figure A.4.C). A linear relationship was found, where basic shifts in solution pH lowered the potential of peak current for the quinone peak. These data indicate that the total charging current and the oxidation potential of the quinone peak are dependent on pH, which could lead to a novel method of pH determination in microenvironments.

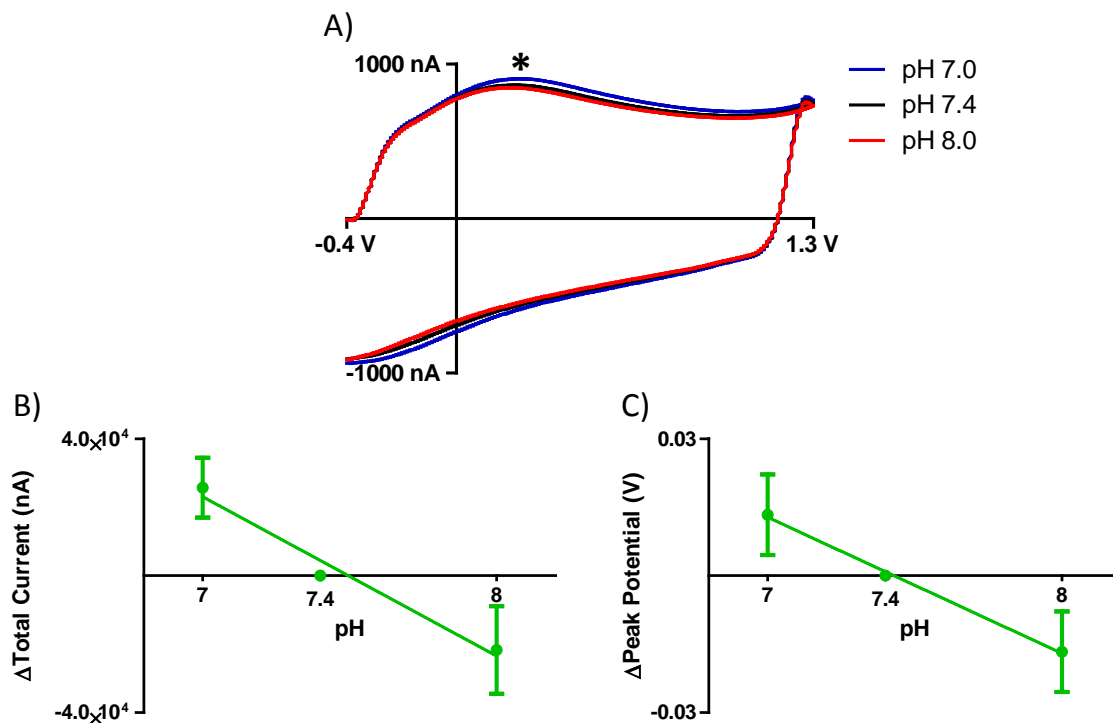


Figure A.4 - Effects of pH on charging current. Representative voltammograms of charging current at pH 7.0 (blue), pH 7.4 (black), pH 8.0 (red) for the applied waveform ranging from -0.4 to +1.3 V at $400 \text{ V}\cdot\text{s}^{-1}$ (A). (B) Relationship between the change in total charging current and solution pH. (C) Shifts in the potential of peak anodic current at $\sim +0.25 \text{ V}$ plotted versus solution pH. ($n = 3$, electrodes)

To determine the effect of pH on dopamine and H_2O_2 detection, representative background-subtracted voltammograms were plotted for $1 \mu\text{M}$ dopamine and $100 \mu\text{M}$ H_2O_2 in Figure A.5.A-B. It was observed that anodic current for dopamine decreased and shifted to a lower potential as the solution pH increased (Figure A.5.A). Anodic current for the detection of H_2O_2 decreased as solution pH decreased, but the potential of peak anodic current did not shift. This data indicate that mildly acidic environments, relative to physiological pH 7.4, would enhance dopamine sensitivity but decrease H_2O_2 sensitivity.

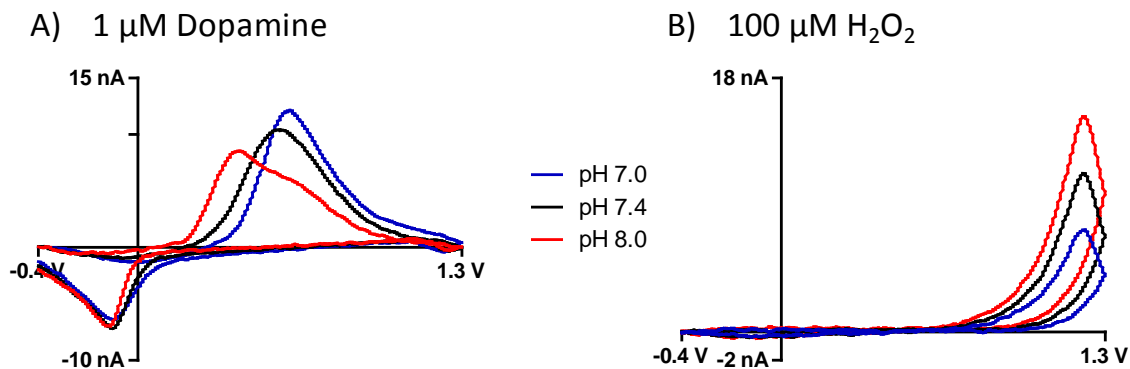


Figure A.5 - Effects of pH on dopamine and H₂O₂ detection. Representative background-subtracted voltammograms of 1 μM dopamine and 100 μM H₂O₂ at pH 7.0 (blue), pH 7.4 (black), pH 8.0 (red) for the applied waveform ranging from -0.4 to +1.3 V at 400 V·s⁻¹ (A and B, respectively).

The shifting of the potential of peak current is likely due to the fact that the oxidation of dopamine to dopamine-*o*-quinone releases two protons, and shifting the pH of the solution alters electron transfer kinetics. It is known that quinone(Q)/hydroquinone(H₂Q) redox couple is pH dependant, where the Nernst equation relates an increase in solution pH to shifts in the formal potential (6, 16). The following equation shows this relationship, at room temperature:

$$E = E_{1/2} - \frac{0.592}{2} \log \frac{[H_2Q]}{[Q]} - 0.592 \cdot pH \quad (2)$$

In Figure A.6, the potential of peak anodic current for the oxidation of dopamine was extracted from the data and plotted versus the solution pH ($n = 6$, electrodes). The peak did not shift in a linear manner, as this is likely due to peak splitting that was observed for pH 8 dopamine (Figure A.5.A). Linear regression resulted in a slope of about -0.21, which was found to be close to that of the standard Nernst equation that divides -0.059 V by the number

of electrons (-0.29 V). This research sheds new light on analyte quantification to make more reliable measurements in biological systems by accounting for shifts in physiological pH.

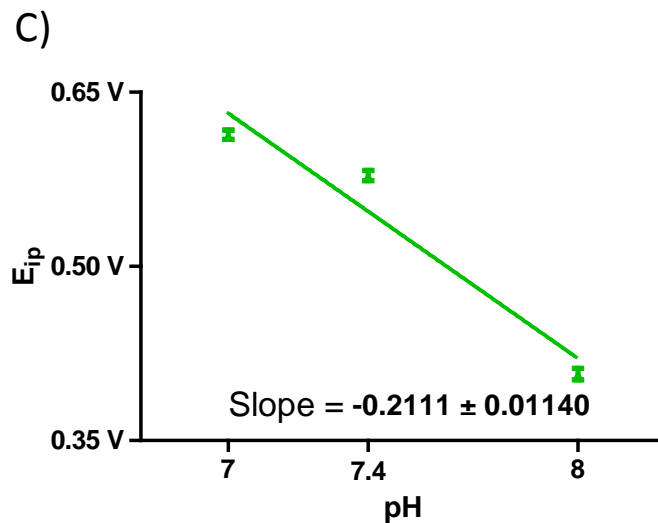


Figure A.6 - pH dependant oxidative peak shifting for dopamine. The potential of peak oxidative current for 1 μ M dopamine was plotted versus solution pH, for the applied waveform ranging from -0.4 to +1.3 V at 400 $V \cdot s^{-1}$. Reliable linearity was not found (n = 6 electrodes).

A.5 References

1. Kawagoe, K. T., Zimmerman, J. B., and Wightman, R. M. (1993) Principles of voltammetry and microelectrode surface states, *J Neurosci Methods* 48, 225-240.
2. Heien, M. L. A. V., Johnson, M. A., and Wightman, R. M. (2004) Resolving neurotransmitters detected by fast-scan cyclic voltammetry, *Anal Chem* 76, 5697-5704.
3. Hermans, A., Keithley, R. B., Kita, J. M., Sombers, L. A., and Wightman, R. M. (2008) Dopamine detection with fast-scan cyclic voltammetry used with analog background subtraction, *Anal Chem* 80, 4040-4048.
4. Sombers, L. A., Beyene, M., Carelli, R. M., and Wightman, R. M. (2009) Synaptic overflow of dopamine in the nucleus accumbens arises from neuronal activity in the ventral tegmental area, *J Neurosci* 29, 1735-1742.
5. Zachek, M. K., Takmakov, P., Moody, B., Wightman, R. M., and McCarty, G. S. (2009) Simultaneous Decoupled Detection of Dopamine and Oxygen Using Pyrolyzed Carbon Microarrays and Fast-Scan Cyclic Voltammetry, *Anal Chem* 81, 6258-6265.
6. Bard, A. J., and Faulkner, L. R. (2001) *Electrochemical Methods: Fundamentals and Applications*, 2nd ed., John Wiley, New York.
7. Zachek, M. K., Takmakov, P., Park, J., Wightman, R. M., and McCarty, G. S. (2010) Simultaneous monitoring of dopamine concentration at spatially different brain locations in vivo, *Biosens Bioelectron* 25, 1179-1185.
8. Zachek, M. K., Park, J., Takmakov, P., Wightman, R. M., and McCarty, G. S. (2010) Microfabricated FSCV-compatible microelectrode array for real-time monitoring of heterogeneous dopamine release, *Analyst* 135, 1556-1563.
9. Dam, V. A., Olthuis, W., and van den Berg, A. (2007) Redox cycling with facing interdigitated array electrodes as a method for selective detection of redox species, *Analyst* 132, 365-370.
10. McCarty, G. S., Moody, B., and Zachek, M. K. (2010) Enhancing Electrochemical Detection by Scaling Solid State Nanogaps, *J Electroanal Chem (Lausanne Switz)* 643, 9-14.
11. Heien, M. L. A. V., Phillips, P. E. M., Stuber, G. D., Seipel, A. T., and Wightman, R. M. (2003) Overoxidation of carbon-fiber microelectrodes enhances dopamine adsorption and increases sensitivity, *Analyst* 128, 1413-1419.

12. Kaila, K., and Ransom, B. R. (1998) *pH and brain function*, Wiley-Liss, New York.
13. Pastuszko, A., Wilson, D. F., and Erecinska, M. (1982) Neurotransmitter metabolism in rat brain synaptosomes: effect of anoxia and pH, *J Neurochem* 38, 1657-1667.
14. Chen, S. M., and Peng, K. T. (2003) The electrochemical properties of dopamine, epinephrine, norepinephrine, and their electrocatalytic reactions on cobalt(II) hexacyanoferrate films, *J Electroanal Chem* 547, 179-189.
15. Takmakov, P., Zachek, M. K., Keithley, R. B., Bucher, E. S., McCarty, G. S., and Wightman, R. M. (2010) Characterization of local pH changes in brain using fast-scan cyclic voltammetry with carbon microelectrodes, *Anal Chem* 82, 9892-9900.
16. Walczak, M. M., Dryer, D. A., Jacobson, D. D., Foss, M. G., and Flynn, N. T. (1997) pH-dependent redox couple: Illustrating the Nernst equation using cyclic voltammetry, *J Chem Educ* 74, 1195-1197.

APPENDIX B

WolfChrome: A LabView Based Chromatography Program

B.1 Description

WolfChrome is a LabView based software package that collects and analyzes chromatograms from a Waters high-performance liquid chromatography (HPLC) system with ultraviolet-visible (UV-VIS) detection. The data collection software utilizes high frequency sampling rates and an oversampling feature to minimize signal noise. Recording of data is initialized upon sample injection to precisely obtain retention times. The supplementary data analysis program is used for data filtering, peak fitting, and data output. Data is exported as both a chromatograph and a database containing peak fitting values. Contact Leslie Sombers (leslie_somers@ncsu.edu) for information on how to obtain WolfChrome.

B.2 Hardware and Software Requirements

B.2.1 National Instruments and MATLAB

The software was developed with LabView (version 9.0.0, National Instruments, Austin, TX) and MATLAB (version R2009b, The MathWorks, Natick, MA). A full version of LabView is not necessary for data collection, only the LabView Run-Time Engine (version 9.0.1) is required. A full version of MATLAB is necessary for data analysis. One data acquisition (DAQ) card (NI-PCI-6251) is required for data collection and sample injector detection. A connector block (NI-CB-68LP) and cable (NI-SHC68-68-EPM) is also

necessary to make the connections from the HPLC system to the DAQ card. An equivalent National Instruments DAQ card that has at least one analog output (16-bit) and two analog inputs (> 1 MHz) can be substituted without alterations to the software. Alternatively, other data acquisition products are available from National Instruments that could be employed with slight alterations to the programming, but these will not be discussed in any detail.

B.2.2 HPLC System

The software was designed for use with a Waters (Milford, MA) HPLC system: detector (model 484), gradient controller (model 680), sample injector (model U6K), and HPLC pump (model 510). The software could easily be adapted to control other chromatography systems, and collect chromatograms, as long as an output voltage for the detector is accessible and the sample injector has a limit switch to indicate an injection.

B.3 Overview of LabView

LabView (Laboratory Virtual Instrumentation Engineering Workbench) is a system design platform and graphical programming language that uses dataflow programming to execute different functions. These functions are connected by drawing wires and these wires propagate information to the next function as the data becomes available. A typical LabView program consists of both a front panel and a block diagram. The front panel is a graphical user interface that allows the user to control the program, settings, data input, and displays the data. The block diagram contains all the graphical code for the program. Each program is called a virtual instrument (VI) and sub-programs are called sub-VIs. To facilitate

programming, LabView supplies a large library of VI functions for creating applications, interfacing devices, data acquisition, and data analysis. This program also interfaces well with MATLAB, to increase the signal processing capability of LabView. LabView also has the ability to compile the VIs and generate executable files that can run without the installation of the full developer's version of the program. This allows the custom program to be distributed and only requires the LabView Run-time engine to be executed, at no cost. Overall, graphical programming benefits a less experienced programmer and the features of LabView make it a highly productive development environment for scientists to acquire and analyze data.

B.4 Background Information on HPLC and UV-VIS Absorbance Detection

HPLC has become one of the most powerful tools in analytical chemistry, because it has the ability to separate, identify, and quantitate compounds that are present in aqueous samples. Typically, compounds in trace concentrations as low as parts per trillion are identified.

Figure B.1 illustrates the components and the flow of solvent and information in a typical HPLC system. A solvent reservoir contains the mobile phase and a high-pressure pump is used to generate and meter a specified flow rate of mobile phase (around $1 \text{ mL}\cdot\text{min}^{-1}$ at 5000 psi). A sample injector introduces small volumes ($5 - 20 \text{ }\mu\text{L}$) of sample into the continuously flowing mobile phase that carries the sample to the column. The column contains a packing material (stationary phase) that facilitates analyte separation by various chemical and physical interactions between the molecules and the stationary phase. As the

eluent exit the column, a flow-through detector monitors the separated compounds. A chromatogram is plotted from the output of this detector (Figure B.2). The mobile phase with eluting compounds exits the detector and can either be collected for further analysis or sent to waste.

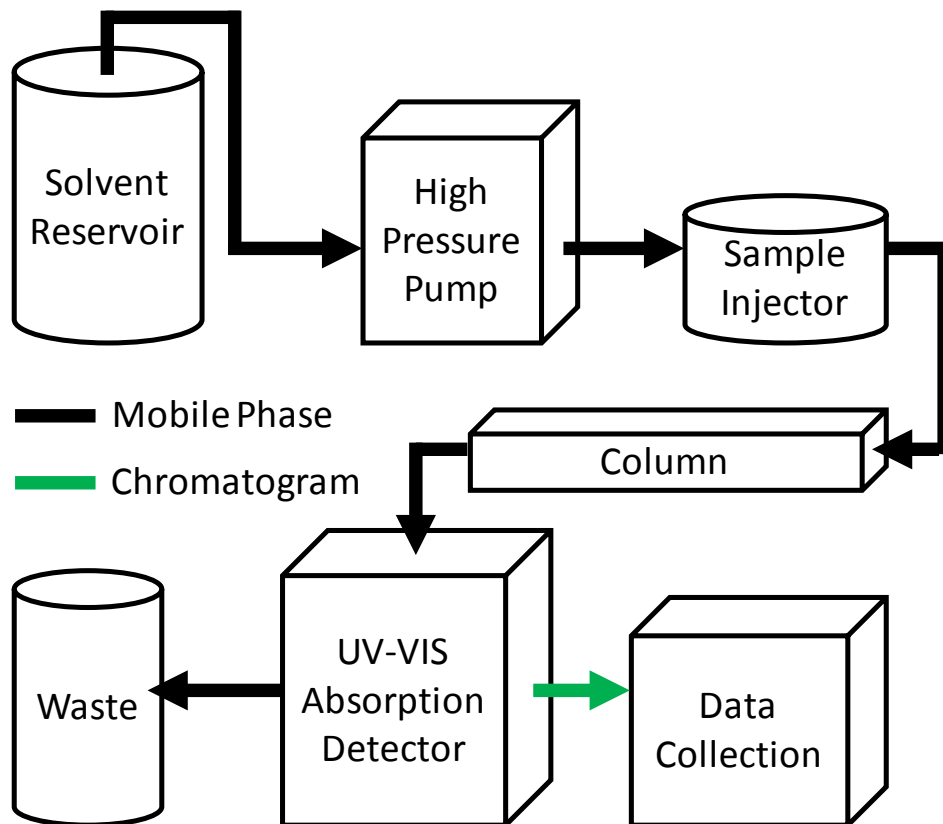


Figure B.1 - Diagram of a typical HPLC system. Black lines represent the flow of mobile phase and green lines represent the flow of chromatographic data.

There is not a universal detection method for all molecules; so many detection schemes have been developed for monitoring the eluting analytes. An appropriate detector must be matched for the sample and for most biological molecules UV-VIS absorbance

spectroscopy is commonly used. In this detection method, an ultraviolet light beam (typically 200 – 800 nm) is directed through a flow cell and a sensor measures the light passing through the eluent. If a compound absorbs this light energy, it will change the amount of light detected by the sensor. The resulting change in this electrical signal is amplified and sent to the data recorder.

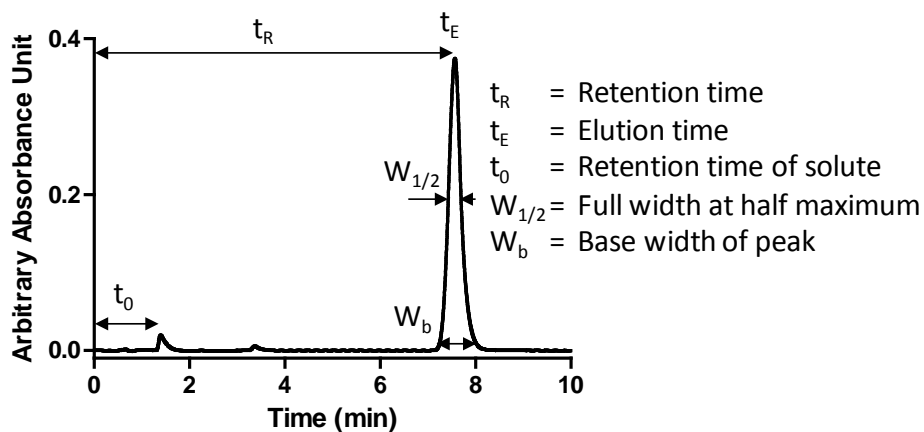


Figure B.2 - Chromatogram collected with WolfChrome. Fundamental properties used in signal analysis are illustrated.

A recording device collects the electrical signal from the detector output and generates a chromatogram. A chromatogram is a temporal representation of the chemical separation that occurred in the HPLC system and is used to identify and quantitate the concentration of the sample constituents. A series of peaks rising from a baseline represents the detector response for each compound. The retention time is correlated with analyte identity and the area of the peak is proportional to analyte concentration.

Reversed-phase HPLC (RP-HPLC) is by far the most popular method of chromatography, where the mobile phase is moderately polar and the stationary phase is non-polar. Two basic modes are used in HPLC to control the rate of sample elution. In isocratic mode the mobile phase composition remains constant with time and gradient mode delivers variable mobile phase composition over the course of the separation. Gradient mode improves the peak resolution of late eluting peaks by decreasing retention times.

The choice of column and packing material is based on the goals of the research. A smaller diameter column is typically used for determination of analyte and concentration, while a larger diameter column is used for the purification of compounds. Longer columns generally increase separation efficiency and result in greater peak resolution, but collection times are longer and solvent consumption is increased. Analyte selectivity is controlled by the choice of stationary phase.

B.5 Hardware Construction and Software Setup for WolfChrome

The construction and setup of the HPLC system would be dependant on the particular research goals and should follow the manufactures guidelines. Access to the output signal of the detector and a momentary switch indicating the position of the sample injector is the only requirement for the HPLC system to be incorporated into the software.

Construction for data recording only requires a minimal comfort level with computer hardware installation and a basic electrical tool set. An appropriate National Instruments DAQ card must be installed on the computer motherboard and the included software needs to be installed, following the manufactures instructions. After installation, the DAQ card will

be given the name “1” in the program Measurements and Automation. It would be beneficial to enclose the connector block (NI-CB-68LP) in a metal electrical enclosure to minimize electrical interference (Figure B.3). The 68-pin cable (NI-SHC68-68-EPM) interconnects the DAQ card installed on the computer and the shielded connector block. Connections to the connector block from the HPLC system are as follows:

- Pin 68 = AI0 - Output voltage of detector
- Pin 67 = AIGND - Detector ground
- Pin 33 = AI1 - Voltage of sample loop
- Pin 22 = AO0 – Voltage output to sample loop

These connections to analog input (AI) and output (AO) channels are software defined, but can be easily altered if these channels are occupied. AI0 accepts the voltage signal from the detector and AIGND is connected to the ground of the detector (Figure B.3, red and black wire, respectively). The Waters sample injector (model U6K) has a cable containing two wires that lead to a limit switch. One wire in this cable is connected to AO0 (Figure B.3, blue wire) to send a +2 V dc signal to the limit switch. The other wire (Figure B.3, blue-black wire) is connected to AI1 to monitor the voltage output by the switch. This limit switch is tripped by a rotating cam connected to the injector lever. Upon every sample injection, the +2 V dc signal will be momentarily sent to AI1 and detected by the software. An oscilloscope could be used to test the input and output signals to ensure a proper setup.

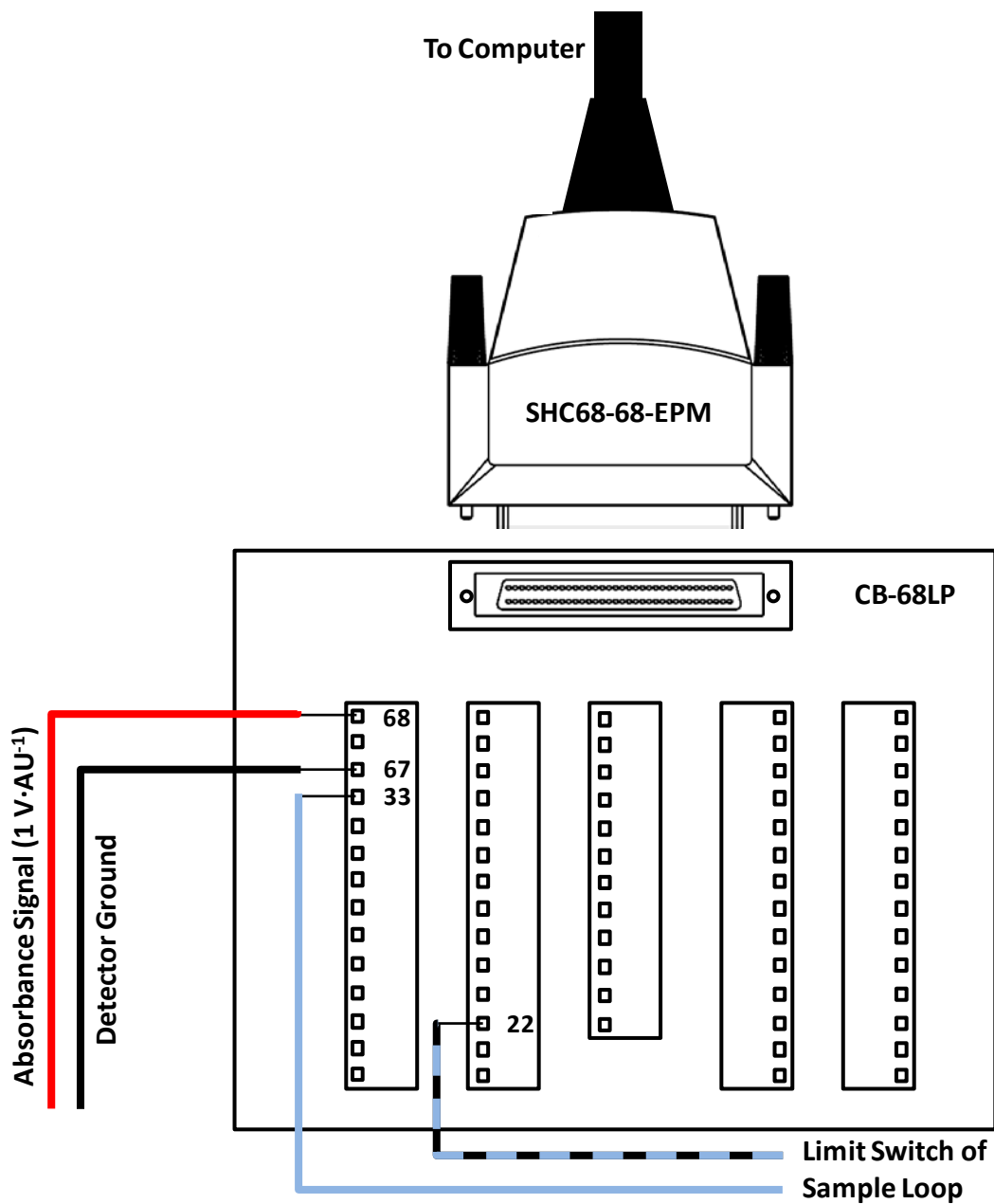


Figure B.3 - Diagram of electrical connections for data recording. A 68-pin connector block is used to make connections from the computer to the HPLC system.

B.6 Data-Collection Software

As stated in the opening sections, WolfChrome is designed to record the voltage output of the UV-VIS detector on an HPLC system and match the start of data collection with the introduction of a sample into the mobile phase. Figure B.4 demonstrates the general flow of information between the HPLC system, the DAQ card and the software. The function of the program is to record a chromatogram from the detector and monitor the position of the sample injector. Once the user has input all necessary experimental parameters and data collection is initiated, recording will not begin until the sample has been injected. After the file is collected the data is written to the specified file location and displayed on the front panel for observation. Once the software is installed, a shortcut to WolfChrome will start the software.

Figure B.5 shows a screenshot of the front panel of the program. There are four main sections to WolfChrome's front panel and these include: file destination, data collection settings, file collection and termination, and data graphs. The file destination section has user input for changing the name of the file and drive location.

The section for data collection settings allows the user to change the total time of data collection in minutes, the frequency of data collection in hertz (Hz), and the oversampling factor. The Waters detector (model 484) has a Hamming filter with time constant settings that range from 0.1 to 5 s. This requires that the frequency of data collection must be at least 20 Hz to satisfy the Nyquist frequency and prevent aliasing. Oversampling is a signal processing method that helps improve peak resolution and reduce signal noise. This feature simply multiplies the data collection frequency by the user specified oversampling factor.

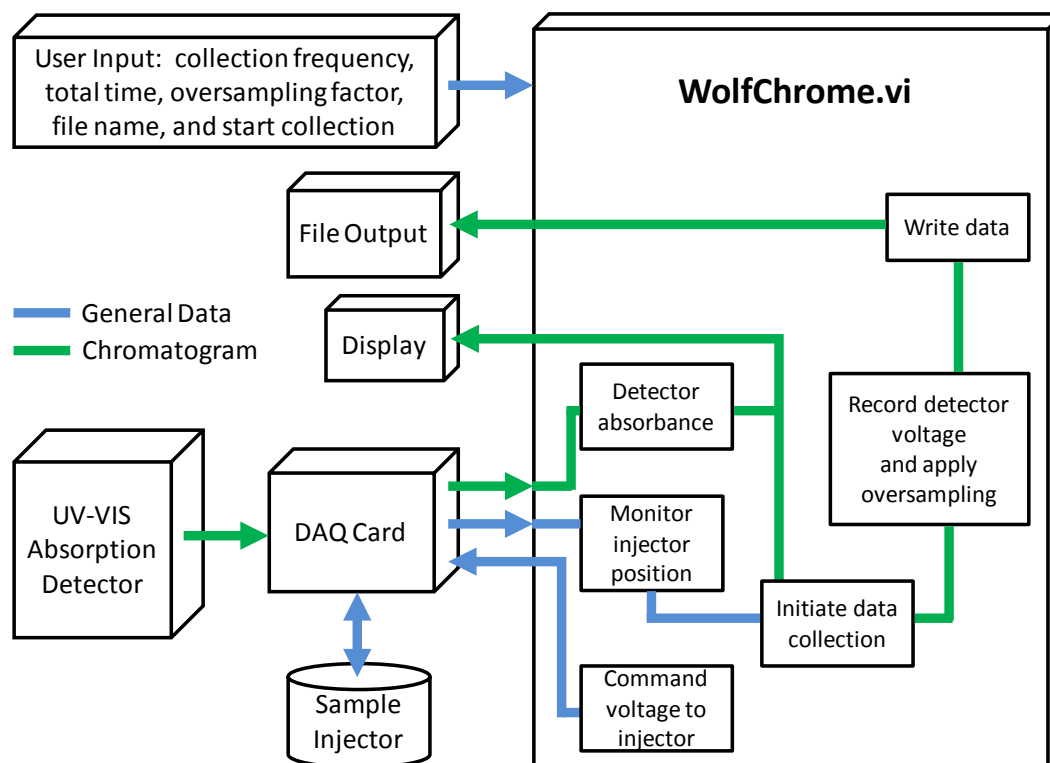


Figure B.4 - Schematic representation of data flow in WolfChrome.

The additional data points collected in response to oversampling are averaged to give a single representative data point at the original collection frequency. For example, a one second file collected with the data collection frequency set to 100 Hz would result in 100 data points. If an oversampling factor of 4 was used, the actual frequency of data collection will be 400 Hz, and every four consecutive data points are averaged. This averaging returns 100 data points collected at 100 Hz and effectively averages out the noise to give a better representation of the real data.

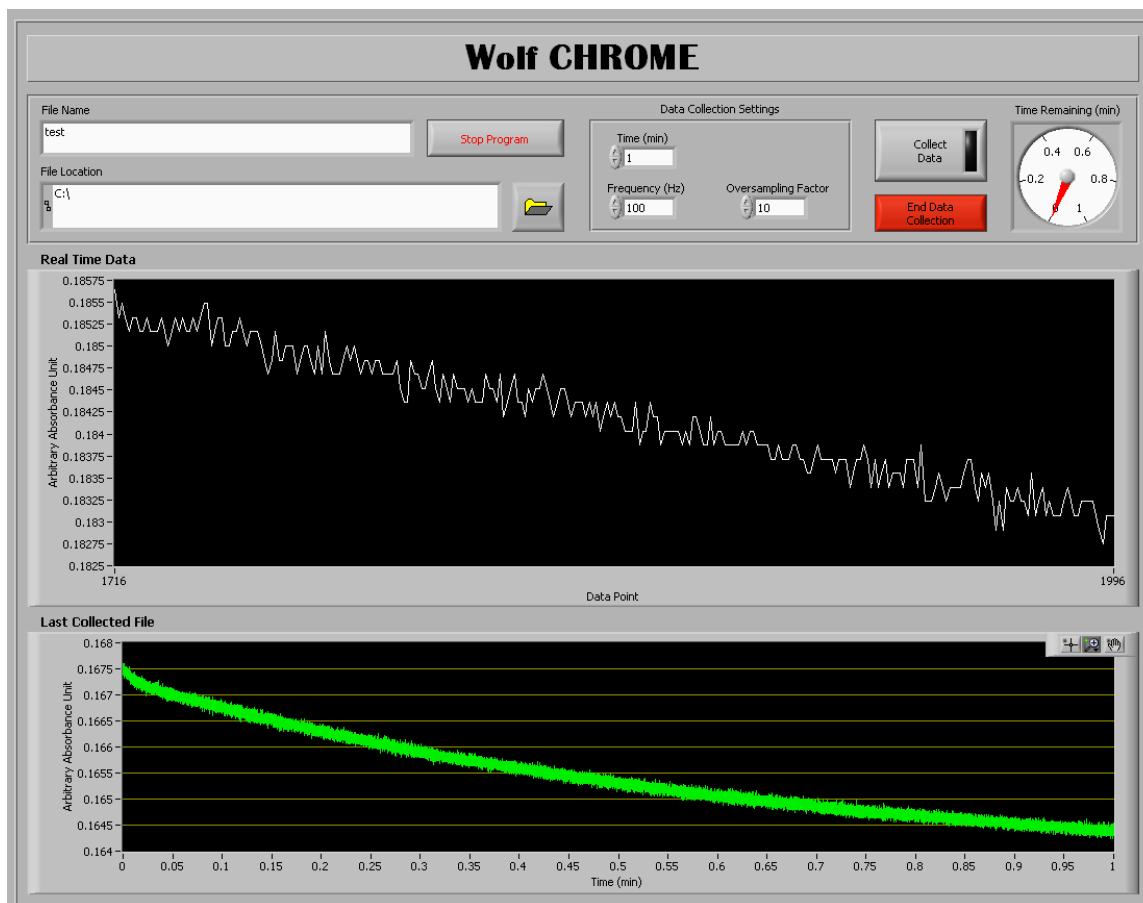


Figure B.5 - Screenshot of WolfChrome front panel.

The file collection and termination section has a button for initiating data collection and one for aborting file collection. When the “Collect Data” button is enabled, the software will pause data recording until the user switches the injector loop, to introduce the sample. This feature defines injection time as zero minutes on the chromatogram and allows more reproducible calculations of retention times. File collection can be aborted at any time by selecting the “End Data Collection” button, and all collected information will be written.

The final section plots both the real time data streaming from the detector and the last file collected with the software. The program will continuously monitor the absorbance of the detector and plot this data in the “Real Time Data” graph, as arbitrary absorbance units versus data point. The “Last Collected File” graph gives the user full control to examine the previously recorded chromatogram with zooming, panning, and windowing features.

After a file is collected, the data is output in LabView’s native data file format (.tdms). This format benefits from smaller file sizes and is more easily integrated into the programming. Other file formats require the data to be retained in memory until collection is finished that could result in lost data from memory dump. To avoid this data loss, the tdms format streams data directly to the file location.

B.7 Data-Analysis Software

In addition to WolfChrome, WolfChrome Analysis is included to explore the chromatogram and extract information by analyzing peak properties. Once the software is installed, a shortcut to WolfChrome Analysis will start the software. Upon startup, the user is presented with a front panel like that shown in Figure B.6. This front panel is divided into three sections: file location, data graphs, and filtering and peak analysis. The file location section has user input for opening the desired file and displays the drive location.

The “Raw Data” graph displays the unaltered chromatogram contained within the selected file. This graph also has two vertical lines (red and green) that can be positioned to span a small region of the graph that best describes a time where no analytes were eluting.

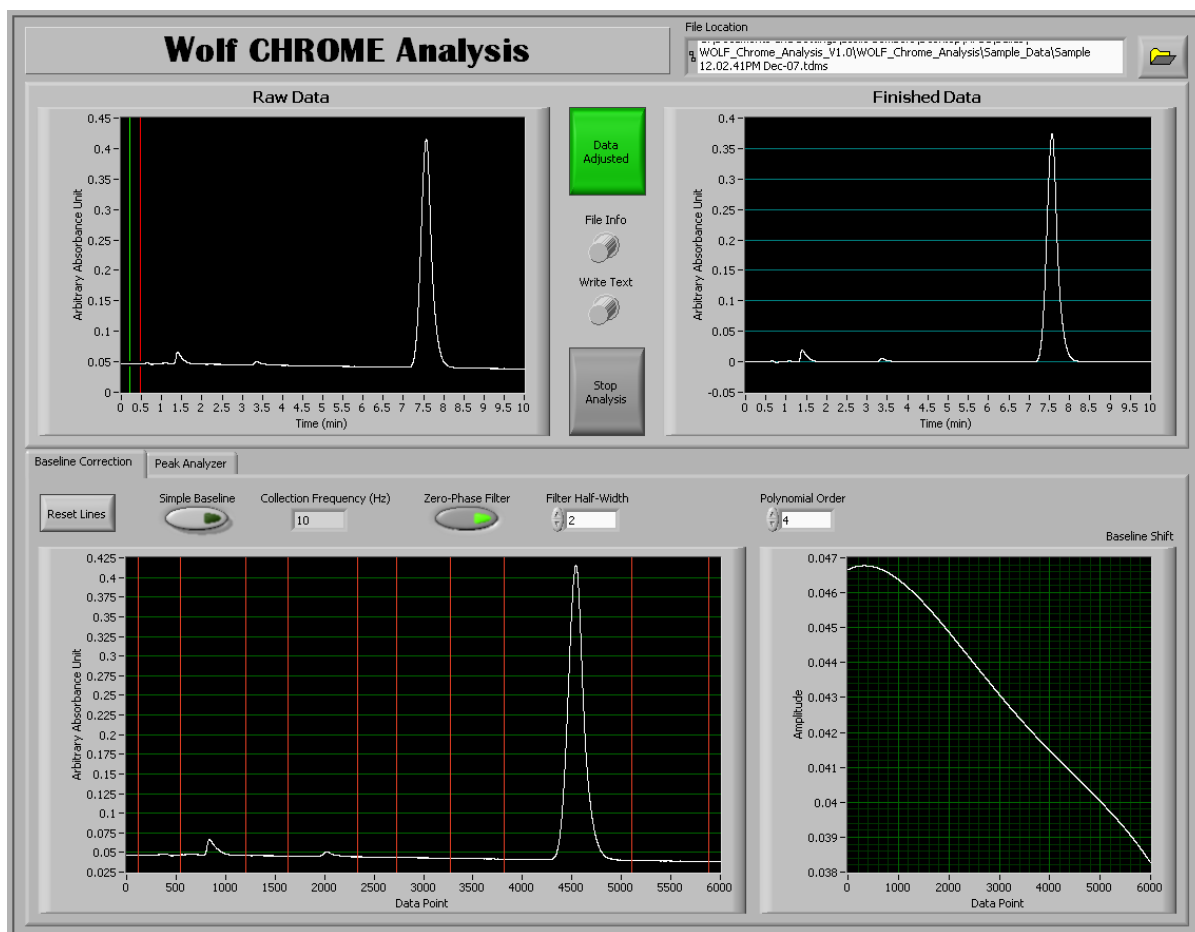


Figure B.6 - Screenshot of WolfChrome Analysis front panel.

This region is used to define the signal to noise ratio that will be used to determine the significance of peaks. The opposing graph, labeled “Finished Data,” displays the chromatogram after baseline correction and filtering. There are controls between the two graphs that enable data correction, display file information, write a text file of the finished data, or stop the program. If data correction is disabled the finished data graph will display the raw data, otherwise the graph will display corrected data based on user settings. The file info button will open another window that shows the properties of the data file and

information that was retained about the data collection settings. The write text button will save a text file of the finished data graph in the same file location of the original data.

The final section is tabulated for baseline correction and peak fitting. Most chromatograms exhibit variability in the baseline of the spectra, as a result of detector drift. The program is setup to either perform a simple baseline correction that offsets the entire spectra about the y-axis, or it can fit a polynomial to the baseline and subtract this curve from the raw data to correct a more complex baseline drift. If the simple baseline is enabled, two vertical red lines appear in the graph and are positioned to span region of the graph that best defines the baseline. The average absorbance value between the vertical lines is plotted in the “Baseline Shift” graph and subtracted from all values in the chromatogram to shift the spectra vertically. If the simple baseline option is disabled, ten red vertical lines are positioned in the graph, where the user adjusts the position of the lines to locations that best describe the baseline. The data points that are intersected by the vertical lines are used to fit a curve with the user defined “polynomial order.” The fitted curve is displayed in the “Baseline Shift” graph and this curve is subtracted from the raw data to correct the baseline. An example of this baseline correction can be seen in Figure B.6, where a polynomial of the fourth order is fit to the raw data and the resulting baseline corrected chromatogram is plotted in the finished data graph. There is also a zero-phase filtering option to smooth the data without altering the location of the peak. When enabled, the zero-phase filter applies the user defined window half-width to filter the raw data. This filtered data is not used in peak fitting, as it is only intended to generate a more aesthetic graph.

The peak fitting section is shown in Figure B.7, which displays a graph of the baseline corrected chromatogram and a graph of the fitted peak. To select a peak for fitting, the first graph has two movable vertical lines to indicate the start (green) and end (red) time of the peak of interest. This graph also displays two horizontal yellow lines that represent the limit of detection based on the user specified number of standard deviations. All peaks that extend beyond the limit of detection lines, with peak widths greater than the user defined values, are identified and labeled with a red dot. An example of this can be seen in Figure B.7, where the program has identified 5 peaks based on the criteria set by the user. To analyze a peak the user will position the start and end lines around the peak of interest, and then select the “calculate peak” button. The data contained within the lines are plotted in the adjacent graph with white dots and the fitted peak is plotted in red. There are controls for assigning the peak a number, adding the peak values to a spreadsheet, clearing the spreadsheet, or exporting the data once all peaks are fitted. These peak fitting parameters include: peak area, elution time, Gaussian width, exponential decay factor, and peak height.

Ideally all peaks should have a Gaussian shape, but other processes inherent to the separation process causes peak asymmetry. For this reason, peak fitting for this program is based on an exponentially modified Gaussian distribution following the equation:

$$f(x) = \frac{a_0}{2a_3} \exp \left[\frac{a_2^2}{2a_3^2} + \frac{a_1 - x}{a_3} \right] \left[\operatorname{erf} \left(\frac{x - a_1}{2^{1/2} a_2} - \frac{a_2}{2^{1/2} a_3} \right) \right] \quad (1)$$

where a_0 is peak area, a_1 is elution time, a_2 is Gaussian width, and a_3 is the exponential decay factor (I). An example of this fitting is shown in Figure B.7, where tailing of the peak is fitted with the convoluted Gaussian function (Equation 1). From these values the retention

time is calculated and used for analyte identification. The peak area is proportional to sample concentration and used for analyte quantification, after instrument calibration has been performed. The Gaussian width (σ) is used to calculate the number of theoretical plates (N) by following the equation:

$$N = \left(\frac{t_R}{\sigma}\right)^2 \quad (2)$$

where t_R is the retention time of the peak.

WolfChrome Analysis is powerful addition to the data collection program that enables rapid quantification of complex chromatograms. Future versions of the program will incorporate more elaborate peak fitting features and more statistical information on curve fitting to determine the goodness of fit.

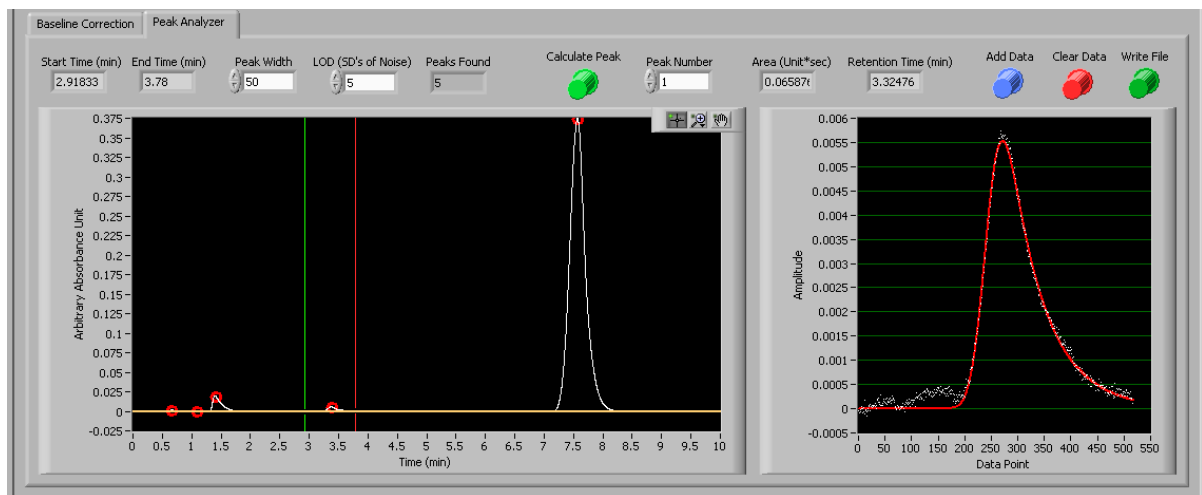


Figure B.7 - Screenshot of the tabulated peak analyzer section.

B.8 Block Diagram of WolfChrome

The following figures are images of the block diagram for the data collection program. Figure B.8 is the entire block diagram for WolfChrome and Figures B.9-10 are enlarged images of Figure B.6 that were split to fit within the page limits. Each programming loop is labeled with letters A – F inside red circles to ease the description of the block diagram. Loop A is the first part of a sequential loop where the DAQ card is initialized. Loop B is the last part of the sequential loop where the channels for the two analog inputs and one analog output are initialized. When the program is ended, this loop is exited after writing a value of zero volts to the analog output. Loop C is the main for loop that runs until the user ends the program. Inside this loop, the voltage from the detector is measured and displayed, the values for data collection are set by the user, and the analog output channel applies a +2 V signal to the sample injector. Loop D is a conditional loop that awaits user input for starting data collection. When this argument is satisfied the analog input channel measures the voltage of the sample injector and when the voltage exceeds +1.5 V, the loop will exit. This will initiate the start of conditional Loop E and F. Loop E takes the file name and location defined by the user and creates a data file that contains information exiting Loop F. After the data is finished streaming, the loop will save the file and display the data in the last file collected graph on the front panel. Loop F records the voltage from the detector, applies the oversampling method at the user specified frequency, calculates the time remaining for the file collection, and displays the data in the real time graph on the front panel.

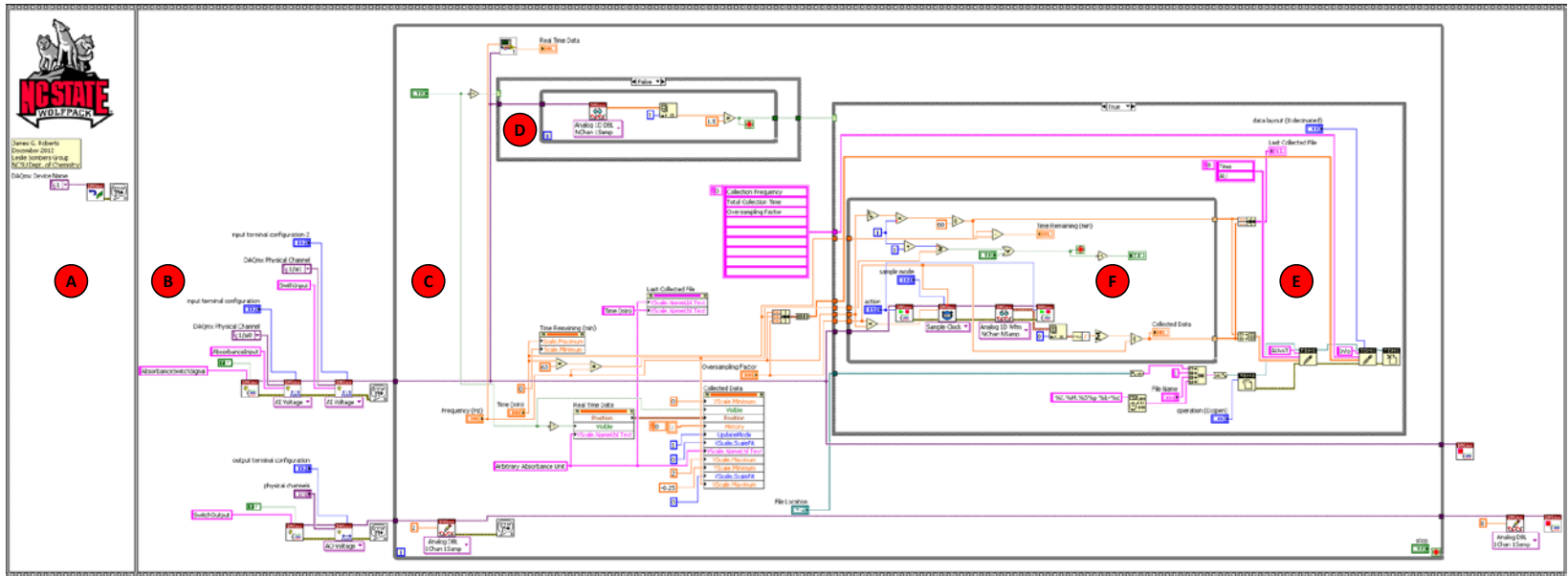


Figure B.8 - Screenshot of WolfChrome block diagram. The red lettered circles (A - F) indicate the separate programming loops.

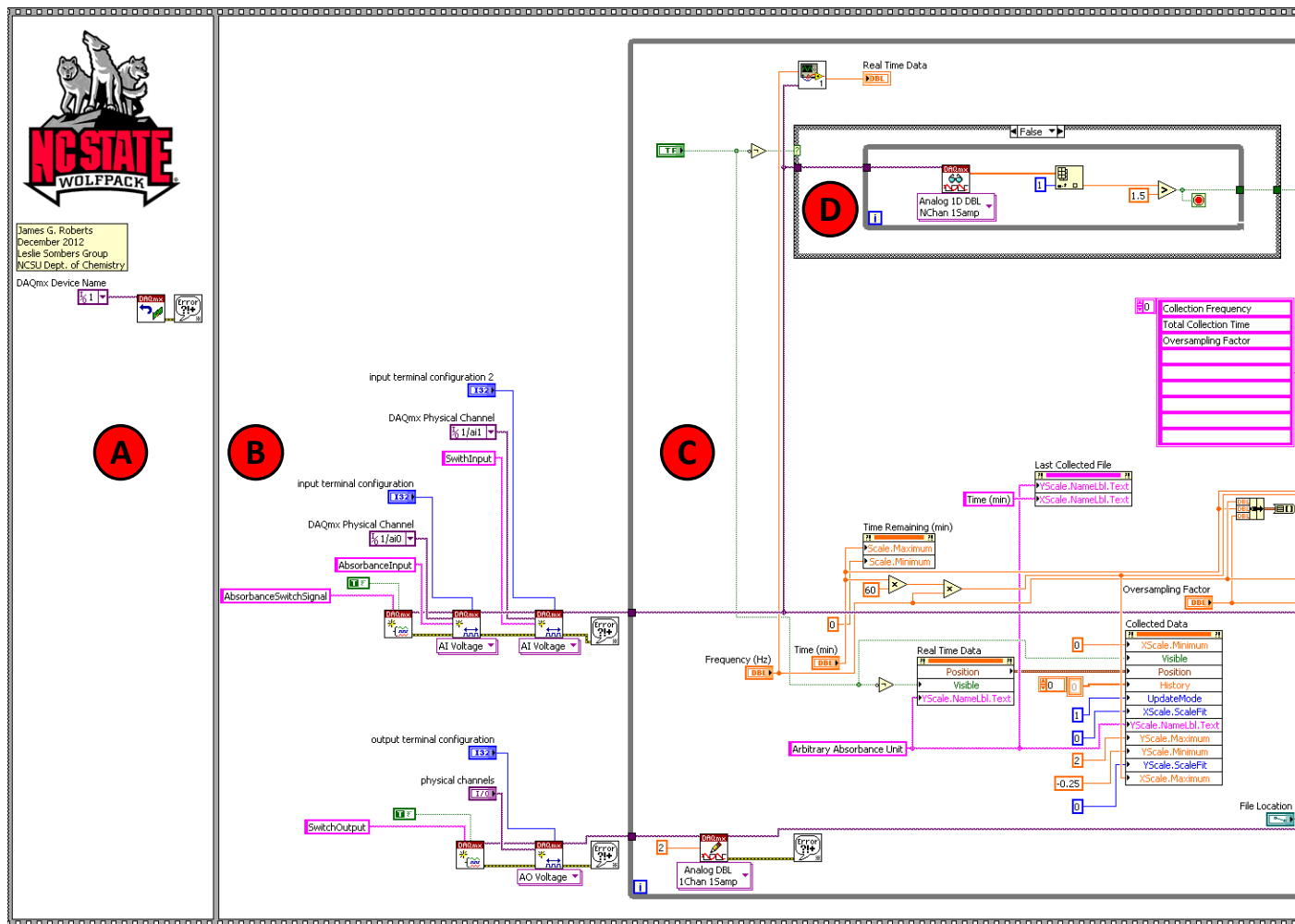


Figure B.9 - WolfChrome block diagram, Part 1 of 2.

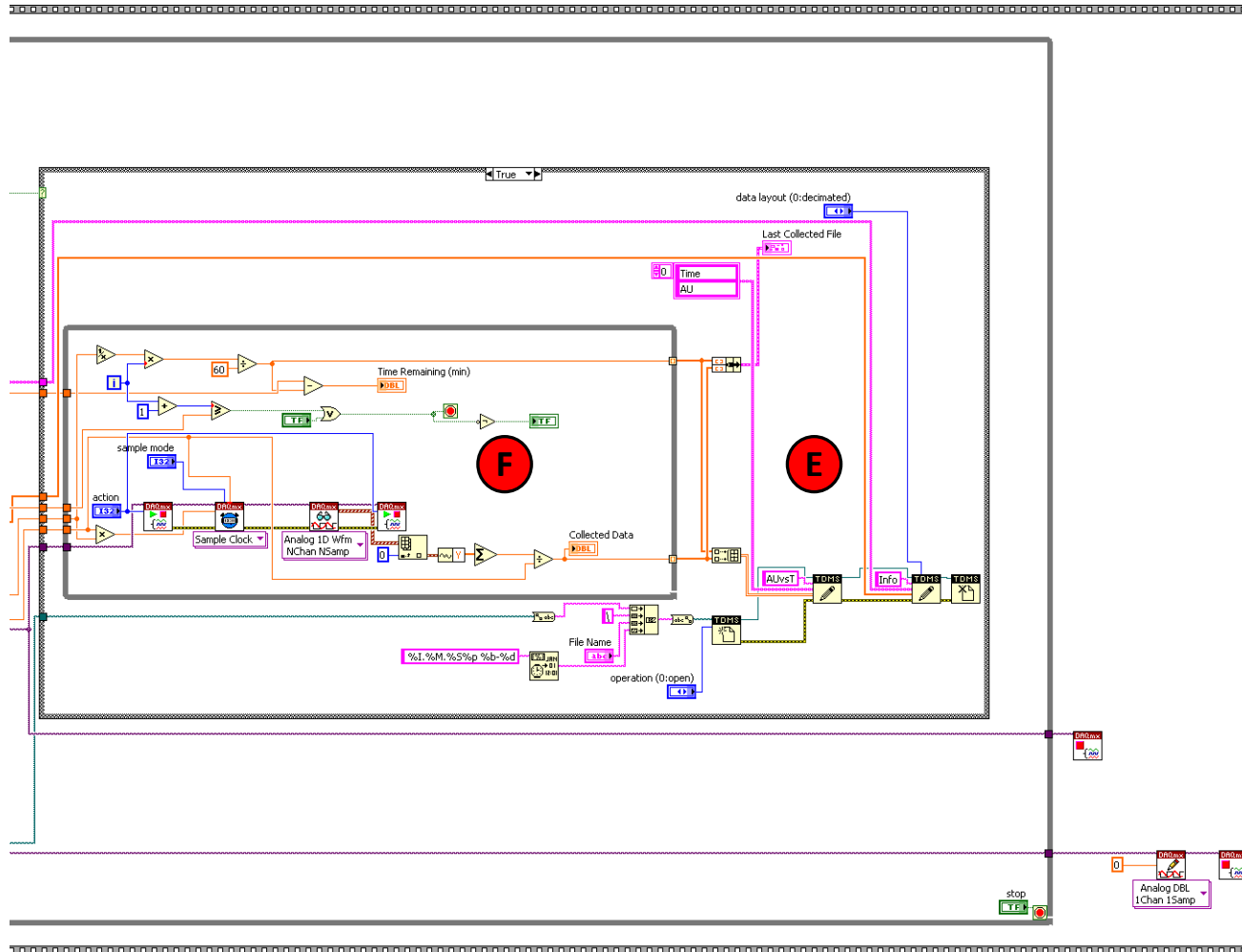


Figure B.10 - WolfChrome block diagram, Part 2 of 2.

B.9 Block Diagram of WolfChrome Analysis

The following figures are images of the block diagram for the data analysis program. Figure B.11 is the entire block diagram for WolfChrome and Figures B.12 – 17 are enlarged images of Figure B.11 that were split to fit within the page limits. Each loop is labeled with letters A – K inside red circles to ease the description of the block diagram.

Loop A is the main for loop that encompasses the whole program and the loop exits when the user closes the program. This loop is responsible for all user input, opening and reading the selected file, displaying all data in all graphs, baseline subtraction, and peak finding. Loop B is a conditional loop that displays the file information that was retained in the collected file, when enabled. Loop C is conditional loop that controls which data is displayed in the finished data graph; either raw data, or data that was baseline corrected and filtered. Loops D and E are conditional loops that control baseline correction. Loop D is responsible for building and graphing the two vertical lines that are present in the simple baseline correction or the ten lines in the polynomial corrected baseline method. Loop E determines the baseline by either averaging the absorbance between the vertical lines or fits a polynomial to the selected ten data points. Loop F is a conditional loop that performs zero-phase filtering on the baseline corrected data, when selected. Loop G is responsible for fitting the selected with the exponentially modified Gaussian equation. This loop utilizes MATLAB and nonlinear regression to iteratively fit the equation. The initial guesses used for the fitting are supplied by first fitting a Gaussian curve to the selected peak. Conditional loops H and I add or remove peak fitting values to the spreadsheet, respectively. Loop J

writes a text file of the chromatogram displayed on the finished data graph and loop K writes the spreadsheet that contains the peak fitting values for all assigned peaks.

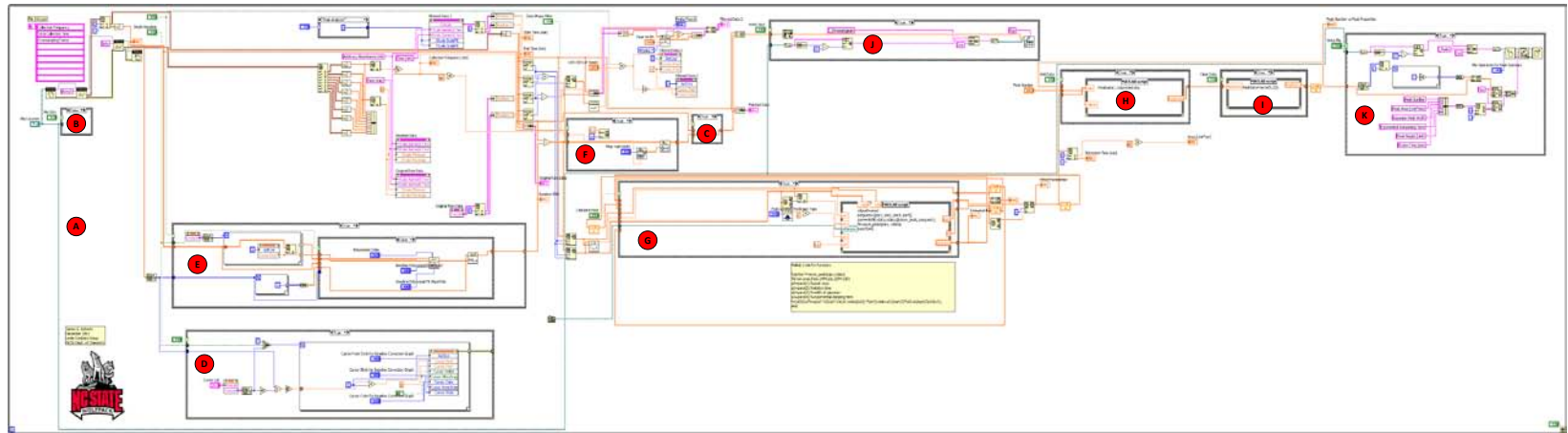


Figure B.11 - Screenshot of WolfChrome Analysis block diagram.

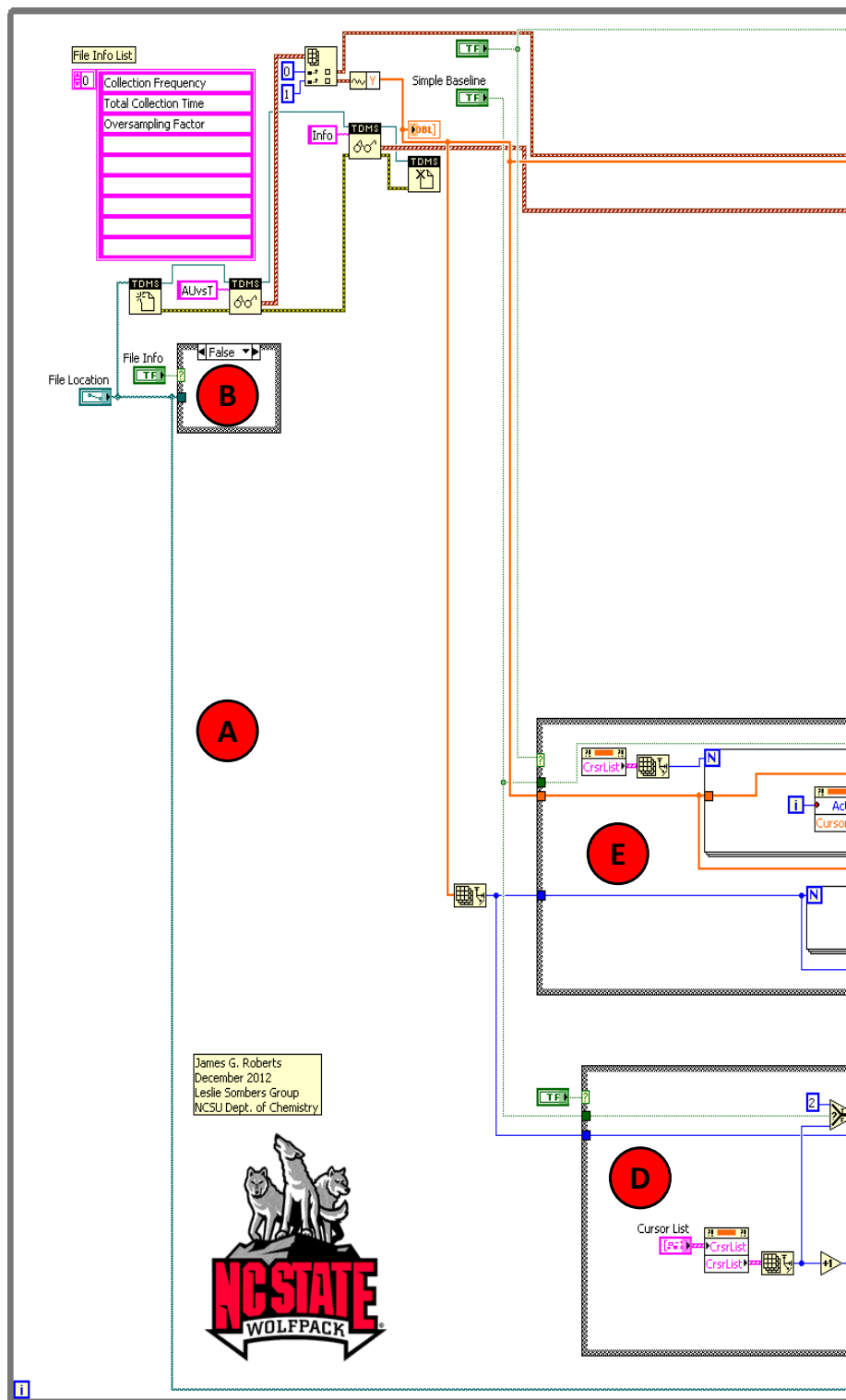


Figure B.12 - WolfChrome Analysis block diagram, Part 1 of 6.

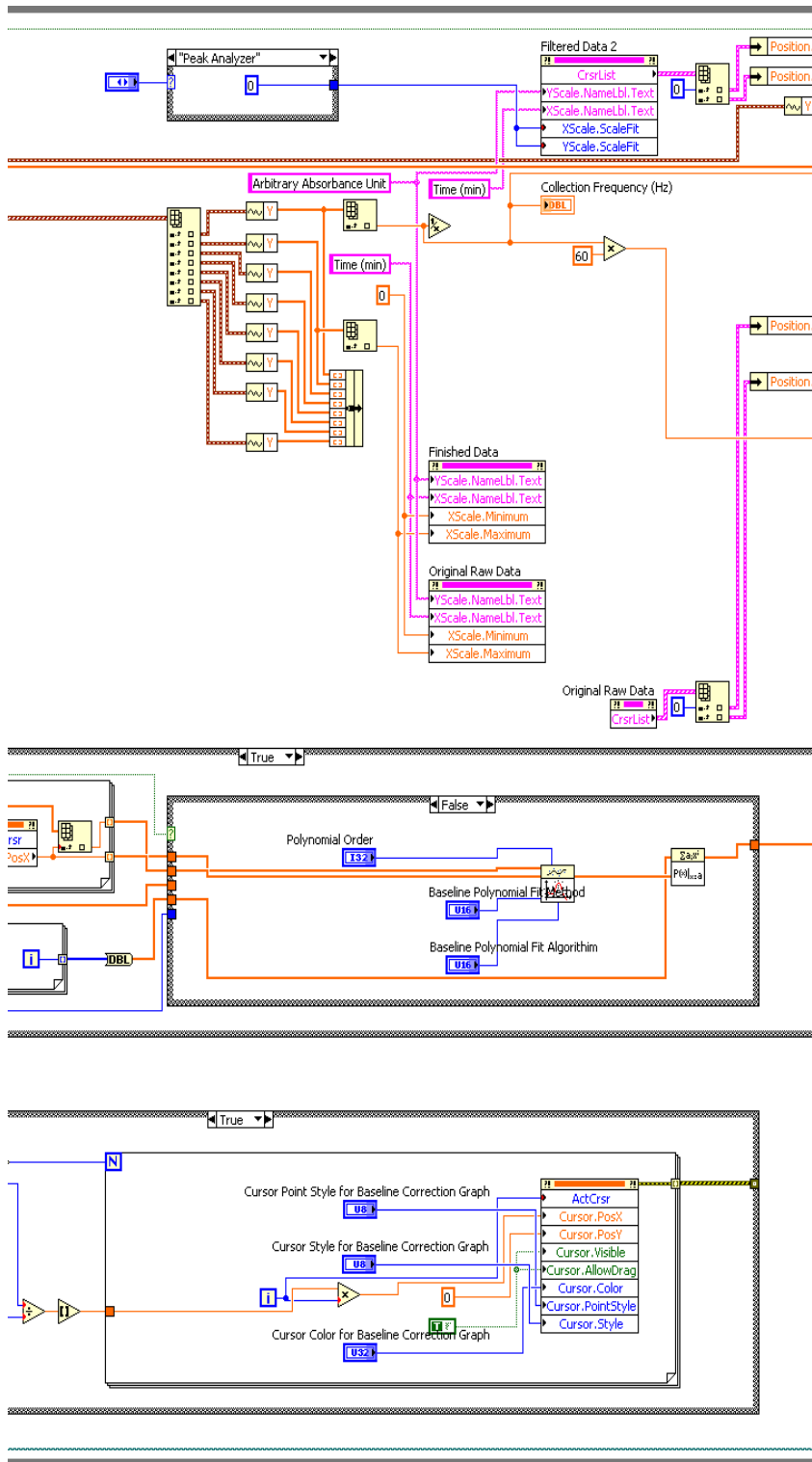


Figure B.13 - WolfChrome Analysis block diagram, Part 2 of 6.

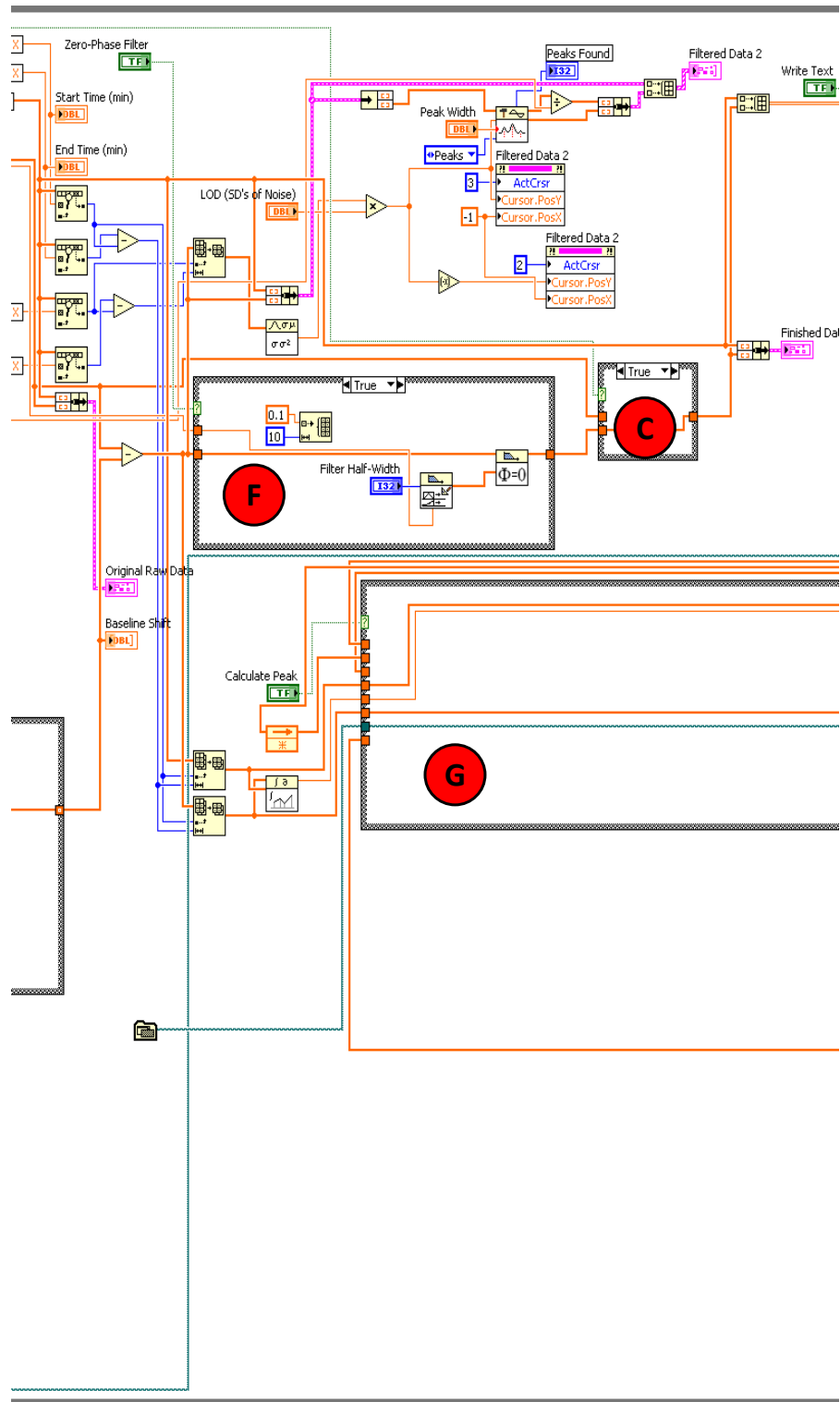


Figure B.14 - WolfChrome Analysis block diagram, Part 3 of 6.

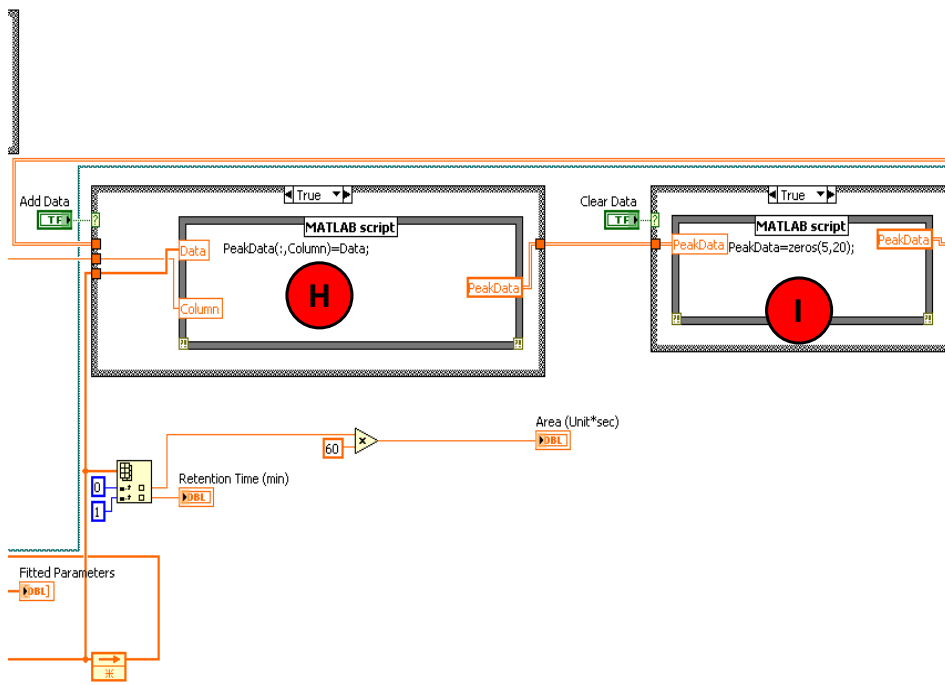


Figure B.16 - WolfChrome Analysis block diagram, Part 5 of 6.

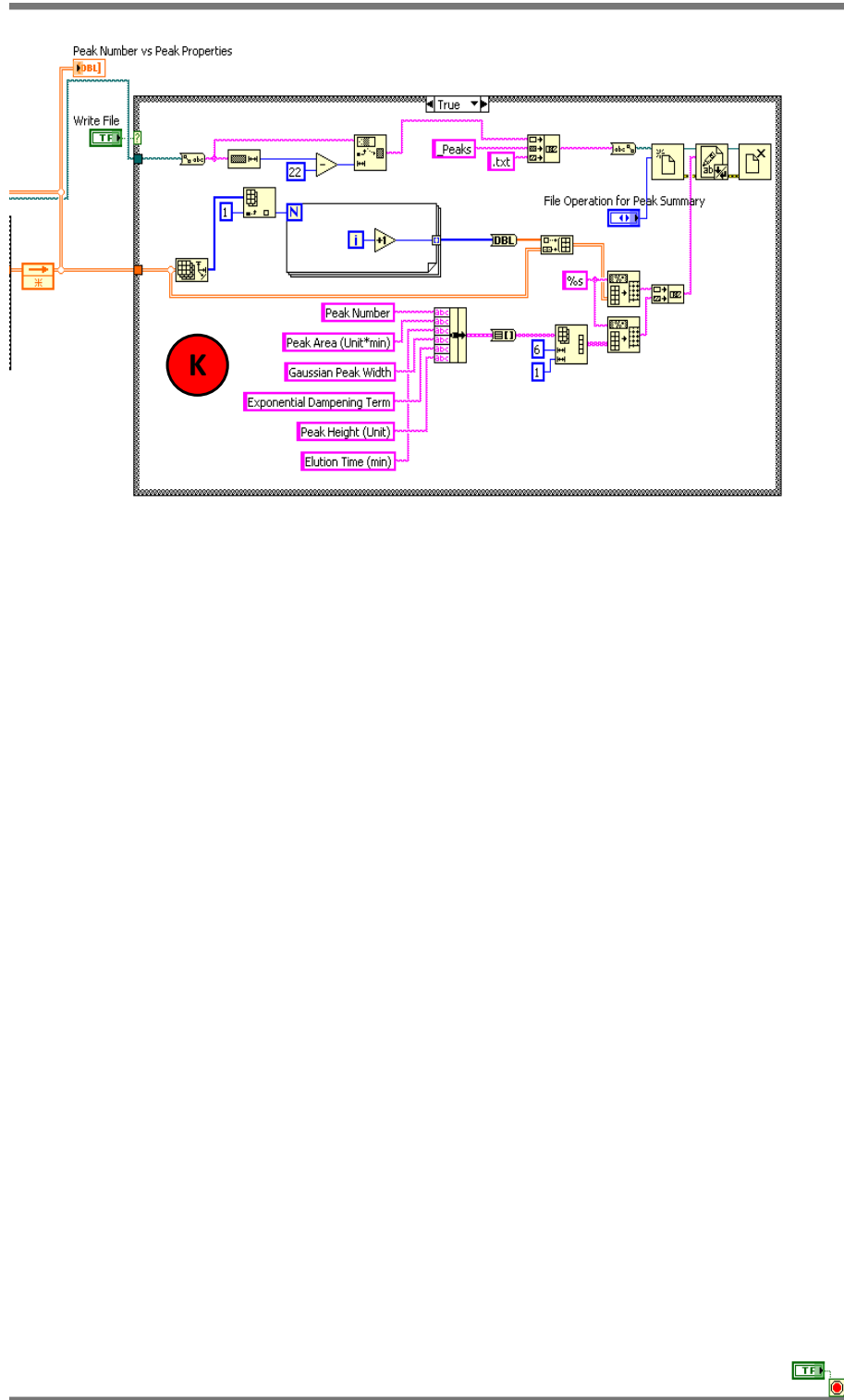


Figure B.17 - WolfChrome Analysis block diagram, Part 6 of 6.

B.10 References

1. Goodman, K. J., and Brenna, J. T. (1994) Curve-Fitting for Restoration of Accuracy for Overlapping Peaks in Gas-Chromatography Combustion Isotope Ratio Mass-Spectrometry, *Analytical Chemistry* 66, 1294-1301.

APPENDIX C

WolfAmp: A LabView Based Amperometry Program

C.1 Description

WolfAmp is a LabView based software package that collects and analyzes amperograms from a patch clamp amplifier. The electrochemical system and software are intended for use with microelectrodes and has been further adapted to perform chronoamperometric experiments. The software also has the capability to control a flow injection system that introduces samples into the continuously flowing electrolyte, in order to induce rapid concentration changes. This injection system is typically used to develop and calibrate electrodes for *in vivo* usage. The data collection software utilizes high frequency sampling rates, digital signal processing, and an oversampling feature to minimize signal noise. A supplementary data analysis program is used for additional data filtering, peak fitting, and data output. This analyzed data is exported as an amperogram, a concentration profile, and a database containing peak fitting values. Contact Leslie Sombers (leslie_somers@ncsu.edu) for information on how to obtain WolfAmp.

C.2 Hardware and Software Requirements

C.2.1 National Instruments and MATLAB

The software was developed with LabView (version 9.0.0, National Instruments, Austin, TX) and MATLAB (version R2009b, The MathWorks, Natick, MA). A full version of LabView is not necessary for data collection, only the LabView Run-Time Engine

(version 9.0.1) is required. A full version of MATLAB is necessary for data analysis. Two data acquisition (DAQ) cards (NI-PCI-6251 and NI-PCI-6711) are required for data collection, potential application, and flow injection control. A connector block (NI-CB-68LP) and two cables (NI-SHC68-68-EPM and NI-SHC68-68-EP) are also necessary to make the connections from the Axopatch and flow injection system to the DAQ card. National Instruments DAQ cards with comparable features can be substituted without alterations to the software. Alternatively, other data acquisition products are available from National Instruments that could be employed with slight alterations to the programming, but these will not be discussed in any detail.

C.2.2 Amperometric System

The software was designed for use with an Axopatch 200B Capacitor Feedback Patch Clamp Amplifier (Molecular Devices, Sunnyvale, CA) and low-noise headstage (model CV-203BU). The Axopatch is capable of making stable ultra-low noise recordings by thermoelectrically cooling the components of the headstage. The Peltier cooling system reduces the temperature of the input circuitry to about -10°C . The potential of the working electrode is controlled by sending a command voltage to the instrument. The instrument outputs a scaled voltage to be recorded as a current by the software. Signal gains and hardware filtering are controlled on the front panel of the Axopatch. All recordings must be taken within a grounded Faraday cage to reduce unwanted electrical noise.

C.2.3 Flow Injection System

The software was also adapted for use with a flow injection system that requires a syringe pump (New Era Pump Systems, Wantagh, NY) to supply a continuous buffer flow of $1 \text{ mL}\cdot\text{min}^{-1}$ across the working and reference electrodes. Single two second bolus injections are accomplished with a six-port HPLC valve and air actuator controlled by a digital valve interface (Valco Instruments, Houston, TX). A transistor-transistor logic (TTL) signal is output to control this valve. The working electrode was positioned in a custom electrochemical cell using a micromanipulator (World Precision Instruments, Sarasota, FL). This flow injection system is an added feature and is not required for amperometric experiments; as such, the PCI-6711 DAQ card, cable and connector block are not necessary.

C.3 Overview of LabView

LabView (Laboratory Virtual Instrumentation Engineering Workbench) is a system design platform and graphical programming language that uses dataflow programming to execute different functions. These functions are connected by drawing wires and these wires propagate information to the next function as the data becomes available. A typical LabView program consists of both a front panel and a block diagram. The front panel is a graphical user interface that allows the user to control the program, settings, data input, and displays the data. The block diagram contains all the graphical code for the program. Each program is called a virtual instrument (VI) and sub-programs are called sub-VIs. To facilitate programming, LabView supplies a large library of VI functions for creating applications, interfacing devices, data acquisition, and data analysis. This program also interfaces well

with MATLAB, to increase the signal processing capability of LabView. LabView also has the ability to compile the VIs and generate executable files that can run without the installation of the full developer's version of the program. This allows the custom program to be distributed and only requires the LabView Run-time engine to be executed, at no cost. Overall, graphical programming benefits a less experienced programmer and the features of LabView make it a highly productive development environment for scientists to acquire and analyze data.

C.4 Amperometry Overview

In constant-potential amperometry, the electrode is continually held at a potential so that any redox active molecule at the electrode surface will either be oxidized or reduced and produce faradaic currents. These currents are recorded and plotted versus acquisition time (amperogram). From these plots, the integral of the current (Q , Coulombs of charge) with respect to time is proportional to the number of molecules (N) electrolyzed at the electrode surface and follows Faraday's Law:

$$Q = nNF \quad (1)$$

where n is the number of electrons transferred and F is defined as Faraday's constant ($96,485 \text{ C}\cdot\text{mol}^{-1}$). When rapid data sampling rates are utilized, amperometry has excellent temporal resolution, due to the fact that electroactive molecules are consumed upon contact with the electrode surface. Amperometry is inherently nonselective, as all electroactive molecules that can be electrolyzed at the holding potential will produce faradaic current. Therefore, it is not ideally suited for making measurements in the complex mixtures.

C.5 Hardware Construction and Software Setup for WolfAmp

The construction and setup of the flow injection system would be dependent on the particular research goals. Figure C.1 shows a typical layout of the electrochemical system with flow injection. Briefly, buffered electrolyte flows through a six port HPLC valve and continues to an electrochemical cell where the working electrode is exposed to the flowing solution, before to the reference electrode. Analytes dissolved in the buffered electrolyte are loaded into the sample loop and upon command the digital-valve interface enables the actuator to switch the flow of buffer to force out the sample in the loop. This induces a rapid

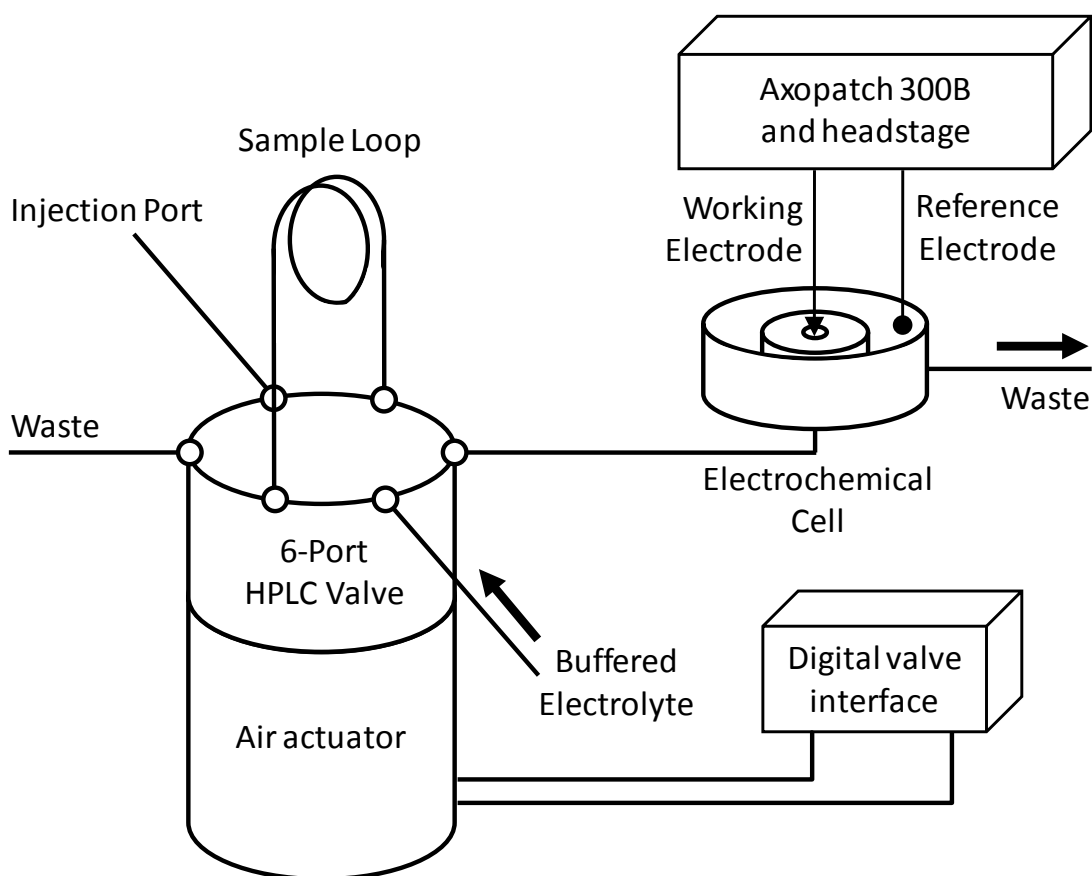


Figure C.1 - Schematic of flow injection system.

change in analyte concentration that is observed by the electrochemical system. Access to the digital valve and the back panel of the Axopatch are the only requirements for the electrochemical system to be incorporated into the software.

Construction for data recording only requires a minimal comfort level with computer hardware installation and a basic electrical tool set. The appropriate National Instruments DAQ cards must be installed on the computer motherboard and the included software needs to be installed, following the manufactures instructions. After the Measurements and Automation software is installed, the DAQ card PCI-6251 is given the name “1” and card PCI-6711 is assigned the name “2” in the program. It would be beneficial to enclose both connector blocks (NI-CB-68LP) in a metal enclosure to minimize electrical interference (Figure C.2). The two 68-pin cables connect the installed DAQ cards in the computer to the shielded connector block. Connections to the connector block from the Axopatch and digital-valve interface are as follows:

PCI-6251 “1”

Pin 68 = AI0 - Output voltage of Axopatch

Pin 34 = AI8 - Axopatch ground

Pin 22 = AO0 – Command voltage to Axopatch

Pin 55 = AOGND – Axopatch ground

PCI-6711 “2”

Pin 2 = CTR0 Out – TTL signal to digital valve

Pin 44 = DGND – Digital ground

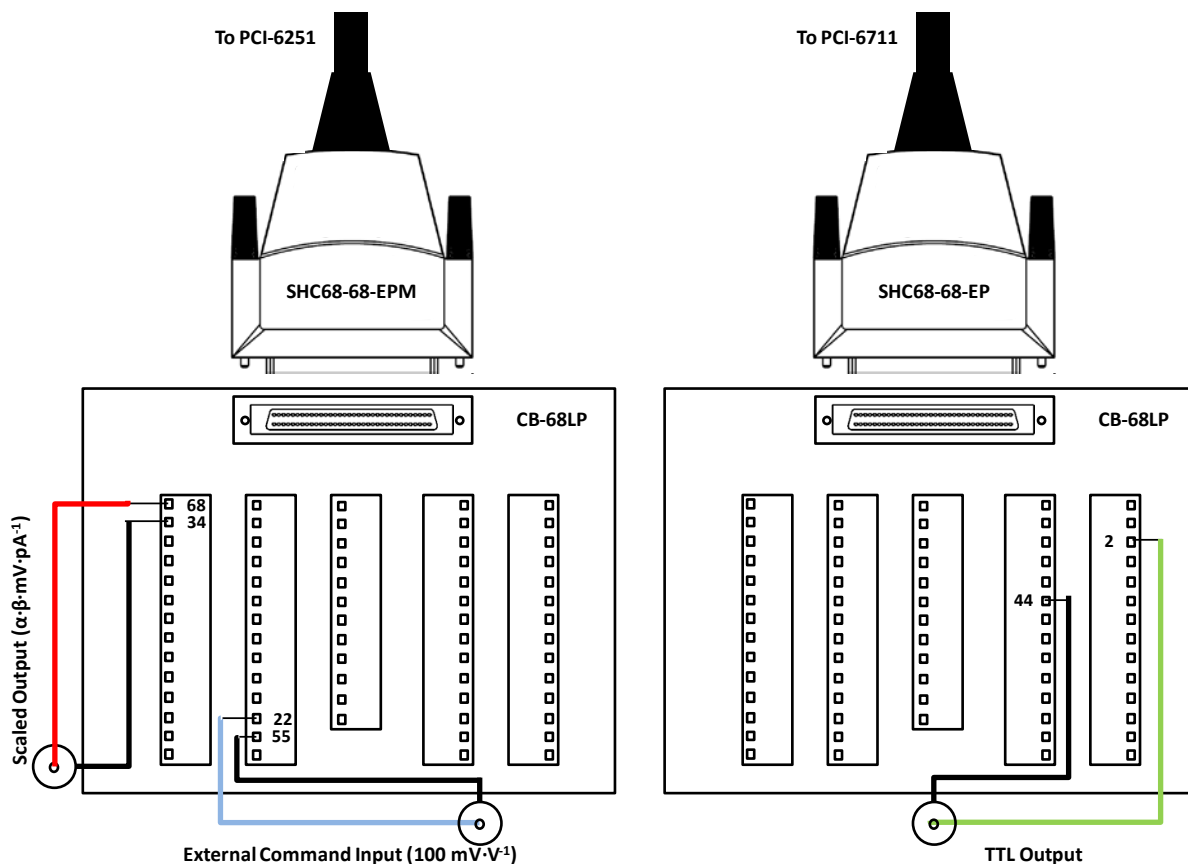


Figure C.2 - Diagram of electrical connections for data recording. A 68-pin connector block is used to make connections from the computer to the electrochemical system. BNC connectors are used to make connection to the Axopatch.

These connections to analog input (AI) and output (AO), counter (CTR) output, and digital ground (DGND) channels are software defined, but can be easily altered if these channels are occupied. AI0 accepts the voltage signal from the Axopatch (Figure C.2, red wire). This output voltage is scaled by gain multipliers (α and β) on the front panel of the Axopatch instrument, where one mV represents one pA of current measured. The Axopatch accepts external command voltage to alter the applied potential to the working electrode (Figure C.2, blue wire). This signal is scaled to a ratio of 100:1 (mV:V), where a 50 mV command

voltage from the computer would apply 0.5 V to the working electrode. To control the position of the HPLC valve for sample injection, a TTL signal is sent from the computer to the injection signal input on the digital valve interface (Figure C.2, green wire). An oscilloscope could be used to test the input and output signals to ensure a proper setup.

C.6 Data-Collection Software

As stated in the opening sections, WolfAmp is designed to record the currents collected from the Axopatch and rapidly alter analyte concentration with the flow injection system. Figure C.3 demonstrates the general flow of information between the electrochemical system, the DAQ cards and the software. Once the software is installed, a shortcut to WolfAmp will start the software.

Figure C.4 shows a screenshot of the front panel of the program. There are four main sections to WolfAmp's front panel and these include: file destination, data collection settings, file collection and termination, and data graphs. The file destination section has user input for changing the name of the file and drive location.

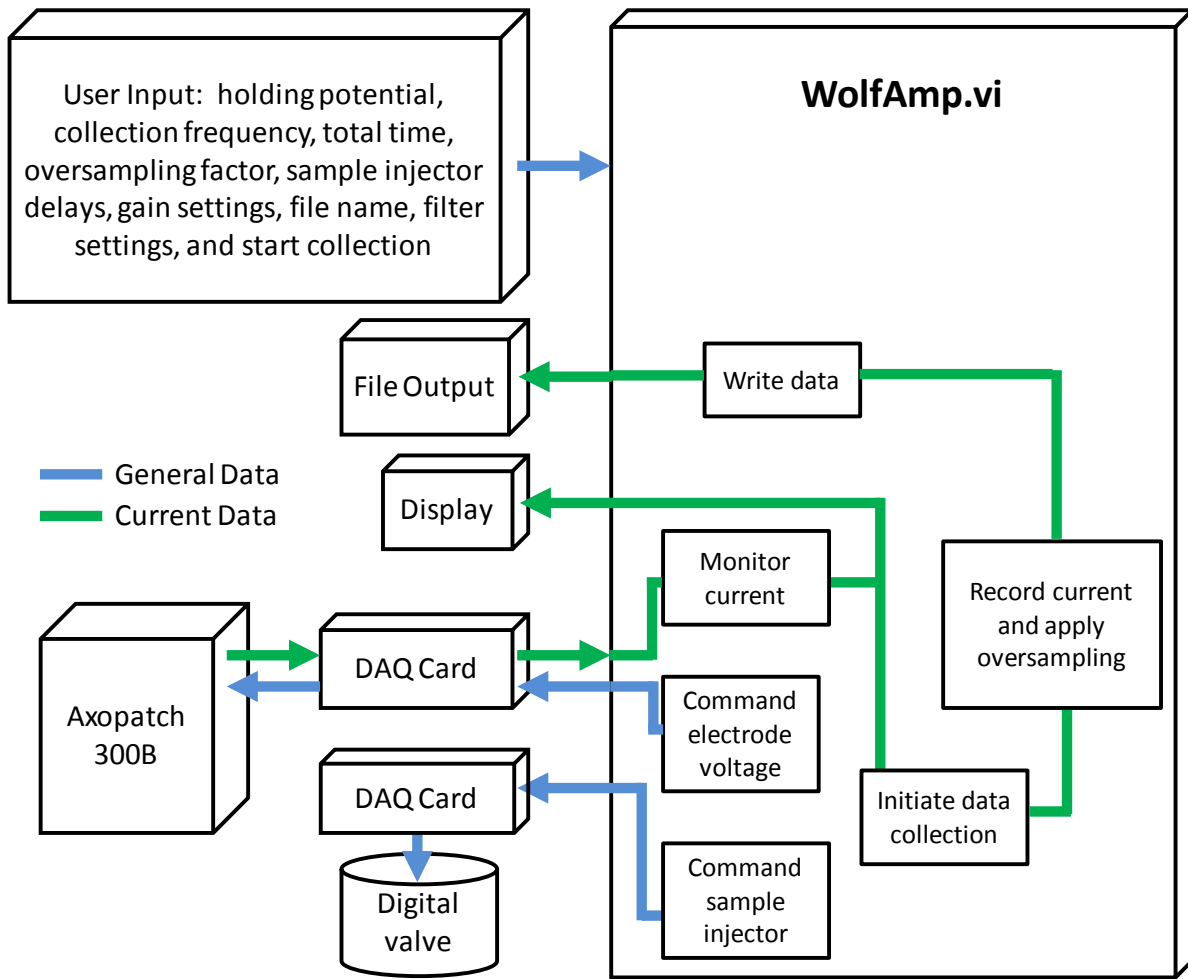


Figure C.3 - Schematic representation of data flow in WolfAmp.

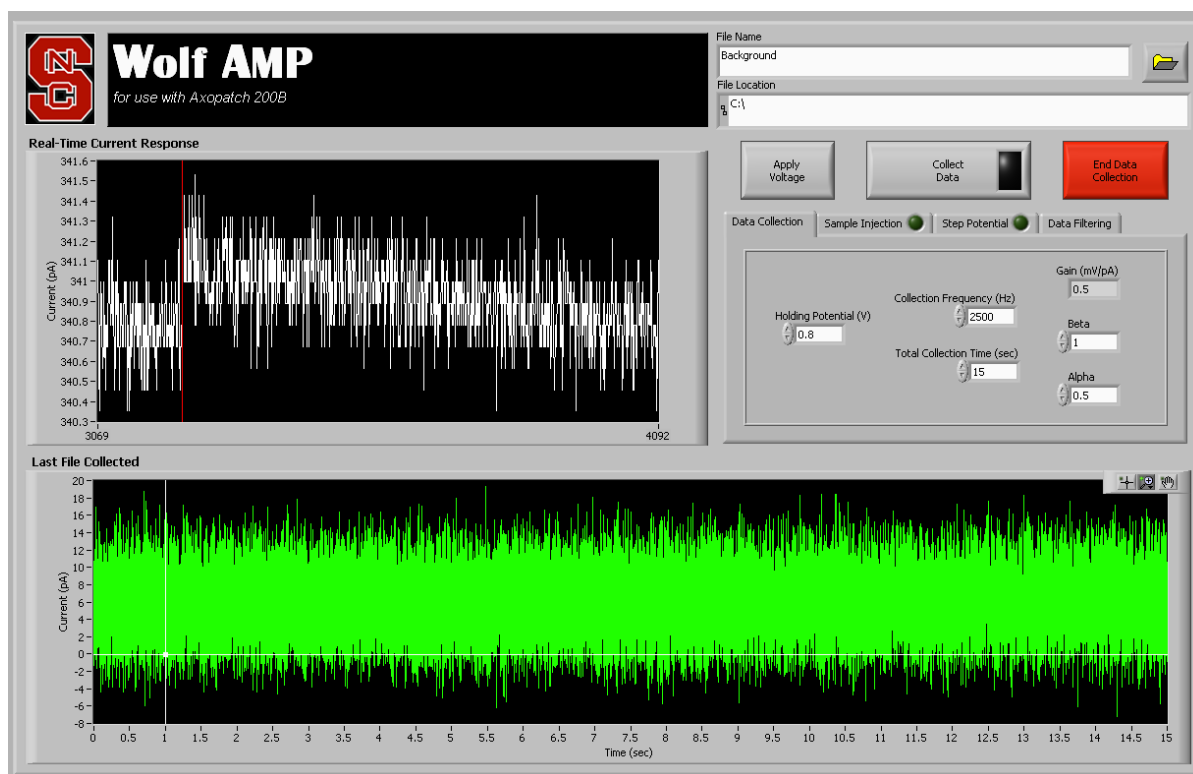


Figure C.4 - Screenshot of WolfAmp front panel.

The section for data collection settings is tabulated into four subfolders that allows the user to change data collection settings, enable sample injection, enable chronoampermetry, and change digital filtering settings (Figure C.5.A-D, respectively). The first tab controls the potential applied to the working electrode (V), the frequency of data collection in hertz (Hz), the total collection time (sec), and gain multipliers (alpha and beta) set on the front panel of the Axopatch. The gain of the amplifier is output in this tab in units of $\text{mV}\cdot\text{pA}^{-1}$. The second tab controls the delay and duration of sample injection (sec) by controlling the digital valve. The delay is relative to the start of file collection and enabling sample injection will illuminate a green light on the tab and switch. The third tab allows the

potential to be stepped during file collection and enabling this feature lights green indicators in the tab and switch. There are controls for changing the delay of the step (sec) and the potential the electrode (V) at the chosen step time. The final tab controls the oversampling factor along with the frequency and order of a digital low-pass filter. The Axopatch has a 4-pole low-pass Bessel filter with frequencies ranging from 1 – 100 kHz. This requires that the frequency of data collection must be at least 2 kHz (at the lowest filter setting) to satisfy the Nyquist frequency and prevent aliasing. Oversampling is a signal processing method that helps improve peak resolution and reduce signal noise. This feature simply multiplies the data collection frequency by the user specified oversampling factor. The additional data points collected in response to oversampling are averaged to give a single representative data point at the original collection frequency. For example, a one second file collected with the data collection frequency set to 100 Hz would result in 100 data points. If an oversampling factor of 4 was used, the actual frequency of data collection will be 400 Hz, and every four consecutive data points are averaged. This averaging returns 100 data points collected at 100 Hz and effectively averages out the noise to give a better representation of the real data.

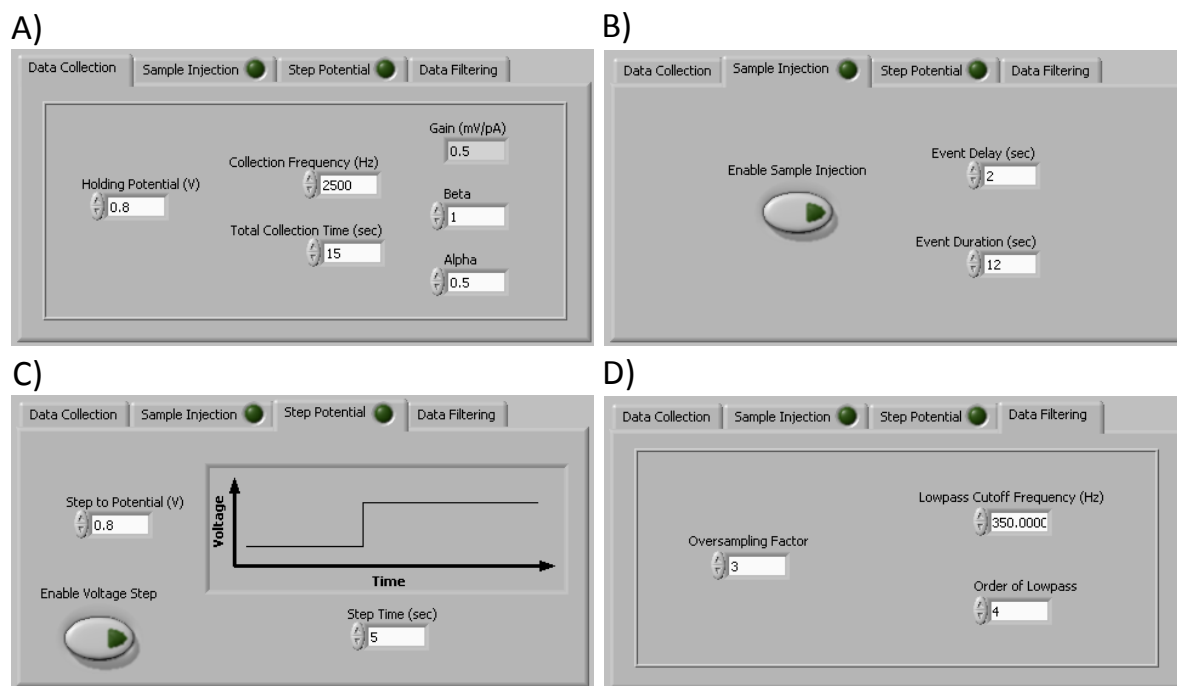


Figure C.5 - Screenshots of the tabulated file-collection settings.

The file collection and termination section has a button for initiating data collection, one for aborting file collection and another for applying the voltage to the working electrode. When the “Apply Voltage” button is enabled, the software will send the value assigned to holding potential to the Axopatch and will set the voltage to zero when disabled. The “Collect Data” button will initiate data recording and begin the other features like sample injection and voltage stepping. File collection can be aborted at any time by selecting the “End Data Collection” button, and all collected information will be written.

The final section plots both the real time data streaming from the detector and the last file collected with the software. The program will continuously monitor the current of the electrochemical cell and plot this data in the “Real Time Data” graph, as current (pA) versus

data point. The “Last Collected File” graph gives the user full control to examine the previously recorded amperogram with zooming, panning, and windowing features.

After a file is collected, the data is output in LabView’s native data file format (.tdms). This format benefits from smaller file sizes and is more easily integrated into the programming. Other file formats require the data to be retained in memory until collection is finished that could result in lost data from memory dump. To avoid this data loss, the tdms format streams data directly to the file location.

C.7 Data-Analysis Software

In addition to WolfAmp, WolfAmp Analysis is included to explore the amperogram, convert the graph to a concentration profile, and extract information by analyzing peak properties. Once the software is installed, a shortcut to WolfAmp Analysis will start the software. Upon startup, the user is presented with a front panel like that shown in Figure C.6. This front panel is divided into three sections: file location, data graphs, and filtering and peak analysis. The file location section has user input for opening the desired file and displays the drive location.

The “Raw Data” graph displays the unaltered amperogram contained within the selected file. This graph also has two vertical lines (red and green) that can be positioned to span a small region of the graph that best describes a time where no analyte was present. This region is used to define the signal to noise ratio that will be used to determine the significance of peaks. The opposing graph, labeled “Finished Data,” displays the amperogram or concentration profile after baseline correction and filtering. There are

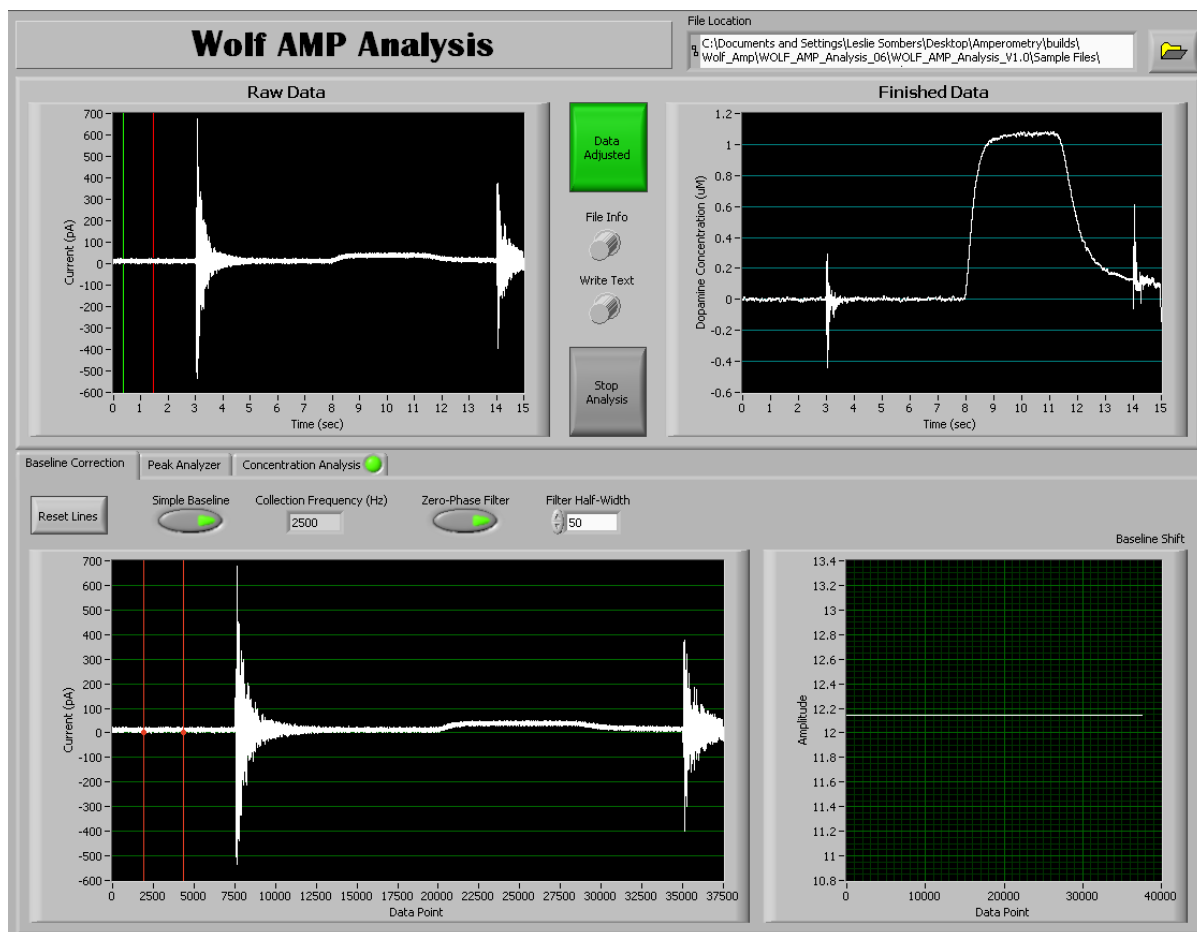


Figure C.6 - Screenshot of WolfAmp Analysis front panel.

controls between the two graphs that enable data correction, displaying file information, writing a text file of the finished data, or stopping the program. If data correction is disabled the finished data graph will display the raw data, otherwise the graph will display corrected data based on user settings. The file info button will open another window that shows the properties of the data file and information that was retained about the data collection settings. The write text button will save a text file of the finished data graph in the same file location of the original data.

The final section is tabulated for baseline correction, peak analysis, and concentration analysis. Some amperograms exhibit variability in the baseline, as a result of electrode drift or current generated from other electroactive species in solution that offset the baseline, and it may be advantageous to correct for this error. To this end, the program is setup to either perform a simple baseline correction that offsets the entire spectra about the y-axis, or it can fit a polynomial to the baseline and subtract this curve from the raw data to correct a more complex baseline drift. If the simple baseline is enabled, two vertical red lines appear in the graph and are positioned to span a region of the graph that best defines the baseline. The average current collected between the vertical lines is plotted in the “Baseline Shift” graph and subtracted from all values in the chromatogram to shift the plot vertically. An example of this baseline correction can be seen in Figure C.6. If the simple baseline option is disabled, ten red vertical lines are positioned in the graph, where the user adjusts the position of the lines to locations that best describe the baseline. The data points that are intersected by the vertical lines are used to fit a curve with the user defined “polynomial order.” The fitted curve is displayed in the “Baseline Shift” graph and this curve is subtracted from the raw data to correct the baseline. There is also a zero-phase filtering option to smooth the data without altering the location of the peak. When enabled, the zero-phase filter applies the user defined window half-width to filter the raw data. This filtered data is not used in peak fitting, as it is only intended to generate a more aesthetic graph.

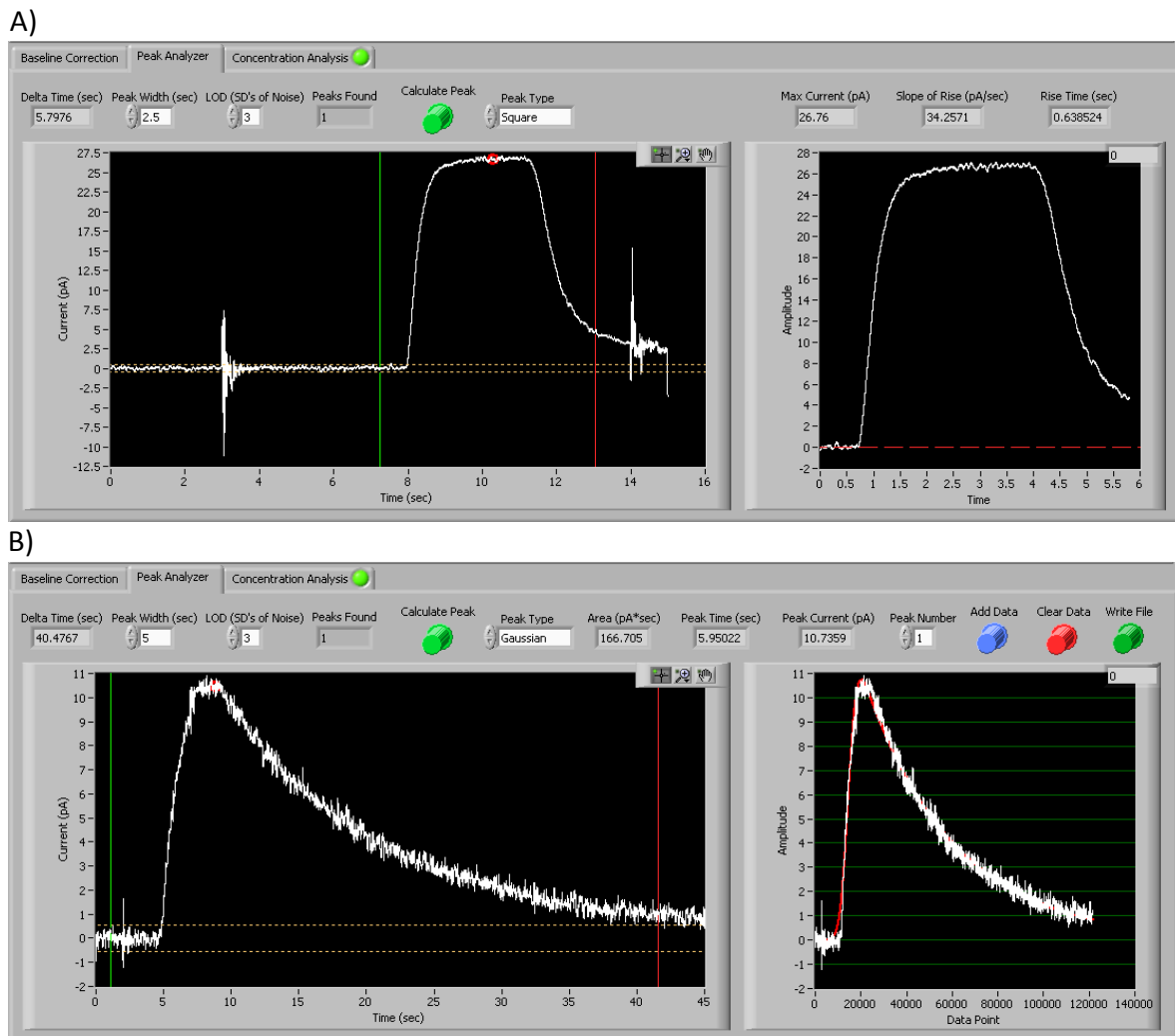


Figure C.7 - Screenshot of the tabulated peak analyzer section. The program can either fit a square wave (A) or an exponentially modified Gaussian curve (B) to the data.

The peak fitting section is shown in Figure C.7, which displays a graph of the baseline corrected chromatogram and a graph of the fitted peak. To select a peak for fitting, the first graph has two movable vertical lines to indicate the start (green) and end (red) time of the peak of interest. This graph also displays two horizontal yellow lines that represent the limit of detection based on the user specified number of standard deviations. All peaks that extend

beyond the limit of detection lines, with peak widths greater than the user defined values, are identified and labeled with a red dot. An example of this can be seen in Figure C.7.A and B, where the program has identified 1 peak based on the criteria set by the user. To analyze a peak the user will define the peak type (square or Gaussian) and position the start and end lines around the peak of interest, and then select the “calculate peak” button. The data contained within the lines are plotted in the adjacent graph with white dots and the fitted peak is plotted in red. There are controls for assigning the peak a number, adding the peak values to a spreadsheet, clearing the spreadsheet, or exporting the data once all peaks are fitted. These peak fitting parameters include: peak area, peak time, Gaussian width, exponential decay factor, and peak current. Ideally rapid changes in concentration should exhibit a square wave response, but other processes inherent to electrochemistry slow the response time of the electrode (Figure C.7.A). For this reason, the time and slope for the current to rise from 10 to 90 % are calculated and displayed. Other rapid concentration changes never reach a saturation point and have slow clearance rates. For this data type, peak fitting is based on an exponentially modified Gaussian distribution following the equation:

$$f(x) = \frac{a_0}{2a_3} \exp \left[\frac{a_2^2}{2a_3^2} + \frac{a_1 - x}{a_3} \right] \left[\operatorname{erf} \left(\frac{x - a_1}{2^{1/2} a_2} - \frac{a_2}{2^{1/2} a_3} \right) \right] \quad (2)$$

where a_0 is peak area, a_1 is elution time, a_2 is Gaussian width, and a_3 is the exponential decay factor (I). An example of this fitting is shown in Figure C.7.B, where tailing of the peak is fitted with the convoluted Gaussian function (Equation 2). From these calculated values, peak current can be used to determine electrode sensitivity to an analyte by plotting this

current versus various concentrations. Linear regression of these data point would give a slope that could be used to predict unknown concentrations.

In the final tabulated section (Figure C.8), an electrodes sensitivity can be input with the appropriate units and by using Faraday's law (Equation 1), the area of the peak, and the number of electrons transferred the total number of molecules detected can be calculated. Enabling this feature will alter the finished data graph to show the proper concentration units and analyte name. WolfAmp Analysis is a powerful addition to the data collection program that enables rapid quantification of amperograms. Future versions of the program will incorporate more elaborate peak fitting features and more statistical information on curve fitting to determine the goodness of fit.



Figure C.8 - Screenshot of the tabulated concentration analyzer section.

C.8 Block Diagram of WolfAmp

The following figures are images of the block diagram for the data collection program. Figure C.9 is the entire block diagram for WolfChrome and Figures C.10-11 are enlarged images of Figure C.9 that were split to fit within the page limits. Each programming loop is labeled with letters A – G inside red circles to ease the description of the block diagram. Loop A is the first part of a sequential loop where the two DAQ cards are initialized. Loop B is the final part of the sequential loop where the channels for the analog input and analog output are initialized. When the program is ended, this loop is exited after writing a value of zero volts to the analog output. Loop C is the main for loop that runs until the user ends the program. Inside this loop, the values for data collection are set by the user, including the name and location of file to be collected. Loop D is a conditional loop that is responsible for changing the voltage during file collection for a chronoamperometry experiment. Loop E is a conditional loop that applies a voltage to the working electrode after the user has enabled the voltage to be applied. Loop F outputs the TTL signal that is sent to the digital valve for sample injection. Finally, Loop G records the voltage from the detector, applies the oversampling method at the user specified frequency, filters the streaming data, and displays this data in the real time graph on the front panel.

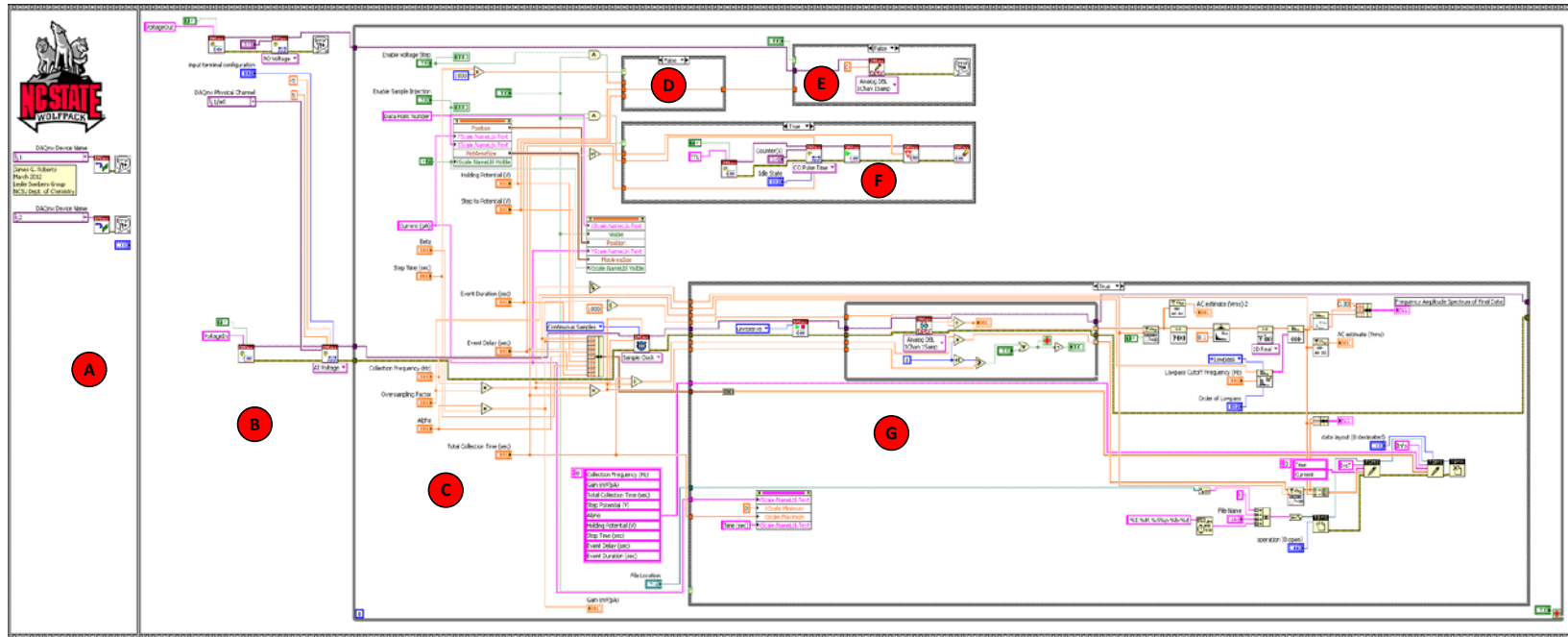


Figure C.9 - Screenshot of WolfAMP block diagram. The red lettered circles (A - G) indicate the separate programming loops.

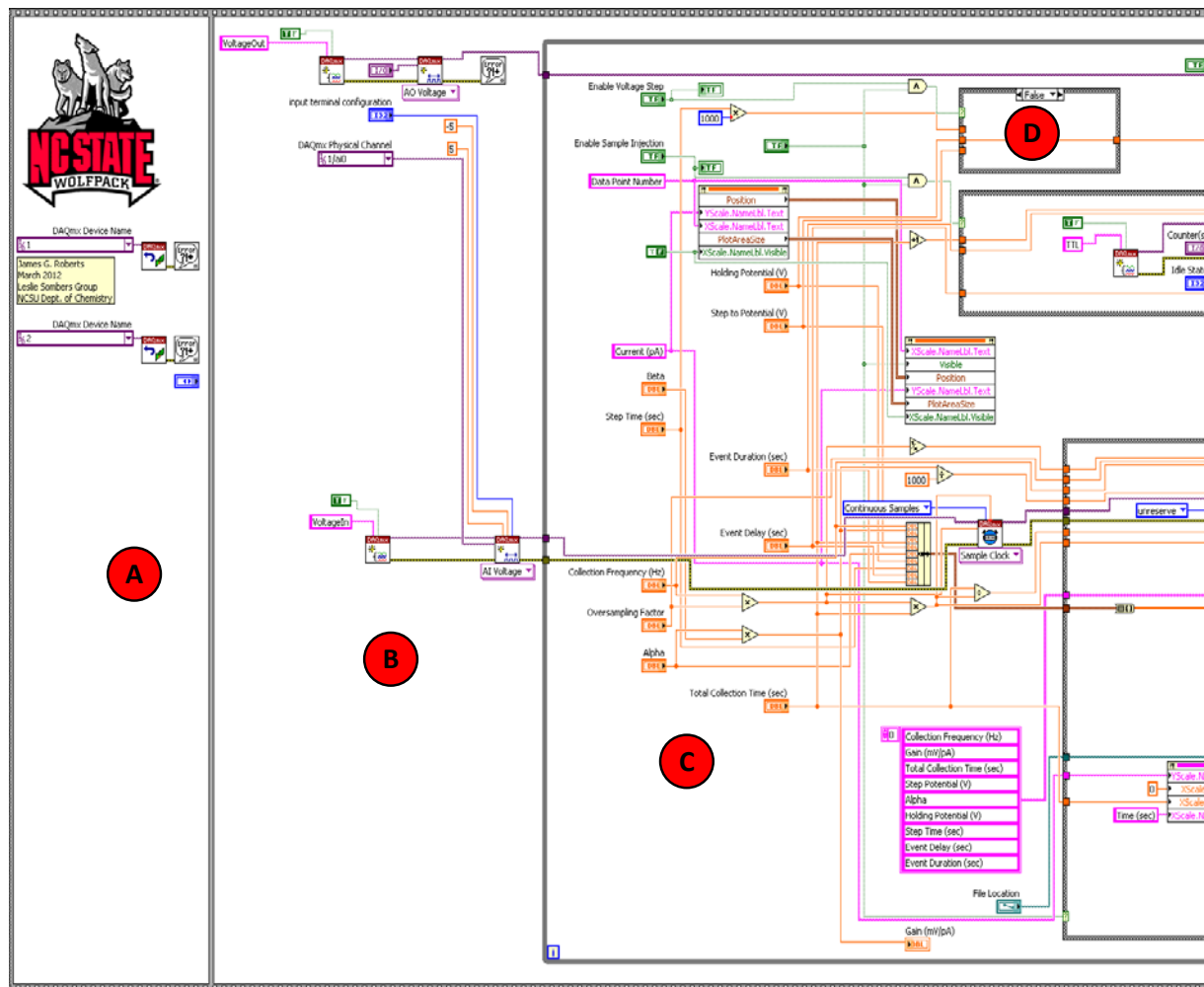


Figure C.10 - WolfAmp block diagram, Part 1 of 2.

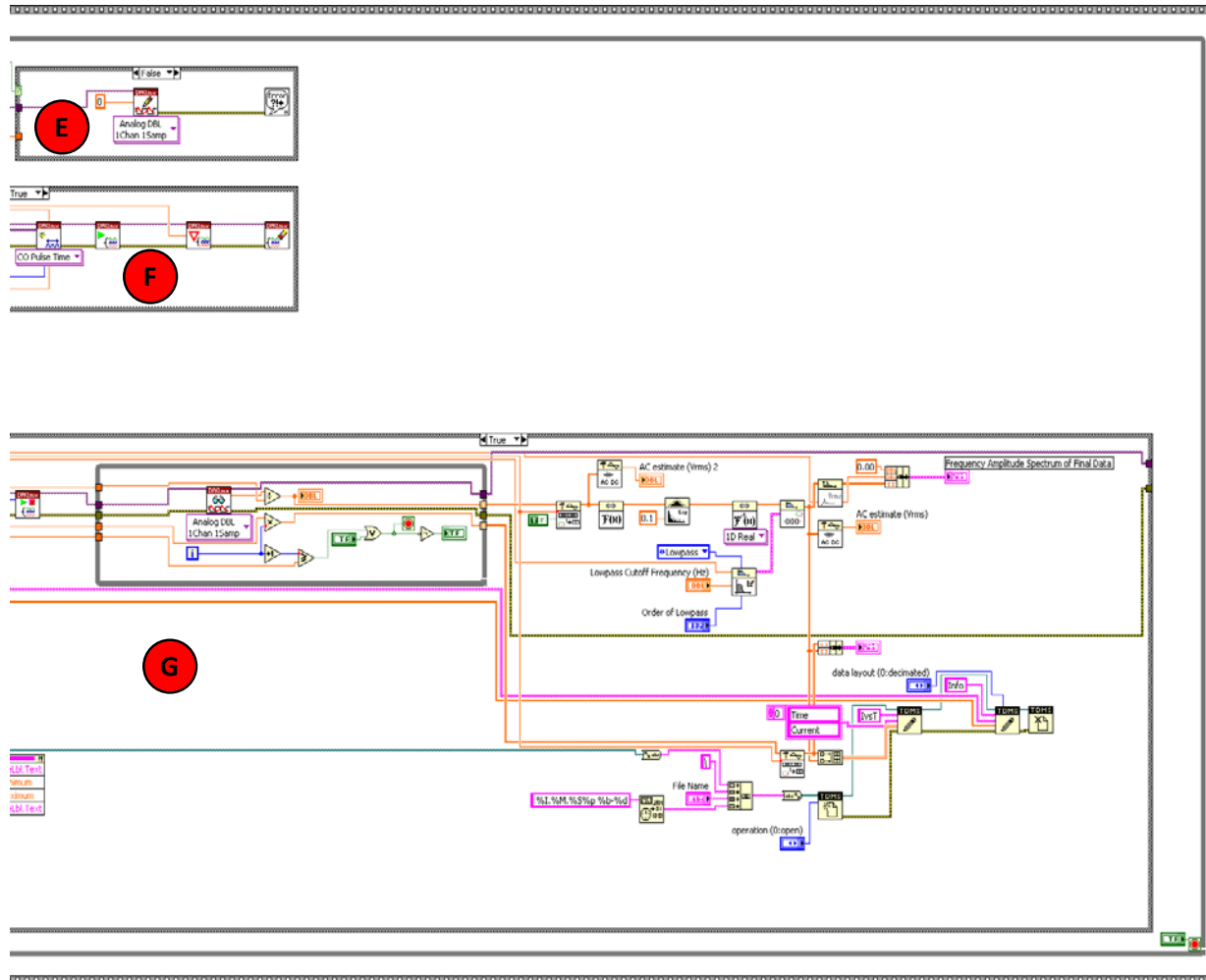


Figure C.11 - WolfAmp block diagram, Part 2 of 2.

C.9 Block Diagram of WolfAmp Analysis

The following figures are images of the block diagram for the data analysis program. Figure C.12 is the entire block diagram for WolfChrome and Figures C.13 – 16 are enlarged images of Figure C.12 that were split to fit within the page limits. Each loop is labeled with letters A – L inside red circles to ease the description of the block diagram.

Loop A is the main for loop that encompasses the whole program and loop exits when the user closes the program. This loop is responsible for all user input, opening and reading the selected file, displaying all data in all graphs, peak finding, and calculates analyte concentration. Loop B is a conditional loop that displays the file information that was retained in the collected file, when enabled. Loop C is conditional loop that controls labeling of the finished data graph and the filenames. Loops D and E are conditional loops that control baseline correction. Loop D is responsible for building and graphing the two vertical lines that are present in the simple baseline correction or the ten lines in the polynomial corrected baseline method. Loop E determines the baseline by either averaging the current between the vertical lines or fits a polynomial to the selected ten data points. Loop F is a conditional loop that performs zero-phase filtering on the baseline corrected data, when selected. Loop G is responsible for fitting the selected peak with the exponentially modified Gaussian equation. This loop utilizes MATLAB and nonlinear regression to iteratively fit the equation. The initial guesses used for the fitting are supplied by first fitting a Gaussian curve to the selected peak. Loop H fits a square wave to the selected peak and calculates the response time. Conditional loops I and J add or remove peak fitting values to the spreadsheet, respectively. Loop K writes a text file of the amperogram or concentration

profile displayed on the finished data graph and loop L writes the spreadsheet that contains the peak fitting values for all assigned peaks.

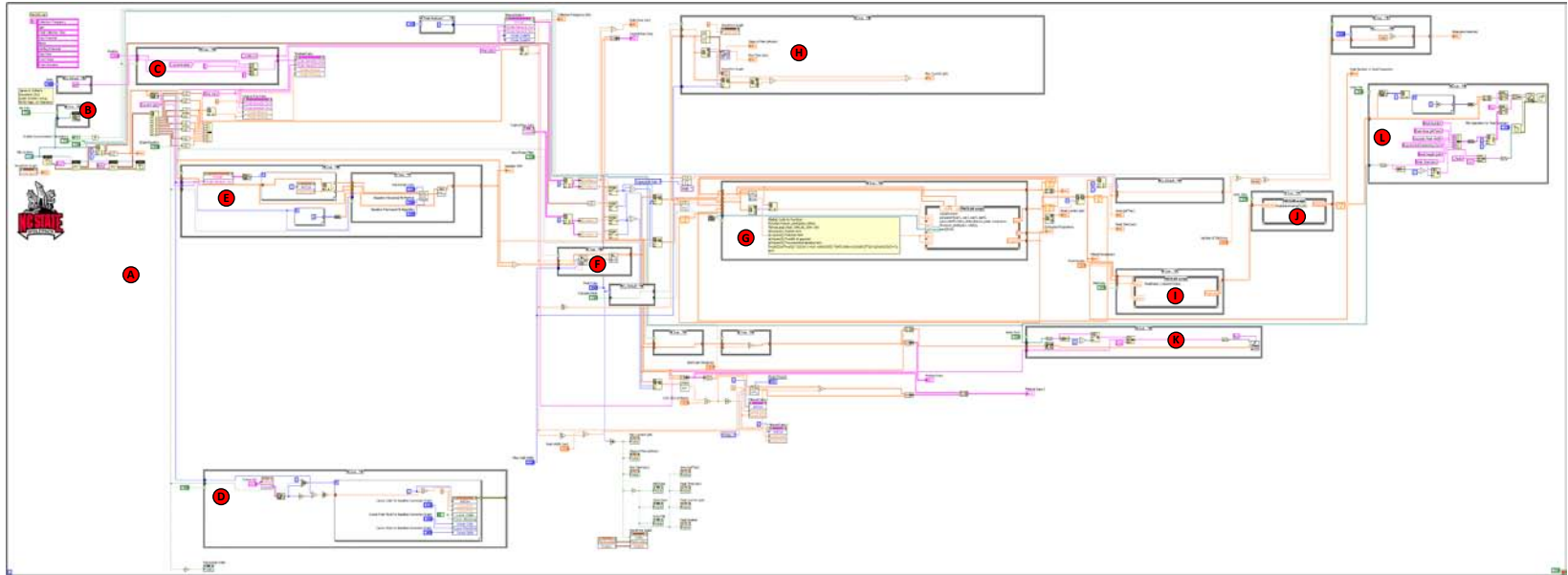


Figure C.12 - Screenshot of WolfAmp Analysis block diagram.

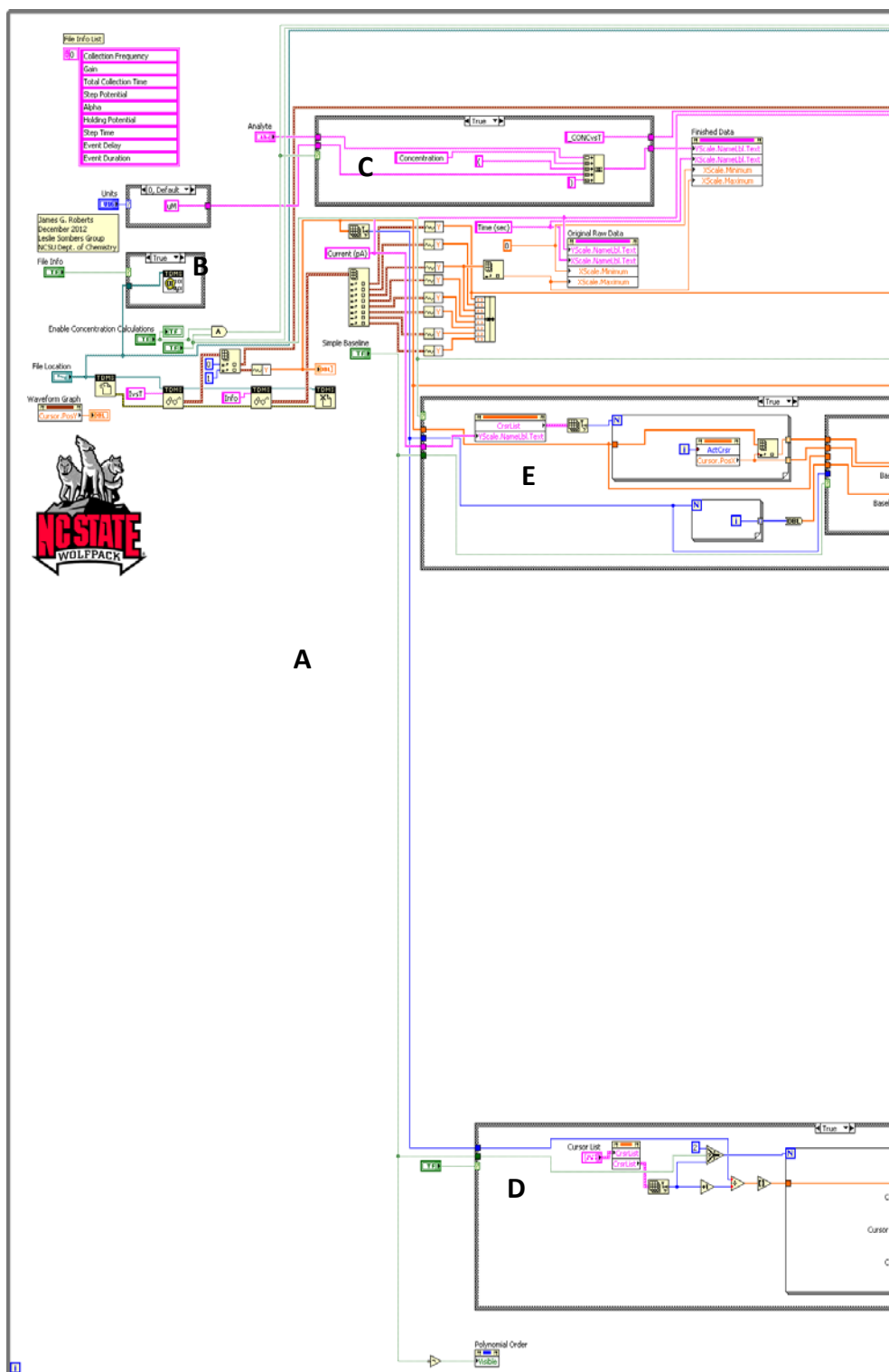


Figure C.13 - WolfAmp Analysis block diagram, Part 1 of 4.

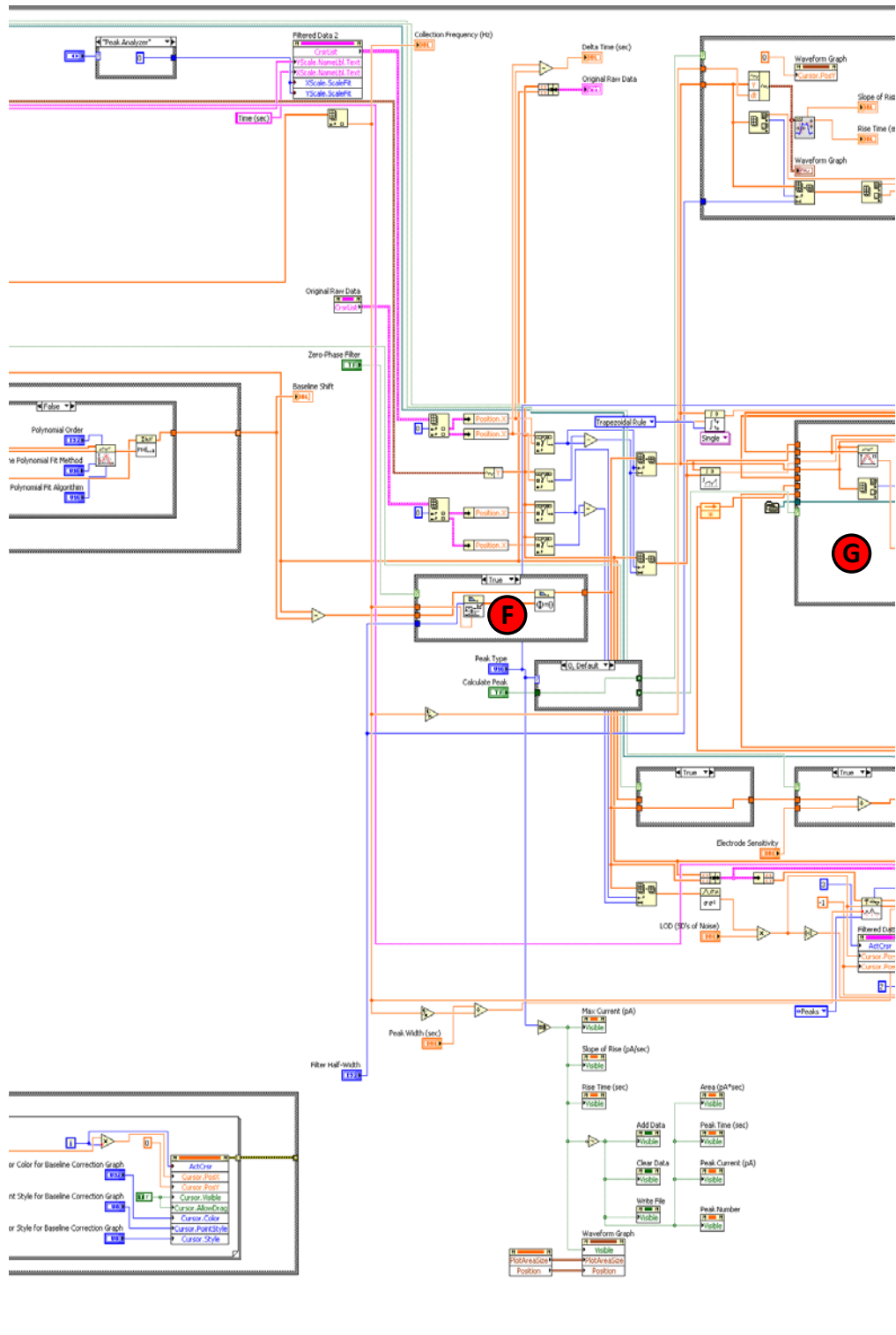


Figure C.14 - WolfAmp Analysis block diagram, Part 2 of 4.

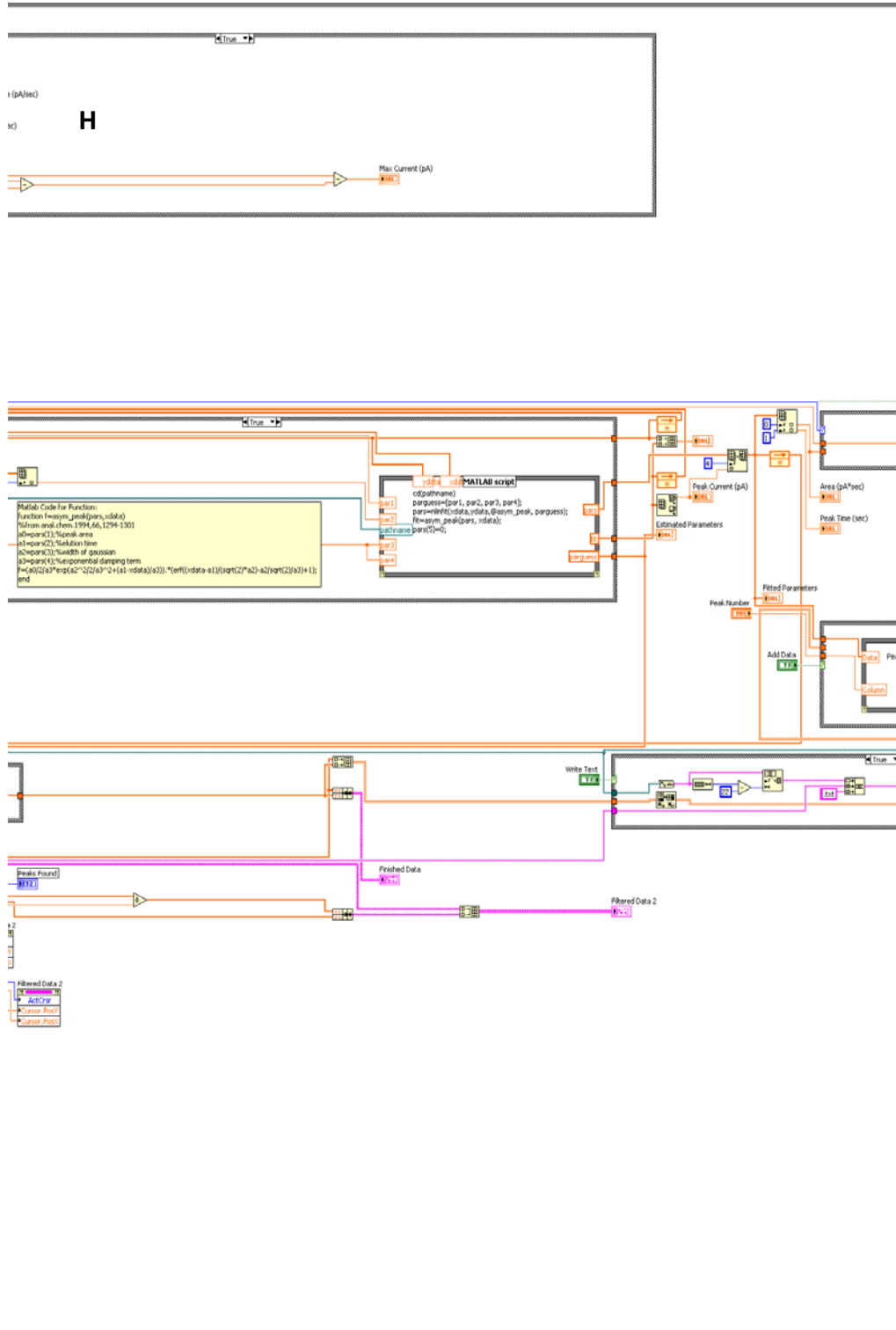


Figure C.15 - WolfAmp Analysis block diagram, Part 3 of 4.

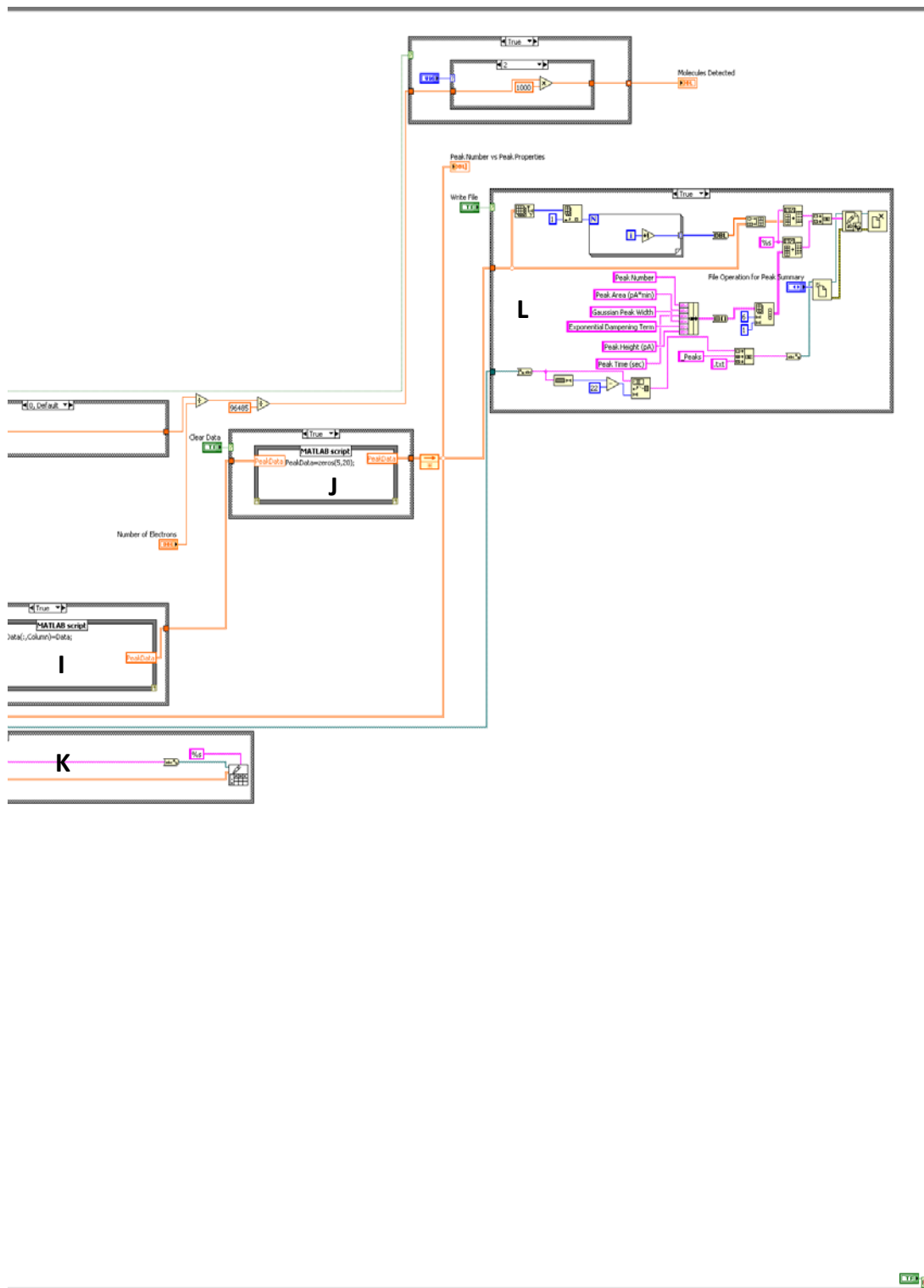


Figure C.16 - WolfAmp Analysis block diagram, Part 4 of 4.

C.10 References

1. Goodman, K. J., and Brenna, J. T. (1994) Curve-Fitting for Restoration of Accuracy for Overlapping Peaks in Gas-Chromatography Combustion Isotope Ratio Mass-Spectrometry, *Analytical Chemistry* 66, 1294-1301.

APPENDIX D

Supplemental Information to Chapter 9:

Trace Metal Complexation by the Triscatecholate Siderophore protochelin: Structure and Stability

The following work was reprinted with kind permission from Springer Science and Business Media: James M. Harrington, John Barger, Andrzej A. Jarzecki, James G. Roberts, Leslie A. Sombers, and Owen W. Duckworth, *Biometals*, 2011, 22, 393-412., Copyright 2011 Springer.

D.1 Preparation of Protochelin complexes

Iron solutions were prepared using a 0.10 M FeCl_3 standard solution, which was made from solid FeCl_3 (99.9%, Fisher Scientific) and was standardized spectrophotometrically. Manganese solutions were prepared using a 0.10 M MnCl_2 standard solution, which was made from solid MnCl_2 (99.9%, Fisher Scientific) and standardized by traditional methods. Co solutions were prepared using a 0.10 M CoCl_2 standard solution, which was made from solid CoCl_2 hexahydrate (99.9%, Fisher Scientific) and standardized by traditional methods. Cr solutions were prepared using a 0.10 M CrCl_3 standard solution, which was made from solid CrCl_3 hexahydrate (99.9%, Fisher Scientific) and standardized by traditional methods.

Protochelin complexes must be prepared carefully due to the low solubility of the ligand at low and moderate pH values. The low solubility is complicated by the propensity of the metals studied here to hydrolyze at higher pH values, making the formation of metal-protochelin complexes difficult. Iron-protochelin complexes were prepared by addition of

deionized water to solid protochelin, followed by addition of an acidic solution of 0.10 M Fe(III) chloride. This was followed by slow addition of small volumes of 0.10 M NaOH to adjust the solution pH. As the solution pH increased, gradual complexation of the metal occurred, as evidenced by the gradual color change of the solution to purple, and then red. The final solution pH was 9.0, ensuring both complete dissolution of the ligand and complete formation of the Fe-protochelin complex. The solution was diluted with background electrolyte to provide the final concentration. The pH of this stock solution could then be adjusted as necessary for use in experiments.

Manganese-protochelin complexes were prepared by addition of deionized water to solid protochelin, followed by addition of 0.10 M base until the solution pH was approximately 7 to promote dissolution of the ligand. Upon dissolution of the ligand, a solution of 0.10 M MnCl_2 was added and the solution pH was readjusted to 8.5 with 0.10 M NaOH. The solution was then left open with stirring to allow air oxidation of the Mn-protochelin complex for a minimum of 3 hours. Upon completion of air oxidation, the solution was diluted to the final volume, and the pH was adjusted to approximately 7.5. Solutions were stored in the refrigerator until use to minimize degradation.

The cobalt-protochelin complex was prepared in a similar manner as the manganese-protochelin complex. The solution color change took place significantly more rapidly than was observed with the manganese-protochelin complex (~30 min at pH 8.5). After allowing air oxidation of the complex, the solution pH was adjusted to 7.5 with 0.10 M HCl. The solution was found to degrade rapidly (over the course of 3 hours), and so was not able to be used for EXAFS measurements or for thermodynamic characterizations.

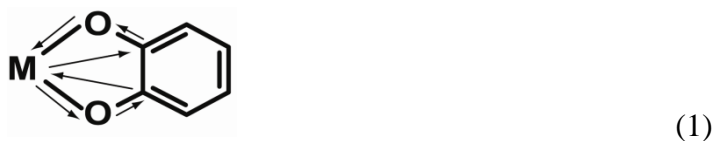
An attempt was made to produce the Cr-protochelin complex by dissolution of solid CrCl_3 in deionized water, followed by addition of solid protochelin and gradual adjustment of the solution pH to 8.0 with 0.10 M NaOH and stirring. The solution was heated for 2 hours at 80°C , resulting in a color change of the solution from green to light brown. EXAFS spectroscopy was used to determine the immediate coordination environment of the metal in the solution (not shown), and no evidence was found of structure beyond the first coordination sphere, suggesting that the complex had not formed.

D.2 Formulation of Structural Models Used to Fit EXAFS Spectra

Both single and multiple scattering paths were utilized in the fitting models for metal-protochelin complexes. Atoms surrounding the central metal (excluding H) in DFT structural models were binned into shells for the EXAFS model as follows: a first shell consisting solely of oxygen atoms first shell (i.e., directly bonded to the central metal), C atoms in binding moieties at an approximate distance of 2.8 \AA , and the proximal C atoms in the rings of catecholates (at distance of $4.1 - 4.3 \text{ \AA}$). Shells based on binding O atoms, C atoms in binding moieties, and the proximal C atoms in “backbone”, were found suitable to the fits all of the samples. This approach has been successful for metal-DFOB complexes (1-5). For Fe(III)-Proto at $\text{pH} = 7.5$, the complex is coordinated by catecholates (6), as is discussed in this report, and will from hereout be referred to as Fe(III)Proto^{3-} . The first shell coordination number (N) was allowed to float; the second and third C shells (cf., Table 2) were fit with $N = 6$ based on the atoms in coordinating moieties. In contrast, a salicylate coordination [$\text{Fe(III)H}_3\text{Proto}$] is found for the Fe(III)-Proto system at $\text{pH} = 4$, similar to what has been

observed for enterobatin (6). For this complex, an additional C 2nd shell with $N = 3$ (in six-membered rings) was added to the model (Figure 9.1), and resulted in an improvement of the fit that was significant at the 95% confidence level, as judged by a Hamilton test (7, 8). For Mn(III)Proto³⁻, the Mn-O shell was partitioned into two subshells with fixed $N = 4$ and $N = 2$ to account for Jahn-Teller distortion (2, 3). Mn(III)Proto³⁻ at acidic pH is not stable as evidenced by a rapid bleaching of the complex, and thus was not measured. Cr and Co complexes were not fit to structural models because of evidence that they did not form stable complexes, as discussed in the main text.

The model fits for metal-protocelin complexes were improved by the addition of multiple scattering shells. Multiple scattering paths calculated by FEFF with ≤ 4 legs and $R < 4.2 \text{ \AA}$ were grouped based on the scattering elements and considered in the model. A triangular three-legged path (insert 1) containing metal-oxygen-carbon paths at ca. 3.0–3.2 \AA (redundancy = 12) associated with the atoms in binding moieties improved the fit for Fe(III)Proto³⁻ and Mn(III)Proto³⁻, as tested at the 95% confidence level (7, 8):



For self-consistency, this shell is also used in the fit for Fe(III)H₃Proto.

Several other multiple scattering paths were considered that did not significantly improve the fit. Utilization of triangular three-legged paths containing metal-oxygen-oxygen paths did not improve the fit, possibly because these paths are distributed over a wide range of distances (3.3–3.8 \AA). Similarly, the inclusion of six triangular three-legged metal-carbon-

carbon paths at ca. 3.5–3.6 Å did not measurably improve the fit, possibly due to interference from metal-oxygen-oxygen paths. Additionally, six four-legged paths metal-oxygen-metal oxygen paths near 4 Å that cross the absorbing atom, previously identified as the most important of several collinear three- and four-legged paths that are possible for multiple scattering interactions between the central metal and surrounding oxygen atoms in the 1st O shell (9), also did not significantly improve the fit.

D.3 Background-subtracted fast-scan cyclic voltammetry (FSCV) and ligand adsorption

Using background-subtracted FSCV, the current generated for the redox reaction of protochelin was found to be adsorption-controlled (rather than diffusion-controlled), by plotting cathodic peak current collected at -0.2 V as a function of scan rate ($r^2 = 0.978$, $n = 3$ electrodes, Figure D.8). Redox reactions of catechols at carbon fiber electrodes have been shown to be adsorption controlled under similar experimental conditions (10, 11). The equation defining peak current due to an adsorbing species defines how the peak current (i_p) is proportional to the scan rate (v) (12):

$$i_p = (9.36 \times 10^5) n^2 v A \Gamma_x \quad (1)$$

Other variables include the surface area of electrode (A) and the surface coverage (Γ_x) of the analyte on the electrode surface.

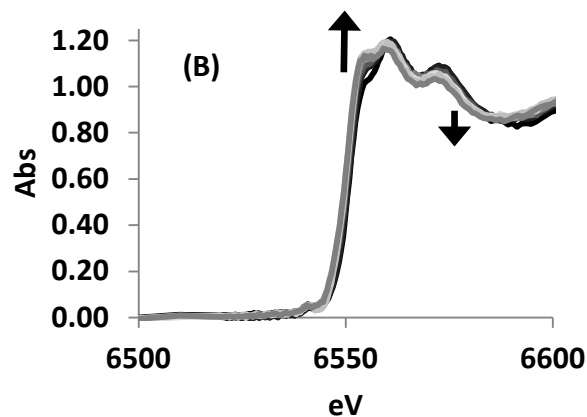


Figure D.1 - Plot showing the change in of the Mn-protocelin EXAFS spectrum with time. The first scan is shown in black, while the subsequent scans are shown in progressively lighter shades of gray.

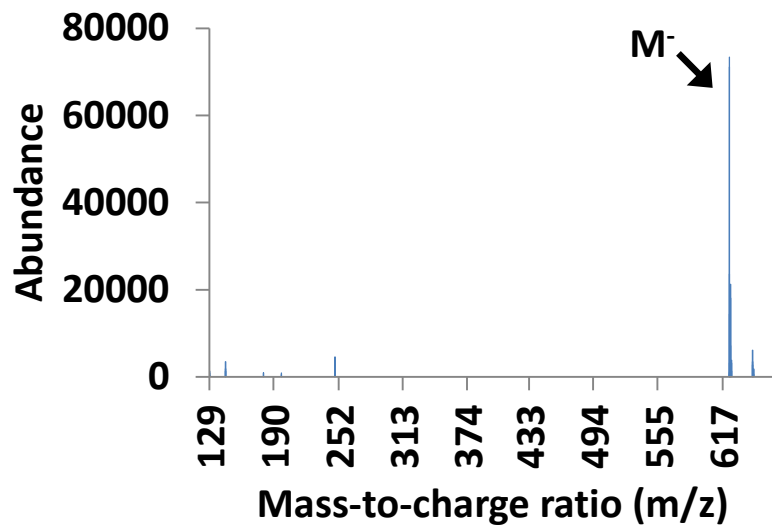


Figure D.2 - ESI mass spectrum measured for protocelin. Conditions: Solution prepared at pH 8.3, [Protocelin] = 1.1 mM, capillary voltage - 3.5 kV, nebulizer pressure - 50 psig, drying gas flow rate - 10 L·min⁻¹, T = 350 °C, fragmentor voltage – 110 V, skimmer voltage - 65 V.

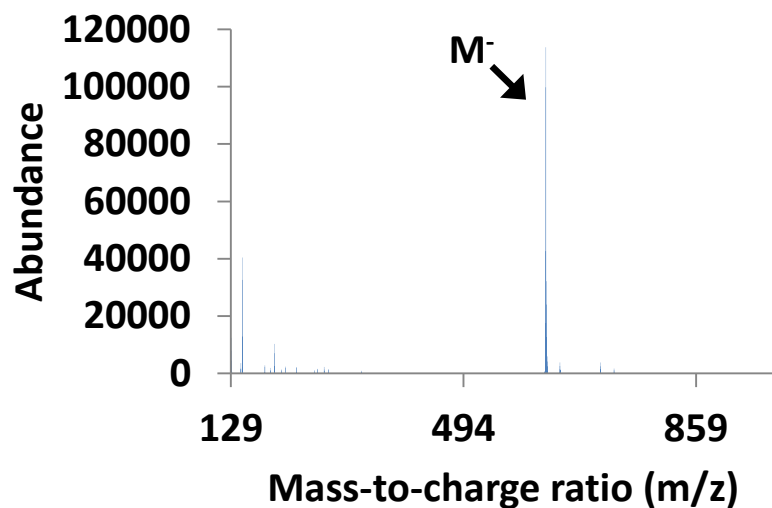


Figure D.3 - ESI mass spectrum measured for protochelin after degradation at high solution pH. Conditions: Solution prepared at pH 10.0, [Protochelin] = 1.05 mM, capillary voltage - 3.5 kV, nebulizer pressure - 50 psig, drying gas flow rate - 10 L/min, T = 350 °C, fragmentor voltage - 110 V, skimmer voltage - 65 V.

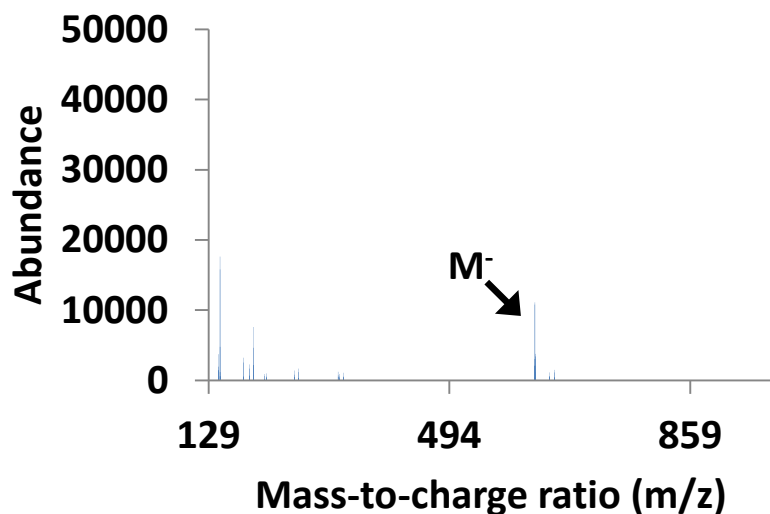


Figure D.4 - ESI mass spectrum measured for the Mn-protochelin complex allowed to air oxidize for 2 hours. Conditions: Solution prepared at pH 8.5, [Protochelin] = 1.1 mM, [Mn²⁺] = 1.07 mM, capillary voltage - 3.5 kV, nebulizer pressure - 50 psig, drying gas flow rate - 10 L/min, T = 350 °C, fragmentor voltage - 110 V, skimmer voltage - 65 V.

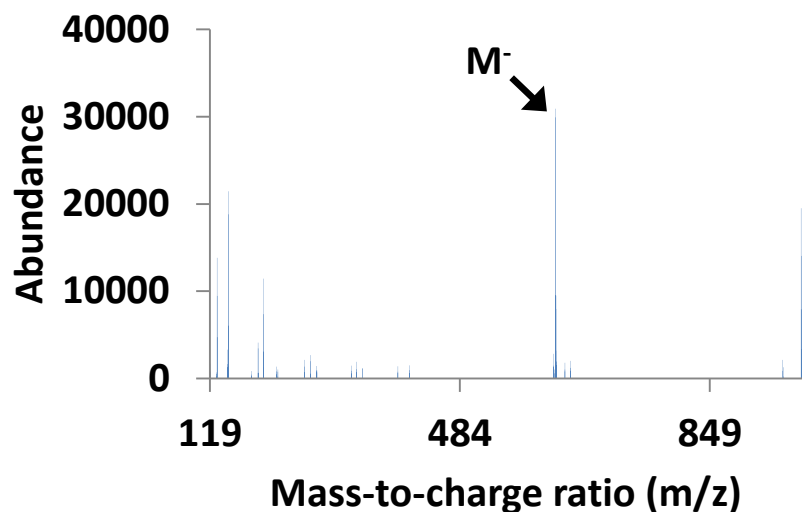


Figure D.5 - ESI mass spectrum measured for the Mn-protochelin complex after degradation for 4 hours. Conditions: Solution prepared at pH 8.5, [Protochelin] = 1.1 mM, $[\text{Mn}^{2+}] = 1.0$ mM, capillary voltage - 3.5 kV, nebulizer pressure - 50 psig, drying gas flow rate - 10 L/min, $T = 350$ °C, fragmentor voltage – 110 V, skimmer voltage - 65 V.

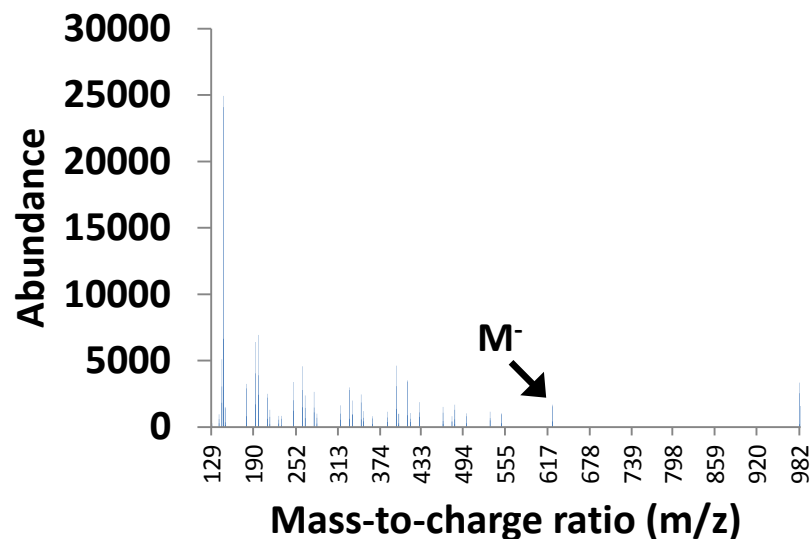


Figure D.6 - ESI mass spectrum measured for the Co-protochelin complex allowed to air oxidize for 30 minutes. Conditions: Solution prepared at pH 8.5, [Protochelin] = 1.0 mM, $[\text{Co}^{2+}] = 1.0$ mM, capillary voltage - 3.5 kV, nebulizer pressure - 50 psig, drying gas flow rate - 10 L/min, $T = 350$ °C, fragmentor voltage – 110 V, skimmer voltage - 65 V.

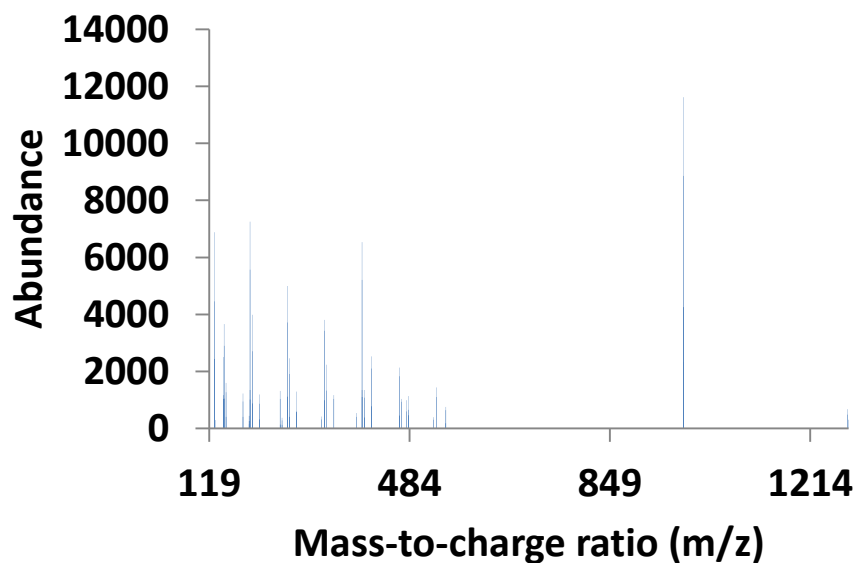


Figure D.7 - ESI mass spectrum measured for the Co-protocochelin complex allowed to air oxidize for 3 hours. Conditions: Solution prepared at pH 8.5, [Protocochelin] = 1.2 mM, $[\text{Co}^{2+}] = 1.13 \text{ mM}$, capillary voltage - 3.5 kV, nebulizer pressure - 50 psig, drying gas flow rate - 10 L/min, $T = 350 \text{ }^\circ\text{C}$, fragmentor voltage - 110 V, skimmer voltage - 65 V.

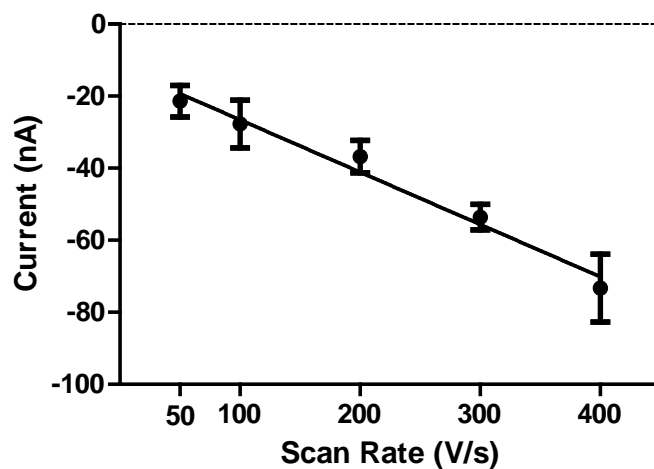


Figure D.8 - Plot of reductive peak current collected at -0.2 V as a function of scan rate for the redox reaction of protocochelin in aqueous solution. Demonstrating an adsorption controlled redox reaction ($n = 3$ electrodes, $r^2 = 0.978$).

Table D.1 - Calculated theoretical bond lengths (Å) of the Fe and Mn complexes of protochelin.

	Fe(III)H ₃ Proto	Fe(III)Proto ³⁻	Mn(III)Proto ³⁻
M-O1	1.939	2.041	1.918
M-O2	2.061	2.030	2.348
M-O3	2.084	2.149	1.934
M-O4	1.938	1.972	2.171
M-O5	1.96	2.038	1.966
M-O6	2.09	2.009	1.930

Table D.2 - Calculated strain energies for M-protochelin complexes bound in the catecholate [M(III)Proto³⁻] and salicylate [M(III)H₃Proto] forms. Energies are reported in units of Hartrees.

Complex	Cr (S ² =4)	Mn (S ² =3)	Fe (S ² =6)	Co (S ² =1)
M(III)Proto ³⁻	-3215.7161	-3322.1859	-3434.8652	-3553.8657
M(III)H ₃ Proto	-3217.1353	-3323.6018	-3436.2758	-3555.2835

^a S² represents the spin multiplicity, determined as number of unpaired electrons plus one.

D.5 References

1. Duckworth, O. W., Bargar, J. R., and Sposito, G. (2008) Sorption of ferric iron from ferrioxamine B to synthetic and biogenic layer type manganese oxides, *Geochim. Cosmochim. Acta* 72, 3371-3380.
2. Duckworth, O. W., Bargar, J. R., and Sposito, G. (2009) Quantitative structure-activity relationships for aqueous metal-siderophore complexes, *Environ. Sci. Technol.* 43, 343-349.
3. Duckworth, O. W., Jarzecki, A. A., Bargar, J. R., Oyerinde, O., Spiro, T. G., and Sposito, G. (2009) An exceptionally stable cobalt(III)-desferrioxamine B complex, *Marine Chem.* 113, 114-122.
4. Karlsson, T., Persson, P., Skyllberg, U., Morth, C. M., and Giesler, R. (2008) Characterization of iron(III) in organic soils using extended X-ray absorption fine structure spectroscopy, *Environ. Sci. Technol.* 42, 5449-5454.
5. Edwards, D. C., and Myneni, S. C. B. (2005) Hard and soft X-ray adsorption spectroscopic investigations of aqueous Fe(III)-hydroxamate siderophore complexes, *J. Phys. Chem. A* 109, 10249-10256.
6. Abergel, R. J., Warner, J. A., Shuh, D. K., and Raymond, K. N. (2006) Enterobactin protonation and iron release: structural characterization of the salicylate coordination shift in ferric enterobactin, *J. Am. Chem. Soc.* 128, 8920-8931.
7. Downward, L., Booth, C. H., Lukens, W. W., and Bridges, F. (2006) A Variation of the F-Test for Determining Statistical Relevance of Particular Parameters in EXAFS Fits In *13th International Conference on X-Ray Absorption Fine Structure* (Hedman, B., and Pianetta, P., Eds.), Stanford Synchrotron Radiation Laboratory, Stanford, CA.
8. Hamilton, W. C. (1965) Significance Tests on the Crystallographic R Factor, *Acta Cryst.* 18, 502-510.
9. Hudson, E. A., Allen, P. G., Terminello, L. J., Denecke, M. A., and Reich, T. (1996) Polarized x-ray-absorption spectroscopy of the uranyl ion: Comparison of experiment and theory, *Physical Review B* 54, 156-165.
10. Roberts, J. G., Moody, B. P., McCarty, G. S., and Sombers, L. A. (2010) Specific Oxygen-Containing Functional Groups on the Carbon Surface Underlie an Enhanced Sensitivity to Dopamine at Electrochemically Pretreated Carbon Fiber Microelectrodes, *Langmuir* 26, 9116-9122.

11. Bath, B. D., Michael, D. J., Trafton, B. J., Joseph, J. D., Runnels, P. L., and Wightman, R. M. (2000) Subsecond adsorption and desorption of dopamine at carbon-fiber microelectrodes, *Analytical Chemistry* 72, 5994-6002.
12. Bard, A. J., and Faulkner, L. R. (2001) *Electrochemical Methods: Fundamentals and Applications*, 2nd ed., John Wiley, New York.